Bayesian calibration and assessment of gas-surface interaction models and experiments in atmospheric entry plasmas

Anabel del Val

To cite this version:

Anabel del Val. Bayesian calibration and assessment of gas-surface interaction models and experiments in atmospheric entry plasmas. Reactive fluid environment. Institut polytechnique de Paris; Ecole Polytechnique (Palaiseau, France); Centre de Mathématiques Appliquées, École Polytechnique, France, 2021. English. NNT : 2021IPPAX081 . tel-03504757

HAL Id: tel-03504757
https://inria.hal.science/tel-03504757

Submitted on 29 Dec 2021

INSTITUT
POLYTECHNIQUE
DE PARIS

von KARMAN INSTITUTE
FOR FLUID DYNAMICS

CMAP

ÉCOLE
POLYTECHNIQUE

IP PARIS

NNT : 2021IPPAX081

Thèse de doctorat

Bayesian calibration and assessment of gas-surface interaction models and experiments in atmospheric entry plasmas

Thèse de doctorat de l'Institut Polytechnique de Paris
préparée au CMAP, École polytechnique et au Département d'aéronautique et d'aérospatiale de l'Institut von Karman de dynamique des fluides

École doctorale n°626 École Doctorale de l'IP Paris (ED IP Paris)
Spécialité de doctorat: mécanique des fluides et des solides

Thèse présentée et soutenue virtuellement, le 19 Novembre 2021, par

Anabel del Val

Composition du Jury :

Prof. Serge Prudhomme Professor, École Polytechnique Montréal	Rapporteur
Prof. Graham V. Candler Professor, University of Minnesota	Rapporteur
Dr. Anne Bourdon Directrice de recherche CNRS, École Polytechnique (LPP)	Examinatrice
Dr. Jean Lachaud Maître de conférences, Université de Bordeaux (I2MC)	Examinateur
Prof. Francesco Panerai Assistant professor, University of Illinois at Urbana-Champaign	Examinateur
Dr. Pietro M. Congedo Directeur de recherche Inria, Inria SIF/École Polytechnique (CMAP)	Co-directeur de thèse
Prof. Thierry E. Magin Professor, von Karman Institute for Fluid Dynamics	Co-directeur de thèse
Prof. Olivier Chazot Professor, von Karman Institute for Fluid Dynamics	Invité
Dr. Olivier P. Le Maître Directeur de recherche CNRS, Inria SIF/École Polytechnique (CMAP)	Invité
Prof. Miguel Hermanns Associate professor, Universidad Politécnica de Madrid	Invité

To all my teachers.

We are survivors of immeasurable events,
Flung upon some reach of land,
Small, wet miracles without instructions,
Only the imperative of change.

- Rebecca Elson, Evolution (A Responsibility to Awe)

Abstract

Space vehicles entering dense planetary atmospheres must withstand extreme heating conditions to protect the astronauts and cargo from damage. Aerospace engineers rely either on catalytic or ablative materials to protect the spacecraft from the intense heat. Qualitatively, both types of materials are different in the way they cope with high temperatures and how they can dissipate large amounts of energy. Catalytic materials re-radiate most of the heat back to the surrounding gas without undergoing fundamental changes in their structure. On the other hand, ablative materials transform the thermal energy into decomposition and removal of the protection material itself. Quantitatively, their differences are related to the physico-chemical models and the amount of model data needed for the simulation of their thermal response, as well as the observations that we can obtain in testing facilities.

The investigation of gas-surface interaction phenomena relies on the development of predictive theoretical models and the capabilities of current experimental facilities. Both resources are strong assets of scientific research. However, due to the complexity of the physics and the various phenomena that need to be investigated in ground-testing facilities, both numerical and experimental processes generate data subjected to uncertainties. Nevertheless, it remains a common practice in the field of aerothermodynamics to resort to calibration and validation methods that are not apt for rigorous uncertainty treatment. Further, as the complexity and level of definition of gas-surface interaction models increase, so does the number of parameters that need estimation. To alleviate this problem, the current state-of-the-art inverse methodology is to project as many assumptions about the physics as considered plausible in order to reduce the number of parameters sought out, potentially biasing the results and substantially slowing down the progress for these aerospace systems.

This thesis investigates the process of scientific inference and its ramifications for selected gas-surface interaction experiments. Its main contributions are the improvement and re-formulation of model calibrations as statistical inverse problems with the consequent extension of current databases for catalysis and ablation. The model calibrations are posed using the Bayesian formalism where a complete characterization of the posterior probability distributions of selected parameters are computed.

The first part of the thesis presents a review of the theoretical models, experiments and numerical codes used to study catalysis and ablation in the context of the von Karman Institute's Plasmatron wind tunnel. This part ends with a summary on the potential uncertainty sources present in both theoretical-numerical and experimental data. Subsequently, the methods used to deal with these uncertainty sources are introduced in detail.

The second part of the thesis presents the various original contributions of this thesis. For catalytic materials, an optimal likelihood framework for Bayesian calibration is proposed. This methodology offers a complete uncertainty characterization of catalytic parameters with a decrease of 20% in the standard deviation with respect to previous works. Building on this framework, a testing strategy which produces the most informative catalysis experiments to date is studied. Experiments and consequent stochastic analyses are per-

formed, enriching existing catalysis experimental databases for ceramic matrix composites with accurate uncertainty estimations.

The last contribution deals with the re-formulation of the inference problem for nitridation reaction efficiencies of a graphite ablative material from plasma wind tunnel data. This is the first contribution in the literature where different measurements of the same flowfield are used jointly to assess their consistency and the resulting ablation parameters. An Arrhenius law is calibrated using all available data, extending the range of conditions to lower surface temperatures where no account of reliable experimental data is found. Epistemic uncertainties affecting the model definition and ablative wall conditions are gauged through various hypothesis testing studies. The final account on the nitridation reaction efficiency uncertainties is given by averaging the results obtained under the different models.

This thesis highlights the fact that the process of scientific inference can also carry deep assumptions about the nature of the problem and it can impact how researchers reach conclusions about their work. Ultimately, this thesis contributes to the early efforts of introducing accurate and rigorous uncertainty quantification techniques in atmospheric entry research. The methodologies here presented go in line with developing predictive models with estimated confidence levels.

Résumé

L'étude des phénomènes d'interaction gaz-surface pour les véhicules d'entrée atmosphérique est basée sur le développement de modèles théoriques prédictifs et sur les capacités des installations expérimentales actuelles. Toutefois, en raison de la complexité de la physique et des divers phénomènes qui doivent être étudiés dans ces installations, les simulations tant numériques qu'expérimentales génèrent des données qui présentent des incertitudes. Cependant, il est courant dans le domaine de l'aérothermodynamique de recourir à des méthodes de calibration et de validation non adaptées à un traitement rigoureux de ces incertitudes.

Cette thèse étudie le processus d'inférence scientifique et ses ramifications dans certaines expériences d'interaction gaz-surface. Ses principales contributions sont l'amélioration et la reformulation de la calibration de modèles en tant que problème statistique inverse et l'extension résultante des bases de données actuelles pour la catalyse et l'ablation. La calibration des modèles utilise le formalisme Bayésien où la caractérisation complète des distributions de probabilités postérieures des paramètres sélectionnés est calculée.

La première partie de la thèse présente une revue des modèles théoriques, des expériences et des codes de simulation numérique utilisés pour étudier la catalyse et l'ablation dans le Plasmatron, la soufflerie à plasma de l'Institut von Karman. Cette partie se termine par un résumé des sources possibles d'incertitude présentes dans les données théoriques-numériques et expérimentales. Ensuite, les méthodes utilisées pour traiter mathématiquement ces sources d'incertitude sont présentées en détail.

La deuxième partie présente les différentes contributions originales de cette thèse. Pour les matériaux catalytiques, une méthodologie de vraisemblance optimale pour l'inférence Bayésienne est développée. Cette méthodologie offre une caractérisation complète de l'incertitude des paramètres catalytiques avec une diminution de 20% de l'écart type par rapport aux travaux antérieurs. En utilisant cette méthodologie, une stratégie de test produisant les données expérimentales de catalyse les plus informatives à ce jour est proposée. Ensuite, des expériences et des analyses stochastiques sont effectuées, enrichissant les bases de données expérimentales de catalyse existantes pour les composés à matrice céramique à l'aide d'estimations précises de l'incertitude.

La dernière contribution est la reformulation du problème d'inférence des efficacités de réaction de l'azote à la surface d'un matériau ablatif en graphite à partir des données de soufflerie à plasma. Il s'agit de la première étude dans la littérature où différentes observations de la même expérience sont utilisées ensemble pour évaluer leur cohérence et les paramètres d'ablation qui en résultent. Une loi d'Arrhenius stochastique est déduite en utilisant toutes les données disponibles, étendant la gamme de conditions à des températures de surface plus basses, là où il n'y a pas de données expérimentales fiables. L'incertitude épistémique qui affecte la définition du modèle et les conditions aux limites d'ablation sont étudiées par des méthodes de test d'hypothèses. L'incertitude finale sur l'efficacité de la réaction azotée est obtenue en moyennant les résultats obtenus avec les différents modèles.

Cette thèse met en évidence que le processus d'inférence scientifique peut également imposer des hypothèses sur la nature du problème et avoir un impact sur la manière dont les chercheurs parviennent à des conclusions sur leur travail. En fin de compte, cette thèse contribue aux premiers efforts d'introduction de techniques précises et rigoureuses de quantification de l'incertitude dans le domaine de recherche de l'entrée atmosphérique. Les méthodologies présentées ici permettront in fine le développement de modèles prédictifs avec estimation de niveaux de confiance.

Acknowledgements

I always wanted to be an astronaut. Or some sort of Space Engineer that would sit at a Mission Control console and see things fly. Then, in my third year of undergraduate studies, I opened a Fluid Mechanics book for the first time and I absolutely fell in love. I struggled to reconcile these two passions in a way that would make sense for me to find a career but then I learned about aerothermodynamics and the rest is in these pages.

Stories are best told from the beginning. Miguel, you were the first to enlighten me on this path. Your classes were exciting and didactic and you made it easy for your students to love the topic. This made my choice very easy and it would have been very different had you not been a good teacher and mentor. You also essentially sent me to VKI to pursue my Master's and PhD theses and I will always be grateful for that. I'm really happy you got to see the end result by attending both my Master's and PhD defenses. Also, Madrid is the best city in the world, period.

At VKI, my academic home, I met one half of my PhD supervisory team: Olivier and Thierry. None of this thesis would have happened without either of you. You believed in me more than I believed in myself and I always found support when turning to you. Olivier, you showed me the big picture of my research. It seems an easy thing to say but, in retrospect, it was the hardest part to grasp. It is very easy to be lost in jargon and technical details, and it is very hard to recognize how your research can impact future work in the field or how we may answer bigger questions. Through discussions in your office, always open, we would follow our own Socratic method and we would both learn from each other. I'll always remember and cherish that. Thierry, I'm pretty sure you were the first one to say the words "uncertainty quantification" to me. I don't think words can make justice to the immense gratitude I owe you. You were always there, always encouraging me, always ready to teach on the blackboard, always ready to listen, always giving me the freedom you recognized I wanted from time to time. You introduced me to the other half of the supervisory team and this was crucial for me and for this thesis. Your students are lucky to have you.

The other half of my supervisory team: Pietro and Olivier. I have learned so so much from you, not only technical things but also your attention to detail and scientific rigor, qualities which I think will be invaluable to me as I begin the rest of my career. You devoted so much of your time to me and my research, and overall you made me a better scientist. Pietro, you welcomed me with open arms to your Inria team, before the Platon team formally started. You helped me navigate the French doctoral school system (not an easy task at all!) and were always available to discuss and provide feedback on everything I have done in this thesis. My papers, thesis manuscript and presentations are much better because of your dedication and I am forever grateful for all the things I learned from you. Olivier, with Pietro you showed me a whole new language. That of UQ. The first time we actually sat down in front of the whiteboard to discuss the catalysis problem was an eye-opening experience. It opened my eyes to how much work I had ahead of me to understand all the things we were discussing. From there on I can only say I liked the topic more and more, and I'm forever grateful to you for your dedicated teaching and hours devoted to

our discussions and feedback. I'm very proud to have been part of your Inria team.

I want to sincerely thank the other thesis committee members for their feedback and insightful questions. Prof. Serge Prudhomme and Prof. Graham Candler have my utmost gratitude for agreeing to review the manuscript and for providing their comments and insights. I would also like to thank Dr. Anne Bourdon for agreeing to chair the committee, as well as Prof. Francesco Panerai and Dr. Jean Lachaud for their helpful questions and comments during the defense.

My VKI colleagues and friends, a part of this thesis belongs to you...Bruno, Tânia, George, Elissavet, Bogdan, Francisco, Federico, Alessandro, Bernd, Erik, Vincent, Sophia, Claudia, Alessia, Fabrizio, Stefano, Alex, Michele, Joffrey, David, Iván, Simon, Alan, Jesús, Diana, Enrico, Andrea, Adriana, Sara and Zuheyr. You encouraged and supported me through thick and thin, and lent a hand when needed. I genuinely appreciate your friendship, wish you the best and that our friendship continues for many years. Of course, VKI also has an extended family...Marina, Chiara, Baris, Grace, Denitsa, Ian, Little Marina, Leo, Timo, Déniz, Gaia, Zeno and Theo, you all made everything better.

Over the years, I have been traveling back and forth between Brussels and Paris for a few months at a time. I had to switch offices and friends but João and Giulio, my Inria and UTOPIAE colleagues, made it worthwhile and easy. I know we are friends for life now and that our research paths are likely to cross! and I couldn't be prouder to have shared this journey with you. The Paris gang wouldn't be complete without Nicolas and Malo with whom I shared great times around Polytechnique and Paris. I wish you success in your endeavors.

My UTOPIAE colleagues, scattered all around Europe: UK, Italy, Germany, Slovenia, France and Belgium. Continuously exchanging with you on UQ topics made me grow in my own research back at home and I owe gratitude to UTOPIAE not only for the financial support of my PhD but also for the lectures we received throughout the years from experts in UQ and optimization while having fun around Europe. The girls, Bárbara, Elisa and Margarita, you made everything so much better and we have supported each other through so much, I'll cherish all of it. Tatha, you welcomed me to Durham, in the UK, and showed me the proper Bayesian way in English pubs (the way Bayes himself would have done it).

No puedo más que agraceder a mi familia, Encarni, Jesús (padre) y Jesús (somos muy originales en esta familia), por todo su apoyo. Gracias por vuestra confianza en mí y por alimentar siempre, desde pequeña, mi curiosidad. Nunca me he visto en la tesitura de tener que elegir entre algo práctico o lo que me gusta porque vuestro amor incondicional me alentó en todo momento durante todos estos años.

I would also like to thank wholeheartedly JB's family - James, Susan, Cameron and Catie - for their support and love throughout the years. And finally, to my best friend and life companion, JB (who, at the time of writing this hasn't read my thesis...). Sharing my daily life with you is a gift, and your support (and Fred's...) was essential to get through this PhD. We are so fortunate to have found each other and share the same love and understanding for the work we do. You make me better in all possible ways while keeping each other inspired. I'm the luckiest person in the world for having you in my life, and looking back, it's amazing what we have built together...Thank you for being my biggest fan, always.

Anabel del Val
North Carolina, 2021

Contents

Publications

The following publications have contributed directly or indirectly to this thesis. The author would also like to gratefully acknowledge the opportunities to present unpublished work at various international meetings as well as seminars. These meetings have significantly contributed to this thesis through collaboration and discussion with experts in the various fields.

Journal articles

1. **A. del Val**, O. P. Le Maître, O. Chazot, T. E. Magin and P. M. Congedo. A surrogate-based optimal likelihood function for the Bayesian calibration of catalytic recombination in atmospheric entry protection materials. *Applied Mathematical Modelling (In press)* - `https://arxiv.org/abs/2010.04649`.

2. **A. del Val**, D. Luís and O. Chazot. Experimental methodology for the accurate stochastic calibration of catalytic recombination affecting reusable spacecraft thermal protection systems. *(Submitted to Experimental Thermal and Fluid Science)* - *https://doi.org/10.13140/RG.2.2.30127.66722*.

3. **A. del Val**, O. P. Le Maître, P. M. Congedo and T. E. Magin. Inference of nitridation reaction efficiencies of graphite in nitrogen plasma flows using a Bayesian formulation. *(To be submitted)*.

4. **A. del Val**, M. Capriati, O. P. Le Maître, P. M. Congedo and T. E. Magin. Assessment and selection of surface balance models through Bayesian evidence for the calibration of nitridation reaction efficiencies under model form uncertainties. *(In preparation)*.

Conference proceedings

1. **A. del Val**, O. P. Le Maître, O. Chazot, P. M. Congedo and T. E. Magin. Inference methods for gas/surface interaction models: from deterministic approaches to Bayesian techniques. *Uncertainty Quantification & Optimization 2020* conference proceedings - `https://hal.inria.fr/hal-03081323`

2. D. Luís, **A. del Val** and O. Chazot. Characterization under Uncertainty of Catalytic Phenomena in Ceramic Matrix Composites Materials for Spacecraft Thermal Protection Systems, 8th European Conference for Aeronautics and Aerospace Sciences (EUCASS), Madrid, June 2019. *DOI: 10.13009/EUCASS2019-257* - `https://www.eucass.eu/doi/EUCASS2019-0257.pdf`.

3. B. Arizmendi, T. Bellosta, **A. del Val**, G. Gori, J. Reis and M.Prazeres. On Real-time Management of On-board Ice Protection Systems by means of Machine Learning, AIAA AVIATION Forum, Dallas, June 2019

Book chapters

1. **A. del Val**, O. Chazot, T. E. Magin and P. M. Congedo (2020). A Bayesian perspective on TPS catalysis phenomena: learning from experiments and proposing new ones, Review of the VKI Doctoral Research 2019-2020, Rhode-St-Genèse, Belgium.

2. **A. del Val**, O. Chazot and T. E. Magin. Uncertainty Treatment Applications: High-Enthalpy Flow Ground Testing, In *Optimization Under Uncertainty with Applications to Aerospace Engineering*, Ed. M. Vasile, Springer Nature 2020

3. **A. del Val**, O. Chazot, T. E. Magin and P. M. Congedo (2019). Towards a Systematic Framework for the Design of Experiments: Application to Catalytic Phenomena in Plasma Wind Tunnels, Review of the VKI Doctoral Research 2018-2019, Rhode-St-Genèse, Belgium.

4. **A. del Val**, O. Chazot, T. E. Magin and P. M. Congedo (2018). Stochastic Inference of the Catalytic Properties of Thermal Protection Materials from Plasma Wind Tunnel Experiments, Review of the VKI Doctoral Research 2017-2018, Rhode-St-Genèse, Belgium.

International meetings, presentations, and seminars

1. **ESA ACT**, European Space Agency Advanced Concepts Team, Online, March 2021: *Surviving the fire: how games of chance are helping us understand spacecraft atmospheric entry.*

2. **Uncertainty Quantification & Optimization Conference**, Online, Nov 2020: *Inference methods for gas/surface interaction models: from deterministic approaches to Bayesian techniques.*

3. **Optimization in Space Engineering (OSE5)**, Ljubljana, November 2019: *On the Inference of Chemical Model Parameters for Tomorrow's Space Journeys: an Overview on Reusable and Ablative Space Systems.*

4. **Stats4Grads, Durham University**, Durham (UK), 6 Nov 2019: *Bayes goes to Space: inferring chemical model parameters for tomorrow's Space journeys.*

5. **International Congress on Industrial and Applied Mathematics (ICIAM)**, Valencia University, Valencia, Spain, 15-19 July 2019: *Bayesian Calibration of Gas/-Surface Interaction Models for Thermal Protection Materials under Spacecraft Reentry Conditions.*

6. **8th European Conference for Aeronautics and Aerospace Sciences (EUCASS)**, Madrid, June 2019: *Characterization under Uncertainty of Catalytic Phenomena in Ceramic Matrix Composites Materials for Spacecraft Thermal Protection Systems.*

7. **Uncertainty Quantification & Optimization Conference**, Sorbonne University, Paris, France, 18-20 March 2019: *Robust calibration of the catalytic properties of thermal protection materials: Application to plasma wind tunnel experiments.*

8. **Fluid Mechanics Seminar Series**, ETSIAE, UPM, Madrid, Spain, 1 Oct 2018: *Characterization of spacecraft reusable heatshield materials from plasma wind tunnel experiments: a Bayesian inference approach.*

9. **Entry Systems and Technology Division Seminar**, NASA Ames Research Center, Moffet Field, CA, 30 August 2018: *Stochastic inference of the catalytic properties of thermal protection materials from plasma wind tunnel experiments.*

10. **7th European Conference on Computational Fluid Dynamics (ECCOMAS)**, Glasgow, UK, 11-15 June 2018: *Stochastic inference of the catalytic properties of thermal protection materials from plasma wind tunnel experiments.*

Code: GitHub repositories

- **SoFIA: So**bol-based sensitivity analysis, **F**orward and **I**nverse uncertainty propagation for **A**pplication to high temperature gases (*Under development*) - `https://github.com/pysofia/SoFIA`

List of Figures

List of Tables

Nomenclature

Roman Symbols

A	Arrhenius pre-exponential factor
A	frontal area of calorimeter
BF	Bayes factor
c_p	specific heat at constant pressure
c_p^E	specific heat at constant pressure of the electronic mode
c_p^R	specific heat at constant pressure of the rotational mode
c_p^V	specific heat at constant pressure of the vibrational mode
c_v	specific heat at constant volume
$\mathscr{D}$	binary diffusion coefficient
e	internal energy
e^F	formation energy
e^T	internal energy of translational mode
e^int	internal energy of internal energy modes
e^E	internal energy of electronic mode
$e^\mathcal{V}$	internal energy of vibrational bath
E	energy of a particle or energy level
$\boldsymbol{E}$	electric field vector
E_a	Arrhenius activation energy
g	degeneracy of a particular energy state
g	Gibbs free energy
G	molar Gibbs free energy
$\boldsymbol{G}$	transport linear systems matrices
H	total enthalpy
$\bar{\bar{I}}$	identity matrix

k_{f}	forward reaction rate
k_{b}	backward reaction rate
K_{eq}	equilibrium constant
$\mathcal{L}$	set of energy levels
$\mathcal{L}$	likelihood function
m	particle mass
$\dot{m}$	mass flow
M	molecular weight
n	number density
$\mathcal{N}$	Gaussian distribution
$n_{\mathcal{H}}$	number of heavy species
$n_{\mathcal{L}}$	number of energy levels
$n_{\mathcal{R}}$	number of reactions
$n_{\mathcal{R}_{\mathrm{w}}}$	number of wall reactions
$n_{\mathcal{S}}$	number of species
$n_{\mathcal{S}^*}$	number of molecules
p	pressure
$\mathcal{P}$	probability distribution
P_{d}	dynamic pressure
P_{el}	coils electric power
P_{plasma}	power transmitted to the plasma
P_{s}	static pressure
p_{e}	electron pressure
q	particle charge
Q	partition function
$\bar{Q}$	reduced collision integral
Q^{T}	translational mode partition function
Q^{int}	internal modes partition function
Q^{E}	electronic mode partition function
Q^{R}	rotational mode partition function

Q^{V}	vibrational mode partition function
$\boldsymbol{q}$	heat flux
$\boldsymbol{q}_{\mathrm{w}}$	wall heat flux
$\boldsymbol{q}^{\mathcal{V}}$	internal heat flux
R	specific gas constant
h	enthalpy
h^{E}	electronic mode enthalpy
h^{T}	translational enthalpy
h^{int}	internal modes enthalpy
$\mathcal{H}$	set of heavy species
$\mathcal{R}^{\mathrm{I}}$	set of reactions involving electron-impact ionization
$\mathcal{R}$	reaction rate of progress
s	entropy
$\dot{s}$	recession rate
s^{T}	translational entropy
s^{int}	internal modes entropy
s^{E}	electronic mode entropy
$\mathcal{S}$	set of species
$\mathcal{S}^{\mathrm{a}}$	set of atoms
$\mathcal{S}^{*}$	set of molecules
T	translational-rotational bath temperature
T_{h}	temperature heavy species
T_{δ}	boundary layer edge temperature
$T_{\delta}^{\mathcal{V}}$	boundary layer edge internal temperature
T_{e}	free electron translational temperature
T_{E}	electronic temperature
T_{T}	heavy translational temperature
T_{R}	rotational temperature
T_{V}	vibrational temperature
T_{w}	wall translational temperature

$T_{\mathrm{w}}^{\mathcal{V}}$	wall internal temperature
$\boldsymbol{u}$	hydrodynamic velocity vector
$\mathcal{U}$	uniform distribution
$\boldsymbol{u}_{\delta}$	boundary layer edge hydrodynamic velocity vector
$\boldsymbol{u}_{\mathrm{w}}$	wall hydrodynamic velocity vector
$\boldsymbol{V}$	diffusion velocity vector
$\mathcal{V}$	vibrational thermal bath
W	body radiance
x	mole fraction
y	mass fraction

Greek Symbols

α	collisional efficiency parameter
β	energy accommodation coefficient
β	Arrhenius exponential factor
β	velocity gradient
δ	boundary layer thickness
ϵ	surface emissivity
γ	catalytic recombination efficiency parameter
γ	ablation efficiency parameter
λ	translational-rotational contribution to the thermal conductivity
λ_{e}	electron contribution to the thermal conductivity
λ^{E}	electronic contribution to the thermal conductivity
λ^{R}	rotational contribution to the thermal conductivity
λ^{T}	translational contribution to the thermal conductivity
$\lambda^{\mathcal{V}}$	vibrational-electronic-electron contribution to the thermal conductivity
μ	viscosity coefficient
μ	mean value
$\nu^{'}$	forward stoichiometry coefficient

ν''	backard stoichiometry coefficient
Π	non-dimensional parameter
ρ	mass density
ρ_δ	boundary layer edge mass density
ρ_{w}	wall mass density
σ	standard deviation
$\bar{\bar{\tau}}$	viscous stress tensor
τ^{eT}	heavy-electron translational energy relaxation time
τ^{VT}	vibrational-translational energy relaxation time
$\dot{\omega}$	mass production rate due to chemical reactions
$\dot{\omega}_{\mathrm{w}}$	mass production rate due to heterogeneous chemical reactions
Ω^{CV}	chemical-vibrational energy coupling term
Ω^{eT}	heavy-electron translational energy relaxation rate
Ω^{I}	thermal energy lost provided by electrons during electron impact reactions
Ω^{VT}	vibrational-translational energy relaxation rate
σ^{V}	effective collision cross-section for internal energy relaxation

Acronyms

AIC	Akaike Information Criterion
AM	Adaptive Metropolis
ANOVA	Analysis of Variances
BB	Blackbody
BIC	Bayesian Information Criterion
BL	Boundary Layer
BMA	Bayesian Model Averaging
CFD	Computational Fluid Dynamics
CFL	Courant-Friedrichs-Lewy
CMC	Ceramic Matrix Composite
CV	Coefficient of Variation

DNRSE	Dimensionally-Reduced Navier-Stokes Equations
DoE	Design of Experiments
EAST	Electric Arc Shock Tube
EM	Electromagnetic
ESA	European Space Agency
EXPERT	European Experimental Reentry Test-Bed
FV	Finite Volume
GP	Gaussian Process
GSI	Gas-Surface Interaction
ICCD	Intensified Charge-Coupled Device
ICP	Inductively-Coupled Plasma
IPM	Institute for Problems in Mechanics
IRS	Institute of Space Systems
LEO	Low Earth Orbit
LHS	Latin Hypercube Sampling
LHTS	Local Heat Transfer Simulation
LIF	Laser-Induced Fluorescence
LTE	Local Thermodynamic Equilibrium
MAP	Maximum A Posteriori
MC	Monte Carlo
MCMC	Markov Chain Monte Carlo
MH	Metropolis-Hastings
MOL	Method-Of-Lines
MTA	MT Aerospace
MUSCL	Monotone Upstream Centered Schemes for Conservation Laws
NASA	National Aeronautics and Space Administration
ODE	Ordinary Differential Equation
PDF	Probability Distribution Function
PDE	Partial Differential Equation
PECOS	Center for Predictive Engineering and Computational Sciences

PLC	Programmable Logic Controller
QMC	Quasi Monte Carlo
RMSE	Root Mean Squared Error
RRHO	Rigid-Rotor Harmonic-Oscillator
SEB	Surface Energy Balance
STS	State-To-State
TCNEQ	Thermochemical Non-Equilibrium
TOF	Time Of Flight
TPS	Thermal Protection System
UQ	Uncertainty Quantification
VKI	von Karman Institute

Chapter 1

Introduction

What's past is prologue

- William Shakespeare, The Tempest

1.1 Atmospheric entry: a complex problem

Space travel, since its beginnings in Low Earth Orbit (LEO) to the exploration of our Solar System, has led to countless scientific advancements in what it is one of the most challenging undertakings of humankind. Venturing into Space requires large amounts of energy to reach orbital and interplanetary velocities. All this amount of energy is dissipated when a space vehicle enters dense planetary atmospheres [6]. The bulk of this energy is exchanged during the entry phase by converting the kinetic energy of the vehicle into thermal energy in the surrounding atmosphere through the formation of a strong bow shock ahead of the vehicle [7]. The interaction between the chemically reacting gas and the Thermal Protection System (TPS) is governed by the material behavior which injects new species into the boundary layer through different mechanisms [8].

Fig. 1.1 shows a schematic representation of the different physical phenomena that occur in atmospheric entry flows. The figure focuses on the vicinity of the stagnation line close to the vehicle's surface. In the zone immediately behind the bow shock, collisions between the gas particles lead to the excitation of the internal degrees of freedom of atoms and molecules. When collisions are energetic enough, dissociation and ionization reactions can occur. The atoms produced as a result of the dissociation can then recombine in the boundary layer with a consequent release of their energy of formation. This causes a substantial increase of the wall heat flux, which becomes the main design parameter for the heat shield. At the surface, different mechanisms are responsible for either enhancing the heat flux to the surface through catalytic recombination or mitigating the convective and diffusive heat fluxes from the gas phase through removal of the material itself.

In general, two different families of materials are used to protect the spacecraft from damage. **Reusable heat shields** rely on low catalytic materials, such as Ceramic Matrix Composites (CMC), which are passively cooled by re-radiating a significant amount of energy back to the surrounding atmosphere. They can withstand mild Earth reentries from orbital velocities (7 km/s) and their structures do not undergo fundamental changes under normal conditions. **Ablative heat shields** also dissipate a significant amount of heat through radiation. However, unlike reusable systems, ablators are designed for single use, dissipating the remaining heat by converting thermal energy into decomposition and degradation of the material itself, causing the surface of the ablator to recess over time. Ablative TPS are generally constructed from rigid carbon fiber or silicon composites, impregnated with an organic resin matrix which serves as a pyrolyzing binder and provides strength to the overall TPS structure.

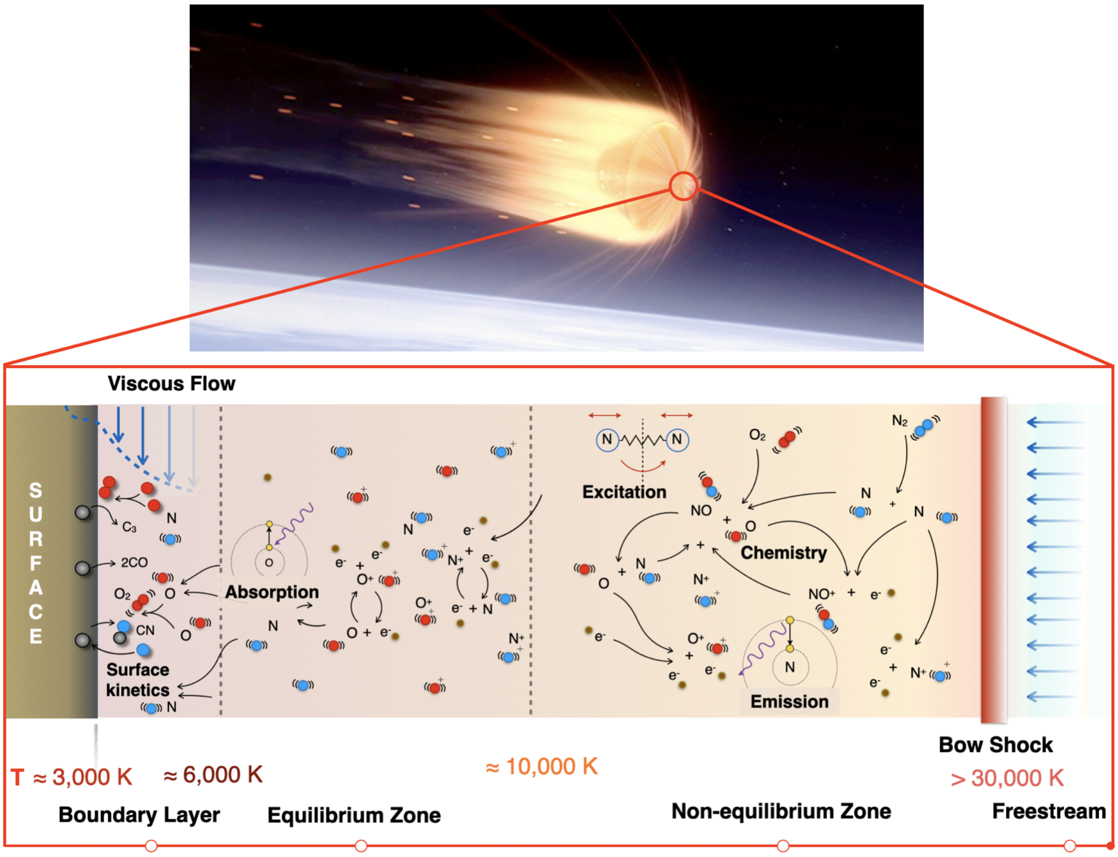

Figure 1.1: *Atmospheric entry capsule (credits: `https://www.nasa.gov/specials/orionfirstflight/`) and schematic representation of the different phenomena taking place in atmospheric entry flows: shock layer radiation and excitation, and gas phase and surface kinetics. The figure represents the vicinity of the stagnation line with the vehicle's surface placed on the left side. Adapted from Scoggins [1].*

From the free stream to the wall state, passing through the shock layer, the flowfield is an interdependent medium where different time scales can be defined. They are representative of the phenomena depicted in Fig. 1.1. For example, we typically define the time scale of the flow as how fast the bulk of the fluid is moving. Other important process-dependent time scales are the time it takes the flow chemistry to equilibrate as well as the characteristic time for the relaxation of the different thermodynamic energy sources within the flow.

In such complex environment, it is not possible to isolate one given effect to study it further, aside from the rest of the flowfield. If we want to study the surface kinetics, we need to understand the mechanisms by which species are fed to the wall and how these affect the resulting surface kinetics. Further, chemical and diffusion mechanisms in the flowfield are affected by the flight conditions, the shape of the space capsule and the composition of the atmosphere we are plunging in. Developing a combined physical understanding on all the aspects of atmospheric entry flight is a task worth of a dedicated community. As such, experimental facilities and techniques have been developed alongside theoretical models to capture and understand all underlying phenomena [9].

Ground testing for gas-surface interaction

Ground testing is essential for the development and design of aerospace vehicles [10]. It represents a convenient step at reduced cost compared to real flight experiments. Further, ground tests allow better control of the environment as well as direct measurements to investigate the complex flowfield and material response in high-speed, reacting flows. In particular, the different time scales related to each physical phenomenon force us to use a set of complementary facilities to fully characterize the flow and material response (Fig. 1.2). The thermal environment can be duplicated in plasma wind tunnels. They are able to run for long testing times overcoming the thermal inertia of the material to properly test its response to the dissociated, reacting flow. Since the flow regime can be either subsonic or supersonic, similarity techniques have to be defined for the duplication of flight conditions [11–13]. Radiation and non-equilibrium effects can be reproduced in high-enthalpy wind tunnels which are able to run for a very short period of time, of the order of miliseconds or lower, depending on the mechanism used to generate the high speed flow [10]. Due to the limited size of the scaled spacecraft models, similarity parameters are also used to link the different phenomena to flight conditions [11].

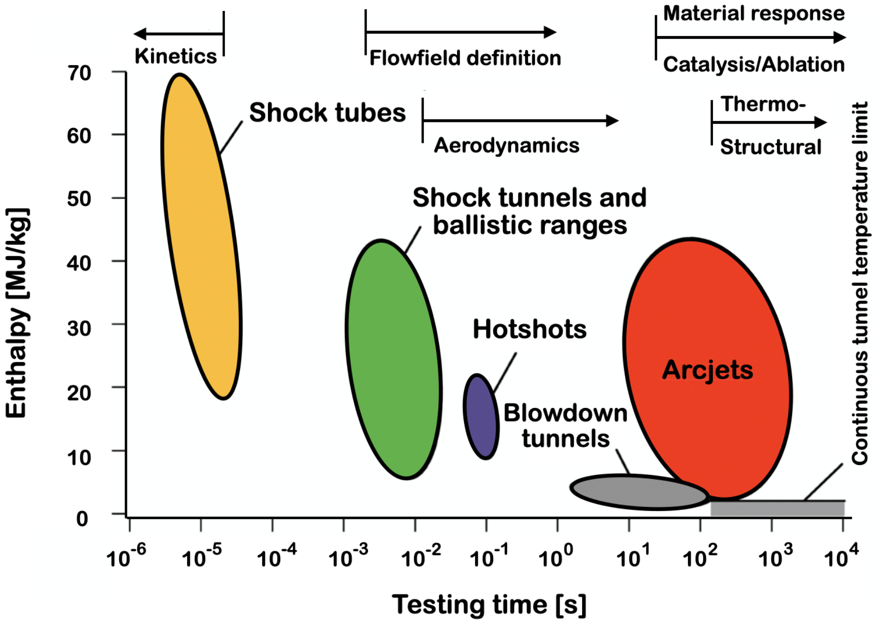

Figure 1.2: *Enthalpy vs testing time of families of experimental facilities available to study atmospheric entry flows. Figure adapted from Wright [2].*

In particular, testing in plasma wind tunnels for gas-surface interactions such as catalysis and ablation, requires the use of several measurement techniques combined with model predictions. The current state-of-the-art plasma wind tunnel testing for material characterization does not have means to directly probe the different surface kinetic mechanisms [3, 14–22]. We can only get indirect information which needs to be processed through theoretical models to isolate and trace back the observed effects to the surface kinetics.

Catalysis testing in plasma wind tunnels relies on heat flux, pressure and surface temperature measurements [14–20]. Generally, more than one material are tested at a given time and their measured wall heat fluxes are compared. In making assumptions for the response of one of the materials, used as reference, we can infer what portion of the heat flux experienced by the TPS material is due to the presence of catalytic recombination. Ablation testing, on the other hand, has access to another set of observations. As ablative materials recess and decompose, we can have a direct probing of such effect in plasma wind tunnels [3, 21, 22]. Recession rates, in contrast with heat fluxes, are a direct effect of ablative processes and their strength for given conditions. Heat fluxes, on the other hand, are the sum observations of gas phase and material effects which poses further challenges for their disentanglement and accurate inference. Further, ablative systems inject carbonaceous species into the boundary layer which can produce strong radiative signatures. These species can also be probed and traced back to ablation mechanisms giving further insight.

Overall, the process of inferring catalysis and ablation parameters based on heat fluxes or recession rates poses many questions that span beyond our experimental capabilities to the assumptions in our models. We still grapple with understanding our own experimental facilities to the point that we must admit ignorance about the relevant physical processes for different experimental conditions in some cases. While experiments are giving us answers to questions, sometimes we must admit that it is not clear what are the questions to which the answers pertain and this is significantly slowing down our progress.

Furthermore, while experimental facilities are capable of providing data regarding the different phenomena acting during atmospheric entry, no information about their coupling mechanisms can be truly recovered. When the surface heating is correctly reproduced for a trajectory point, shock layer radiation and non-equilibrium effects are not correctly duplicated at the same time. Conversely, reproducing shock layer radiation and non-equilibrium effects in high enthalpy facilities provides no information on the TPS surface heating. Only flight experiments and theoretical models can bridge that gap. Flight experiments are quite costly and they are generally used to validate the design approach rather than to study and validate physical models. Therefore, approaches that can combine several sources of information to produce a consistent and realistic picture of the involved physics would be desirable.

Theoretical modeling for gas-surface interaction

On the side of the theoretical modeling, we have to deal with the multiscale and multiphysics nature of the problem. It requires the integration of different subjects such as chemical kinetics, quantum and statistical mechanics, electromagnetism, material science and computational methods. An accurate modeling of hypersonic flows must account for all the relevant physico-chemical phenomena occurring both in the gas and solid phases. The accurate modeling of these high temperature flows is important not only for obtaining an efficient design of the spacecraft TPS but also for a correct interpretation of experimental measurements in high-enthalpy and plasma wind tunnels.

In the particular case of gas-surface interaction from the flow perspective, the surface acts as a boundary which modifies the species concentrations, momentum and energy of the flow. Surface balances are proposed for the approximate modeling of the action of the wall on the surrounding gas phase [23–25]. Many assumptions feed these surface models, from the phenomena we take into account in the surface balances to their particular closure models for heterogeneous chemistry, conductive heat flux to the material, etc. In particular, the complexity of heterogeneous chemistry models range from simple empirical correlations and simplified relationships to detailed multi-step processes such as adsorption, site hopping, bond breaking and formation, desorption, etc. To date, validated models for flight-relevant surface chemistry do not exist. This is an active area of research in the aerothermodynamics community. Moreover, the predictions of the different models established in the literature differ significantly from each other.

In general, empirical or phenomenological models for heterogeneous chemistry have a smaller number of parameters that need definition. They tend to describe the gas-surface interaction from the macroscopic point of view. Conversely, detailed chemistry models need a larger number of parameters and they are built to describe the surface kinetics in a more comprehensive manner. While phenomenological models tend to lump together different phenomena under a handful of parameters, detailed chemistry models tend to assign different parameters and mathematical structure to each microscopic phenomenon. A relevant consequence is that detailed chemistry models have the ability to describe a more refined physical structure and their interpretation is very straightforward. Resolving finer physics in our models means being able to generalize them to broader conditions in a more consistent way. Nevertheless, as long as the experimental data lack such physical depth in what can be resolved from the observations, we are largely left in the dark about most of the parameters involved in detailed chemistry models. In other words, in most cases the experimental data available are not able to leverage the more refined physical description offered by the detailed chemistry models. Making informed physical assumptions about their parameters becomes then common for the use of such models, which is problematic for the assessment of their predictive performance.

Novel experimental and theoretical approaches seek to bridge this gap. On the experimental side, the microscopic study of porous ablators before and after well-controlled flow reactor tests can offer insights on the link between their microscopic descriptions and their macroscopic properties. Concerning gas-surface interaction, oxidation has been assessed thoroughly this way [26–28]. Although its determination and modeling from such experimental approach did not deal with the features needed in detailed surface chemistry models, future work could use more detailed simulations to resolve complex gas-surface chemistry features. Along these lines, molecular beam experiments are also well equipped to resolve the fundamental processes involved in flight-relevant ablation phenomena [29, 30]. On the theoretical side, we can also resort to more sophisticated models to extract the detailed chemistry parameters while being consistent with the physics at different scales [31, 32].

Despite their simplicity, empirical and coarser models can still attain good preditive performance upon calibration. As long as these models can predict the experimental data in the regimes for which we intend to use them, there is no consistent reason to abandon them unless proven otherwise.

1.2 The role of uncertainties in scientific inference

The design of atmospheric entry systems relies heavily on experimental facilities and their capability to reproduce relevant flight conditions. Mathematical and numerical models are validated against the experimental evidence gathered, and improved accordingly. Both resources are strong assets of scientific research. However, due to the complexity of the physics and the different aspects that need to be modeled and experimentally tested, both numerical and experimental data-generating processes are subjected to uncertainties. Nevertheless, it is still common practice in the field to resort to deterministic approaches when it comes to calibrating and validating the proposed models.

Deterministic methods can undermine all theoretical progress in the field by providing no account of confidence in our model predictions and experiments, thereby making comparisons and model fittings very sensitive to parameter choices and particular realizations of noisy experimental data. More importantly, there exists a constant update of legacy models on the basis of better experimental data and computations which still hinders on the same deterministic methods [19–22, 33, 34]. In turn, this makes those newly proposed models stand on the same basis as the legacy ones with still many questions left to be answered and many gaps remaining in the understanding of these phenomena.

The process of scientific inference can also carry deep assumptions about the nature of the problem and it can impact how researchers reach conclusions about their work. Model calibration and validation with experimental data need to account for uncertainties to have fair assessments on the models. Nowadays, it is indisputable that statistical reasoning has become an essential component of modern scientific thinking [35]. Ultimately, scientists are interested in developing predictive models to be able to predict and control natural phenomena. Model validation should reflect the attained capability to predict future outcomes of a statistical experiment in within the explicit domain of the model given the uncertain nature of our knowledge and observations. Quantifying uncertainties in our predictions is essential to the final objective of model validation. As such, accurate model calibration is a necessary step towards validation.

Fig. 1.3 depicts the different domains that play a role in the final objective of developing predictive models. The figure has been explicitly adapted from Oberkampf [36] where, in the original, “reality” takes the place of “measurement”. In our physical sciences domain, where fluid mechanics, and in particular aerothermodynamics, belongs, it is difficult to claim that any given observation relates directly to the reality we are trying to understand. That is why, in practical terms, the best we can do is to rely on proxies to reality which are the measurements we can perform.

Going into the details of Fig. 1.3, we can start by saying that, in general, the broad objective is to accurately predict some physical phenomenon. We can formulate some hypotheses and obtain some sort of experimental data in the available facilities. On the side of the model, we can propose a mathematical structure and parameters within it that, to our knowledge, best represent the phenomenon we observe at the level of definition of the experimental data. The formal definition of model qualification is the *determination of adequacy of the conceptual model to provide an acceptable level of agreement for the domain of intended application* ([36]). Using computational techniques, we can then discretize and solve such models to provide solutions and the corresponding theoretical predictions. The task that bridges this gap is model verification, described as *the process of determining that a computational model accurately represents the undelying mathematical model and its solution* ([36]). Before attempting a final step in the form of model validation, the computer model needs to be calibrated to fix some of its parameters with aditional calibration data. Ideally, the calibration data belongs to the same domain of intended application for our conceptual model.

In this discussion, it is important to stress that it is still a common issue in the aerothermodynamics literature to consider the experimental data as the underlying physical reality. This lopsided view can no longer be held in the study of complex systems, such as aerothermodynamics. Experimental data are not direct proxies to the physical reality. Measurement techniques are employed to record some sort of observations, such as photon counts, images or voltage differences. These inputs are direct consequences of the physical reality we are studying in experimental facilities. The raw data must be converted into meaningful physical quantities that our model can predict. To do so, the measurement device's response can be also theoretically modeled with a set of model parameters that need definition. If the theoretical model entails complex dynamical equations, we might need to discretize them and use a computer model to go from the raw data (input to the model) to the physical quantity we are measuring and want to report (output of the measurement device model). Along the way, a calibration of the measurement device's model must be carried out to determine its model parameters and associated uncertainties. All in all, using measurements entails going through another set of model qualification, verification and validation for the model of the experimental apparatus.

Examples in gas-surface interaction testing abound. Measurements of heat fluxes in reusable TPS make use of a pyrometer to measure the surface temperature. Through the assumption of radiative equilibrium, the surface temperature is related to the reported measured heat flux. Measurements of species concentrations in flowfields affected by ablative TPS are usually based on Boltzmann population assumptions for the energy levels. Our assumed experimental measurement might not be the actual true quantity due to deviations stemming from the modeling involved in post-processing the measurement raw data into meaningful physical quantities. In turn, this could generate model discrepancies and inadequacies that are frequently traced back to the physical model we want to validate, when it is actually the experimental data that are wrongly post-processed. As with data generated through theoretical models, experimental data should also be studied through the same lenses.

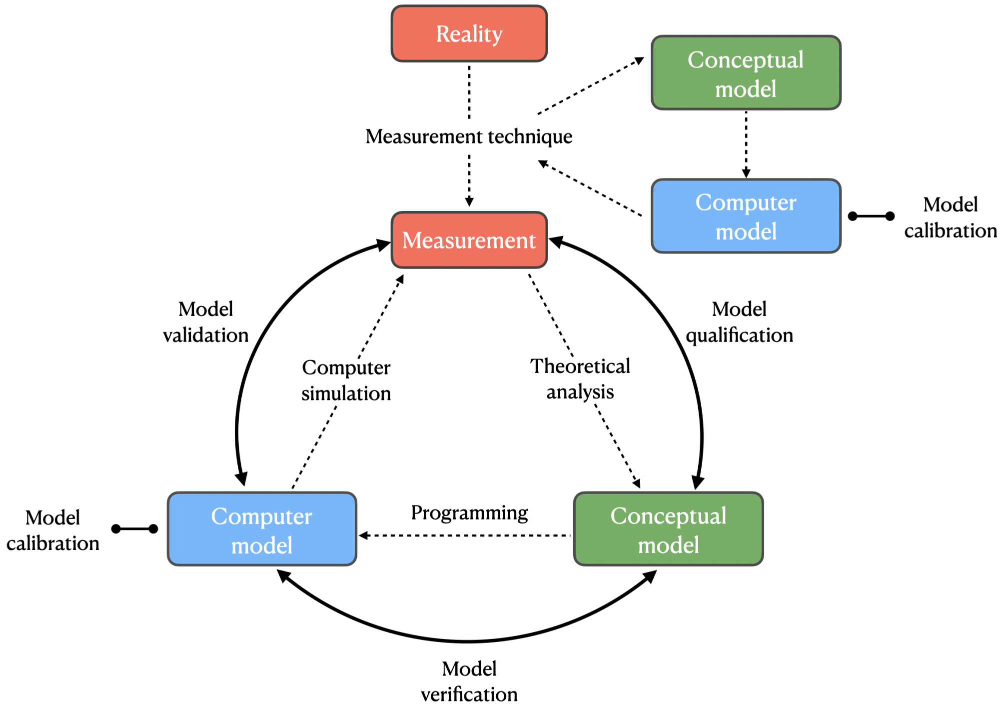

Figure 1.3: *Schematic representation of the different domains involved in the development of predictive models.*

Different types of uncertainty stem from each of these domains. Conceptual models rely on assumptions of different nature. In this case, we need to account for different types of uncertainty in our analyses depending on how much knowledge we have regarding the validity of the assumptions. These assumptions take the form of model parameters and model structure itself. Both characteristics of the conceptual models can carry aleatory uncertainty. The fundamental nature of aleatory uncertainty is randomness. Parameters and operators that carry aleatory uncertainty can be expressed as randomly distributed quantities that may take on values in a known range, but for which the exact value will vary by chance from unit to unit, point to point in space, or time to time.

Conversely, uncertainties associated to model parameters and model structure that are not known to a good degree must reflect the fact that there exists a lack of knowledge. This type of uncertainty is called epistemic and it is also referred to as reducible uncertainty, knowledge uncertainty, and subjective uncertainty. The lack of knowledge can also be related to computational issues of the model, or experimental data needed for validation. Computational issues include programming mistakes, estimation of numerical solution errors, and numerical approximations in algorithms. Experimental data issues include incomplete knowledge of experimental information that is needed for simulation of the experiment and approximations or corrections that are made in the processing of the experimental data.

Further, epistemic uncertainties can come in two flavors: conscious and blind. Conscious ignorance or known unknowns would include, for example, any assumptions or approximations made in modeling, the use of expert opinion, and numerical solution errors. Known unknowns can stem when making decisions concerning the modeling of a system where one chooses the physics that will be included in the model and what will be ignored. When certain type of physical phenomenon is included or ignored, or a specific type of conceptual model is chosen we should acount for conscious uncertainties. Regardless of what level of physics modeling fidelity is chosen there are always spatial and temporal scales of physics, as well as coupled physics, that are ignored.

Blind ignorance is defined as ignorance of self-ignorance or unknown unknowns. In experimental activities, some examples of unknown unknowns are unrecognized bias errors in diagnostic techniques or experimental facilities and improper procedures in using a reference standard in the calibration of experimental equipment. There are no reliable methods for estimating or bounding the magnitude of blind uncertainties, their impact on a model, its simulation, or on the system's response. One possibility is to try to identify them by combining independent experimental measurements to get information about the same phenomenon. This can help uncover some issues which, in turn, can inform new hypotheses and identify inconsistent measurements due to poor understanding of the experimental conditions or modeling and calibration of the measurement chain.

1.3 Model calibration in aerothermodynamics

In the literature of most scientific disciplines, statistical tools for model calibration and validation are deeply ingrained as part of their analysis methods [37–39]. In contrast, aerothermodynamics is still in its infancy with regard to the wide use of such methods.

From 2010 to 2012, a variety of works from the Center for Predictive Engineering and Computational Sciences (PECOS) group laid the foundations for these statistical methods to grow in the community. Their pioneering works concerned the Bayesian calibration of models from shock tube data. The first work was an attempt to (in)validate Park's two-temperature thermochemical model. In it, Miki et al. [40] laid the foundations of their calibration and validation methodologies. They applied them to the NASA Ames Electric Arc Shock Tube (EAST) data where they considered a certain number of model parameters for calibration. The parameters ranged from the flow definition and kinetics to radiation and statistical modeling. Overall, they showed they were able to learn sufficiently well all parameters but the quality of the experimental data was brought into question, and only one model scenario was explored. The predictions of radiative intensities performed with the resulting calibrated model showed excellent agreement between the predicted mean intensity and the experimental observations, but also indicated that uncertainties were very large.

The subsequent work of Panesi et al. [41] tackled precisely the fact that spectrometer experimental data is the result of an elaborated process involving the modeling of radiative intensities emanating from the dissociated flow. As such, estimating accurate uncertainty levels on these data is proven challenging. In that work, they proposed and calibrated reduced models of the internal functioning of a spectrometer for the conversion from the photon count produced by the Intensified Charge-Coupled Device (ICCD) camera to radiative intensities. Several models for the dynamics of the apparatus were proposed and studied. Issues concerning the calibration and validation of such models were also discussed and brought forth. Miki et al. [42] used data from the same facility to calibrate atomic nitrogen ionization rates with different model scenarios. They used a 1D flow solver coupled to a radiation solver to obtain radiative signatures. The full methodology includes a sensitivity analysis to study the important sources of uncertainty for radiative heating, calibration with manufactured and experimental data, and the final validation with legacy experimental data. Overall, the predictions obtained with the final calibrated models compare well with the legacy experimental data while the calibrated atomic nitrogen ionization rates are fully consistent with Park's model.

Upadhyay et al. [43] were the first ones to focus on gas-surface interaction. They inferred nitridation reaction efficiencies from Zhang et al.'s data [44]. The data consisted in measuring the mass loss of a graphite sample placed in a furnace-heated quartz tube fed by a microwave discharge which produced the stream of dissociated nitrogen. The atomic nitrogen concentrations at the inlet/outlet of the furnace along with temperatures and pressures were also measured. They managed to calibrate power laws with different models for the dependency of nitridation reaction efficiencies with surface temperatures. Terejanu et al. [45] posed the problem of optimal data collection to efficiently learn the model parameters of the graphite nitridation experiment in the context of Bayesian analysis using both synthetic and real experimental data.

On the other side of the pond, Tryoen et al. [46] in 2014 studied the sensitivities of common flight data, such as stagnation pressures and heat fluxes, to the free stream conditions and chemical parameters for the gas phase and material catalytic response. They proposed a surrogate-based methodology aimed at reconstructing free stream pressures and Mach numbers from stagnation pressures with fixed values for the flow chemistry and material catalytic response. Given the complex dependencies of the heat flux to the free stream and chemical parameters, it was discussed that novel methods were needed to introduce heat fluxes and chemical model parameters in the inference. The methodology was tested on manufactured data for a point in the entry trajectory of the European Experimental Reentry Test-Bed (EXPERT). In recent years, Cortesi et al. [47] introduced novel methods to be able to include heat fluxes in the reconstruction of the free stream density and the material catalytic response. The flow angles were also included as quantities of interest in the inference framework. Two data points along the EXPERT entry trajectory were chosen to test the methods with manufactured data.

More recent works by Sanson et al. [5] in 2018 focused on learning catalytic parameters for reusable TPS from plasma wind tunnel data. For the first time, the assumption regarding the catalytic parameter of a reference material was not needed anymore [14–20]. The catalytic parameter of the reference material could be learned along with the flow conditions and the TPS catalytic parameter, objective of the study. They put forth a Bayesian inference methodology which was not able to accurately learn the TPS catalytic parameter. Their work highlighted the challenges we face when learning from heat fluxes which, as recounted in Sec. 1.1, contain overall information about different phenomena.

Ray et al. [48] in 2020 proposed a probabilistic framework for assessing the consistency of an experimental dataset. They wanted to know whether the stated experimental conditions were consistent with the measurements provided. Their framework used heat flux and stagnation pressure measurements along the surface of a double cone to infer the inflow conditions in a shock tunnel. As the heat fluxes and wall pressures were deemed more trustworthy than the inflow measurements, they were used to infer the inflow conditions through the lens of the model and compare to the reported measured quantities.

Fig. 1.4 contains a schematic representation of the state-of-the-art model calibration for aerothermodynamics. The experiments refer to the main measurements from which model parameters are inferred. Other measurements such as static and dynamic pressures, as well as surface temperatures are generally included in the experimental data although they are not explicitly depicted here. The arrows represent the flow of information. While some of these works also include flow state and gas-surface interaction parameters in their calibrations, only the targeted parameters of such inferences are explicitly depicted.

Despite the above-mentioned efforts, there is still a lack of response from the community in the widespread adoption of these methods for model calibration and validation. It is still difficult to find a sense of continuity in such works where the findings and suggested improvements would actually be taken into account and studied further. Moreover, the state of the art is still deeply rooted in deterministic approaches even though computational power has been increasing since then. One of the issues that face current researchers in the field is the need of a different mathematical background to properly tackle these problems. Even though there has been a continuous flourishing of computational libraries for inverse methods and algorithms [49–51], the scarce nature of the experimental data and the complexities of the physical models prevent their straightforward use.

1.4 Objectives and outline of the thesis

The state-of-the-art aerothermodynamics is still in its early stages regarding the widespread use of stochastic methods for model calibration and validation. Only a handful of works exist and they cover a wide range of topics regarding the data they use, the models they seek to (in)validate, and how they use the information (from the experiments to the model and/or viceversa). Even though there are works where several models are proposed for the inference problem, there is no account of proper hypothesis testing studies where competing models are assessed in light of each other. More complex models are proposed as alternative to simple ones yet they need of additional assumptions to lower the number of parameters to be inferred or the inference is carried out with more parameters altogether [41–43]. This

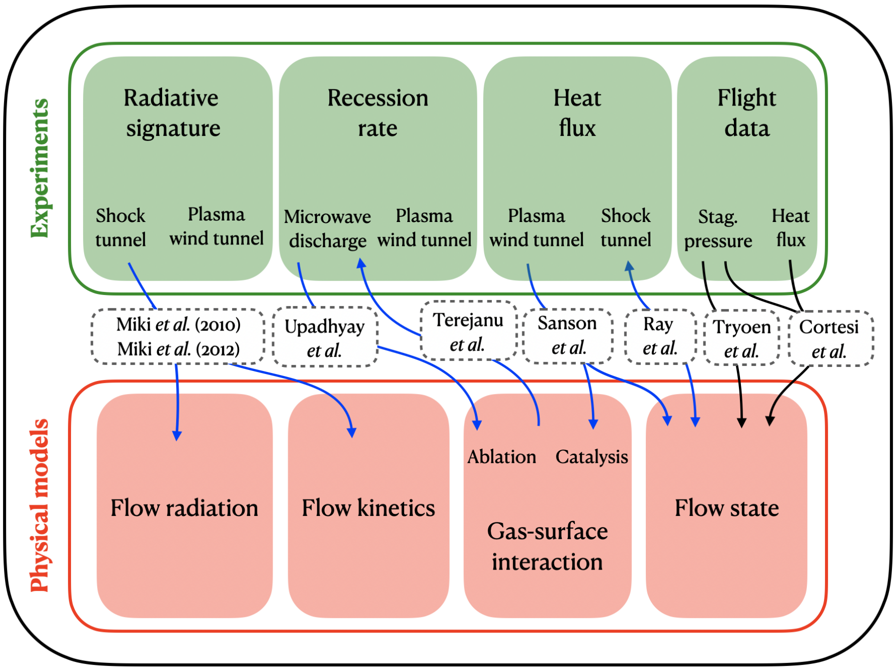

Figure 1.4: *Visual representation of the state-of-the-art model calibration for aerothermodynamics. The works which do not address the link between flow physical models and experiments have been omitted. The arrows represent the flow of information. In blue, the works that used real experimental data, and in black, the works that used only manufactured data to develop the methods.*

characteristic is not properly discussed or gauged in the obtained results nor is how it impacts the predictive performance of the models. Further, even though some works also used this family of methods to inform or improve some aspects of the experiments, none of them have been implemented in practice to actually consolidate those contributions. So far, it has not gone beyond theoretical analyses and methods [41, 45]. Another aspect that lacks in the aerothermodynamics literature is the fact that none of these works combine more than one measurement technique to infer the model parameters of interest. To state this more clearly, the cited works used more than one distinct measurement technique to infer model parameters but they are all complementary to each other. Only one type of measurement is carrying the actual information on the parameters of interest, the others are there to inform the boundary and testing conditions. Combining more than one type of measurement with information about the main inference parameters was never attempted, holding back a whole set of novel insights.

Apart from missing studies in the literature, some of the published methods did not give satisfactory answers in their abilities to learn model parameters. The improvement of such methods is another active niche of research.

The broad goal of this thesis is to develop stochastic methodologies for the accurate inference of selected gas-surface interaction model parameters and assessment of flow models and experimental data for atmospheric entry plasmas. In particular, this thesis is focused on calibrating reacting flow models from plasma wind tunnel data and studying the various ramifications of such stochastic analyses. The work is focused on experimental data coming from the VKI plasma wind tunnel, the Plasmatron. The research ranges from improving and re-formulating existing inference methods to designing more informative experiments through the use of the developed stochastic analyses. Further, this thesis provides continuation to the introduction of stochastic methods for model calibration in the aerothermodynamics community.

The two main objectives of this thesis are:

1. **Accurate inference of catalytic parameters for reusable TPS:**
   - **Improvement of existing stochastic inference frameworks** by proposing novel approaches tailored to the experimental methodologies available and typical plasma wind tunnel data.
   - **Design of an experimental methodology** using the improved stochastic inference framework to propose experiments that can yield more accurate catalytic parameters and inlet flow conditions, enriching current CMC databases.
2. **Calibration and assessment of graphite ablation models for nitrogen flows:**
   - **Development of a Bayesian calibration approach** for nitridation reaction efficiencies and Arrhenius law parameters for the baseline stagnation line model combining all available measurements.
   - **Use of hypothesis testing and Bayesian model averaging** to include epistemic uncertainties beyond the baseline model, obtaining a robust Arrhenius law for a wide span of surface temperatures.

While the literature tends to equate inference and calibration, we make the distinction here to formulate the objectives. Inference pertains to the reconstruction of parameters, such as boundary conditions or model parameters, in the context of a specific experimental case. Conversely, we refer to calibration when we obtain model parameters that can be used for a broad range of conditions. However, both terms are used interchangeably throughout the thesis.

Through these objectives, we make possible the introduction of rigorous and systematic uncertainty treatments for plasma wind tunnel experimental data. The methodologies have the impact of tackling a set of issues that affect these data as well as being able to update current gas-surface interaction databases with accurate uncertainty estimates.

Fig. 1.5 depicts a schematic representation of the objectives of this thesis in the same context as the state of the art included in Sec. 1.3. Objective 1 tackles the link between heat flux measurements in plasma wind tunnels and the inference of the flow state at the free stream together with the material catalytic response. The link goes both ways: first, the experimental data are used to inform the model parameters in order to establish a suitable methodology; second, the model charateristics are exploited to design a more informative experimental methodology. Objective 2 seeks to infer model parameters for nitrogen ablation by combining all available measurements. In this case, CN concentrations and material recession rates are used jointly to inform the model. Conversely, through the lens of the model we can assess the consistency and validity of both sets of measurements, providing feedback to the experiments. Both objectives involve the use of real experimental data.

The thesis is divided into 8 chapters including this introduction. Most outcomes have already been presented at international conferences and meetings, as well as being published

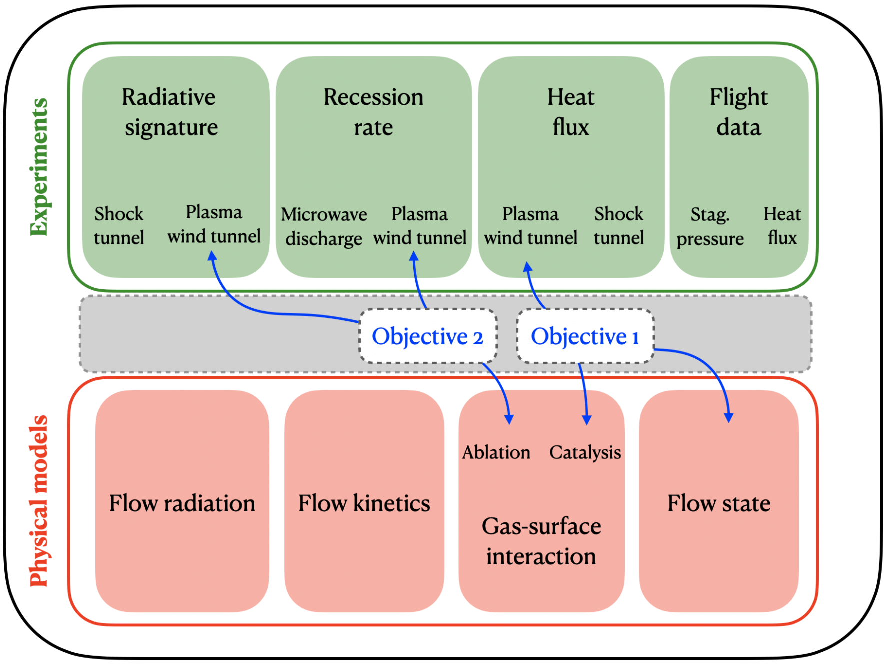

Figure 1.5: *Main objectives of this thesis and their position in the same context as the state-of-the-art model calibration in aerothermodynamics.*

or in the process of being published in peer-reviewed journals (See Publications). When relevant, the publications where the contents of each chapter can be found are referenced in footnotes.

Chapter 2 reviews the state-of-the-art modeling of high temperature, chemically reacting flows. The objective of this chapter is twofold. First, we aim at presenting in detail the different models used to explain the underlying physical phenomena present in plasma wind tunnel subsonic ground testing. The secondary objective of the chapter is to highlight the diverse landscape in terms of data fidelities, models and complexity.

Chapter 3 explains in detail the experimental and numerical tools that are used in this work. From the numerical codes which solve reduced sets of the governing equations exposed in Chapter 2, to the experimental set-ups. The chapter ends by identifying the different uncertainty sources present in both data-generating processes.

Chapter 4 introduces the fundamentals of statistical inverse analysis by means of Bayesian methods. The different constitutive steps of Bayesian inference analyses are reviewed in light of the needs addressed in this thesis to deal with the uncertainty sources identified in Chapter 3.

Chapter 5 proposes a novel Bayesian inference formulation for the calibration of the catalytic parameters of reusable thermal protection materials. The calibration gives estimates of the material catalytic parameter through its marginal posterior probability distribution. The approach is tested and compared to previous works in a case study with real experimental data.

Chapter 6 builds on the contribution of Chapter 5 by proposing a more informative experimental methodology and performing stochastic analyses on the resulting plasma wind tunnel data, enriching current catalysis databases.

Chapter 7 presents a methodology to infer nitridation reaction efficiencies from plasma wind tunnel experiments. The inference is splitted in terms of the experimental data used. We want to gauge the different levels of information that recession rates and CN radiation bring to the inference of nitridation efficiencies. The final part of this contribution is devoted to model selection and averaging. Model averaging is performed for the nitridation efficiencies and Arrhenius law parameters inferred under each proposed model. Complete and accurate characterization of their posterior uncertainties is provided to update the current state of the art.

Chapter 8 summarizes the different results and presents a synthesis of the derived conclusions for each phenomenon studied. Suggestions for future investigations are given.

Chapter 2

Modeling of high temperature, chemically reacting flows

This chapter is devoted to a review of the state-of-the-art modeling of high temperature, chemically reacting laminar flows in the continuum regime used to describe atmospheric entry phenomena. A closed description of the hydrodynamics equations is given by combining the governing equations in open form with the physico-chemical closure models. This thesis is centered around the understanding of gas-surface interaction phenomena from experimental and theoretical points of view and the interplay between them. The relevant parts of the modeling of gas-surface interactions for chemically reacting flows are also presented. These models govern the flow behavior in the presence of catalytic or ablative materials when imposed as boundary conditions. It is important to understand the intricacies and complexities of the models that are commonly adopted in the literature to appreciate the relevance of methods dealing with lack of knowledge and uncertainty as presented in this thesis.

2.1 Governing equations

An exploration of the mathematical description of the physical problem is introduced. The governing equations, being introduced first, represent the stencil which additional physico-chemical models come to feed. In the mechanics of continuum media such as gas flows in the continuum regime, general balancing equations govern the dynamics of a system [52]. They balance the variations of mass, momentum and energy of the given macroscopic state of the system. The density of a quantity in a given volume changes in time due to exchanges with the external environment (fluxes) and internal production (source terms). Overall, balancing equations relate variations in time with reasons of change.

The particular open form of the balancing equations for high temperature, chemically reacting flows is introduced here. These equations describe a multi-component dilute gas whose mass, momentum, and energy are conserved in an arbitrarily small volume, and they hold whenever the hypotheses for continuum flow are satisfied [9]. In this thesis, the work revolves around the modeling of flows in testing facilities capable of reproducing the thermal environment relevant for atmospheric entry applications. The VKI Plasmatron facility, central in this thesis, only pertains flow descriptions in the continuum regime.

In general, atmospheric entry flows are characterized by complex processes taking place within the gas. When the time required for a certain process to accommodate itself to the local flow conditions within some region is almost negligible, the process is said to be in local thermodynamic equilibrium. However, in many applications, the chemical kinetics and internal energy relaxation time scales are similar to the characteristic flow time scales, defining a state of thermochemical non-equilibrium [53]. In this case, balancing equations for the internal energies related to different molecular degrees of freedom and partial densities for the mixture components must be additionally solved, adding complexity to the system. Further, when the internal energy levels population depart from Boltzmann distributions, a more detailed approach, such as state-to-state, should be followed [54–56]. This last modeling option is beyond the scope of this thesis.

A first layer of model hypotheses must be introduced when defining the governing equations of a given system. In this thesis, we are interested in subsonic plasma flows at subatmospheric pressures (10 hPa - 100 hPa) representative of the stagnation point conditions at peak heating of spacecraft atmospheric entry. Pressure plays an important role in speeding up or slowing down chemical reactions and energy exchange mechanisms. Further, we are mainly interested in reproducing boundary layers, where gradients of flow quantities are predominant. These gradients drive the time scale of the flow which is important to assess whether equilibrium assumptions hold. The edge of the boundary layers are assumed in thermochemical equilibrium following the studies of Cipullo et al. [57]. They showed experimentally the validity of thermochemical equilibrium assumptions to account for the inlet conditions in reacting flow simulations for the VKI Plasmatron testing. The rest of the fluid domains encompassing the boundary layers are assumed in thermal equilibrium at a single temperature. Thermochemical non-equilibrium (TCNEQ) is only considered in the case of nitrogen ablation as experimental measurements of vibrational and rotational energy modes of molecules indicate thermal non-equilibrium.

In the next section, the more general case of a chemically reacting flow in thermochemical non-equilibrium is presented first, where the condition of thermal equilibrium is a particular case. The governing equations under Local Thermodynamic Equilibrium (LTE) assumptions are introduced next. LTE conditions require additional thermodynamics background for the computation of equilibrium compositions.

2.1.1 Thermochemical non-equilibrium

The general equations describing a multi-component chemically reacting gas in thermochemical non-equilibrium are introduced. The equations are presented in their open form, as they lack constitutive relations that link transport fluxes, mass production terms and thermodynamics to flow properties and their gradients.

In this open formulation, radiative processes within the gas are not included given that facilities such as the VKI Plasmatron do not allow to reproduce relevant shock layer radiation. Moreover, due to the complexity involved in their modeling and computation [58, 59] we do not take into account radiative processes within the flow. Nevertheless, radiation absorption in the boundary layer can be significant in flight as well as on ground, in particular enhanced by the presence of ablation products. In addition, the thermal non-equilibrium modeling that concerns this thesis does not involve the resolution of pseudo-species of different energy levels and photochemical processes as in a detailed state-to-state formulation [54–56]. The thermal non-equilibrium nature of the flow is resolved by a multi-temperature model which assumes that the translational mode of atoms and molecules, and rotational mode of molecules thermalize to the same temperature T while the vibrational mode of molecules, electronic mode of atoms and molecules, and electron translational degree of freedom thermalize to another temperature $T^{\mathcal{V}}$. This approach is widely used in simulations of atmospheric entry flows [60] even though the underlying assumptions are being revisited [61, 62]. In such case, the mathematical description of the problem is limited to representing two distinct molecular contributions to the total energy, assuming that all degrees of freedom can be associated to one or another.

The governing equations for such non-equilibrium model extend by the number of independent internal energy modes considered in the mixture while gas phase chemistry and energy transfer mechanisms need to be modeled to account for mass and internal energy source terms.

Species mass conservation equations. The evolution of the chemical composition of the different species in the gas is governed by the conservation of mass per individual species in terms of partial densities ρ_i. These equations read

$$\frac{\partial}{\partial t}(\rho_i) + \boldsymbol{\nabla} \cdot (\rho_i \boldsymbol{u} + \rho_i \boldsymbol{V}_i) = \dot{\omega}_i, \ \ \forall i \in \mathcal{S}, \tag{2.1}$$

where $\mathcal{S}$ is the set of all species in the mixture which contains electrons and heavy species $\mathcal{S} = \{\mathrm{e}\} \cup \{\mathcal{H}\}$, respectively. Quantity $\boldsymbol{u}$ is the mass-averaged gas velocity for which

$$\rho \boldsymbol{u} = \sum_{i \in \mathcal{S}} \rho_i \boldsymbol{u}_i, \tag{2.2}$$

and $\boldsymbol{u}_i$ is the average velocity of species i.

The term $\rho_i \boldsymbol{V}_i$ is the mass flux of species i due to diffusion. Diffusion velocities are defined as $\boldsymbol{V}_i \equiv \boldsymbol{u}_i - \boldsymbol{u}$ and are linearly dependent such that the mixture diffusion flux vanishes

$$\sum_{i \in \mathcal{S}} \rho_i \boldsymbol{V}_i = 0. \tag{2.3}$$

The term $\dot{\omega}_i$ is the volumetric chemical production or destruction of species i within the gas. All chemical processes additionally satisfy element and charge conservation. This leads to

$$\sum_{i \in \mathcal{S}} \dot{\omega}_i = 0. \tag{2.4}$$

The evaluation of the chemical terms $\dot{\omega}_i$, together with the computation of the diffusion velocities from the Stefan-Maxwell equations are presented in Sec. 2.2.

Total mass conservation equation. The summation of Eq. (2.1) over all chemical species and the substitution of Eqs. (2.2)-(2.4) yields the following equation for the conservation of the mixture mass

$$\frac{\partial}{\partial t}(\rho) + \boldsymbol{\nabla} \cdot (\rho \boldsymbol{u}) = 0. \tag{2.5}$$

Note that in practice, we solve all species mass conservation equations given that the system is closed for $n_{\mathcal{S}}$ equations, being $n_{\mathcal{S}}$ the number of species considered in the mixture.

Momentum conservation equation. The momentum conservation equation reads

$$\frac{\partial}{\partial t}(\rho \boldsymbol{u}) + \boldsymbol{\nabla} \cdot (\rho \boldsymbol{u} \otimes \boldsymbol{u} + p \bar{\bar{\boldsymbol{I}}} + \bar{\bar{\boldsymbol{\tau}}}) = \boldsymbol{0}, \tag{2.6}$$

where p is the thermodynamic pressure of the mixture, related to the other fluid variables by a combination of Dalton's law and equation of state for a perfect gas mixture, resulting in $p = \sum_{i\in\mathcal{H}} \rho_i R_i T + \rho_\mathrm{e} R_\mathrm{e} T_\mathrm{e}$, with the species gas constant $R_i = k_\mathrm{B}/m_i$ for species i, being k_B the Boltzmann constant. The subscript e refers to electron quantities. The term $\bar{\bar{\boldsymbol{I}}}$ is the identity tensor and $\bar{\bar{\boldsymbol{\tau}}}$ is the viscous stress tensor (Sec. 2.2). In the general case, the right-hand side contains all the external forces acting on the gas in the considered volume. In Eq. (2.6), the gravitational contribution is omitted due to the typical circumstances in high temperature, reacting flows that assume gravitational effects to be negligible with respect to effects due to the tensional state of the gas. Additionally, most of the conditions covered in this thesis deal with quasi-neutral unmagnetized mixtures, rendering the Lorentz force in the right-hand side of Eq. (2.6) negligible.

Total energy conservation equation. The total energy of the system is balanced according to

$$\frac{\partial}{\partial t}(\rho E) + \boldsymbol{\nabla}\cdot(\rho \boldsymbol{u} H + \bar{\bar{\boldsymbol{\tau}}}\boldsymbol{u} + \boldsymbol{q}) = 0, \tag{2.7}$$

where the total energy $E = e + 1/2(\boldsymbol{u}\cdot\boldsymbol{u})$ is the sum of the thermal and kinetic energy of the gas. Quantity $H = E + p/\rho$ is the total enthalpy, $\bar{\bar{\boldsymbol{\tau}}}\boldsymbol{u}$ is the work of the viscous forces and $\boldsymbol{q}$ is the heat flux accross element boundaries due to convection and diffusion. We recall that radiation is neglected. The thermal energy of the gas e can also be expressed in terms of species thermal energies as a weighted sum $e = (1/\rho)\sum_{i\in\mathcal{S}} \rho_i e_i$.

Internal energy conservation equation. In this formulation, the resolution of the thermodynamic state of the gas is done through a multi-temperature model attributed to the works of Lee [63, 64] and Park [65, 66]. The model considers two different thermal baths, one for the translational-rotational modes (referred to as translational bath in this thesis) and another for the vibrational-electronic-electron translational modes (referred to as vibrational bath in this thesis). One conservation equation per bath ought to be specified. It is convenient to solve one internal energy equation along with the total energy equation Eq. (2.7). In a general compacted formulation this equation reads

$$\frac{\partial}{\partial t}(\rho e^{\mathcal{V}}) + \boldsymbol{\nabla}\cdot(\rho e^{\mathcal{V}}\boldsymbol{u} + \boldsymbol{q}^{\mathcal{V}}) = -p_\mathrm{e}\nabla\cdot\boldsymbol{u} + \Omega^{\mathrm{VT}} + \Omega^{\mathrm{eT}} + \Omega^{\mathrm{CV}} - \Omega^{\mathrm{I}}, \tag{2.8}$$

where the first term on the right-hand side is the work done on electrons induced from an electron pressure gradient. The treatment of this term as a source term is a strong approximation that simplifies the resulting Eigen system for the convective flux, necessary in various upwind schemes [9, 67]. The term Ω^{VT} denotes the energy transfer between the vibrational and translational baths through collisional processes, Ω^{eT} refers to the energy transferred from heavy particle to electron translational modes through elastic collisions, Ω^{CV} represents the transfer of energy to the vibrational bath through chemical reactions, and Ω^{I} is the electron-impact ionization transfer mechanism. The latter term is due to free electrons acting as means of delivering energy to heavy particles causing ionization controlling the avalanche phenomenon [68]. This also results in free electrons losing translational energy, contributing to energy changes of the vibrational $\mathcal{V}$ thermal bath. The internal energy heat fluxes $\boldsymbol{q}^{\mathcal{V}}$ and source terms are discussed in Sec. 2.2.

2.1.2 Local Thermodynamic Equilibrium

The more general non-equilibrium formulation being introduced in the previous section eases the presentation of LTE flows. The major aspect of this assumption is the fact that chemical reactions and relaxation of internal energy modes are fast enough when compared to the flow characteristic time scales. The composition of the mixture and energy distribution of internal modes are therefore considered to instantaneously adapt themselves to changes in the flow. The plasma can be thought of as a single gas of defined composition provided that the diffusive fluxes of chemical elements are neglected, which remains a strong approximation for chemically reacting flows [69, 70]. The pressure and temperature of the gas are sufficient to uniquely define the distribution of the species, which is not dependent on the history of the flow, and a single temperature can be used to describe the energy distributions. By knowing the elemental molar fractions, the system-wide Gibbs free energy is minimized for the given thermodynamic state. This procedure computes the species partial densities ρ_i. The computation of the Gibbs free energy is reviewed in Sec. 2.2.1.

Further, the set of governing equations for such system collapses the energy balance equations into just the conservation of total energy. All the different thermal baths are assumed equilibrated with each other at temperature T.

It is straightforward to see why this assumption is quite suitable for the simulation of experiments. Only a reduced amount of information about the state of the flow at the inlet of the chosen domain (free stream, boundary layer edge, etc) is needed to define proper boundary conditions for the governing equations. This goes inline with the fact that little experimental data are available from plasma wind tunnel experiments. The LTE assumption in the free stream at high enough pressure considered in this thesis is also supported by extensive experimental and numerical databases related to experiments in the VKI Plasmatron over the years. The experimental data are attributed, among others, to Cipullo [57], Panerai [4] and Helber [3].

To conclude what has been exposed in this section, Table 2.1 shows the different terms that need additional layers of modeling to close the thermochemical non-equilibrium and LTE governing equations, respectively. These terms are based on the assumption that the set of equations introduced are solved on the conservative variables $\rho_i, \rho\boldsymbol{u}, \rho E$, and $\rho e^{\mathcal{V}}$ from which the mixture density is directly computed as $\rho = \sum_i^{ns} \rho_i$. They are classified according to the phenomenon they represent.

Apart from closure models, the governing equations need boundary conditions at the domain inlet and the material surface. This information depends on the particular structure of the system we solve, which is different for the cases of catalysis and ablation due to the various simplifications adopted in the different numerical codes. In general, we can say that the boundary conditions for both problems are obtained based on either assumptions, such as equilibrium for the mass and energy balance equations, or no slip for the momentum equations, additional models, such as surface balance equations, or direct/indirect experimental observations. More detailed accounts of the particular boundary conditions needed for each problem are given in Chapters 5 and 7.

The following two sections are dedicated to the models that close the governing equations. In Sec. 2.2, the physico-chemical models that affect the definition of the gas phase are introduced in detail. Given the particularities and overall focus of this thesis on gas-surface interaction model parameters, Sec. 2.3 is exclusively devoted to the discussion and

Table 2.1: *Overview of the terms that need closure in the TCNEQ and LTE governing equations.*

Conservation equation	Transport	Thermodynamics	Gas phase kinetics
TCNEQ			
Species mass (2.1)	$\boldsymbol{V}_i$	-	ω_i
Momentum (2.6)	$\bar{\bar{\boldsymbol{\tau}}}$	p	
Total energy (2.7)	$\boldsymbol{q}$	H	-
Internal energy (2.8)	$\boldsymbol{q}^{\mathcal{V}}$	-	$\Omega^{\mathrm{VT}}, \Omega^{\mathrm{eT}}, \Omega^{\mathrm{CV}}$, and Ω^{I}
LTE			
Momentum (2.6)	$\bar{\bar{\boldsymbol{\tau}}}$	p	-
Total energy (2.7)	$\boldsymbol{q}$	H	-

presentation of the closure models used as suitable surface boundary conditions in this work.

2.2 Physico-chemical models

The open form of the governing equations provides little information in their mathematical description, only conservation properties. So far, the balancing equations are just the mathematical scaffolding upon which we can define additional closure in the form of physico-chemical models, such as thermodynamics, transport and gas phase kinetics.

These models define the physical characteristics of the chemically reacting flows under study. They close the governing equations and link the fluid quantities, or macroscopic state variables, to the microscopic characteristics of the flow. This is important as the flow variables are the common language among the conservative quantities, flux tensors and source terms in the governing equations. In most cases, the relationship is explicit, such as for the thermodynamic pressure via Dalton's law in Eq. 2.6, but, generally, additional structure and algorithms are introduced.

In this section, thermodynamic and transport properties are introduced first, followed by the gas phase kinetics (chemistry and energy exchange mechanisms). This layer of complexity adds many caveats to the numerical and experimental studies of these flows. It is not clear when different models hold for a given testing condition, making the process of understanding the physics more complicated.

2.2.1 Thermodynamics

Irreversible thermodynamics provides relationships between the state of a thermodynamic system and its reasons for change. Particularly, it states how the thermal energy and entropy of a system change, but it does not provide expressions or models for these thermodynamic properties. The thermodynamic relationships for energy, enthalpy, entropy and specific heats are derived from first principles using statistical mechanics [71] as a mesoscale method between the macroscopic and microscopic scales of the flow. Different hierarchies are found in these models. The mixture hierarchy, where the mixture properties are derived from the individual species properties, and the energy partition hierarchy, where the total energies and enthalpies for each species are derived from the different thermal bath contributions.

The object of study can have different physical properties, namely, it can be an electron, atom or molecule. In thermodynamic terms, they are distinct in the way they can store energy internally. Free electrons only have the capability to move which is translated into translational energy and spin. Atoms can move but also can have bound electrons in different orbitals, defined by the quantum mechanic nature of the atomic system. Molecules can do all that plus vibrate and rotate, or a quantum mechanical version of a classical vibrator and rotator [72]. Further, the chemical bonds that make up the different particles also contribute to the overall energy of the flow. Under thermal equilibrium assumptions, the characteristic times of translational and internal energy relaxation are way smaller than the characteristic times of the flow. This guarantees that enough collisions take place rapidly, equilibrating all possible modes of energy storage. This condition collapses the mathematical description of the thermodynamic models to the point where only one temperature parameter is needed to describe the system.

Any physical object considered as single species (electron, atom, molecule) has quantized energy levels [71]. While translational energy levels are discrete, they are tightly packed together. For all practical purposes, this permits a semi-classical approach in which it is assumed that the populations of internal energy levels satisfy Maxwell-Boltzmann statistics, such that the quantum effects differentiating bosons and fermions are negligible [71].

In this section, a bottom-up approach is adopted where the properties for inert pure gases made of molecules (pure polyatomic gases) in thermal equilibrium are presented first. A generalization to two thermal baths is introduced next. The mixture rules for the summation of each species contribution are presented last, adding the contributions of atoms and electrons in the mixture to the thermodynamic properties as well as the thermodynamic effects of chemical reactions in the mixture properties. Further, in the formulation here presented, we differentiate between the contributions of the heavy translational-rotational and vibrational-electronic-electron translational energy baths. The translational energy of the heavy species is referred to as simply translational energy in this thesis, in contrast with electron translational energy.

Pure polyatomic gases in thermal equilibrium. The population of a single level for species i can be expressed in terms of the overall species population $n_i = \sum_{l \in \mathcal{L}_i} n_i^l$ with $\mathcal{L}_i$ being the set of energy levels for species i. The total contribution to the thermodynamic properties of a single species is a direct consequence of the different energy levels that are populated. To obtain an expression for the population of the different levels, we need to link the most probable macroscopic state of the system with the number of possible microstates. This is what constitutes the central problem of statistical thermodynamics, where we have a certain number of particles n_i belonging to species i with a total thermal energy E_i confined in a volume v. For such constraints we must find the macrostate that results from the largest number of different microstates. If every microstate is fundamentally indistinguisable in terms of energy and total number of particles for the given volume, the macrostate that has the maximum number of microstates is the most probable one, or the one we will see in the system most of the time. For a high temperature system, the Boltzmann limit is reached [71] and the Boltzmann distribution defines the population of the different levels as

$$\frac{n_i^l}{n_i} = \frac{g_i^l \exp\left(-\dfrac{E_i^l}{k_\mathrm{B}T}\right)}{Q_i(T)}, \ \forall i \in \mathcal{S}^*, \quad \forall l \in \mathcal{L}_i, \tag{2.9}$$

for each molecule i in the set $\mathcal{S}^*$ and level l in $\mathcal{L}_i$. The term g_i^l is the degeneracy of level l, which reflects how many microscopic combinations can populate the energy level equally. The term E_i^l is the internal energy associated to such level relative to the zero point energy of species i, while Q_i is the partition function for species i which represents the sum of the contributions of all energy levels. In the case of thermal equilibrium, only one temperature has to be used to define Q_i, which reads

$$Q_i = \sum_{l\in\mathcal{L}_i} g_i^l \exp\left(-\frac{E_i^l}{k_\mathrm{B}T}\right), \quad \forall i \in \mathcal{S}^*. \tag{2.10}$$

Note that Q_i is defined such that the number of particles in the system amounts to the prescribed n_i. Eq. (2.9) only requires the specification of species number density n_i and temperature T, for given degeneracies and energy levels.

Having resolved the population of the energy levels and the partition function, thermodynamic quantities can be derived with simple relationships from irreversible thermodynamics. The total thermal energy associated to species i is $E_i = \sum_{l\in\mathcal{L}_i} n_i^l E_i^l$, which by substituting n_i^l from Eq. (2.9) and re-arranging terms, the expression for E_i as function of the partition function reads

$$E_i = n_i k_\mathrm{B} T^2 \left(\frac{\partial(\ln Q_i(T))}{\partial T}\right)_{\mathrm{v},n_i}, \quad \forall i \in \mathcal{S}^*, \tag{2.11}$$

which allows to derive the specific thermal energy per unit mass as $e_i = E_i/\rho_i$. The partial derivative of the natural logarithm of the partition function with respect to the temperature T is performed at constant volume v and number of particles n_i. Translational and internal energy modes are split in their contributions to the total thermodynamic properties. In the case of the specific thermal energy e_i this can be expressed as

$$e_i = e_i^\mathrm{T}(T) + \sum_{l\in\mathcal{L}_i} e_i^{\mathrm{int},l}(T) + e_i^\mathrm{F}, \quad \forall i \in \mathcal{S}^*, \tag{2.12}$$

where e_i^T is the specific translational energy of species i, the term $e_i^{\mathrm{int},l}$ refers to the specific energy related to the internal modes of energy storage for energy level l, that is, excluding the translational energy, and e_i^F is the formation energy [1]. It is defined as the energy needed in order to form one mole of that substance from its elements in their standard state at pressure 1 atm. No temperature is imposed in this case. Its choice does not affect the results since only the change in energy is important for modeling thermochemical processes and not its absolute value. Therefore, without loss of generality, the reference temperature for the chemical processes is chosen to be the one of the standard conditions (298.15 K).

The internal energy is expressed as function of each individual mode as $e_i^\mathrm{int} = e_i^\mathrm{R} + e_i^\mathrm{V} + e_i^\mathrm{E}$, with the superscripts $\mathrm{R}, \mathrm{V}, \mathrm{E}$ being the rotational, vibrational and electronic contributions to the internal energy e_i^int. By adopting this separation of energy mode contributions in the thermodynamics modeling one neglects the coupling effects between the rotational and vibrational modes, which are essential at high temperatures. This is important for studying the phenomenon of radiation but not for the balance of energy in the flow [73]. Additional effects that are ignored include centrifugal distortion induced by the rotation of the nuclei widening the intermolecular distance between the atoms [71].

Consequently, the partition function can also be broken down to its constituents in the form of different energy modes. In this case

$$Q_i = Q_i^{\mathrm{T}} Q_i^{\mathrm{int}}, \quad \forall i \in \mathcal{S}^*, \tag{2.13}$$

where Q_i^{T} is the partition function of the translational mode, and $Q_i^{\mathrm{int}} = Q_i^{\mathrm{R}} Q_i^{\mathrm{V}} Q_i^{\mathrm{E}}$ is the partition function of the internal modes.

From Eq. (2.11), e_i^{int} is derived as

$$e_i^{\mathrm{int}} = \sum_{l \in \mathcal{L}_i} e_i^{\mathrm{int},l} = R_i T^2 \left(\frac{\partial (\ln Q_i^{\mathrm{int}}(T))}{\partial T} \right)_{\mathrm{v}}, \quad \forall i \in \mathcal{S}^*. \tag{2.14}$$

The expression for $e_i^{\mathrm{T}}(T)$ is the same as Eq. (2.14) with a different partition function Q_i^{T} for the translational energy. Solving the quantum mechanical version of a particle in a box and summing up all the energy levels, the partition function for the translational energy is expressed as

$$Q_i^{\mathrm{T}} = \mathrm{v} \left(\frac{2\pi m_i k_{\mathrm{B}} T}{h^2} \right)^{3/2}, \quad \forall i \in \mathcal{S}^*, \tag{2.15}$$

where h is the Planck constant. Substituting Eq. (2.15) in Eq. (2.14) returns the internal energy associated to the translational mode

$$e_i^{\mathrm{T}} = \frac{3}{2} R_i T, \quad \forall i \in \mathcal{S}^*. \tag{2.16}$$

The energy of the system is defined with a single temperature for the given energy levels of the species and their degeneracies, always assuming that the population of energy levels follows a Boltzmann distribution.

Species enthalpies and entropies are likewise splitted between translational and internal modes

$$h_i = h_i^{\mathrm{T}}(T) + \sum_{l \in \mathcal{L}_i} h_i^{\mathrm{int},l}(T) + e_i^{\mathrm{F}}, \quad \forall i \in \mathcal{S}^* \tag{2.17}$$

$$s_i = s_i^{\mathrm{T}}(T, p_i) + \sum_{l \in \mathcal{L}_i} s_i^{\mathrm{int},l}(T), \quad \forall i \in \mathcal{S}^*, \tag{2.18}$$

for which

$$h_i^{\mathrm{T}} = e_i^{\mathrm{T}}(T) + R_i T, \quad \forall i \in \mathcal{S}^*, \tag{2.19}$$

$$h_i^{\mathrm{int}} = e_i^{\mathrm{int}}(T), \quad \forall i \in \mathcal{S}^*, \tag{2.20}$$

$$s_i^{\mathrm{T}} = R_i \left(\frac{5}{2} + \ln Q_i^{\mathrm{T}}(T) - \ln n_i(T, p_i) \right), \quad \forall i \in \mathcal{S}^*, \tag{2.21}$$

$$s_i^{\mathrm{int}} = R_i T \left(\frac{\partial (\ln Q_i^{\mathrm{int}}(T))}{\partial T} \right)_{\mathrm{v}} + R_i \ln Q_i^{\mathrm{int}}(T), \quad \forall i \in \mathcal{S}^*, \tag{2.22}$$

$$p_i = n_i k_{\mathrm{B}} T, \quad \forall i \in \mathcal{S}^*, \tag{2.23}$$

where the dependencies on T and p_i have been made explicit for clarity.

Species Gibbs free energies g_i are necessary for the computation of equilibrium constants, as will be shown in Section 2.2.3, as well as equilibrium compositions under LTE assumptions. The Gibbs energy for a given species is defined as

$$g_i \equiv h_i - T\ s_i, \quad \forall i \in \mathcal{S}^*. \tag{2.24}$$

Using Eq. 2.24 and the relationships of the species energies, enthalpies and entropies Eqs. 2.11-2.22 with the species partition function $Q_i(T)$, the Gibbs free energy g_i can be worked out to be expressed as

$$g_i = -R_i \ln \frac{Q_i(T)}{n_i} + e_i^{\mathrm{F}}, \quad \forall i \in \mathcal{S}^*. \tag{2.25}$$

Apart from energies, enthalpies and entropies, other thermodynamic properties also play a role in the modeling of these flows. Specific heats are important for transport properties as will be seen in Sec. 2.2.2 as well as when we need to compute the temperature for given energies when solving the flowfield equations. The specific heats read

$$c_{\mathrm{p}_i} \equiv \left(\frac{\partial h_i}{\partial T} \right)_{\mathrm{p}}, \quad \forall i \in \mathcal{S}^*, \tag{2.26}$$

$$c_{\mathrm{v}_i} \equiv \left(\frac{\partial e_i}{\partial T} \right)_{\mathrm{v}}, \quad \forall i \in \mathcal{S}^*, \tag{2.27}$$

for which h_i and e_i are evaluated at temperature T.

Pure polyatomic gases in thermal non-equilibrium. In the case where the time it takes the energy of different modes to relax and equilibrate is greater than the characteristic time of the flow, the modeling of the thermodynamic properties has to be recast. Let us recall that in this thesis, we adopt a non-equilibrium model consisting of maximum two different thermal baths. One thermal bath is equilibrated between translational and rotational energies, while the other is equilibrated among vibrational, electronic and electron translational modes. In this case, the internal energy modes are expicitly splitted between rotational R and vibrational-electronic $\mathrm{V,E}$. The internal partition function is now expressed as $Q_i^{\mathrm{int}} = Q_i^{\mathrm{R}} Q_i^{\mathrm{VE}}$ with $Q_i^{\mathrm{VE}} = Q_i^{\mathrm{V}} Q_i^{\mathrm{E}}$.

The expressions for translational internal energy, enthalpy and entropy are the same as presented before, the only change being that they are now defined for the specific temperatures of the translational-rotational mode $T^{\mathrm{T}} = T^{\mathrm{R}}$ and the vibrational-electronic-electron mode $T^{\mathrm{V}} = T^{\mathrm{E}} = T_{\mathrm{e}}$ referred to as T and $T^{\mathcal{V}}$ for the remainder of the manuscript. The internal thermodynamic properties for the two thermal baths now read

$$e_i^{\mathrm{R}} = R_i T^2 \left(\frac{\partial (\ln Q_i^{\mathrm{R}}(T))}{\partial T} \right)_{\mathrm{v},n_i}, \quad \forall i \in \mathcal{S}^*, \tag{2.28}$$

$$e_i^{\mathrm{VE}} = R_i \left(T^{\mathcal{V}}\right)^2 \left(\frac{\partial (\ln Q_i^{\mathrm{VE}}(T^{\mathcal{V}}))}{\partial T^{\mathcal{V}}} \right)_{\mathrm{v},n_i}, \quad \forall i \in \mathcal{S}^*, \tag{2.29}$$

$$e_i^{\mathrm{int}} = e_i^{\mathrm{R}}(T) + e_i^{\mathrm{VE}}(T^{\mathcal{V}}), \quad \forall i \in \mathcal{S}^*, \tag{2.30}$$

$$h_i^{\mathrm{int}} = e_i^{\mathrm{R}}(T) + e_i^{\mathrm{VE}}(T^{\mathcal{V}}), \quad \forall i \in \mathcal{S}^*, \tag{2.31}$$

$$s_i^{\mathrm{int}} = \frac{e_i^{\mathrm{R}}(T)}{T} + \frac{e_i^{\mathrm{VE}}(T^{\mathcal{V}})}{T^{\mathcal{V}}} + R_i \left[\ln Q_i^{\mathrm{R}}(T) + \ln Q_i^{\mathrm{VE}}(T^{\mathcal{V}}) \right], \quad \forall i \in \mathcal{S}^*. \tag{2.32}$$

Even though the model is more expressive and can capture a larger family of underlying phenomena, the issues have been moved downstream to the microscopic scale. Assuming that the thermodynamic state of the gas follows indeed a two temperature model, with two groups of thermal baths completely equilibrated among themselves, other parameters need definition. The introduction of an additional governing equation for the internal modes demands the definition of the excitation and de-excitation of the resolved energy modes. By resolving more adequately the flow scales, the problem becomes more data intensive and relaxing assumptions demands additional data that we might not posses or be totally certain about.

In terms of the specific heats, the same additive formula follows

$$c_{\mathrm{p}_i}^m = \left(\frac{\partial h_i^m(T)}{\partial T} \right)_{\mathrm{p}}, \quad \forall i \in \mathcal{S}^*, \forall m \in \{\mathrm{T}, \mathrm{R}\}, \tag{2.33}$$

$$c_{\mathrm{p}_i}^{\mathrm{VE}} = \left(\frac{\partial h_i^{\mathrm{VE}}(T^{\mathcal{V}})}{\partial T^{\mathcal{V}}} \right)_{\mathrm{p}}, \quad \forall i \in \mathcal{S}^*, \tag{2.34}$$

$$c_{\mathrm{p}_i} = \sum_{m \in \{\mathrm{T},\mathrm{R}\}} c_{\mathrm{p}_i}^m + c_{\mathrm{p}_i}^{\mathrm{VE}}, \quad \forall i \in \mathcal{S}^*. \tag{2.35}$$

$$c_{\mathrm{v}_i}^{m} = \left(\frac{\partial e_i^m(T)}{\partial T}\right)_{\mathrm{v}}, \quad \forall i \in \mathcal{S}^*, \forall m \in \{\mathrm{T}, \mathrm{R}\}, \tag{2.36}$$

$$c_{\mathrm{v}_i}^{\mathrm{VE}} = \left(\frac{\partial e_i^{\mathrm{VE}}(T^{\mathcal{V}})}{\partial T^{\mathcal{V}}}\right)_{\mathrm{v}}, \quad \forall i \in \mathcal{S}^*, \tag{2.37}$$

$$c_{\mathrm{v}_i} = \sum_{m \in \{\mathrm{T},\mathrm{R}\}} c_{\mathrm{v}_i}^{m} + c_{\mathrm{v}_i}^{\mathrm{VE}}, \quad \forall i \in \mathcal{S}^*. \tag{2.38}$$

Reacting mixture in thermal non-equilibrium. The most general case includes different thermal baths and species in the mixture. All the properties depicted here are now added for each single species to compute the mixture properties through mixing rules. To the properties previously reviewed we should add the contributions of atoms and electrons to account for a full mixture. Atom contributions have the same expressions as molecules but account only for translational and electronic modes. In this case, the full mixture properties, accounting for atomic and electron contributions, read

$$e = \frac{1}{\rho}\left[\sum_{i \in \mathcal{S}^*} \rho_i e_i + \sum_{i \in \mathcal{S}^{\mathrm{a}}} \rho_i \left(e_i^{\mathrm{T}} + e_i^{\mathrm{E}} + e_i^{\mathrm{F}}\right) + \frac{3}{2} R_{\mathrm{e}} T^{\mathcal{V}} + e_{\mathrm{e}}^{\mathrm{F}}\right], \tag{2.39}$$

$$h = \frac{1}{\rho}\left[\sum_{i \in \mathcal{S}^*} \rho_i h_i + \sum_{i \in \mathcal{S}^{\mathrm{a}}} \rho_i \left(h_i^{\mathrm{T}} + h_i^{\mathrm{E}}\right) + \frac{5}{2} R_{\mathrm{e}} T^{\mathcal{V}}\right], \tag{2.40}$$

$$s = \frac{1}{\rho}\left[\sum_{i \in \mathcal{S}^*} \rho_i s_i + \sum_{i \in \mathcal{S}^{\mathrm{a}}} \rho_i \left(s_i^{\mathrm{T}} + s_i^{\mathrm{E}}\right) + \rho_{\mathrm{e}} s_{\mathrm{e}} - \sum_{i \in \mathcal{S}} \rho_i R_i \ln x_i\right], \tag{2.41}$$

with $s_{\mathrm{e}} = R_{\mathrm{e}}\left(5/2 + \ln Q_{\mathrm{e}}^{\mathrm{T}}(T^{\mathcal{V}}) - \ln n_{\mathrm{e}}\right) + R_{\mathrm{e}} \ln 2$ being the contribution to the mixture entropy of electrons due to their spin. In Eqs. 2.39-2.41, x_i is the molar mass of species i and the term $R_i \ln x_i$ refers to the entropy of mixing. Note that the quantity $\ln x_i$ is negative as it will always be $x_i < 1$, therefore, the entropy of mixing is adding to the total entropy due to different initially separated systems of different compositions (species).

Fig. 2.1 shows the evolution of the different mixture enthalpy contributions with temperature for an air11 $\{\mathrm{e}^-, \mathrm{N}^+, \mathrm{O}^+, \mathrm{NO}^+, \mathrm{N}_2^+, \mathrm{O}_2^+, \mathrm{N}, \mathrm{O}, \mathrm{NO}, \mathrm{N}_2, \mathrm{O}_2\}$ equilibrium mixture at 1 atm. The embedded small upper left graph is a close-up snapshot of lower enthalpies where the contributions of both the rotational and vibrational energy modes can be appreciated. As seen, the formation enthalpy is the largest contribution past 6,000 K, approximately, together with the heavy translational contribution. The rotational and vibrational contributions are only due to the molecules present in the mixture. As the temperature goes up, the rovibrational contribution increases up to a certain point, after which it decreases until it reaches zero. This behavior is underlined by the chemical reactions that are being entertained in the flow as the temperature increases, leading to the dissociation of molecules. The energy stored in the form of rotations and vibrations in molecules is now stored as translational and electronic energies for which we can see the change in slope once the rovibrational contribution starts to decrease.

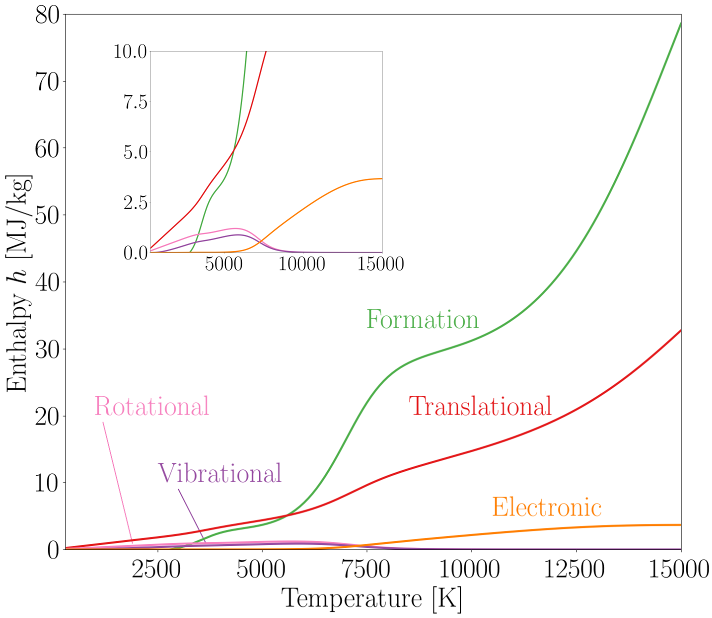

Figure 2.1: *Mixture enthalpy contributions of the different energy modes and formation energies for equilibrium air (air11) at 1 atm.*

The chemical changes in the flow are better appreciated in Fig. 2.2 which shows the changes in mass fractions as the temperature increases. Molecular oxygen starts to dissociate first, where we can see a dip in y_{O_2} and a simultaneous rise in y_{O}. This would be already enough to start decreasing the rovibrational enthalpy contribution but it is not the case in Fig. 2.1. This is due to the simultaneous creation of NO which, in turn, adds to the rovibrational contribution. Once the molecular nitrogen starts dissociating at higher temperatures together with NO, the rovibrational contribution to the mixture enthalpy starts dropping while the translational and electronic contributions ramp up.

Similar to enthalpies, energies and entropies, specific heats for the mixture are added

$$c_{\mathrm{p}} = \frac{1}{\rho}\left[\sum_{i\in S^{*}} \rho_i c_{\mathrm{p},i} + \sum_{i\in S^{\mathrm{a}}} \rho_i \left(c^{\mathrm{T}}_{\mathrm{p},i} + c^{\mathrm{E}}_{\mathrm{p},i}\right) + \rho_{\mathrm{e}}\frac{5}{2}R_{\mathrm{e}}\right], \tag{2.42}$$

$$c_{\mathrm{v}} = \frac{1}{\rho}\left[\sum_{i\in S^{*}} \rho_i c_{\mathrm{v},i} + \sum_{i\in S^{\mathrm{a}}} \rho_i \left(c^{\mathrm{T}}_{\mathrm{v},i} + c^{\mathrm{E}}_{\mathrm{v},i}\right) + \rho_{\mathrm{e}}\frac{3}{2}R_{\mathrm{e}}\right]. \tag{2.43}$$

Note that for a mixture in LTE, applying the definition of specific heats as seen in Eqs. (2.26)-(2.27), we obtain two contributions. One regarding the change with temperature in enthalpy or internal energy for each species and another one concerning the change of composition with temperature in the flow. The equilibrium mixture specific heats are then expressed as

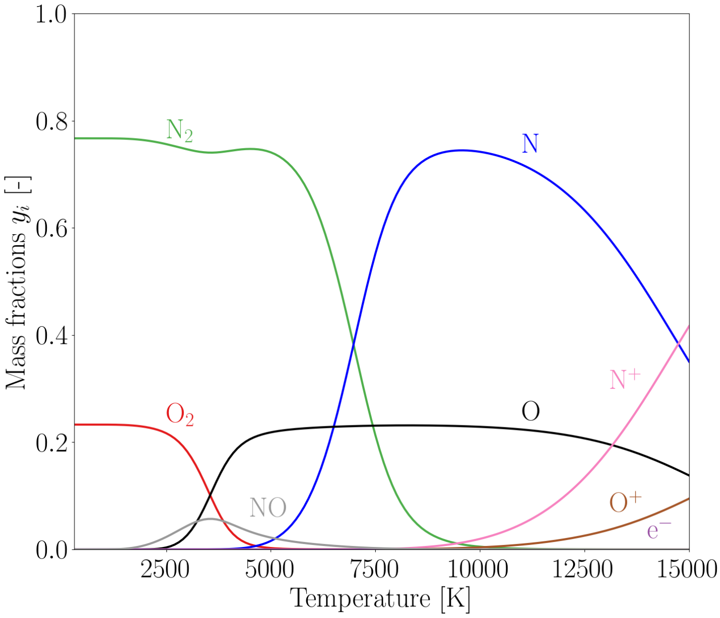

Figure 2.2: *Mass fractions of selected species in equilibrium air (air11) as function of the temperature at 1 atm.*

$$c_{\mathrm{p,eq}} \equiv \left(\frac{\partial h}{\partial T}\right)_{\mathrm{p}} = c_{\mathrm{p}} + \sum_{i\in S^*} h_i \left(\frac{\partial y_i}{\partial T}\right)_{\mathrm{p}} + \sum_{i\in S^{\mathrm{a}}} \left(h_i^{\mathrm{T}} + h_i^{\mathrm{E}}\right) \left(\frac{\partial y_i}{\partial T}\right)_{\mathrm{p}} + \frac{5}{2} R_{\mathrm{e}} T \left(\frac{\partial y_{\mathrm{e}}}{\partial T}\right)_{\mathrm{p}}, \tag{2.44}$$

$$c_{\mathrm{v,eq}} \equiv \left(\frac{\partial e}{\partial T}\right)_{\mathrm{v}} = c_{\mathrm{v}} + \sum_{i\in S^*} e_i \left(\frac{\partial y_i}{\partial T}\right)_{\mathrm{v}} + \sum_{i\in S^{\mathrm{a}}} \left(e_i^{\mathrm{T}} + e_i^{\mathrm{E}}\right) \left(\frac{\partial y_i}{\partial T}\right)_{\mathrm{v}} + \frac{3}{2} R_{\mathrm{e}} T \left(\frac{\partial y_{\mathrm{e}}}{\partial T}\right)_{\mathrm{v}}, \tag{2.45}$$

where the first contributions on the right-hand side are referred to as the frozen specific heats and correspond to the expressions in Eqs. (2.42)-(2.43). The other contributions pertain to the change in mass fractions $y_i = \rho_i/\rho$ of molecules, atoms and electrons in the mixture as consequence of chemical reactions in equilibrium. The resulting sum of these contributions are referred to as reactive specific heats. The impact of the chemistry in the specific heats is better appreciated in Fig. 2.3. We can see two well-defined peaks for both the equilibrium specific heats which correspond with the dissociation of molecular oxygen and nitrogen as seen in Fig. 2.2. The ramping up of the last peak for both specific heats coincides with the onset of ionization reactions.

2.2.2 Transport

Transport phenomena in a gas is defined in the molecular scale as it represents the diffusion of mass, momentum and energy due to the random motion of particles in the flow.

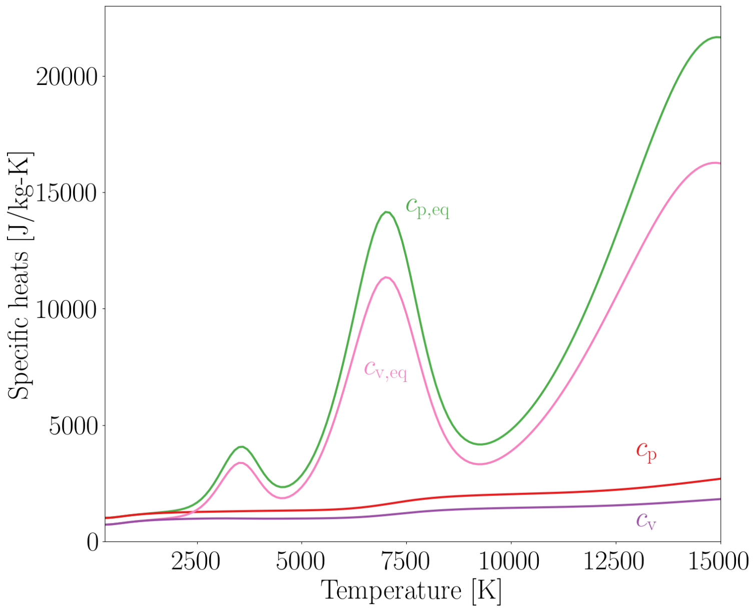

Figure 2.3: *Equilibrium and frozen specific heats for equilibrium air (air11) as function of the temperature at 1 atm.*

This random motion, superimposed to the bulk motion of the gas, entails macroscopic irreversible effects such as mass diffusion fluxes, shear stresses and heat fluxes. Transport coefficients link the gradients of macroscopic flow quantities, such as temperature, chemical composition and pressure, to the corresponding fluxes.

For transport phenomena to be manifest, we need to have a gas out of equilibrium at the kinetic scale. This is achieved through the imposition of the Chapman-Enskog perturbative solution method for the velocity distribution [74, 75]. Solving the Boltzmann equation for the different orders of magnitude of the perturbation parameter gives us an expression for the first order perturbative solution from which to derive the transport fluxes. The obtained kinetic formulations lead to macroscopic expressions for the shear stresses, heat fluxes and mass diffusion fluxes from which to derive the transport coefficients through the solution of linear systems.

The solutions of such systems are obtained using spectral Galerkin projection methods with Laguerre–Sonine polynomials of varying order [76]. This formulation relies on binary collision integrals data which link the macroscopic coefficients with the microscopic properties of different colliding pairs of particles. It is out of the scope of this thesis to unpack the derivation process of the transport coefficients. The final accounts on the obtained expressions are given by Magin and Degrez [77] for weakly ionized and unmagnetized plasmas. A rigorous generalization of the Chapman-Enskog method for the internal energy modes of a gas in thermal non-equilibrium is still an open problem [78].

Mass diffusion flux. The diffusion fluxes can be obtained by solving the generalized Stefan-Maxwell equations. The expression for the diffusion velocities $\boldsymbol{V}_i$ of species i is then given by the solution of the following system

$$\sum_{i\in\mathcal{S}} G_{ij}^V \boldsymbol{V}_i = \left(\boldsymbol{d}'_j + k_j \boldsymbol{E}\right)\Theta_j, \tag{2.46}$$

where $\Theta_j = T_\mathrm{h}/T_j$, $\forall j \in \mathcal{S}$ with T_j being the translational temperature of the different species in the mixture and T_h the translational temperature of the heavy species. In a two-temperature model, only electrons have different translational temperature, belonging in the same group as the vibrational and eletronic. The term $\boldsymbol{E}$ is the electric field while the grouping parameter k_j is

$$k_j = \frac{x_j q_j}{k_\mathrm{B} T_\mathrm{h}} - \frac{y_i q}{k_\mathrm{B} T_\mathrm{h}}, \quad \forall j \in \mathcal{S}, \tag{2.47}$$

$$\text{with } q = \sum_{i\in\mathcal{S}} x_i q_i, \tag{2.48}$$

where the last equation refers to the mixture charge q. Neglecting thermo-and barodiffusion, the modified driving force reads

$$\boldsymbol{d}'_j = \frac{p}{n k_\mathrm{B} T_\mathrm{h}} \boldsymbol{\nabla} x_j, \quad \forall j \in \mathcal{S}. \tag{2.49}$$

The multicomponent Stefan-Maxwell matrix $\boldsymbol{G}^V$ is singular. Magin and Degrez [76] have shown that $\boldsymbol{G}^V$ can be replaced with the non-singular form $\boldsymbol{G}^V + \alpha \boldsymbol{y}\boldsymbol{y}^\mathrm{T}$, where α is a constant with the same order as the $\boldsymbol{G}^V$, such as $1/\max(\mathscr{D}_{ij})$, where $\mathscr{D}_{ij}$ is the binary diffusion coefficient whose expression can be found in Appendix A. The solution of the linear system in Eq. (2.46) is obtained by adding a mass constraint

$$\sum_{i\in\mathcal{S}} y_i \boldsymbol{V}_i = 0. \tag{2.50}$$

In this thesis, we assume ambipolar diffusion, meaning that an electric field develops naturally to keep quasi-neutrality between the charged species such that

$$\sum_{j\in\mathcal{S}} x_j q_j \boldsymbol{V}_i = 0. \tag{2.51}$$

This assumption leads to a diffusion velocity of electrons and ions of the same order. The ambipolar assumption combined with the mass constraint yields

$$\sum_{i\in\mathcal{S}} k_i \boldsymbol{V}_i = 0, \tag{2.52}$$

where this expression is preferred to Eq. (2.51) to keep a symmetric formulation of the Stefan-Maxwell system in thermal equilibrium.

The diffusion transport system matrix $\boldsymbol{G}^V$ is function of the species binary collision integrals and compositions. In particular, the reduced collision integrals of different Laguerre-Sonine polynomial orders of species i, j [76] must be fed to the diffusion transport system matrix. These parameters are defined as weighted averages with respect to the Maxwellian distribution of collisional cross-sections. These cross-sections are defined for each species pair based on their deflection angles and impact parameters. For a multi-component plasma this means that lots of data on pair collisions are needed to feed these models and the data requirements scale as the species included in the mixture squared. As a comparison, the data requirements for thermodynamics properties grow at a significantly lower rate with the species included in the mixture (linearly). The exact expressions for these matrices are given in Appendix A.

The preferred way to obtain collisional data for the collison integrals is by solving the quantum system for each collision and numerically integrate from accurate *ab initio* potential energy surfaces. When this is not possible, we need models for the interaction potentials which split the characeteristics of the collision pairs among neutral, charged, electron and ion particles. A thorough review of interaction potentials models is given by Scoggins [1].

Viscous stress tensor. The shear stresses equilibrate the forces in the volume by acting on the volumetric surface. The viscous stress tensor reads

$$\bar{\bar{\tau}} = -\mu \left[\boldsymbol{\nabla} \boldsymbol{u} + (\boldsymbol{\nabla} \boldsymbol{u})^T - \frac{3}{2} \boldsymbol{\nabla} \cdot \boldsymbol{u} \bar{\bar{I}} \right], \tag{2.53}$$

where μ is the viscosity coefficient and for which the bulk (volumetric) viscosity and the chemical pressure term have been neglected. Giovangigli et al. [79] and Bruno [80] give an account on these neglected terms and the conditions for which they are important.

Kinetic theory is used to obtain an expression for the viscosity coefficient through the first Laguerre-Sonine polynomial approximation. The expression comes out of the solution of the linear transport systems

$$\boldsymbol{G}^{\mu} \boldsymbol{\alpha} = \boldsymbol{x}, \tag{2.54}$$

resulting in the inner product of the solution of the system $\boldsymbol{\alpha}$ and the species mole fractions x_i

$$\mu = \sum_{i \in \mathcal{H}} \alpha_i x_i. \tag{2.55}$$

$\boldsymbol{G}^{\mu}$ is a symmetric positive definite matrix dependent on the binary collision integrals and species mole fractions. Details and expression can be found in Appendix A.

Heat flux. The contributions to the total heat flux are splitted according to the physical phenomenon responsible for each. In this fashion, we have conductive and diffusive heat fluxes for a mixture in thermal non-equilibrium

$$\boldsymbol{q} = -\lambda \nabla T - \lambda^{\mathcal{V}} \nabla T^{\mathcal{V}} + \sum_{i \in \mathcal{S}} h_i \rho_i \boldsymbol{V}_i, \tag{2.56}$$

where λ is the translational-rotational contribution to the thermal conductivity and $\lambda^{\mathcal{V}}$ is the resulting contribution of the vibrational-electronic-electron translational modes. Both thermal conductivities can be expressed explicitly as functions of the their individual contributions as

$$\lambda = \lambda^{\mathrm{T}} + \lambda^{\mathrm{R}}, \tag{2.57}$$

$$\lambda^{\mathcal{V}} = \lambda^{\mathrm{V}} + \lambda^{\mathrm{E}} + \lambda_{\mathrm{e}}, \tag{2.58}$$

where λ^{T} and λ^{R} are the translational and rotational contributions, respectively. $\lambda^{\mathrm{V}}, \lambda^{\mathrm{E}}$ and λ_{e} are the vibrational, electronic and electron translational contributions to the thermal conductivity.

The translational thermal conductivity λ^{T} is computed through the transport linear systems that result from the solution of the Chapman-Enskog expansion, as the second Laguerre-Sonine approximation

$$\boldsymbol{G}^{\lambda}\boldsymbol{\alpha} = \boldsymbol{x}, \tag{2.59}$$

with the conductivity being expressed in terms of the solution of the linear system $\boldsymbol{\alpha}$

$$\lambda^{\mathrm{T}} = \sum_{i \in \mathcal{H}} \alpha_{ij} x_i. \tag{2.60}$$

Again, $\boldsymbol{G}^{\lambda}$ is a symmetric positive definite matrix of size $n_{\mathcal{S}} \times n_{\mathcal{S}}$ dependent on collision integral data and species concentrations (see Appendix A).

The internal energy is not considered in the systems. However, the contributions of the different modes are taken into account through the Eucken corrections [75] which read

$$\lambda^{\mathrm{R}} = \sum_{i \in \mathcal{S}^*} \frac{\rho_i c_{\mathrm{p}_i}^{\mathrm{R}}}{\sum_{j \in \mathcal{H}} x_j / \mathscr{D}_{ij}}, \tag{2.61}$$

$$\lambda^{\mathrm{V}} = \sum_{i \in \mathcal{S}^*} \frac{\rho_i c_{\mathrm{p}_i}^{\mathrm{V}}}{\sum_{j \in \mathcal{H}} x_j / \mathscr{D}_{ij}}, \tag{2.62}$$

$$\lambda^{\mathrm{E}} = \sum_{i \in \mathcal{H}} \frac{\rho_i c_{\mathrm{p}_i}^{\mathrm{E}}}{\sum_{j \in \mathcal{H}} x_j / \mathscr{D}_{ij}}, \tag{2.63}$$

with $c_{\mathrm{p}_i}^{\mathrm{R}}, c_{\mathrm{p}_i}^{\mathrm{V}}$ and $c_{\mathrm{p}_i}^{\mathrm{E}}$ being the specific heats for species i for the corresponding internal energy modes. The contributions due to both Dufour's and Soret's effects haven been neglected in this formulation. Expressions for the thermal conductivity of the electron translational mode λ_{e} are obtained from the second or third order Laguerre-Sonine approximations as

$$\lambda_{\mathrm{e}}(2) = \frac{x_{\mathrm{e}}^2}{\Lambda_{\mathrm{ee}}^{11}}, \tag{2.64}$$

$$\lambda_{\mathrm{e}}(3) = \frac{x_{\mathrm{e}}^2 \Lambda_{\mathrm{ee}}^{22}}{\Lambda_{\mathrm{ee}}^{11}\Lambda_{\mathrm{ee}}^{22} - (\Lambda_{\mathrm{ee}}^{12})^2}, \tag{2.65}$$

where the $\Lambda_{\mathrm{ee}}^{lk}$ matrices are complex functions of the binary collision integrals for heavy-electron and electron-electron interactions. These matrices can also be found in Appendix A.

Similarly, when in thermal equilibrium $T = T^{\mathcal{V}}$ and Eq. (2.56) can be re-written

$$\boldsymbol{q} = -\lambda^{\mathrm{tot}} \nabla T + \sum_{i \in \mathcal{S}} h_i \rho_i \boldsymbol{V}_i, \tag{2.66}$$

with $\lambda^{\mathrm{tot}} = \lambda + \lambda^{\mathcal{V}}$.

The resolution of thermal non-equilibrium requires solving an additional governing equation for which closure of the internal heat flux needs to be provided

$$\boldsymbol{q}^{\mathcal{V}} = -\lambda^{\mathcal{V}}\nabla T^{\mathcal{V}} + \sum_{i\in\mathcal{S}} h_i^{\mathcal{V}}\rho_i \boldsymbol{V}_i. \tag{2.67}$$

Fig. 2.4 shows an example of viscosity and thermal conductivity coefficients for an equilibrium air mixture at 1 atm. The thermal conductivity is splitted in its different contributions. It is interesting to outline features that both the viscosity and heavy translational thermal conductivity share. The first is that both tend to increase with temperature. The second is that they both decrease with increasing levels of ionization, which according to Fig. 2.2 starts around 10,000 K. Both trends can be explained by considering the viscosity of a pure gas i (see Appendix A)

$$\mu_i = \frac{5}{16}\frac{\sqrt{\pi k_{\mathrm{B}} T_{\mathrm{h}} m_i}}{\bar{Q}_{ii}^{(2,2)}}. \tag{2.68}$$

with m_i and $\bar{Q}_{ii}^{(2,2)}$ being the particle mass and reduced collision integral of the gas. The monoatomic thermal conductivity is directly proportional to μ_i and it is expressed as

$$\lambda_i = \frac{15}{4}\frac{k_{\mathrm{B}}}{m_i}\mu_i. \tag{2.69}$$

The collision integrals for resonant charge transfer and charged interactions are significantly larger than other collisions due to Coulomb forces [81]. As the level of ionization increases, these interactions dominate and both the viscosity and heavy translational thermal conductivity decrease due to the inverse proportionality with $\bar{Q}_{ii}^{(2,2)}$ of μ_i.

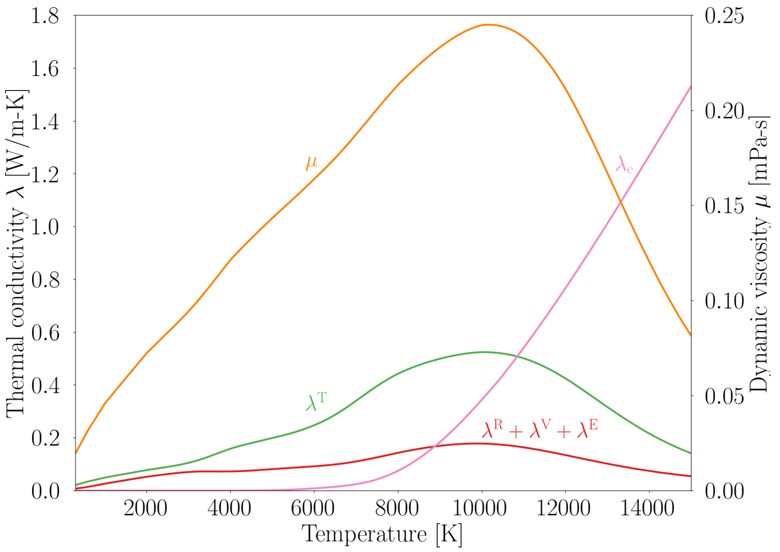

Figure 2.4: *Dynamic viscosity and various contributions to the total thermal conductivity as functions of temperature for equilibrium air (air11) at 1 atm.*

2.2.3 Gas phase chemistry

In the study of gas-surface interactions conducted in the context of this thesis, gas phase chemistry plays an important role. The chemical composition of the gas upon impacting on the material surface determines the feeding mechanism for such surface interactions to take place. In turn, this is highly coupled to how we perceive the material surface to be in terms of its response to the reacting flow. While thermodynamics and transport properties rely on theoretical models that are well established and understood, together with high fidelity numerical data from quantum or kinetic theory, chemistry models are based heavily on experimental data and rely on a more macroscopic description of the system. The mathematical structure that defines the chemical interaction between components is the law of mass action [82]. The general expression for any given reaction can be summed up as

$$\sum_{i \in \mathcal{S}} \nu'_{i,r} S_i \rightleftharpoons \sum_{i \in \mathcal{S}} \nu''_{i,r} S_i, \tag{2.70}$$

where $\nu'_{i,r}$ and $\nu''_{i,r}$ are the forward and backward stoichiometric coefficients for species S_i in reaction r. Mathematically, we can capture the advance of such reaction through the coefficient of molar rate-of-progress

$$\mathcal{R}_r = k_{\mathrm{f},r} \prod_{i \in \mathcal{S}} \left(\frac{\rho_i}{M_i} \right)^{\nu'_{i,r}} - k_{\mathrm{b},r} \prod_{i \in \mathcal{S}} \left(\frac{\rho_i}{M_i} \right)^{\nu''_{i,r}}, \tag{2.71}$$

with $k_{\mathrm{f},r}$ and $k_{\mathrm{b},r}$ as the reaction rate coefficients for the forward and backward reaction r and M_i the molar mass of species i. Eq. (2.71) intervenes in the mass production rates $\dot{\omega}_i$ of the species mass conservation equations. The expression reads

$$\dot{\omega}_i = M_i \sum_{r \in \mathcal{R}} (\nu''_{i,r} - \nu'_{i,r}) \mathcal{R}_r, \ \forall i \in \mathcal{S}, \tag{2.72}$$

for which $\mathcal{R}$ is the set of all chemical reactions considered. The model for the production term $\dot{\omega}_i$ needs the information about the reaction rates $k_{\mathrm{f},r}$ and $k_{\mathrm{b},r}$. In the case of chemical equilibrium, which is considered along thermal equilibrium when in LTE, the rate-of-progress $\mathcal{R}_r$ of all reactions r is zero. We can then define an equilibrium constant for reaction r as

$$K_{\mathrm{eq},r} = \frac{k_{\mathrm{f},r}}{k_{\mathrm{b},r}} = \prod_{i \in \mathcal{S}} \left(\frac{\rho_i^*}{M_i} \right)^{(\nu''_{i,r} - \nu'_{i,r})}, \tag{2.73}$$

where the superscript $*$ refers to the density of species i in equilibrium conditions. This equilibrium constant is related to the change in Gibbs free energy ΔG_r° across reaction r

$$K_{\mathrm{eq},r} = \left(\frac{p^\circ}{RT} \right)^{\sum_{i \in \mathcal{S}} (\nu''_{i,r} - \nu'_{i,r})} \exp\left(-\frac{\Delta G_r^\circ}{RT} \right), \tag{2.74}$$

where the superscript $^\circ$ refers to the quantities at standard conditions of 1 atm and 273.15 K. The term ΔG_r° denotes the difference of molar Gibbs energies between products and reactants at standard conditions for reaction r,

$$\Delta G_r^\circ = \sum_{i \in S} \left(\nu''_{i,r} - \nu'_{i,r} \right) G_i^\circ, \tag{2.75}$$

where G_i° is the standard state molar Gibbs energy of species i,

$$G_i^\circ = H_i^\circ - T S_i^\circ, \quad \forall i \in \mathcal{S}, \tag{2.76}$$

with H° and S° being the molar enthalpy and entropy at standard conditions, respectively.

The advantage of this quantity is that the left-hand side is only dependent on the reaction temperature while the right-hand side is only dependent on composition. The computation of the backward reaction rates can be done through the equilibrium constant even outside equilibrium conditions as $K_{\mathrm{eq},r}$ maintains its value.

In terms of the reaction rate coefficients, which are the only missing piece of data, we only need to specify the forward rates

$$k_\mathrm{f} = A T_\mathrm{f}^\beta \exp\left(-\frac{E_\mathrm{a}}{R T_\mathrm{f}} \right), \tag{2.77}$$

being A the pre-exponential factor, E_a the activation energy of the reaction and T_f the temperature of the thermal bath which provides the energy for the reaction to proceed in the forward way. Eq. (2.77) is known as the modified Arrhenius law where the parameters A, β and E_a are fitted to some experimental data. Not all reactions considered follow this law. First order reactions such as pre-dissociation do not depend on the rates of collision as they occur spontaneously. A molecule with a quasi-bound vibrational energy state can spontaneously dissociate if the energy is above the dissociation threshold. Second and third order reactions do follow Eq. (2.77). There exists a hierarchy on the dependencies of the reaction rates. They can increase with the frequency of collisions between reactants. Of those collisions, some of them will have enough energy to surpass some threshold so that the chemical reaction is possible. From all those possibilities, a subset will actually react. This last fraction is difficult to determine and it is the reason why we commonly rely on experimental data to identify these rate coefficients. More accurate reaction rates can be obtained theoretically from quantum mechanics. In the literature, Jaffe et al. [83] have computed them for selected systems.

Often, there are species in some reactions that do not participate. These are called third-body reactions and their molar rates-of-progress differ only by a constant factor [1]. The role of the third body is only to provide the energy needed for the reaction to take place, and different third bodies provide different unique pathways for the reaction to occur, differing only in the energy delivered. Therefore, no stoichiometric coefficients assigned to any third body play a role in the computation of the rate-of-progress.

Thermal non-equilibrium effects in chemical kinetics. In this thesis, non-equilibrium phenomena is modeled following a two temperature model. It is important to state possible couplings between the thermal state of the flow and chemical kinetics. In this case, forward reactions rates read

$$k_{\mathrm{f},r} = k_{\mathrm{f},r}^{\mathrm{eq}}(T_\mathrm{f}) \Phi(T_\mathrm{f}, T^\mathcal{V}), \tag{2.78}$$

with the term $\Phi(T_\mathrm{f}, T^\mathcal{V})$ being a non-equilibrium factor dependent on the internal heat bath temperature. Some common models for the non-equilibrium factor can be found in the work of Scoggins [1]. The most widely used model for CFD being the one developed by Park [65, 66]. It is a simple phenomenological model used to describe the non-equilibrium dissociation of nitrogen. The non-equilibrium factor for this particular model reads

$$\Phi(T_\mathrm{f}, T^\mathcal{V}) = T_\mathrm{m}^\beta T^{-\beta} \exp\left(\frac{E_\mathrm{a}}{RT} - \frac{E_\mathrm{a}}{RT_\mathrm{m}}\right), \tag{2.79}$$

with $T_\mathrm{m} = T^q \left(T^\mathcal{V}\right)^{q-1}$ and $q \in [0, 1]$, where T_m is an average temperature and q is fitted to experimental data. In practice, this model is implemented here by considering $\Phi = 1$ and taking the reaction temperature $T_\mathrm{f} = T_\mathrm{m}$.

Overall, all reaction mechanisms and associated data used in this thesis can be found in detail in Appendix B.

2.2.4 Energy transfer mechanisms

Resolving the thermodynamic state of the gas to accommodate non-equilibrium effects has a cost. Not only we are solving an extra governing equation for the internal energy mode (in our chosen 2T model), but also we need data regarding the excitation and de-excitation of the extra mode. In the case of the two temperature model considered, we take into account elastic collisions which entail energy transfer between translational and vibrational modes for the different molecules in the mixture Ω_i^VT, and between electron and heavy translational energies Ω^eT. Inelastic collisions which affect the energy that gets added or substracted to the vibrational bath due to chemical reactions Ω_i^CV are also taken into account. The last energy exchange mechanism reviewed is electron-impact ionization Ω^I.

Energy exchange between modes. The mathematical relation for the term Ω_i^VT follows a Landau-Teller formulation [84]

$$\Omega_i^\mathrm{VT} = \rho_i \frac{e_i^\mathrm{V}(T) - e_i^\mathrm{V}(T^\mathcal{V})}{\tau_i^\mathrm{VT}}, \ \forall i \in \mathcal{S}^*, \tag{2.80}$$

where τ_i^VT is the characteristic relaxation time for the vibrational heat bath of molecule i due to collisions. This result is derived from the dynamics of a harmonic-oscillator interacting with a single bath of translational energy. The rate of change of the average vibrational energy of such oscillator is posed and assumptions are made regarding the weakly interactions between the oscillator and the heat bath around it, limiting the possible transitions of energy to just neighbouring vibrational states. Under these assumptions, a rate equation for the number density of the different vibrational levels is derived and substituted in to obtain the final expression of Eq. (2.80). Nikitin and Troe [85] also provide a historical overview of the landmark paper of Landau and Teller in 1936 [84].

In a later work, Panesi et al. [86] showed that such formulation can also be derived from more general principles, being able to correctly capture the energy transfer process in a state-to-state method.

The characteristic time is derived by Millikan and White [87] using an empirical formula for diatomic molecules below 8,000 K which reads

$$\tau_i^\mathrm{MW} = \frac{\sum_{j\in\mathcal{S}} x_j \exp\left[a_{ij}\left(T^{-1/3} - b_{ij}\right) - 18.42\right]}{1.01325 \cdot 10^5 p}, \ \forall i \in \mathcal{S}^*, \tag{2.81}$$

where $a_{ij} = 0.00116\sqrt{\mu_{ij}}\left(T^{\mathcal{V}}\right)^{4/3}$ and $b_{ij} = 0.015\mu_{ij}^{5/4}$ with μ_{ij} being the reduced mass of species i with collision partner j.

Park [88, 89] proposed a correction for the characteristic time term to account for the finiteness of the cross-sections involved in the collision pairs at high temperature. He argued that this collision-limited correction avoids predicting an excessively fast relaxation as shown by Millikan and White. The corrected term reads

$$\tau_i^{\mathrm{VT}} = \tau_i^{\mathrm{MW}} + \tau_i^{\mathrm{P}} = \tau_i^{\mathrm{MW}} + \frac{1}{n_i\sqrt{\dfrac{8k_{\mathrm{B}}T}{\pi m_i}}\sigma_i^{\mathrm{V}}}, \ \forall i \in \mathcal{S}^*, \tag{2.82}$$

with σ_i^{V} being the effective collision cross-section for internal energy relaxation. To account for the total energy transfer between modes, we ought to sum all the contributions from each molecule in the mixture

$$\Omega^{\mathrm{VT}} = \sum_{i\in\mathcal{S}^*} \Omega_i^{\mathrm{VT}}. \tag{2.83}$$

Free electron and heavy translational energy exchange. The term Ω^{eT} corresponds to the energy transfer due to elastic collisions between free electrons and heavy particles. Similar to the Ω^{VT} term, this energy exchange follows a Landau-Teller formulation

$$\Omega^{\mathrm{eT}} = \rho_e \frac{e_e^{\mathrm{T}}(T) - e_e^{\mathrm{T}}\left(T^{\mathcal{V}}\right)}{\tau^{\mathrm{eT}}}, \tag{2.84}$$

where the relaxation time

$$\frac{1}{\tau^{\mathrm{eT}}} = \sum_{i\in\mathcal{H}} \frac{8}{3}\frac{m_{\mathrm{e}}}{m_i} n_i \sqrt{\frac{8k_{\mathrm{B}}T^{\mathcal{V}}}{\pi m_{\mathrm{e}}}}\bar{Q}_{\mathrm{e}i}^{(1,1)} \tag{2.85}$$

is derived from kinetic theory with $\bar{Q}_{\mathrm{e}i}^{(1,1)}$ being the reduced collision integral for electron-heavy interactions (Appendix A).

Energy exchange due to chemical reactions. Energy can also be added or removed through chemical reactions. Particularly, recombination and dissociation can cause the vibrational energy of the flow to increase or decrease by means of the source term

$$\Omega_i^{\mathrm{CV}} = h_i^{\mathrm{V}}\dot{\omega}_i, \ \forall i \in \mathcal{S}^*, \tag{2.86}$$

which represents each molecule's contribution to the energy exchange. The total contribution is the summation over all participating molecules

$$\Omega^{\mathrm{CV}} = \sum_{i\in\mathcal{S}^*} \Omega_i^{\mathrm{CV}}. \tag{2.87}$$

Different probabilities can be associated to molecules with different vibrational states. Highly vibrationally excited molecules will generally tend to dissociate first than those with lower vibrational energies [73]. In this thesis, we adopt a non-preferential model in which all molecules have the same chance to contribute to the chemical-internal energy exchange and the average enthalpy h_i^{V} of molecule i is used for the computation. It is important to note that the chemical production terms $\dot{\omega}_i$ and transfer mechanism for thermal non-equilibrium are tightly coupled through this term. This creates a dependency of the vibrational energy distribution and the rate of creation or destruction of molecule i. Therefore, this choice of modeling affects chemical kinetics and internal energy distributions.

Energy exchange due to electron-impact ionization. Another form of energy transfer is due to electron impacts causing ionization as result. In this case, free stream electrons act as a mean of delivering energy to a heavy particle causing it to ionize. This also results in the free electron losing translational energy. The term describing this transfer mechanism reads

$$\Omega^{\mathrm{I}} = \sum_{r \in \mathcal{R}^{\mathrm{I}}} \Delta h_r \mathcal{R}_r, \tag{2.88}$$

where $\mathcal{R}^{\mathrm{I}}$ is the set of reactions involving electron-impact ionization and Δh_r and $\mathcal{R}_r$ are the molar reaction enthalpy and molar rate-of-progress of reaction r. The term Δh_r represents the change in average enthalpy needed to ionize the heavy particle in a particular reaction r from the ground state. Hartung et al. [90] and Greendyke [91] suggested to set Δh_r equal to the change in average enthalpy required to ionize a species from an already excited state as was suggested originally by Lee [63]. In this thesis, this modification is also adopted.

2.3 Gas-surface interaction

In this thesis, the big question mark is posed on the modeling and testing of gas-surface interactions in atmospheric entry flows. Specifically, we focus our attention to two different types of materials: catalytic and ablative. Qualitatively, they are different in the way they cope with high temperatures and how they can dissipate large amounts of energy. Catalytic materials re-radiate most of the heat back to the surrounding gas without undergoing fundamental changes in their structure. Due to this main feature, they are often referred to as materials for re-usable TPS. On the other hand, ablative materials are chemically consumed when exposed to plasma flows and they can only be used once. The consumption of the material is what dissipates the energy of the incoming flow and protects the inside of the spacecraft.

Quantitatively, their differences are related to the modeling, the amount of data needed for each and the observables that we can obtain in a testing facility. In terms of the modeling, the number of different phenomena that need mathematical definition is what distinguishes catalysis from ablation processes. The data needed to simulate both also vary. Ablation products, which commonly entail carbonaceous species, need to be characterized to the kinetic and quantum levels for certain closure models such as thermodynamics, transport and chemistry, in addition to the gas species. This difficulty is not faced in catalytic systems where no additional species are injected in the flow.

The observables that can be obtained in a plasma wind tunnel are also different. Heat fluxes are easier to obtain for catalytic materials as we can make the assumption that all radiation is due to the incoming heat flux that the material experiences. This is not known for ablative materials, where a small part of the heat is re-radiated back and the rest goes into increasing the surface temperature and degrading the surface. On the other hand, ablative materials recess, which means that a great deal of information is available to us from measurements of the recession rate, due only to ablation chemical reactions. Furthermore, one of the strongest radiative signatures in these flows is due to the cyanogen molecule (CN) which is a product of ablation processes, allowing us to obtain information about particular chemical reactions taking place at the material surface.

All in all, these two different systems present characteristics that set them apart and we are compel to offer a summary of the modeling used in this thesis.

2.3.1 Surface mass and energy balances

In this work, the modeling of gas-surface interactions is done from the flow perspective. Ideally, one would solve the governing equations for the fluid and material domains in a fully coupled fashion. As this is a quite challenging undertaking, it is common to resort to approximations of the modeling of the surface interface when looking at it from the flow or material perspective. This methodology was first introduced by Milos and Rasky [23] for surfaces involving thermochemical processes such as ablation and catalysis. In general, the surface is treated as a boundary that injects or absorbs mass, momentum and energy. Detailed balances of mass, momentum and energy are considered within the thin lamina of gas in contact with the surface by consideration of certain physical phenomena at the interface. The balances are solved in a coupled fashion in terms of the macroscopic properties of the gas such as partial densities, velocities and temperatures, imposing suitable boundary conditions.

Surface balances can be more generally derived from the Reynolds transport theorem, as explained by Martin et al. [92], for any conserved quantity. By assuming steady-state on the surface and taking limits on the volumetric quantities as one dimension goes to zero, the fluxes reduce to

$$[\boldsymbol{F}_{\mathrm{g}} - \boldsymbol{F}_{\mathrm{s}}] \cdot \boldsymbol{n} = \dot{\Omega}_{\mathrm{s}}, \tag{2.89}$$

in which $\boldsymbol{F}_{\mathrm{g}}$ and $\boldsymbol{F}_{\mathrm{s}}$ refer to the flux leaving the gas interface and surface fluxes injected in the interface, respectively. The term $\boldsymbol{n}$ is the normal to the surface, pointing to the gas and $\dot{\Omega}_{\mathrm{s}}$ is the source term for different surface processes. In this thesis, we are interested in mass and energy balances but when mechanical removal such as spallation becomes important, momentum balances must be solved additionally. A no-slip boundary condition is assumed to close the momentum conservation equations at the surface.

Surface mass balance. The fluxes leaving the gas-surface interface for both materials $\boldsymbol{F}_{\mathrm{g}}$ are substituted in Eq. (2.89). The different contributions take the form of convective fluxes $\rho_i \boldsymbol{u}$ and diffusive fluxes $\rho_i \boldsymbol{V}_i$ per species. The source terms account for the surface chemical reactions taking place $\dot{\omega}_{\mathrm{w},i}$. Fig. 2.5 shows a schematic view of the different components of the surface mass balance and their direction relative to the thin lamina that is the gas-surface interface.
Overall, the balance reads

$$[\rho_{\mathrm{w},i}(\boldsymbol{u}_{\mathrm{g}} - \boldsymbol{u}_{\mathrm{r}}) + \rho_{\mathrm{w},i}\boldsymbol{V}_{\mathrm{w},i}] \cdot \boldsymbol{n} = \dot{\omega}_{\mathrm{w},i}, \ \forall i \in \mathcal{S}, \tag{2.90}$$

where the subscript w refers to wall quantities. $\boldsymbol{u}_{\mathrm{g}}$ is the velocity of the gas leaving the interface and $\boldsymbol{u}_{\mathrm{r}}$ the velocity at which the interface is moving. As we are not solving mo-

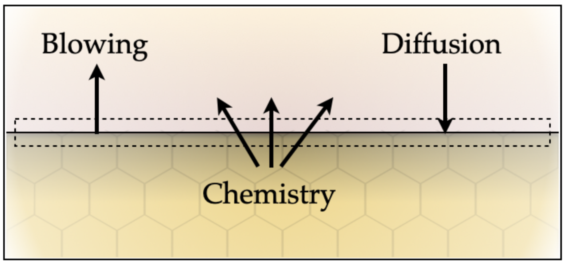

Figure 2.5: *Schematic representation of the different fluxes involved in the surface mass balances considered in this work.*

mentum surface balances, we impose the no-slip condition as follows $\boldsymbol{u}_\mathrm{g} \cdot \boldsymbol{n} = 0$. Summing up the mass balance equations for all species, the magnitude for $\boldsymbol{u}_\mathrm{g}$ reads

$$u_\mathrm{g} = \frac{\dot{m}_\mathrm{blow}}{\sum_{i\in\mathcal{S}} \rho_{\mathrm{w},i}}, \tag{2.91}$$

with $\dot{m}_\mathrm{blow}$ being the blowing mass due to ablation products being injected in the gas. In terms of the interface receeding velocity $\boldsymbol{u}_\mathrm{r}$, the equation for its magnitude reads

$$u_\mathrm{r} = \frac{\sum_{i\in\mathcal{S}} \dot{\omega}_{\mathrm{abla},i}}{\rho_\mathrm{s}}, \tag{2.92}$$

being ρ_s the density of the solid surface which is generally known. The term $\dot{\omega}_{\mathrm{abla},i}$ is the production of species due to ablation processes, the only ones producing surface recession.

Surface energy balances. In general, surface temperatures can be measured for both catalytic and ablative systems. Modeling the physics involved in surface energy balances can be avoided if the surface temperature information is directly fed to the model. The Bayesian approaches developed in the context of this thesis make use of such possibility. Nevertheless, surface energy balances are put into question when dealing with nitrogen ablation. The introduction of additional surface chemical mechanisms, such as nitrogen recombination, can impact such balance considerably.

In terms of energies conservation, Eq. (2.89) is recast for the total energy as

$$\begin{multlined}\Bigg[\rho_\mathrm{w}(\boldsymbol{u}_\mathrm{g} - \boldsymbol{u}_\mathrm{r})h_\mathrm{w} + \sum_{i\in\mathcal{S}} \rho_{\mathrm{w},i} h_{\mathrm{w},i} \boldsymbol{V}_{\mathrm{w},i} + \lambda_\mathrm{w}\nabla T_\mathrm{w} + \\ + \lambda_\mathrm{w}^\mathcal{V}\nabla T_\mathrm{w}^\mathcal{V} - \boldsymbol{q}_\mathrm{cond} - \rho_\mathrm{s}\boldsymbol{u}_\mathrm{r}h_\mathrm{s} - \rho_\mathrm{p}\boldsymbol{u}_\mathrm{p}h_\mathrm{p}\Bigg] \cdot \boldsymbol{n} = \dot{\Omega}_\mathrm{w},\end{multlined} \tag{2.93}$$

where the terms $\sum_{i\in\mathcal{S}} \rho_{\mathrm{w},i} h_{\mathrm{w},i} \boldsymbol{V}_{\mathrm{w},i}$, $\lambda_\mathrm{w}\nabla T_\mathrm{w}$ and $\lambda_\mathrm{w}^\mathcal{V}\nabla T_\mathrm{w}^\mathcal{V}$ are the diffusive and conductive heat fluxes for translational and vibrational thermal baths, respectively. The components $\boldsymbol{q}_\mathrm{cond}$, $\rho_\mathrm{s}\boldsymbol{u}_\mathrm{r}h_\mathrm{s}$, and $\rho_\mathrm{p}\boldsymbol{u}_\mathrm{p}h_\mathrm{p}$ are the conduction flux exiting the interface towards the material, the convected enthalpy due to the recession of the surface or gases blowing in the interface, and the convected enthalpy due to the pyrolysis gases, respectively. The only source term taken into account in Eq. (2.93) as the effect of the surface in the surrounding gas is the radiative flux. This term follows the Stefan-Boltzmann law for a body in thermodynamic equilibrium at temperature T_w

$$\dot{\Omega}_{\mathrm{w}} = \sigma\epsilon\left(T_{\mathrm{w}}\right)^4, \tag{2.94}$$

where σ is the Stefan-Boltzmann constant and ϵ the emissivity coefficient of the surface.

In this thesis, the ablation modeling is restricted to carbon preforms as it constitutes the material of choice for wind tunnel testing for nitridation. For carbon preforms the binding resine is non-existent, allowing us to drop the modeling of the physics associated to pyrolysis in the energy balances [93, 94]. Consequently, Eq. 2.93 can be further simplified by neglecting the presence of pyrolysis gases and approximating the conductive heat flux.

In Eq. (2.95), the conductive heat flux on the solid has been approximated by assuming steady-state conditions for the energy equation in the solid phase and integrating over the semi-infinite material [24, 25]

$$\left[\rho_{\mathrm{w}}(\boldsymbol{u}_{\mathrm{g}} - \boldsymbol{u}_{\mathrm{r}})h_{\mathrm{w}} + \sum_{i\in\mathcal{S}} \rho_{\mathrm{w},i} h_{\mathrm{w},i} \boldsymbol{V}_{\mathrm{w},i} + \lambda_{\mathrm{w}}\nabla T_{\mathrm{w}} + \lambda_{\mathrm{w}}^{\mathcal{V}}\nabla T_{\mathrm{w}}^{\mathcal{V}}\right]\cdot\boldsymbol{n} = \dot{\Omega}_{\mathrm{w},i}, \ \forall i\in\mathcal{S}. \tag{2.95}$$

In cases where the material has low thermal conductivity, approximate methods like steady-state ablation can be used without compromising the accuracy of the computations. Ideally, a material code should be coupled to the flow solutions or the energy equation in the solid should be solved for a proper balance of fluxes at the interface [92]. Fig. 2.6 presents a schematic view of the different fluxes contained in Eq. (2.95) together with their relative orientation regarding the thin lamina of the gas-surface interface.

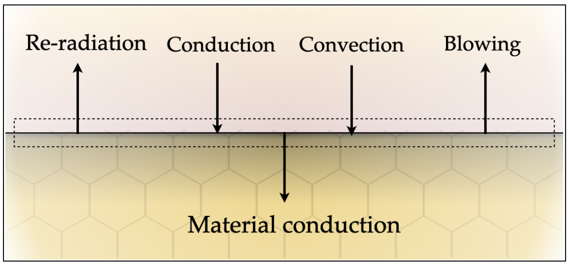

Figure 2.6: *Schematic representation of the different fluxes involved in the surface energy balances considered in this work.*

To close all the conservation equations seen in Sec. 2.1.1, we also need to impose a wall condition for the internal energy. Traditionally, thermal equilibrium is considered and the condition $T_{\mathrm{w}} = T_{\mathrm{w}}^{\mathcal{V}}$ is imposed. In this thesis, we choose to be agnostic about the thermal state of the flow at the wall. In a recent work, Capriati et al. [95] proposed a surface energy balance for the vibrational bath in a two-temperature model. The internal energy surface balance reads

$$\left[\rho_{\mathrm{w}}(\boldsymbol{u}_{\mathrm{g}} - \boldsymbol{u}_{\mathrm{r}})h_{\mathrm{w}}^{\mathcal{V}} + \sum_{i\in\mathcal{S}} \rho_{\mathrm{w},i} h_{\mathrm{w},i}^{\mathcal{V}} \boldsymbol{V}_{\mathrm{w},i} + \lambda_{\mathrm{w}}^{\mathcal{V}}\nabla T_{\mathrm{w}}^{\mathcal{V}}\right]\cdot\boldsymbol{n} = \dot{\Omega}_{\mathrm{w}}^{\mathcal{V}\mathrm{T}} + \dot{\Omega}_{\mathrm{w}}^{\mathrm{C}\mathcal{V}}, \tag{2.96}$$

where the convective and conductive terms in Eq. (2.95) are now only associated to the internal energies $\mathcal{V}$. The first source term $\dot{\Omega}_{\mathrm{w}}^{\mathcal{V}\mathrm{T}}$ is the relaxation of internally excited particles by collision with the surface (heterogeneous quenching). This term was derived by adapting the volumetric Landau-Teller gas-gas collisions formulation (Sec. 2.2.4) to surface gas-surface collisions. The expression reads

$$\dot{\Omega}_{\mathrm{w}}^{\mathcal{V}\mathrm{T}} = \sum_{i\in\mathcal{S}} \alpha_i \mathcal{F}_i^{\downarrow} m_i \left(h_{\mathrm{w},i}^{\mathcal{V}} \left(T^{\mathcal{V}} \right) - h_{\mathrm{w},i}^{\mathcal{V}} \left(T \right) \right), \tag{2.97}$$

where α_i is a parameter that considers that only the α_i fraction of the collisional events of species i leads to a relaxation. The term $\mathcal{F}_i^{\downarrow}$ represents the impinging flux of species i and m_i is the particle mass of species i. The second source term in Eq. (2.96) is a chemical source term which takes into account that not all the energy from chemical reactions is accommodated on the surface. It reads

$$\dot{\Omega}_{\mathrm{w}}^{\mathrm{C}\mathcal{V}} = \sum_{i\in\mathcal{S}} \left(1-\beta_i\right) \left(h_{\mathrm{w},i}^{\mathcal{V}} - h_{\mathrm{w},i} \right), \tag{2.98}$$

where the β_i coefficient is an adaptation for a two-temperature model of the energy accommodation term defined by Halpern and Rosner [96], and that a $1-\beta$ quota of the heat flux is transferred into the internal energy modes of the products. More details on the two-temperature surface energy balance here presented can be found in the work of Capriati et al. [95].

In the next sections, we hone in the source terms of the surface mass balances for both catalysis and ablation. These balances contain the defining features we are after when performing the different inferences.

2.3.2 Catalysis

Heterogeneous catalytic reactions only involve chemistry among gas species as the material itself does not get consumed (Sec. 2.3). An important character of catalytic or recombination reactions at the surface is the fact that they are in general exothermic, releasing a considerable amount of energy to be absorbed by the surface or distributed among species to excite their internal states. Coupling mechanisms with the flow add to the difficulty of modeling the heat flux to the material due to these recombination reactions. Gas phase chemistry and diffusion models are tightly coupled to the surface reactions by acting as main feeding mechanisms of atomic species. This coupling has been a matter of ongoing research efforts by different researchers [97–99], among others.

The surface mass balance for catalytic materials reads

$$\rho_{\mathrm{w},i} \boldsymbol{V}_{\mathrm{w},i} \cdot \boldsymbol{n} = \dot{\omega}_{\mathrm{w},i}, \ \forall i \in \mathcal{S}, \tag{2.99}$$

where the only term that needs closure is the production term $\dot{\omega}_{\mathrm{w},i}$. Different models are available in the literature that can capture the underlying physics of heterogeneous chemistry at the surface. These models range from defining catalytic reactions as macroscopic, non-elementary processes (the so-called gamma model) to detailed finite-rate chemistry as proposed by different authors [100–102], among many. The former is widely used in the aerothermodynamics community because of its simplicity and lack of microscopic model data. It is quite suitable for learning its parameters from wind tunnel experimental data.

First proposed by Goulard [103], gamma models aim at explaining catalytic reactions by introducing a model parameter γ_i which defines the probability that a certain species has of recombining at the surface. The expression for γ_i reads

$$\gamma_i = \frac{\mathcal{F}_i^{\text{react}}}{\mathcal{F}_i^{\downarrow}}, \ \forall i \in \mathcal{S}, \tag{2.100}$$

where $\mathcal{F}_i^{\downarrow}$ represents the impinging flux of species i and $\mathcal{F}_i^{\text{react}}$ the part of that flux that actually reacts upon impingement. The recombination parameter γ_i appears in the source term as

$$\dot{\omega}_{\text{w},i} = \gamma_i m_i \mathcal{F}_i^{\downarrow}, \ \forall i \in \mathcal{S}. \tag{2.101}$$

Assuming a surface interface in thermal equilibrium, the impinging flux $\mathcal{F}_i^{\downarrow}$ can be approximated by a Maxwellian distribution at temperature T_w

$$\mathcal{F}_i^{\downarrow} = n_i \sqrt{\frac{k_\text{B} T_\text{w}}{2\pi m_i}}, \ \forall i \in \mathcal{S}. \tag{2.102}$$

This formulation is used in this thesis for the simulation of boundary layer flows in the VKI Plasmatron facility when exposed to catalytic materials. This model represents a good trade-off between the limited flow information coming from the experimental data, namely pressures and heat fluxes, and a model for a detailed mechanism as the chemistry at the material surface. By assuming one single parameter per material, we can begin to learn the relative importance of recombination reactions in the measured heat flux. Furthermore, this parameter allows us to learn about the free stream by acting as a fitting parameter to close the surface mass balance equation.

The more detailed models found in the literature, as for example the one proposed by Barbato [98], generally rely on finely-tuned data parameters. The argument for the development and use of these detailed models is that they can be easily extrapolated to model unexplored conditions based on physical arguments. However, the capability to efficiently learn the model parameters from actual data in such cases is lost and additional experimental data and/or methodologies should be explored to avoid the issue of fine-tuning. The experimental data explored in this thesis are not suitable for this undertaking. The aim of this work is to provide consistent calibrations of the recombination efficiencies in gamma models, providing objective uncertainty estimates against which one could compare a posteriori the performances of finite-rate models.

2.3.3 Ablation

In the case of ablative materials, the surface mass balances are reviewed. The model here introduced does not account for mechanical ablation or spallation either [104], only gaseous species are included in the ablation mechanism. For the mass balance, blowing fluxes are added to Eq. (2.99)

$$[\rho_{\text{w},i}(\boldsymbol{u}_\text{g} - \boldsymbol{u}_\text{r}) + \rho_{\text{w},i}\boldsymbol{V}_{\text{w},i}] \cdot \boldsymbol{n} = \dot{\omega}_{\text{w},i}, \ \forall i \in \mathcal{S}, \tag{2.103}$$

where the source term $\dot{\omega}_{\text{w},i}$ represents the sum for species i of the production rates of individual heterogeneous reactions with the surface $\dot{\omega}_{\text{w},i} = \sum_{r=1}^{n_{\mathcal{R}_\text{w}}} \dot{\omega}_{\text{w},i}^r$, with $n_{\mathcal{R}_\text{w}}$ being the number of considered reactions.

As with the catalysis surface mass balance, we need to introduce closure terms for the production of species $\dot{\omega}_{\text{w},i}^r$. The approach for the production term considered in this work is a phenomenological one for the same reason as for the catalysis model: there is only so much that we can learn from the present data. We are only concerned with ablation models for surface reactions involving nitrogen on the side of the flow and carbon on the material side. The model for the production rate is defined in the same fashion as for catalysis

$$\dot{\omega}^{r}_{\mathrm{w},i} = \gamma^{r}_{i} m_i \mathcal{F}^{\downarrow}_{i}, \ \forall i \in \mathcal{S}, \ \forall r \in n_{\mathcal{R}_{\mathrm{w}}}. \tag{2.104}$$

In this case, the following reaction mechanisms are taken into account.

Carbon nitridation. A reaction of the type $\mathrm{C(s)} + \mathrm{N} \rightarrow \mathrm{CN}$ is considered, where the label s refers to carbon adsorbed by the material surface. The definition of the model rests on a recombination probability parameter $\gamma_{\mathrm{N}}^{\mathrm{CN}}$ which is generally expressed as an Arrhenius rate

$$\gamma_{\mathrm{N}}^{\mathrm{CN}} = A \exp\left(\frac{-T_{\mathrm{a}}}{T_{\mathrm{w}}}\right), \tag{2.105}$$

with T_{a} being the equivalent activation energy, taken as $E_{\mathrm{a}}/k_{\mathrm{B}}$ with E_{a} being the activation energy of the nitridation reaction. A first Arrhenius model for the parameter $\gamma_{\mathrm{N}}^{\mathrm{CN}}$ was derived by Suzuki et al. [21] considering only low surface temperatures. An updated version was proposed by Helber et al. [22] including higher surface temperatures.

Nitrogen recombination. Ablation mechanisms are richer in the way that they can also include recombination reactions as seen for catalysis. In the case of nitrogen plasma flows, nitrogen recombination $\mathrm{N(s)} + \mathrm{N} \rightarrow \mathrm{N_2}$ can have a large impact in the surface energy balance due to its exothermic nature. Included in the original model of Zhluktov and Abe [105], nitrogen recombination is a competing mechanism to nitridation, consuming available atomic nitrogen which, in turn, has the potential to impact the former reaction in a coupled fashion. In this work, we choose to add this reaction to the ablation mechanism to be calibrated from experiments. In this case, nitrogen recombination is taken as a parameter $\gamma_{\mathrm{N}}^{\mathrm{N_2}}$ without further resolution into Arrhenius law parameters.

2.4 On the complexity of the modeling

In this mix of governing equations, constitutive relations and data coming from different sources with various fidelities, uncertainty treatments become important. In order to consistently gauge our actual knowledge about the system we want to simulate, and how it compares to experiments, objective uncertainty estimates are needed to avoid fine-tuning of parameters and reaching biased conclusions. This is particularly important in simulation scenarios where learning about some parameter effects is masqueraded by the effects of different phenomena that need assumptions for which we lack proper understanding. Such is the case in the conundrum among gas phase chemistry, diffusion processes and gas-surface interactions. The overall result in terms of surface heating, for example, depends strongly on the modeling of those processes as well as their coupling. Assumptions affecting these processes can strongly impact deterministic validations and the conclusions that ensue. This issue is accentuated along this thesis and the work developed goes inline with providing methodologies for achieving full uncertainty characterization on the different layers of complexity presented in this chapter.

From an uncertainty perspective, the different assumptions included in Sec. 2.1 about characteristic time scales and simplifications can be considerable sources of uncertainty as they directly affect the number of governing equations to be solved and their interactions. Additionally, more uncertainty stems from the terms chosen to be included in the governing equations as representative of the different physico-chemical processes considered in the definition of the problem. Table 2.1 is prone to change depending on the degree of understanding we have at a given moment and the different quantities that we consider important to include in our governing equations. Further, each of the terms that need closure in Table 2.1 is the result of additional assumptions, models and computations which also need proper uncertainty analyses.

On the other hand, getting accurate boundary conditions to close the governing equations can also entail the resolution of complex problems in some cases. As we recall, prescribing proper boundary conditions can be based on assumptions, additional models and/or experimental data. Assumptions and additional models can introduce false certainty about the boundary conditions, considerably altering and biasing the results of validation and calibration studies. This is particularly problematic for reaching consistent conclusions from our simulations. Moreover, the different nature of the boundary conditions need of different techniques to estimate their uncertainties.

Tables 2.2-2.3 show a summary of all the equations needed to solve for the conservation of mass, momentum and energy, the different possible choices for boundary conditions, the number of flow variables involved, the closure models and the data needed. In particular, Table 2.3 shows an overview of the closure models, model parameters and number of model parameters involved in solving for all the various terms that need closure in the governing equations and boundary conditions. The table avoids repetition of equations and data in such a way that solving for a particular term requires the models explicitly depicted and any other equation introduced before. The data needed are introduced only once with the closure model that first needs them. Other models might need the same data but they do not get added to the overall sum to avoid repetition. The same applies to the number of model parameters column. The system summarized in Table 2.2 governs the macroscopic quantities of the flow which are then used in the various closure models depicted in Table 2.3 to compute the terms needed in the governing equations and boundary conditions.

To have a more precise idea of the amount of model parameters needed to resolve these flows, we imagine a three-dimensional non-equilibrium flow composed of 5-species air with no surface reactions at steady-state. Using common chemical mechanisms and thermodynamic data for this system, the ratios of data to variables amount to: 162 to 5 species densities and 3 velocity components for the conservation of mass and momentum, and 219 to 2 temperatures for the energies conservation. Overall, we need to prescribe 381 parameters to solve a flowfield composed of 10 variables changing in space. As the number of species and phenomena considered increases, this ratio grows considerably. Unless we have complete confidence on all the data sources for our simulations, our predictions will be necessarily affected by uncertainty stemming from any of the 381 data parameters, in this particular case. Moreover, understanding the differences among solutions when studying a particular phenomenon is a complex task subjected to many assumptions made to fulfill the models need for closure.

2.5 Summary

The objective of this chapter is twofold. First, we aim at presenting in detail the different models used to explain the underlying physical phenomena present in plasma wind tunnel subsonic ground testing. We focus on this particular type of flows given that the main objective is to devise calibration strategies based on plasma wind tunnel data. The models are exposed respecting a certain hierarchy in their mathematical structure.

First, the governing equations are introduced, the bare bones of modeling a continuum media. These equations impose balances of mass, momentum and energy. The data associated come down to the choosing of phenomena to be included in the detailed balances as well as the energy partition model chosen. Radiative processes are neglected in this case, as well as external forces such as gravity and electromagnetism. The former is assumed negligible in high temperature flows with respect to the tensional state of the gas. Electromagnetic forces are also negligible given the quasi-neutrality of the gas. A two-temperature model is assumed for modeling thermal non-equilibrium which resolves two distinct thermal baths, each of them in equilibrium with a subset of modes. This choice results in the prescription of a whole set of energy transfer terms.

Most of the mathematical structure introduced is in the form of physico-chemical models. These models are quite data-intensive and require a large number of parameters to be specified in order to resolve the flow variables. Transport properties are presented based on a perturbative Chapmann-Enskog solution of the scaled Boltzmann equation, which results in linear transport systems defined in terms of temperature dependent collision integrals and species concentrations. General relations for thermodynamic properties are also provided, based on the statistical mechanics description of individual species energy partitioning models and associated partition functions. Chemical production rates are formulated in terms of the Law of Mass Action. The effect of thermal nonequilibrium is also considered and its effect on non-equilibrium rate coefficients is presented. In addition, several important energy transfer models are discussed in the context of non-equilibrium two-temperature models. Part of the data, such as for computing thermodynamics and transport properties, come from quantum mechanical and statistical mechanics computations, both being well-established theories. Gas chemical kinetics and energy transfer terms rely on legacy experimental data for reaction rates and relaxation times.

Once the structure of the mathematical models and assumptions behind them have been introduced, the secondary objective of the chapter is to highlight the diverse landscape in terms of data fidelities, models and complexity. Most of the phenomena here depicted are coupled, especially due to the nature of the balancing equations with respect to the flow variables we want to resolve. Particularly problematic for gas-surface interactions are the assumptions and data behind transport processes of mass diffusion and gas chemical kinetics. Diffusion and chemistry act as feeding mechanisms of atomic species to the material surface, enhancing or limiting its reactivity and, therefore, the sensitivity of our models to the experimental data.

Table 2.2: *Overview of the governing equations and boundary conditions proposed in this work for the modeling of high temperature, chemically reacting flows in the VKI Plasmatron.*

Unknowns	**Governing equations / constraints**	**Boundary conditions**
ρ_i	$\frac{\partial}{\partial t}(\rho_i) + \boldsymbol{\nabla} \cdot (\rho_i \boldsymbol{u} + \rho_i \boldsymbol{V}_i) = \dot{\omega}_i$	$\rho_{\delta,i} = \rho_{\delta,i}(T_\delta, p_\delta)$
	$\frac{\partial}{\partial t}(\rho) + \boldsymbol{\nabla} \cdot (\rho \boldsymbol{u}) = 0$	$[\rho_{\mathrm{w},i}(\boldsymbol{u}_\mathrm{g} - \boldsymbol{u}_\mathrm{r}) + \rho_{\mathrm{w},i} \boldsymbol{V}_{\mathrm{w},i}] \cdot \boldsymbol{n} = \dot{\omega}_{\mathrm{w},i}$
	$\sum_{i\in\mathcal{S}} \rho_i \boldsymbol{V}_i = 0$	$u_\mathrm{r} = \sum_{i\in\mathcal{S}} \dot{\omega}_{\mathrm{abla},i}/\rho_\mathrm{s}$
	$\sum_{i\in\mathcal{S}} \dot{\omega}_i = 0$	$u_\mathrm{g} = \dot{m}_\mathrm{blow}/\sum_{i\in\mathcal{S}} \rho_{\mathrm{w},i}$
$\boldsymbol{u}$	$\frac{\partial}{\partial t}(\rho \boldsymbol{u}) + \boldsymbol{\nabla} \cdot (\rho \boldsymbol{u} \otimes \boldsymbol{u} + p\bar{\bar{\boldsymbol{I}}} + \bar{\bar{\boldsymbol{\tau}}}) = \boldsymbol{0}$	$\boldsymbol{u}_\delta$ from experimental data $\boldsymbol{u}_\mathrm{w} = \boldsymbol{u}_\mathrm{g}$ $\boldsymbol{u}_\mathrm{g} \cdot \boldsymbol{n} = 0$
T	$\frac{\partial}{\partial t}(\rho E) + \boldsymbol{\nabla} \cdot (\rho \boldsymbol{u} H + \bar{\bar{\boldsymbol{\tau}}} \boldsymbol{u} + \boldsymbol{q}) = 0$	T_δ from experimental data T_w from experimental data Or $\left[\rho_\mathrm{w}(\boldsymbol{u}_\mathrm{g} - \boldsymbol{u}_\mathrm{r})h_\mathrm{w} + \sum_{i\in\mathcal{S}} \rho_{\mathrm{w},i} h_{\mathrm{w},i} \boldsymbol{V}_{\mathrm{w},i} + \lambda_\mathrm{w} \nabla T_\mathrm{w} + \lambda_\mathrm{w}^\mathcal{V} \nabla T_\mathrm{w}^\mathcal{V}\right] \cdot \boldsymbol{n} = \dot{\Omega}_\mathrm{w}$
$T^\mathcal{V}$	$\frac{\partial}{\partial t}(\rho e^\mathcal{V}) + \boldsymbol{\nabla} \cdot (\rho e^\mathcal{V} \boldsymbol{u} + \boldsymbol{q}^\mathcal{V}) = -p_\mathrm{e} \nabla \cdot \boldsymbol{u} + \Omega^\mathrm{VT} + \Omega^\mathrm{eT} + \Omega^\mathrm{CV} - \Omega^\mathrm{I}$	$T_\delta^\mathcal{V} = T_\delta$ $T_\mathrm{w}^\mathcal{V} = T_\mathrm{w}$ Or $\left[\rho_\mathrm{w}(\boldsymbol{u}_\mathrm{g} - \boldsymbol{u}_\mathrm{r})h_\mathrm{w}^\mathcal{V} + \sum_{i\in\mathcal{S}} \rho_{\mathrm{w},i} h_{\mathrm{w},i}^\mathcal{V} \boldsymbol{V}_{\mathrm{w},i} + \lambda_\mathrm{w}^\mathcal{V} \nabla T_\mathrm{w}^\mathcal{V}\right] \cdot \boldsymbol{n} = \dot{\Omega}_\mathrm{w}^{\mathcal{V}\mathrm{T}} + \dot{\Omega}_\mathrm{w}^{\mathrm{C}\mathcal{V}}$

Table 2.3: *Overview of the closure models and their model parameters used in this work to model the physico-chemical phenomena included in the governing equations and boundary conditions for high temperature, chemically reacting flows in the VKI Plasmatron. The parameter* a^{e} *is 1 if there are electrons in the considered mixture.*

Unknowns	**Closure models/constraints**	**Model parameters**	**# parameters**
$\boldsymbol{V}_i$	$\sum_{i\in\mathcal{S}} G^V_{ij}\boldsymbol{V}_i = \left(\boldsymbol{d}'_j + k_j\boldsymbol{E}\right)\Theta_j$	$\boldsymbol{G}^V \leftarrow \bar{Q}^{(1,1-3)}_{ij}, \bar{Q}^{(1,1-3)}_{i\mathrm{e}}, \bar{Q}^{(2,2)}_{ij}, \bar{Q}^{(2,2)}_{\mathrm{ee}}$	$2n^{\mathcal{H}}\left(n^{\mathcal{H}}+1\right) + a^e\left(3n^{\mathcal{H}}+1\right)$
	$k_j = \frac{x_j q_j}{k_{\mathrm{B}}T} - \frac{y_i q}{k_{\mathrm{B}}T}$	from kinetic theory	
	$q = \sum_{i\in\mathcal{S}} x_i q_i$		
	$\boldsymbol{d}'_j = \frac{p}{nk_{\mathrm{B}}T}\boldsymbol{\nabla}x_j$		
	$\sum_{i\in\mathcal{S}} y_i\boldsymbol{V}_i = 0$		
	$\sum_{i\in\mathcal{S}} k_i\boldsymbol{V}_i = 0$		
$\dot{\omega}_i$	$\dot{\omega}_i = M_i\sum_{r\in\mathcal{R}}(\nu''_{i,r} - \nu'_{i,r})\mathcal{R}_r$	$\nu'_{i,r}, \nu''_{i,r}$ chemical mechanism	$n_{\mathcal{S}}\cdot n_{\mathcal{R}}$
	$\mathcal{R}_r = k_{\mathrm{f},r}\prod_{i\in\mathcal{S}}\left(\dfrac{\rho_i}{M_i}\right)^{\nu'_{i,r}} - k_{\mathrm{b},r}\prod_{i\in\mathcal{S}}\left(\dfrac{\rho_i}{M_i}\right)^{\nu''_{i,r}}$	$k_{\mathrm{f},r}$ from experimental data	$n_{\mathcal{R}}$
	$k_{\mathrm{b},r} = k_{\mathrm{f},r}/K_{\mathrm{eq},r}$	g_i^l, E_i^l from quantum mechanics	$2\cdot\sum_i^{n_{\mathcal{S}}} n_{\mathcal{L}_i}$
	$K_{\mathrm{eq},r} = \left(\frac{p^\circ}{R_uT}\right)^{\sum_{j\in\mathcal{S}}(\nu''_{ir}-\nu'_{ir})}\exp\left(-\dfrac{\sum_{i\in\mathcal{S}}\left(\nu''_{ir}-\nu'_{ir}\right)G_i^\circ}{R_uT}\right)$		
	$G_i^\circ = \dfrac{h_i^0 - Ts_i^0}{M_i}$		
	$h_i = \dfrac{5}{2}R_iT + R_i\left[T^2\left(\dfrac{\partial(\ln Q_i^{\mathrm{R}})}{\partial T}\right) + \left(T^{\mathcal{V}}\right)^2\left(\dfrac{\partial(\ln Q_i^{\mathrm{VE}})}{\partial T^{\mathcal{V}}}\right)\right],\quad \forall i\in\mathcal{S}^*$		
	$h_i = \dfrac{5}{2}R_iT + R_i\left[\left(T^{\mathcal{V}}\right)^2\left(\dfrac{\partial(\ln Q_i^{\mathrm{E}})}{\partial T^{\mathcal{V}}}\right)\right],\quad \forall i\in\mathcal{S}^{\mathrm{a}}$		
	$h_{\mathrm{e}} = \dfrac{5}{2}R_{\mathrm{e}}T^{\mathcal{V}}$		

Continues in next page

Continuation

Unknowns	Closure models/constraints	Model parameters	# parameters
	$s_i = \frac{3}{2}R_iT + R_i\left[T\left(\frac{\partial(\ln Q_i^{\mathrm{R}})}{\partial T}\right) + T^{\mathcal{V}}\left(\frac{\partial(\ln Q_i^{\mathrm{VE}})}{\partial T^{\mathcal{V}}}\right)\right], \quad \forall i \in \mathcal{S}^*$ $s_i = \frac{3}{2}R_iT + R_i\left[T^{\mathcal{V}}\left(\frac{\partial(\ln Q_i^{\mathrm{E}})}{\partial T^{\mathcal{V}}}\right)\right], \quad \forall i \in \mathcal{S}^{\mathrm{a}}$ $s_{\mathrm{e}} = R_{\mathrm{e}}\left(5/2 + \ln\left(\frac{2\pi m_i k_{\mathrm{B}} T^{\mathcal{V}}}{h^2}\right)^{3/2}\left(T^{\mathcal{V}}\right) - \ln n_{\mathrm{e}}\right) + R_{\mathrm{e}}\ln 2$ $Q_i^{\mathrm{R}} = \sum_{l\in\mathcal{L}_i} g_i^l \exp\left(-\frac{E_i^l}{k_{\mathrm{B}}T}\right)$ $Q_i^m = \sum_{l\in\mathcal{L}_i} g_i^l \exp\left(-\frac{E_i^l}{k_{\mathrm{B}}T^{\mathcal{V}}}\right), \quad \forall m \in \{\mathrm{E}, \mathrm{VE}\}$		
$\dot{\omega}_{\mathrm{w},i}$	$\dot{\omega}_{\mathrm{w},i} = \gamma_i m_i \mathcal{F}_i^{\downarrow}$ $\mathcal{F}_i^{\downarrow} = n_i\sqrt{\frac{k_{\mathrm{B}}T_{\mathrm{w}}}{2\pi m_i}}$	γ_i from experimental data	$n_{\mathcal{R}_{\mathrm{w}}}$
$\bar{\bar{\boldsymbol{\tau}}}$	$\bar{\bar{\boldsymbol{\tau}}} = -\mu\left[\boldsymbol{\nabla}\boldsymbol{u} + (\boldsymbol{\nabla}\boldsymbol{u})^T - \frac{3}{2}\boldsymbol{\nabla}\cdot\boldsymbol{u}\bar{\bar{I}}\right]$ $\mu = \sum_{i\in\mathcal{H}} \alpha_i x_i$ $\boldsymbol{G}^{\mu}\boldsymbol{\alpha} = \boldsymbol{x}$		
E	$E = e + 1/2(\boldsymbol{u}\cdot\boldsymbol{u})$ $e = \frac{1}{\rho}\left[\sum_{i\in\mathcal{S}^*}\rho_i e_i + \sum_{i\in\mathcal{S}^{\mathrm{a}}}\rho_i\left(e_i^{\mathrm{T}} + e_i^{\mathrm{E}}\right) + \frac{3}{2}R_{\mathrm{e}}T^{\mathcal{V}}\right]$ $e_i = e_i^{\mathrm{T}} + e_i^{\mathrm{R}} + e_i^{\mathrm{VE}}$		

Continues in next page

Continuation

Unknowns	**Closure models/constraints**	**Model parameters**	**# parameters**
	$e_i^{\mathrm{T}} = \frac{3}{2} R_i T$ $e_i^{\mathrm{R}} = R_i T^2 \left(\frac{\partial (\ln Q_i^{\mathrm{R}})}{\partial T} \right)$ $e_i^m = R_i \left(T^{\mathcal{V}} \right)^2 \left(\frac{\partial (\ln Q_i^m)}{\partial T^{\mathcal{V}}} \right), \quad \forall m \in \{\mathrm{E}, \mathrm{VE}\}$		
h	$h = \frac{1}{\rho} \left[\sum_{i \in \mathcal{S}^*} \rho_i h_i + \sum_{i \in \mathcal{S}^{\mathrm{a}}} \rho_i \left(\frac{5}{2} R_i T + e_i^{\mathrm{E}} \right) + \frac{5}{2} R_{\mathrm{e}} T^{\mathcal{V}} \right]$ $h_i = \frac{5}{2} R_i T + e_i^{\mathrm{R}} + e_i^{\mathrm{VE}}$		
$\boldsymbol{q}$	$\boldsymbol{q} = -\lambda \nabla T - \lambda^{\mathcal{V}} \nabla T^{\mathcal{V}} + \sum_{i \in \mathcal{S}} h_i \rho_i \boldsymbol{V}_i$ $\lambda = \lambda^{\mathrm{T}} + \sum_{i \in \mathcal{S}^*} \frac{\rho_i \left(\partial e_i^{\mathrm{R}} / \partial T^{\mathcal{V}} \right)_{\mathrm{p}}}{\sum_{j \in \mathcal{H}} x_j / \mathscr{D}_{ij}}$ $\lambda^{\mathrm{T}} = \sum_{i \in \mathcal{H}} \alpha_{ij} x_i$ $\boldsymbol{G}^{\lambda} \boldsymbol{\alpha} = \boldsymbol{x}$ $\lambda^{\mathcal{V}} = \sum_{i \in \mathcal{S}^*} \frac{\rho_i \left(\partial e_i^{\mathrm{V}} / \partial T^{\mathcal{V}} \right)_{\mathrm{p}}}{\sum_{j \in \mathcal{H}} x_j / \mathscr{D}_{ij}} + \sum_{i \in \mathcal{H}} \frac{\rho_i \left(\partial e_i^{\mathrm{E}} / \partial T^{\mathcal{V}} \right)_{\mathrm{p}}}{\sum_{j \in \mathcal{H}} x_j / \mathscr{D}_{ij}} + \frac{x_{\mathrm{e}}^2}{\Lambda_{\mathrm{ee}}^{11}} + \frac{x_{\mathrm{e}}^2 \Lambda_{\mathrm{ee}}^{22}}{\Lambda_{\mathrm{ee}}^{11} \Lambda_{\mathrm{ee}}^{22} - \left(\Lambda_{\mathrm{ee}}^{12} \right)^2}$	$\Lambda_{\mathrm{ee}}^{12}, \Lambda_{\mathrm{ee}}^{22} \leftarrow \bar{Q}_{ie}^{(1,4-5)}, \bar{Q}_{ee}^{(2,3-4)}$ from kinetic theory	$a^{\mathrm{e}}(2 \cdot n_{\mathcal{H}} + 2)$
$\boldsymbol{q}^{\mathcal{V}}$	$\boldsymbol{q}^{\mathcal{V}} = -\lambda^{\mathcal{V}} \nabla T^{\mathcal{V}} + \sum_{i \in \mathcal{S}} h_i^{\mathcal{V}} \rho_i \boldsymbol{V}_i$		

Continues in next page

Continuation

Unknowns	**Closure models/constraints**	**Model parameters**	**# parameters**
Ω^{VT}	$\Omega^{\mathrm{VT}} = \sum_{i\in\mathcal{S}^*} \Omega_i^{\mathrm{VT}}$ $\Omega_i^{\mathrm{VT}} = \rho_i \dfrac{e_i^{\mathrm{V}}(T) - e_i^{\mathrm{V}}(T^{\mathcal{V}})}{\tau_i^{\mathrm{VT}}}$	τ_i^{VT} from experimental data	$n_{\mathcal{S}^*}$
Ω^{eT}	$\Omega^{\mathrm{eT}} = \rho_e \dfrac{e_e^{\mathrm{T}}(T) - e_e^{\mathrm{T}}\left(T^{\mathcal{V}}\right)}{\tau^{\mathrm{eT}}}$	τ^{eT} from experimental data	1
Ω^{CV}	$\Omega^{\mathrm{CV}} = \sum_{i\in\mathcal{S}^*} \Omega_i^{\mathrm{CV}}$ $\Omega_i^{\mathrm{CV}} = h_i^{\mathrm{V}} \dot{\omega}_i$		
Ω^{I}	$\Omega^{\mathrm{I}} = \sum_{r\in\mathcal{R}^{\mathrm{I}}} \Delta h_r \mathcal{R}_r$	h_r from chemistry	$n_{\mathcal{R}_{\mathrm{I}}}$
$\dot{\Omega}_{\mathrm{w}}$	$\dot{\Omega}_{\mathrm{w}} = \sigma\epsilon \left(T_{\mathrm{w}}\right)^4$	ϵ from experimental data	1
$\dot{\Omega}_{\mathrm{w}}^{\mathcal{V}\mathrm{T}}$	$\dot{\Omega}_{\mathrm{w}}^{\mathcal{V}\mathrm{T}} = \sum_{i\in\mathcal{S}} \alpha_i \mathcal{F}_i^{\downarrow} m_i \left(h_{\mathrm{w},i}^{\mathcal{V}}\left(T^{\mathcal{V}}\right) - h_{\mathrm{w},i}^{\mathcal{V}}(T)\right)$	α_i from experimental data	$n_{\mathcal{S}}$
$\dot{\Omega}_{\mathrm{w}}^{\mathrm{C}\mathcal{V}}$	$\dot{\Omega}_{\mathrm{w}}^{\mathrm{C}\mathcal{V}} = \sum_{i\in\mathcal{S}} (1-\beta_i)\left(h_{\mathrm{w},i}^{\mathcal{V}} - h_{\mathrm{w},i}\right)$	β_i from experimental data	$n_{\mathcal{S}}$

Chapter 3

Data-generating tools

In this chapter, the different tools for data generation are reviewed. The chapter opens with a follow-up on the theoretical modeling aspects of the thesis, focusing on the particular models and numerical methods used to obtain relevant solutions in the context of this work. We introduce the boundary layer equations that are adopted as a valid and efficient alternative to the full set of the governing equations for the problems that deal with catalysis. The full set of dimensionally reduced Navier-Stokes equations are also introduced which are relevant for the one-dimensional simulation of reacting flows including ablative processes at the wall. The numerical methods and physico-chemical data used for each case are also addressed. Following the numerical tools, we review the experiments related to this thesis. From the facility in which the different phenomena are studied to the specific set-ups and measurement devices that make up the dedicated testing campaigns. The link between the facility operating conditions and the resulting boundary layer edge quantities over the different probes in the testing chamber is subsequently addressed. The chapter ends with a review of the sources of uncertainties that are present in both data-generating processes as well as the nature of these uncertainties.

3.1 Numerical tools

The governing equations exposed in Chapter 2 are studied for the conditions and relevant characteristics of the flows and objects under consideration in this thesis. In order to accurately capture the phenomena we want to study and, at the same time, ease the computational effort, different approximations to the full set of the Navier-Stokes equations are used under relevant assumptions. The overall set of governing equations applies to both catalysis and ablation simulations. They are different in their surface boundary conditions and the species that must be taken into account. The simplified sets of equations need to be discretized in order to obtain plausible solutions. The discretization schemes and numerical implementations are also introduced. The remaining closure terms and wall boundary conditions are obtained through the different physico-chemical models reviewed in Chapter 2 whose data sources are specifically addressed in this section.

The boundary layer solver is used to address the problems that concern catalysis given its extensive verification and comparison to experimental data concerning the Plasmatron facility [5, 19, 106–108]. Further, the boundary layer solver is more efficient than a general Navier-Stokes solver as it benefits from suitable boundary layer assumptions to simplify and speed up the computing of solutions with more accurate results. For ablation, on the other hand, additional data, species and boundary conditions need to be handled. In this case, the more general stagnation line solver is used given its extensive verification for ablation problems [3, 61, 109, 110] as well as the possibility of prescribing thermal non-equilibrium models, which are used in this thesis. Overall, the choice of using two different solvers for the simulation of catalysis and ablation phenomena rests on the availability of tools and their efficiencies, the confidence we have in them for the flows we want to simulate, and the different physico-chemical models and data that need to be handled in both cases. Further, we want to be able to compare our methodologies for inverse problems to previous works in the literature, and this is done more consistently on the basis of using the same numerical solvers, data and overall assumptions when possible.

3.1.1 1D boundary layer solver

In this work, we are primarily interested in the simulation of gas-surface interactions between the hot plasma flow and the exposed material surface. As these interactions happen in a thin layer around the face of the material, we can reduce the computational domain to just the boundary layer which contains the physics of the phenomena we want to study. Focusing on the boundary layer instead of the full flow domain offers a great deal of simplification over the full set of the Navier-Stokes equations depicted in Sec. 2.1, both in terms of mathematical and numerical complexity. Moreover, we only need to focus our attention on simulating the stagnation line given that the relevant experimental information available generally refers to the probes' stagnation point quantities. In this thesis, the 1D boundary layer solver developed by Barbante [106] is used to simulate the boundary layers of catalytic probes in the experimental facility, given its efficiency in simulating the relevant features of the experiments as well as having readily available the phenomenological catalysis model commonly used (Sec. 2.3.2). The following Fig. 3.1 zooms in the region we are interested in and schematizes the phenomenon of catalytic recombination present in the boundary layer region.

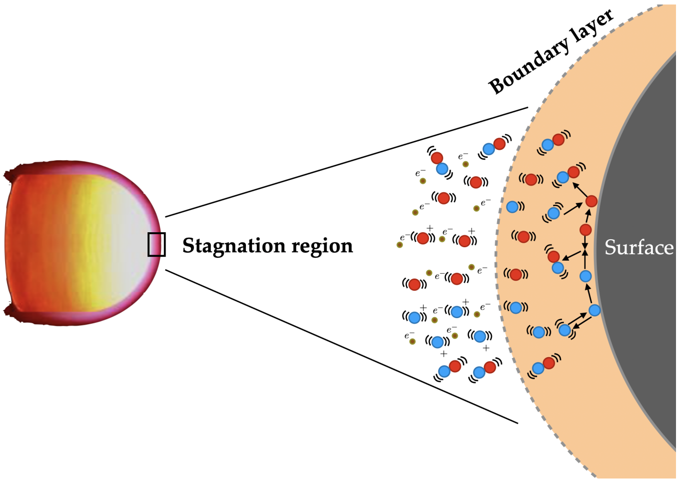

Figure 3.1: *Schematic representation of a testing probe (left, courtesy of Helber [3]) zooming in the stagnation region with catalytic recombination occurring in the boundary layer.*

The boundary layer equations. Obtaining exact solutions of the Navier-Stokes equations have always been a matter of intense research efforts. Even today, with the field of computational fluid dynamics fully developed, we struggle to get good numerical solutions as they require lots of computational power and human resources. These issues gave rise in the past to suitable order-of-magnitude reductions of the full set of the Navier-Stokes equations, such as the boundary layer equations [111].

The basic assumptions behind the boundary layer order-of-magnitude reduction is that the boundary layer is very thin in comparison with the scale of the body and the Reynolds number is large. However, this is generally not true for subsonic, high temperature, reacting flows where the low Mach number, high viscosity, high temperature and small dimensions of the testing body result in very low Reynolds numbers and the boundary layer has to be considered of finite thickness. These characteristics would invalidate the applicability of the classical boundary layer equations to our problems of interest. Nevertheless, Barbante [106] showed that other approximate approaches which take into account the effects of boundary layer finite thickness and low Reynolds number [112, 113], reduce to the same set of classical boundary layer equations when applied to the vicinity of the stagnation line. These results allow us to use this reduced set of equations for the cases we study in this thesis.

The boundary layer equations are derived from the governing equations depicted in Sec. 2.1 by performing an order-of-magnitude reduction which can be found in detail in [111]. Specifically, the equations here presented are derived for an axisymmetric, laminar flow in steady-state under thermal equilibrium and chemical non-equilibrium. A Cartesian system of reference where the x axis goes along the body surface and the y axis is normal to the surface at every point is considered. Under these considerations, the equations read

- Continuity

$$\frac{\partial \rho u r}{\partial x} + \frac{\rho v r}{\partial y} = 0, \tag{3.1}$$

- Species continuity

$$\rho \left(u \frac{\partial y_i}{\partial x} + v \frac{\partial y_i}{\partial y} \right) + \frac{\partial J_i^y}{\partial y} = \dot{\omega}_i, \tag{3.2}$$

- Momentum

$$\rho \left(u \frac{\partial u}{\partial x} + v \frac{\partial u}{\partial y} \right) = -\frac{\mathrm{d}p_\delta}{\mathrm{d}x} + \frac{\partial}{\partial y} \left(\mu \frac{\partial u}{\partial y} \right), \tag{3.3}$$

- Energy

$$\rho \left(u \frac{\partial h}{\partial x} + v \frac{\partial h}{\partial y} \right) = u \frac{\mathrm{d}p_\delta}{\mathrm{d}x} + \mu \left(\frac{\partial u}{\partial y} \right)^2 - \frac{\partial q^y}{\partial y}, \tag{3.4}$$

where u and v are the tangential and normal velocity components, respectively. The symbol p_δ refers to the pressure at the boundary layer outer edge, given that the boundary layer thickness is δ. The superscript y for the heat flux q^y and the diffusion fluxes J_i^y refers to the components along the y axis.

The Lees-Dorodnitsyn transformation [114, 115] is applied to these equations through a series of steps as explained by Anderson [7]. The application of this transformation has as a result a set of partial differential equations which are easier to analyze and solve. The transformed independent variables are defined as

$$\xi(x) = \int_0^x \rho_\delta \mu_\delta u_\delta r^2 \mathrm{d}s, \tag{3.5}$$

$$\hat{\eta}(x, y) = \mathcal{K} \frac{u_\delta r}{\sqrt{2\xi}} \int_0^y \rho \mathrm{d}t, \tag{3.6}$$

where

$$\mathcal{K} = \frac{1}{\delta} \frac{\sqrt{2\xi}}{u_\delta r} \int_0^{\hat{\eta}_{\max}} \frac{1}{\rho} \mathrm{d}\hat{\eta} \tag{3.7}$$

The dependent variables are also transformed as

$$F = \frac{u}{u_\delta}, \tag{3.8}$$

$$V = \mathcal{K}\frac{2\xi}{\partial\xi/\partial x}\left(F\frac{\partial\eta}{\partial x} + \frac{\rho v r}{\sqrt{2\xi}}\right), \tag{3.9}$$

$$g = \frac{h}{h_\delta}. \tag{3.10}$$

The transformed equations then read

- Continuity
$$\frac{\partial V}{\partial\hat{\eta}} + F = 0, \tag{3.11}$$
- Species continuity
$$V\frac{\partial y_i}{\partial\hat{\eta}} + \mathcal{K}\frac{\partial \hat{J}_i^{\hat{\eta}}}{\partial\hat{\eta}} = \dot{\mathcal{W}}_i, \tag{3.12}$$
- Momentum
$$V\frac{\partial F}{\partial\hat{\eta}} = \frac{1}{2}\left(\frac{\rho_\delta}{\rho} - F^2\right) + \frac{1}{2}\frac{\rho_\delta v_\delta}{\rho(\partial u_\delta/\partial x)}\frac{\partial}{\partial y}\left(\frac{\partial u_\delta}{\partial x}\right) + \frac{\partial}{\partial\hat{\eta}}\left(\mathcal{K}^2 l_0\frac{\partial F}{\partial\hat{\eta}}\right), \tag{3.13}$$
- Energy
$$V\frac{\partial g}{\partial\hat{\eta}} = \frac{\partial}{\partial\hat{\eta}}\left(\mathcal{K}^2\frac{l_0}{\mathrm{Pr}}\frac{\partial g}{\partial\hat{\eta}}\right) - \frac{\partial}{\partial\hat{\eta}}\left(\mathcal{K}^2\frac{l_0}{\mathrm{Pr}}\sum_{i=1}^{N_\mathrm{s}}\frac{\partial y_i}{\partial\hat{\eta}}\frac{h_i}{h_\delta}\right) - \frac{\partial}{\partial\hat{\eta}}\left(\mathcal{K}\sum_{i=1}^{N_\mathrm{s}}\hat{J}_i^y\frac{h_i}{h_\delta}\right), \tag{3.14}$$

where $\hat{J}_i^{\hat{\eta}}$ is the dimensionless diffusion flux

$$\hat{J}_i^{\hat{\eta}} = \frac{J_i^y}{\sqrt{2\rho_\delta\mu_\delta(\partial u_\delta/\partial x)}}, \tag{3.15}$$

and $\dot{\mathcal{W}}_i$ is the dimensionless chemical production term

$$\dot{\mathcal{W}}_i = \frac{\dot{\omega}_i/\rho}{2\partial u_\delta/\partial x}. \tag{3.16}$$

Pr is the Prandtl number and l_0 is the Chapman-Rubesin parameter, defined, respectively, as

$$\mathrm{Pr} = \frac{\mu c_\mathrm{p}}{k}, \tag{3.17}$$

$$l_0 = \frac{\rho\mu}{\rho_\delta\mu_\delta}. \tag{3.18}$$

Under this transformation, the boundary condition at the outer edge is expressed as $F = 1$ and $g = 1$, while at the wall $F = 0$ and $g = h_\mathrm{w}/h_\delta$. For the species continuity equation, the outer edge condition is set to the equilibrium composition $y_i = y_{i,\mathrm{equilibrium}}(T_\delta, P_\delta)$ as function of the edge temperature T_δ and pressure P_δ. In this case, the boundary layer edge δ is defined as the inflection point of the velocity gradient $\partial u/\partial x$. Fig. 3.2 depicts the velocity gradient and axial velocity profiles along the stagnation line. The thickness of the boundary layer is denoted by the non-dimensional number δ/R_m, where R_m refers to the model radius.

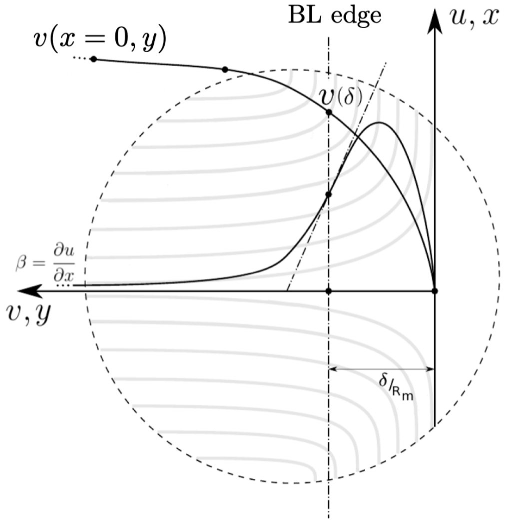

Figure 3.2: *Velocity gradient and axial velocity profiles in the stagnation region.*

At the wall, the diffusion flux must be balanced with the corresponding contributions. In the case of a catalytic surface, the diffusion fluxes are balanced with the production term $J_i^y = \dot{\omega}_i$, for which the quantity $\dot{\omega}_i$ is computed using the catalysis model depicted in Sec. 2.3.2.

Numerical implementation. Discretizations are performed in the ξ and $\hat{\eta}$ directions. In the ξ direction, 2^nd order Lagrangian polynomials are used as follows for a generic streamwise location and unknown quantity w

$$w(\xi,\hat{\eta}) = L_m(\xi)w_m(\hat{\eta}) + L_{m-1}(\xi)w_{m-1}(\hat{\eta}) + L_{m-2}(\xi)w_{m-2}(\hat{\eta}), \tag{3.19}$$

with w_{m-1} and w_{m-2} known from previous iterations. The coefficients L_{m-i} are the 2^nd order Lagrangian polynomials with the property that $L_{m-j}(\xi_i) = \delta_{ij}$ such that $w(\xi,\hat{\eta}) = w_{m-i}(\hat{\eta})$ at all points ξ_{m-i}. The definition of the Lagrangian polynomials is

$$L_{m-i}(\xi) = \frac{\prod_{j=0,j\neq i}^{2}(\xi - \xi_{m-j})}{\prod_{j=0,j\neq i}^{2}(\xi_{m-i} - \xi_{m-j})}. \tag{3.20}$$

From Eq. (3.19) we can then differentiate w with respect to the variable ξ to replace the derivative terms included in the transformed equations.

In the $\hat{\eta}$ direction, the discretization is performed upon the ξ direction discretization $w_m(\hat{\eta})$ by using 4^th order Hermite polynomials such that

$$w_m(\hat{\eta}) = \frac{1}{2}w_{m,n+1}(t^2+t)+w_{m,n}(1-t^2)+\frac{1}{2}w_{m,n-1}(t^2-t)+\alpha t(1-t^2)+\beta t^2(1-t^2). \quad (3.21)$$

The terms $w_{m,n+1}, w_{m,n}$ and $w_{m,n-1}$ are the values taken by $w_m(\hat{\eta})$ at the locations $\hat{\eta}_{n+1}, \hat{\eta}_n$ and $\hat{\eta}_{n-1}$, respectively. The variable t is defined as $t = \hat{\eta} - \hat{\eta}_n/\Delta\hat{\eta}$, while the parameters α and β can be freely chosen. Ideally, α and β are chosen so that the polynomial equals the exact solution in 3 collocation points. It is useful to choose the collocation points at the levels $n+1, n$ and $n-1$ in the $\hat{\eta}$ direction.

At the end of this discretization process, we end up with discrete implicit representations of the original transformed equations. Collecting all the equations we obtain a linear system which by certain manipulations can be expressed in matrix form and solved using Thomas algorithm [106, 116]. The procedure is fourth order accurate in step size across the boundary layer. In principle, all equations could be solved coupled together but in practice, the system is split and only the species continuity equations are solved in a coupled fashion with the Stefan-Maxwell equations as explained by Barbante [106].

Physico-chemical data. Closure models for the equations and boundary conditions need data concerning a series of model parameters. The solver considers flows in thermal equilibrium and chemical non-equilibrium. Thermodynamic properties for one single thermal bath are obtained through the Rigid Rotor Harmonic Oscillator (RRHO) model [71]. The transport properties are computed through the second order perturbation of the Chapman-Enskog expansion of the Boltzmann equation as explained in Sec. 2.2.2. The thermodynamic and transport data are inquired through the library PEGASE, developed by Bottin [117]. The mixture used is air-7 to model the flow with species $\{\mathrm{O_2, N_2, NO, O, N, NO^+, e^-}\}$. The rates used for the gas chemistry are taken from the Dunn and Kang data [118]. For the catalytic boundary condition, the model depicted in Sec. 2.3.2 is used with uncertain catalytic parameters γ taken equal for both catalytic reactions considered $\mathrm{N + N \rightarrow N_2}$ and $\mathrm{O + O \rightarrow O_2}$. This assumption is consistent with previous catalysis studies concerning the VKI Plasmatron data [4, 119]. The complexity of the wall models cannot be resolved using only heat fluxes. For the purpose of developing accurate inverse methodologies, assuming equal probabilities for nitrogen and oxygen atoms is a practical convenience that does not change the nature of the inverse problem.

3.1.2 Stagnation line code

Generally, stagnation streamline quantities are relevant for hypersonic flows when predicting the heat flux experienced by re-entering vehicles. The stagnation point heat flux is commonly used as the upper limit of the heating experienced by the protection material [7]. Computing the flow quantities along the stagnation line is important to understand the physics involved in these reacting flows. As such, stagnation line computations offer a great test bench for physico-chemical models at a reduced cost while accurately capturing the relevant features of re-entry flows. Further, most measurements used in this thesis refer to stagnation point quantities which focus the computational aspects of the problem on stagnation line quantities. All in all, the stagnation line code provides a suitable data-generating tool for our Bayesian approaches concerning ablation.

In this section, the reduced set of equations together with their numerical implementation are introduced. Further, the particular models taken into account to feed the closure terms are also reviewed.

Dimensionally-reduced Navier-Stokes equations. We start with the governing equations already depicted in Sec. 2.1 for the general case of a flow in chemical and thermal non-equilibrium, and follow the methodology first introduced by Klomfass and Müller [120]. The governing equations are cast in spherical coordinates (r, θ, ϕ) following the convention depicted in Fig. 3.3. The advantage of the spherical formulation is that for stagnation streamline quantities, non-spherical bodies can be approximately modeled with an equivalent sphere radius R_0 which manages to capture relevant flow features around the stagnation point, such as the heat flux as shown by Turchi et al. [121]

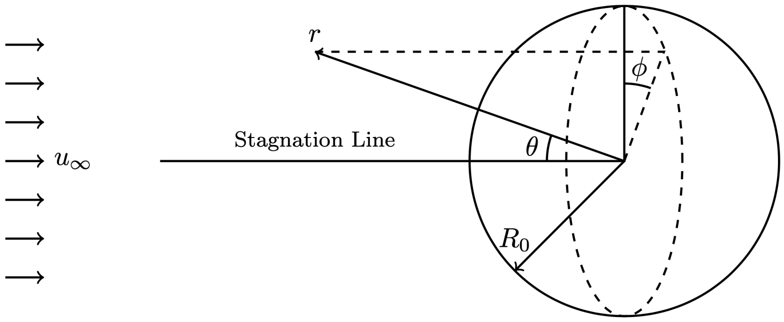

Figure 3.3: *Spherical body of radius R_0 subjected to a hypersonic flow with uniform velocity u_∞. Azimuth and zenith angles are ϕ and θ, respectively. Courtesy of Scoggins [1].*

Klomfass and Müller applied a separation of variables to a suitable set of flow quantities

$$u_r = \bar{u}_r(r)\cos\theta, \tag{3.22}$$

$$u_\theta = \bar{u}_\theta(r)\sin\theta, \tag{3.23}$$

$$p - p_\infty = \bar{p}(r)\cos\theta^2, \tag{3.24}$$

$$y_i = \bar{y}_i(r), \tag{3.25}$$

$$T = \bar{T}(r), \tag{3.26}$$

$$T^{\mathcal{V}} = \bar{T}^{\mathcal{V}}(r), \tag{3.27}$$

where the bar symbols indicate stagnation line quantities. To keep the notation simple, the bar symbol is omitted in the equations that follow. Introducing this decomposition into the full set of the Navier-Stokes equations under physical considerations, the assumption of axisymmetric flow ($\partial/\partial\phi = 0$), and taking the limit $\theta \to 0$, the set of Dimensionally-Reduced Navier-Stokes Equations (DRNSE) is obtained. This set of equations can be compactly written in the form

$$\frac{\partial \boldsymbol{U}}{\partial t} + \frac{\partial \boldsymbol{F}^{\mathrm{I}}}{\partial r} + \frac{\partial \boldsymbol{F}^{\mathrm{V}}}{\partial r} = \boldsymbol{S}^{\mathrm{I}} + \boldsymbol{S}^{\mathrm{V}} + \boldsymbol{S}^{\mathrm{k}}, \tag{3.28}$$

with $\boldsymbol{U}$ being the vector of conservative variables, while $\boldsymbol{F}^{\mathrm{I}}$ and $\boldsymbol{F}^{\mathrm{V}}$ are the vectors of inviscid and viscous fluxes. The term $\boldsymbol{S}^{\mathrm{k}}$ refers to the kinetic source terms while $\boldsymbol{S}^{\mathrm{I}}$ and

$\boldsymbol{S}^{\mathrm{V}}$ are the inviscid and viscous source terms, respectively. For the non-equilibrium two-temperature model here considered, the different terms are defined as

$$\boldsymbol{U} = \left[\rho_i, \rho u_r, \rho u_\theta, \rho E, \rho e^{\mathcal{V}}\right]^{\mathrm{T}}, \tag{3.29}$$

$$\boldsymbol{F}^{\mathrm{I}} = \left[\rho_i u_r, \rho u_r^2 + p, \rho u_r u_\theta, \rho u_r H, \rho u_r e^{\mathcal{V}}\right]^{\mathrm{T}}, \tag{3.30}$$

$$\boldsymbol{F}^{\mathrm{V}} = \left[J_{r,i}, -\tau_{rr}, -\tau_{r\theta}, q_r - \tau_{rr} u_r, q_r^{\mathcal{V}}\right]^{\mathrm{T}}, \tag{3.31}$$

$$\boldsymbol{S}^{\mathrm{I}} = -\frac{(u_r + u_\theta)}{r}\left[2\rho_i, 2\rho u_r, 3\rho u_\theta - 2\frac{p - p_\infty}{u_r + u_\theta}, 2\rho H, 2\rho e^{\mathcal{V}}\right]^{\mathrm{T}}, \tag{3.32}$$

$$\begin{aligned} \boldsymbol{S}^{\mathrm{V}} = -\frac{1}{r}\,[\, & 2J_{r,i}, 2(\tau_{\theta\theta} - \tau_{rr} + \tau_{r\theta}), \\ & \tau_{\theta\theta} - 3\tau_{r,\theta}, 2(q_r - \tau_{rr} u_r - \tau_{\theta\theta} u_r - \tau_{r\theta} u_\theta), 2q_r^{\mathcal{V}}\,]^{\mathrm{T}}, \end{aligned} \tag{3.33}$$

$$\boldsymbol{S}^{\mathrm{k}} = \left[\dot{\omega}_i, 0, 0, 0, \Omega^{\mathcal{V}} + \Omega^{\mathrm{C}\mathcal{V}} - \Omega^{\mathrm{I}}\right]^{\mathrm{T}}, \tag{3.34}$$

with $\rho E = \sum_{i=1}^{n_{\mathcal{S}}} \rho e + \rho u_r^2/2$ being the energy per unit volume and $H = E + p/\rho$ the total enthalpy. In this system of coordinates, $J_{i,r} = \rho_i V_{i,r}$ are the radial species diffusion fluxes with diffusion velocities $V_{i,r}$, obtained by solving the Stefan-Maxwell equations (Sec. 2.2.2), and $q_r, q_r^{\mathcal{V}}$ are the total and internal heat fluxes, respectively,

$$q_r = \sum_{i=1}^{n_{\mathcal{S}}} J_{r,i} h_i - \lambda^{\mathrm{T}} \frac{\partial T}{\partial r} - \lambda^{\mathcal{V}} \frac{\partial T^{\mathcal{V}}}{\partial r}, \tag{3.35}$$

$$q_r^{\mathcal{V}} = \sum_{i=1}^{n_{\mathcal{S}}} J_{r,i} h_i^{\mathcal{V}} - \lambda^{\mathcal{V}} \frac{\partial T^{\mathcal{V}}}{\partial r}. \tag{3.36}$$

The terms $\lambda^{\mathrm{T}}, \lambda^{\mathcal{V}}$ are the translational-rotational and the vibrational-electron-electronic thermal conductivities, respectively. Under this formulation the stress tensor components are expressed as

$$\tau_{rr} = \frac{4}{3}\mu\left(\frac{\partial u_r}{\partial r} - \frac{u_r + u_\theta}{r}\right), \tag{3.37}$$

$$\tau_{r\theta} = \mu\left(\frac{\partial u_\theta}{\partial r} - \frac{u_r + u_\theta}{r}\right), \tag{3.38}$$

$$\tau_{\theta\theta} = -\frac{1}{2}\tau_{rr}, \tag{3.39}$$

with μ being the shear viscosity (Sec. 2.2.2).

Numerical implementation. The numerical solution of the DRNSE was originally proposed by Munafò [61]. His work focused on state-to-state models for nitrogen flows. In this thesis, the numerical discretization of the DRNSE for a two-temperature model remains unchanged from the original work of Munafò. The discretization is done by means of the method-of-lines (MOL) with separation of the spatial and temporal discretizations.

- Spatial discretization

The spatial discretization is performed using the Finite Volume (FV) method with which an ODE describing the time evolution of the conservative variable vector at the cell i is obtained

$$\frac{\partial \boldsymbol{U}_i}{\partial t}\Delta r_i + \tilde{\boldsymbol{F}}^{\mathrm{I}}_{i+\frac{1}{2}} - \tilde{\boldsymbol{F}}^{\mathrm{I}}_{i-\frac{1}{2}} + \tilde{\boldsymbol{F}}^{\mathrm{V}}_{i+\frac{1}{2}} - \tilde{\boldsymbol{F}}^{\mathrm{V}}_{i-\frac{1}{2}} = \left(\boldsymbol{S}^{\mathrm{I}}_i + \boldsymbol{S}^{\mathrm{V}}_i + \boldsymbol{S}^{\mathrm{k}}_i\right)\Delta r_i. \tag{3.40}$$

The term $\Delta r_i = r_{i+\frac{1}{2}} - r_{i-\frac{1}{2}}$ is the length of cell i. The numerical inviscid flux at the cell interface $\tilde{\boldsymbol{F}}^{\mathrm{I}}_{i+\frac{1}{2}}$ is computed using the AUSM^{+}-up2 scheme [122], which splits the flux into a convective and a pressure terms such that

$$\tilde{\boldsymbol{F}}^{\mathrm{I}}_{i+\frac{1}{2}} = \dot{m}\psi + p\mathbf{N}, \tag{3.41}$$

where the scalar mass flux $\dot{m} = \rho u_r$, $\boldsymbol{\psi} = \left[y_i, u_r, u_\theta, H, e^{\mathcal{V}}\right]^T$, and $\mathbf{N} = [0, 1, 0, 0, 0]^T$. The upwind inviscid flux is approximated as

$$\tilde{\boldsymbol{F}}^{\mathrm{I}}_{i+\frac{1}{2}} = \frac{\tilde{m} + |\tilde{m}|}{2}\psi_{\mathrm{R}} - \frac{\tilde{m} - |\tilde{m}|}{2}\psi_{\mathrm{L}} + \tilde{p}\mathbf{N}, \tag{3.42}$$

where $\tilde{p}$ is the interface pressure flux and $\tilde{m}$ is the upwind interface mass flux. The different expressions for these terms can be found in the work of Dias [123].

Second-order accuracy in space is achieved by reconstructing upwind variables at the cell interface. The reconstruction is performed on the primitive variables $\boldsymbol{P} = \left[\rho_i, u_r, u_\theta, T, T^{\mathcal{V}}\right]^{\mathrm{T}}, i \in \mathcal{S}$ [124]. For a generic primitive variable p, the reconstructed "left" (L) and "right" (R) values at the interface $i + 1/2$ are computed by means of the Monotone Upstream Centered Schemes for Conservation Laws (MUSCL) scheme [125]

$$p^{\mathrm{L}}_{i+\frac{1}{2}} = p_i + \frac{1}{2}\phi(r^{\mathrm{L}}_i)\left(p_i - p_{i-1}\right), \tag{3.43}$$

$$p^{\mathrm{R}}_{i+\frac{1}{2}} = p_{i+1} - \frac{1}{2}\phi(r^{\mathrm{R}}_{i+1})\left(p_{i+2} - p_{i+1}\right), \tag{3.44}$$

where $\phi(r)$ is a slope limiter function and r represents the ratios of consecutive differences such that

$$r^{\mathrm{L}}_i = \frac{p_{i+1} - p_i}{p_i - p_{i-1}}, \tag{3.45}$$

$$r^{\mathrm{R}}_{i+1} = \frac{p_{i+2} - p_{i+1}}{p_{i+1} - p_i}. \tag{3.46}$$

In this thesis, the van Albada limiter [126] is used as implemented by Munafò [61]. Conservative variables $\boldsymbol{U}$ are then built from the reconstructed primitive variables and the second-order numerical flux is computed as $\tilde{\boldsymbol{F}}^{\mathrm{I}}_{i+1/2} = \tilde{\boldsymbol{F}}^{\mathrm{I}}_{i+\frac{1}{2}}\left(\boldsymbol{U}^{\mathrm{L}}_{i+1/2}, \boldsymbol{U}^{\mathrm{R}}_{i+1/2}\right)$. Having computed the inviscid fluxes at the cell interface, we are left with the computation of the viscous fluxes and source terms. In this case, both quantities are evaluated in terms of the primitive variables $\boldsymbol{P}$. The primitive variables are computed at the face $i+1/2$ for the viscous fluxes using a simple weighted average such that for a generic variable p

$$p_{i+\frac{1}{2}} = \frac{p_{i+1}\Delta r_{i+1} + p_i \Delta r_i}{\Delta r_{i+1} \Delta r_i}. \tag{3.47}$$

Similarly, primitive variable gradients are computed by means of a central difference scheme at the interface

$$\left(\frac{\partial p}{\partial r}\right)_{i+\frac{1}{2}} = 2\left(\frac{p_{i+1} - p_i}{\Delta_{i+1} + \Delta r_i}\right). \tag{3.48}$$

Cell-centered gradients are computed using a two point central finite difference for the viscous flux source term such as

$$\left(\frac{\partial p}{\partial r}\right)_{i} = 2\left(\frac{p_{i+1} - p_{i-1}}{\Delta r_{i+1} + 2\Delta r_i + \Delta_{i-1}}\right). \tag{3.49}$$

- Temporal discretization

The integration of eq. (3.40) in time from an initial time level $n = 0$ is performed using the fully implicit Backward-Euler method, the full discretized equation reads

$$\begin{aligned} \frac{\partial \boldsymbol{U}^n_i}{\Delta t_i}\Delta r_i + \tilde{\boldsymbol{F}}^{\mathrm{I}\ n+1}_{i+\frac{1}{2}} - \tilde{\boldsymbol{F}}^{\mathrm{I}\ n+1}_{i-\frac{1}{2}} + \tilde{\boldsymbol{F}}^{\mathrm{V}\ n+1}_{i+\frac{1}{2}} - \tilde{\boldsymbol{F}}^{\mathrm{V}\ n+1}_{i-\frac{1}{2}} = \\ = \left(\boldsymbol{S}^{\mathrm{I}\ n+1}_i + \boldsymbol{S}^{\mathrm{V}\ n+1}_i + \boldsymbol{S}^{\mathrm{k}\ n+1}_i\right)\Delta r_i, \end{aligned} \tag{3.50}$$

where $\partial \boldsymbol{U}^n_i = \boldsymbol{U}^{n+1}_i - \boldsymbol{U}^n_i$ and Δt_i is the local time-step given by the Courant-Friedrichs-Lewy (CFL) number [127]

$$\Delta t_i = \frac{\mathrm{CFL}\Delta r_i}{\left[|u_r| + a + \frac{1}{\Delta r}\max\left(\frac{4}{3}\frac{\eta}{\rho}, \frac{\lambda}{c_{\mathrm{V}}}\right)\right]_i}, \tag{3.51}$$

with a being the numerical speed of sound presented in [1]. In practice, the CFL number is set to change from 10^{-4} to 10^3 by multiplying by 10 every 10-20 iterations. A reference solution is used for the initialization of the solver. The numerical inviscid flux is linearized using the method of Liou and van Leer [128]

$$\tilde{\boldsymbol{F}}^{\mathrm{I}\ n+1}_{i+\frac{1}{2}} \approx \tilde{\boldsymbol{F}}^{\mathrm{I}\ n}_{i+\frac{1}{2}} + \boldsymbol{A}^+_i \partial \boldsymbol{U}^n_i + \boldsymbol{A}^-_{i+1}\partial \boldsymbol{U}^n_{i+1}, \tag{3.52}$$

with positive and negative split Jacobians $\boldsymbol{A}^{\pm} = \boldsymbol{R}\boldsymbol{\Lambda}^{\pm}\boldsymbol{L}$ [1]. The viscous fluxes and source terms are linearized in two steps. Firstly, the fluxes and source terms are expressed as sums of the terms which are linearly dependent on the gradient of the conservative variables and those which are not, such that

$$\boldsymbol{F}^{\mathrm{V}\ n}_{i+\frac{1}{2}} = \boldsymbol{A}^{\mathrm{V}\ n}_{i+\frac{1}{2}} \left(\frac{\partial \boldsymbol{U}}{\partial r}\right)^{n}_{i+\frac{1}{2}} + \boldsymbol{B}^{\mathrm{V}\ n}_{i+\frac{1}{2}}, \tag{3.53}$$

$$\boldsymbol{S}^{\mathrm{V}\ n}_{i} = \boldsymbol{A}^{\mathrm{V}\ n}_{s\ i} \left(\frac{\partial \boldsymbol{U}}{\partial r}\right)^{n}_{i} + \boldsymbol{B}^{\mathrm{V}\ n}_{s\ i}. \tag{3.54}$$

The matrices $\boldsymbol{A}^{\mathrm{V}}$ and $\boldsymbol{A}^{\mathrm{V}}_{s}$ are computed assuming a Fickian diffusion model using the self-consistent effective diffusion coefficients of Ramshaw and Chang [129]. The expressions for the matrices $\boldsymbol{A}^{\mathrm{V}}, \boldsymbol{A}^{\mathrm{V}}_{s}, \boldsymbol{B}^{\mathrm{V}}$, and $\boldsymbol{B}^{\mathrm{V}}_{s}$ can be found in the works of Munafò [61] and Scoggins [1]. In the second linearitazion step, the viscous fluxes and source terms are expanded by means of Taylor series expansions, where the gradients in Eqs. (3.53)-(3.54) are computed according to Eqs. (3.48)-(3.49) and the resulting expressions are linearized around time level n. The final expressions of the viscous fluxes and source terms yield

$$\boldsymbol{F}^{\mathrm{V}\ n+1}_{i+\frac{1}{2}} \approx \boldsymbol{F}^{\mathrm{V}\ n}_{i+\frac{1}{2}} + 2\boldsymbol{A}^{\mathrm{V}\ n}_{i+\frac{1}{2}} \left(\frac{\partial \boldsymbol{U}_{i+1} - \partial \boldsymbol{U}_{i}}{\Delta r_{i+1} + \Delta r_{i}}\right) + \frac{\partial \boldsymbol{B}^{\mathrm{V}\ n}_{i+1/2}}{\partial \boldsymbol{U}^{n}_{i}} \partial \boldsymbol{U}^{n}_{i} + \frac{\partial \boldsymbol{B}^{\mathrm{V}\ n}_{i+1/2}}{\partial \boldsymbol{U}^{n}_{i+1}} \partial \boldsymbol{U}^{n}_{i+1}, \tag{3.55}$$

$$\boldsymbol{S}^{\mathrm{V}\ n+1}_{i} \approx \boldsymbol{S}^{\mathrm{V}\ n}_{i} + 2\boldsymbol{A}^{\mathrm{V}\ n}_{s\ i} \left(\frac{\partial \boldsymbol{U}_{i+1} - \partial \boldsymbol{U}_{i}}{\Delta r_{i+1} + 2\Delta r_{i} + \Delta r_{i-1}}\right) + \frac{\partial \boldsymbol{B}^{\mathrm{V}\ n}_{s\ i}}{\partial \boldsymbol{U}^{n}_{i}} \partial \boldsymbol{U}^{n}_{i}, \tag{3.56}$$

with the matrices $\boldsymbol{A}^{\mathrm{V}}$ and $\boldsymbol{A}^{\mathrm{V}}_{s}$ assumed constant during the linearization. The last two Jacobians in Eq. (3.55) are approximated as

$$\frac{\partial \boldsymbol{B}^{\mathrm{V}\ n}_{i+1/2}}{\partial \boldsymbol{U}^{n}_{i}} \approx \frac{\partial \boldsymbol{B}^{\mathrm{V}\ n}_{i}}{\partial \boldsymbol{U}^{n}_{i}}, \tag{3.57}$$

$$\frac{\partial \boldsymbol{B}^{\mathrm{V}\ n}_{i+1/2}}{\partial \boldsymbol{U}^{n}_{i+1}} \approx \frac{\partial \boldsymbol{B}^{\mathrm{V}\ n}_{i+1}}{\partial \boldsymbol{U}^{n}_{i+1}}. \tag{3.58}$$

The expressions for $\partial \boldsymbol{B}^{\mathrm{V}}/\partial \boldsymbol{U}$ and $\partial \boldsymbol{B}^{\mathrm{V}}_{s}/\partial \boldsymbol{U}$ can be found in the works of Munafò [61] and Scoggins [1].

Finally, the inviscid and kinetic source terms are linearized following simple Taylor series expansions giving

$$\boldsymbol{S}^{\mathrm{I}\ n+1}_{i} \approx \boldsymbol{S}^{\mathrm{I}\ n}_{i} + \frac{\partial \boldsymbol{S}^{\mathrm{I}\ n}_{i}}{\partial \boldsymbol{U}^{n}_{i}} \partial \boldsymbol{U}^{n}_{i}, \tag{3.59}$$

$$\boldsymbol{S}^{\mathrm{k}\ n+1}_{i} \approx \boldsymbol{S}^{\mathrm{k}\ n}_{i} + \frac{\partial \boldsymbol{S}^{\mathrm{k}\ n}_{i}}{\partial \boldsymbol{U}^{n}_{i}} \partial \boldsymbol{U}^{n}_{i}. \tag{3.60}$$

Eqs. (3.52)-(3.60) are substituted into Eq. (3.50), leading to a block-tridiagonal linear system of equations which is solved at each time-step by means of the Thomas algorithm [116] for the update of the conservative variables. The procedure is repeated until steady-state is reached.

Physico-chemical data. The computation of the closure terms present in the DRNSE needs models and data. The stagnation line code is coupled to the MUTATION^{++} library [130] which centralizes data and algorithms for the accurate implementation of state-of-the-art physico-chemical models for CFD simulating high temperature, reacting flows. The library has been designed, implemented and extensively tested to ensure high-fidelity together with low computational costs.

In the particular case of this thesis and the experiments we want to simulate, thermodynamic data is based on the RRHO model [71]. Transport properties are computed through the second order perturbation of the Chapman-Enskog expansion of the Boltzmann equation (Sec. 2.2.2). The chemical production rates for species, based on elementary chemical reactions including third body, are calculated by taking the forward reaction rate coefficients specified by the user in an Arrhenius law form. In this work, a nitrogen-carbon mixture set of 9 species $\{\mathrm{e}^-, \mathrm{C}^+, \mathrm{C}_2, \mathrm{C}_3, \mathrm{CN}, \mathrm{C}, \mathrm{N}, \mathrm{N}^+, \mathrm{N}_2\}$ is used. The chemical mechanism considered is a subset of the full air ablation mechanism proposed by Olynick [131] for which only the reactions taking into account any of the species considered are included. The backward rate coefficient is determined by satisfying the equilibrium relation (Sec. 2.2.3). The energy exchange term between translational and vibrational modes is computed with a Landau-Teller formulation depicted in Sec. 2.2.4, where the characteristic relaxation time is computed through the Millikan and White empirical formula [87]. The energy added/-substracted to the vibrational model due to chemical reactions is evaluated according to [124]. The energy exchange between free electrons and heavy particles is also evaluated with a Landau-Teller formulation (Sec. 2.2.4).

Lastly, the wall ablative boundary condition needs additional data. The interaction of the material with the surrounding gas can be approximately modeled through mass and energy balances in a thin lamina enveloping the material surface and the surrounding flow (Sec. 2.3.1). For the nitrogen ablation mechanism considered in Sec. 2.3.3, the different coefficients are taken as uncertain in order to learn them from the experimental data. The ablative boundary condition is accessed through the MUTATION^{++} library which also includes a generalization of gas-surface interaction boundary conditions for different models [110].

3.2 Experiments

In this section, we review the facility, its operating principles, and set-ups involved in generating the experimental data. The facility is common for both catalysis and ablation experiments. The particular procedures and set-ups for catalysis and ablation are reviewed separately with a discussion on the importance of the experimental data on the inference of each set of model parameters.

3.2.1 The VKI Plasmatron

We consider the experimental set-up of the Plasmatron facility at the von Karman Institute (VKI), an Inductively-Coupled Plasma (ICP) wind tunnel powered by a high-frequency, high-power, high-voltage (400 kHz, 1.2 MW, 2 kV) generator [132]. This facility is able to reproduce relevant re-entry conditions by producing a high-enthalpy, highly dissociated subsonic gas flow which simulates the stagnation point effects on the material sample tested. A schematic view of the Plasmatron facility and all its integrated systems is shown in Fig. 3.4.

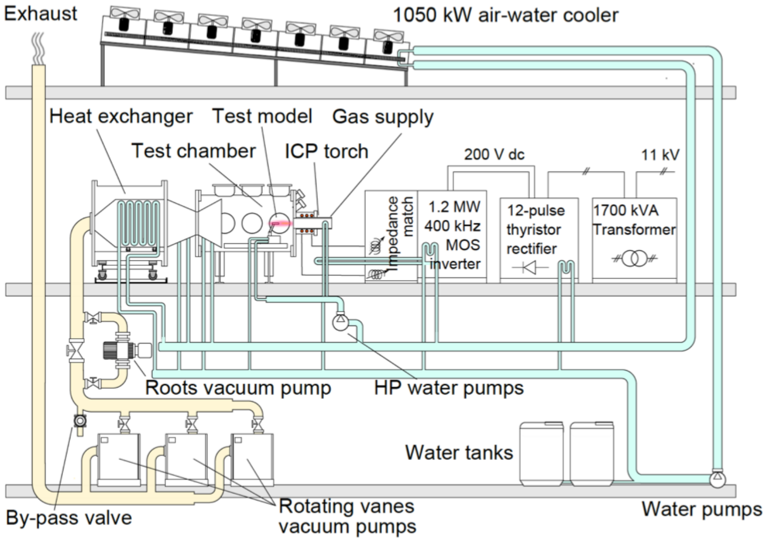

Figure 3.4: *Schematic view of the VKI Plasmatron system, including vacuum and water-cooling loops [4].*

The operating principles of the Plasmatron consist of a cold gas annular injection in a quartz tube surrounded by a coil. The coil is connected to the generator, providing high voltage, high frequency current. This induces an electromagnetic (EM) field inside the tube, with induction lines coaxial with the tube itself. Argon is used as driving gas for the initial discharge, thanks to the long lifetime of free electrons at low pressure compared to air plasma. The EM field forces residual charged particles to form eddy currents in the opposite direction of the primary current. The injected gas is then heated by Joule effect, promoting further ionization. This process is balanced by the creation of new electrons through collisions and the recombination of electrons with argon ions. The hot gas accelerates out of the torch in form of a plasma jet and is then switched to the desired test gas (air, N_2, CO_2). Once being in equilibrium, this process can run uninterruptedly given that enough electricity, supply gas and cooling are provided. More details about this facility can be found in the works of Bottin [133].

From the 160 mm plasma torch, the generated plasma is then discharged to a testing chamber 2.5 m long and 1.4 m in diameter kept in under-atmospheric pressure with range 1000-22000 Pa. The cooling of all the facility components is provided by a 1050 kW cooling system using a closed water loop (2090 liters/min) and fan-driven air coolers on the roof, providing cooling for the torch, test chamber, sample retention system, and holding arms. The hot gas from the test chamber exits through a 700 kW heat exchanger to a group of three rotary-vane vacuum pumps and a roots pump, which are capable of extracting 3900 m^3/h, with a terminal vacuum capability of 0.02 hPa. The facility is computer controlled using a 719 I/O lines Programmable Logic Controller (PLC), and two desktop computers for controlling and monitoring the input regulation.

Overall, this facility allows a broad range of test article dimensions. The holding probes for material samples and the probes for flow characterization measurements are mounted on water-cooled arms that can be swung into and out of the flow by a displacement mechanism. Several optical accesses to the chamber allow flow and samples diagnostics: the lateral windows (on both sides of the facility) allow for perpendicular side views of the plasma jet and probes, while the torch-side windows allow for a frontal oblique view of the material surface.

The interest of testing in such facility lays in the fact that it can reproduce relevant flight conditions. The Local Heat Transfer Simulation (LHTS) framework developed at the Institute for Problems in Mechanics (IPM, Moscow, Russia) by Kolesnikov [13] shows how a subsonic ground-test facility, such as the VKI Plasmatron, is able to provide a complete duplication of re-entry flight conditions. Kolesnikov's works state that, under the assumption of LTE at the outer edge of the boundary layer δ, the stagnation point heat flux in flight and on ground are identical if the boundary layer edge total enthalpy H_δ, the pressure P_δ, and the radial velocity gradient in the radial direction $\beta_\delta = (\partial u/\partial x)\big|_\delta$ are locally matched. These results are based on the boundary layer theory for dissociated reacting gases following the works of Fay and Riddell [134], and Goulard [103].

Even though our focus is in the calibration and eventual reconstruction of theoretical models for the different phenomena considered, the fact that the Plasmatron can simulate relevant flow environments by duplicating selected effects found in flight is of major importance. In these lines, the Plasmatron can handle different gas mixtures to simulate different planetary atmospheres, such as the ones from Earth (air) and Mars (CO_2). The Plasmatron can also provide a uniquely wide testing envelop (see Fig. 3.5). Heat fluxes from ~90 kW/m^2 up to ~10 MW/m^2 guarantee enthalpies between ~5 and ~60 MJ/kg or above.

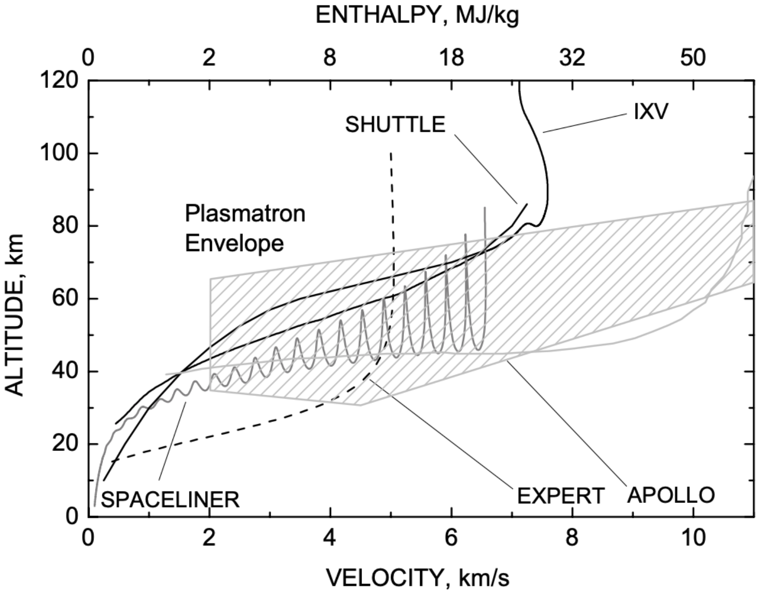

Figure 3.5: *Plasmatron operating envelope compared against typical Earth re-entry trajectories [4].*

3.2.2 Catalysis testing

The efficient design and assessment of TPS materials require extensive experimental databases obtained under relevant flight conditions. In this sense, we have seen the capabilities of the VKI Plasmatron to reproduce typical atmospheric entries (Fig. 3.5). Building on the Plasmatron facility, researchers can now study different aspects of gas-surface interactions by means of different measurement techniques combined together in unique set-ups.

Surface catalytic activity can be characterized by measuring different signatures in the flowfield and the material surface. Catalytic surfaces modify the amount of heat flux experienced by the material, the boundary layer chemical composition and the material surface temperature. In the past, researchers have devised experimental set-ups aimed at reconstructing material catalysis coefficients (see Sec. 2.3.2) together with validation of their reconstruction approaches by using independent measurements of different relevant quantities which are influenced by the presence of catalytic activity [4, 119, 135]. While their original interest was in defining values of the catalytic coefficients for different materials under different conditions for design and flight certification, our aim is different. In this thesis, we look at incorporating such experimental data into our models where we also include measures of uncertainty. Along with this, we devise a way to obtain the most informative experiments which can help us define catalytic coefficients with low uncertainty levels, paving the way for the construction of calibrated, accurate models in the future.

For these tasks, we first select experiments performed by Panerai [4] in his thesis work. These experiments provide good benchmarks for the comparison of our methodology to previous works [5]. Another set of experimental data is produced within the work of this thesis to address the question of how to obtain the most informative experiments for catalysis determination in TPS materials. These last set-up and methods are addressed in Chapter 6 as part of the outcomes of this work.

Experimental set-up and procedures. The experimental set-up envisioned by Panerai [4] for the cases used in this thesis is depicted in Fig. 3.6. In it, Panerai made use of three different probes submerged in the flowfield, together with other non-intrusive measurements for surface properties determination.

In a typical experiment, one sequentially exposes two probes to the plasma flow: a reference probe made of a well-known material (copper), having a catalytic coefficient γ_{ref}, and a probe which holds a sample of the TPS material with the catalytic coefficient we want to infer, γ_{TPS}. For the TPS probe, we measure directly the heat flux $q_{\mathrm{w}}^{\mathrm{TPS}}$ and surface temperature $T_{\mathrm{w}}^{\mathrm{TPS}}$, while for the reference probe only the heat flux $q_{\mathrm{w}}^{\mathrm{ref}}$ is measured.

The underlying idea of the experimental procedure is to perform first measurements of the heat flux $q_{\mathrm{w}}^{\mathrm{ref}}$, dynamic pressure P_{d} and chamber static pressure P_{s} with the reference probe set in the plasma jet. As these measurements depend on the state of the free stream flow, in particular on the enthalpy H_δ at the boundary layer edge, the free stream conditions can be deduced if one knows the catalytic coefficient γ_{ref} of the reference probe. Further, in a second stage, the TPS probe is set in place of the reference probe in the plasma jet. The corresponding steady-state wall temperature $T_{\mathrm{w}}^{\mathrm{TPS}}$ and emissivity ϵ are measured, leading to the computation of the experimental heat flux $q_{\mathrm{w}}^{\mathrm{TPS}}$. Consequently, assuming that the free stream flow conditions have not changed, the catalytic coefficient γ_{TPS} of the TPS probe can be determined.

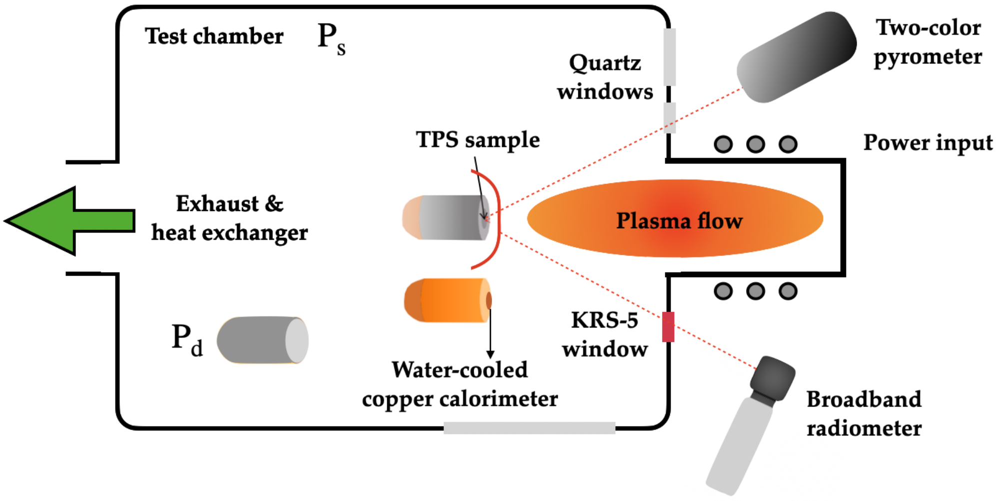

Figure 3.6: *Schematic view of the experimental set-up for the Plasmatron facility.*

Measurement techniques. The following instruments equip the Plasmatron in the context of the described experiments. The reference probe is a flat-faced device (25 mm radius) equipped with a water-cooled copper calorimeter at the center of its front face (see Fig. 3.7). The calorimeter has a cooling water system that maintains the surface temperature of the reference probe at around 350 K. The heat flux $q_\mathrm{w}^\mathrm{ref}$ is deduced from the mass flow (controlled by a calibrated rotameter) circulating in the cooling system and the inlet/outlet water temperature difference measured by thermocouples as a result of the exposure to the plasma flow. The relationship between $q_\mathrm{w}^\mathrm{ref}$ and the water line temperature difference reads

$$q_\mathrm{w}^\mathrm{ref} = \frac{\dot{m} c_\mathrm{p} \left(T_\mathrm{out} - T_\mathrm{in}\right)}{A}, \tag{3.61}$$

where $\dot{m}$ is the mass flow in the cooling line, A is the frontal area exposed to the plasma flow, c_p is the water specific heat, and $T_\mathrm{out}, T_\mathrm{in}$ are the temperature readings of the incoming cooling water line and the outcoming one.

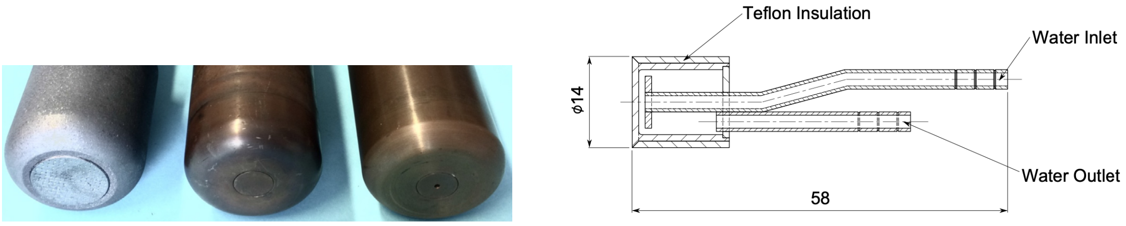

Figure 3.7: *From left to right: TPS heat flux probe, reference probe and Pitot probe, respectively (left). Sketch of the water-cooled copper calorimeter positioned at the center of the reference probe's front face (right), from [4].*

As seen in Fig. 3.7, the copper calorimeter has teflon insulation on the side walls to provide proper adiabatic conditions. For the TPS sample, a sample holder with the same geometry as the reference probe is used. The holder stem is composed of two coaxial tubes with water circulating for cooling. A cap support for the TPS sample is attached to the rest of the holder body by three metallic pins. Such cap is made out of graphite to endure very high heat flux testing. In its center, the TPS sample is positioned. An insulation layer is placed as back support for the samples, to limit the material conduction which is not taken into account for heat flux computations in these cases.

For pressures, a water-cooled Pitot probe measures the dynamic pressure P_d within the plasma jet. The Pitot probe has the same geometry than the water-cooled calorimeter holder as seen in Fig. 3.7. An absolute pressure transducer records the static pressure P_s in the Plasmatron chamber. It is important to take into account that the proper calibration and retrieval of the measured physical quantities (P_d in this case) is made more challenging in the presence of high enthalpy, low Reynolds number, viscous flows, where one has to consider possible viscous effects as shown by Barker [136]. In particular, for the correct retrieval of the velocity from Pitot measurements, we have to take into account viscous corrections aimed at quantifying the discrepancies between the measured Pitot pressure and the theoretical total pressure. For this purpose, Homann defined a coefficient $K_\mathrm{H} = P_\mathrm{Pitot} - P_\mathrm{ref}/P_\mathrm{t} - P_\mathrm{ref}$ for spheres and cylinders [137].

The determination of the TPS probe heat flux assumes a radiative equilibrium at the surface, with the relation $q_\mathrm{w}^\mathrm{TPS} = \sigma\epsilon\left(T_\mathrm{w}^\mathrm{TPS}\right)^4$, where σ is the Stefan-Boltzmann constant and ϵ is the emissivity measured with a broadband infrared radiometer which provides the integrated thermal radiation over the selected spectrum 0.6 - 39 μm within a span of temperature 0-3000°C. The emissivity values are used to correct for the assumption of blackbody radiation. The emissivity coefficient takes care of the fact that real bodies emit less at the same temperature than their blackbody counterparts. In this context, the emissivity of a body in a certain wavelength λ is defined as

$$\epsilon_{\lambda,T} = \frac{W_\lambda}{W_\lambda^0}, \tag{3.62}$$

where W_λ is the actual radiance of the body, while W_λ^0 is the radiance of a blackbody at the same temperature T. In general, the waveband 0.6 - 39 μm contains most of the resulting thermal radiation that the sample under study is emitting. Given this, the Stefan-Boltzmann's approximation gives a good estimation of the actual radiance, with the measured emissivity value taken as the total emissivity of the sample. Nevertheless, Panerai [4] goes over a detailed procedure for blackbody Planck's law integration which was initially proposed by Widger and Woodall [138], such that some inaccuracies in the assumptions previously mentioned can be overcome. The broadband radiometer used in the cited experiments is located at $\sim 47°$ angle relative to the surface normal in front of a 1.8 cm thick KRS-5 window. Such material, also known as thallium bromoiodide is one of the few existing crystals that offers about 70% transparency in the whole radiometer operating waveband.

Having measured the spectral radiance and emissivity at a given wavelength, we could easily determine the temperature at which the surface is emitting radiation. Nevertheless, due to how radiation-based measurements are quite prone to errors in their calibration and measurement chain, it is worth investing in another measurement technique for the measurement of surface temperatures. The surface temperature $T_\mathrm{w}^\mathrm{TPS}$ is measured using a two-color pyrometer. This device measures the spectral radiance at two different wavelength which are very close together in the spectrum. This last characteristic makes possible the assumption of graybody, where the emissivity in all wavelength remains the same. In the pyrometer case, we would be comparing the emissivities at two neighbouring wavelengths which makes this assumption feasible. Having measured two different spectral radiances, we can compute their ratios assuming their emissivities are the same. As a result we obtain an expression which only depends on the temperature the body is emitting at [4]. The pyrometers used by Panerai [4] in his experiments work at around 1 micron wavelength and are set at 1 Hz acquisition frequency, which is judged sufficient for steady state measurements. The pyrometers are pointed and focused in the stagnation area of the sample through a 1 cm thick quartz window, at an angle of $\sim 35°$ with respect to the surface normal.

3.2.3 Ablation testing

As with catalysis testing, we are interested in using the capabilities offered by the VKI Plasmatron to study now ablative materials. In particular in this work, we are focused on graphite without the bonded resin, thus avoiding the modeling of pyrolysis processes and focusing only on thermochemical ablation phenomena.

Thermochemical ablation also changes properties in the flowfield as well as the material surface. Ablation modifies the amount of heat flux experienced by the surface, the chemical composition in the flowfield by adding not only catalyzed species but also carbonaceous ones, it modifies the surface temperature, and, unlike catalysis, changes also the shape of the material. The presence of carbonaceous species in the flowfield together with the recession of the material surface makes the experimental data obtained from ablation testing quite different in nature. The access to these experimental data through dedicated measurement techniques brings a wealth of information to the model, especially if the surface reaction mechanism is straightforward to propose due to well designed experiments.

In this thesis, we question our two sources of information (experiments and models) on equal footing. The same way we want to compare different models against the same experimental data, we want to assess the different experimental data to make sure it can be trusted to begin with. Once this has been accomplished, different models can be compared against each other in light of consistent experimental data (Chapter 7). For these tasks, we recast the inference problem performed by Helber et al. [22] where they propose an experimental set-up for graphite testing in the VKI Plasmatron, followed by a numerical reconstruction method to extract nitridation reaction efficiencies $\gamma_{\mathrm{N}}^{\mathrm{CN}}$ for different wall temperatures T_{w}. In the following part of this section, we focus our attention to the experimental set-up and the measurement techniques as proposed by Helber et al. [22].

Experimental set-up and procedures. The experimental set-up for nitridation studies was proposed by Helber [3] and it is depicted in Fig. 3.8. The ablative material sample, graphite, consists of a 25 mm radius hemisphere with a 25 mm long cylindrical after-body, machined in-house. The raw graphite material is a superfine grain, high-density extruded graphite rod obtained from Graphtek LLC. The density of the graphite rod is reported to be $\rho_{\mathrm{s}} = 1760\mathrm{kg/m}^3$, with a thermal conductivity of 130 W/(m K) at room temperature.

From the schematic of the testing set-up (Fig. 3.8), it is seen that several non-intrusive measurements of the material surface are taken. The total stagnation point recession, from which the recession rate $\dot{s}$ is derived, is measured using a digital camera (Nikon D5000) attached to a 400 mm lens, giving a resolution of about 0.03 mm per pixel. A two-color pyrometer is used to measure the surface temperature T_{w}. The emission spectroscopy set-up consists of an Acton Series SP-2750 spectrograph of 75 cm focal length combined with an ICCD PI-MAX camera with a frame of 1024 x 1024 pixels. The spectroscopy set-up is used to record the strong radiative signature of the CN molecule [139, 140] from which to derive flow temperatures and CN densities ρ_{CN}.

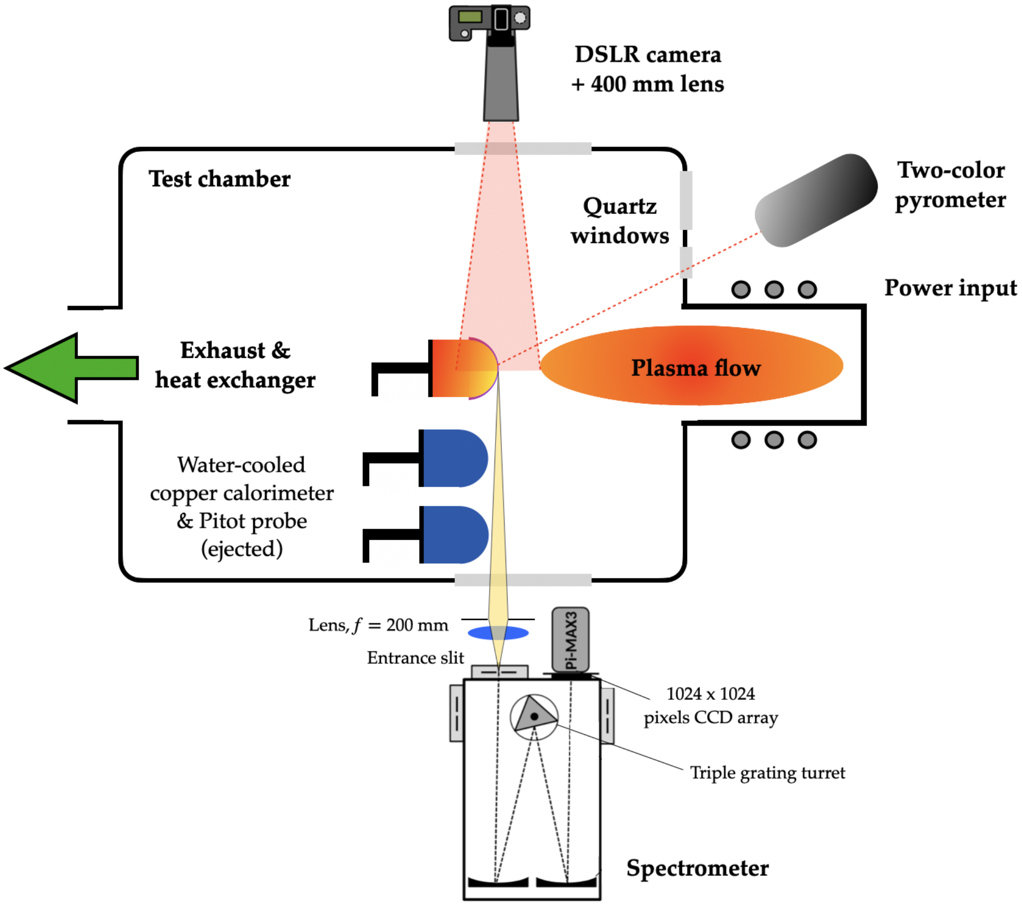

Figure 3.8: *Schematic view of the ablation experimental set-up for the Plasmatron facility. Figure adapted from Helber [3].*

The test sample is pre-heated (cleaned and dried) by the argon plasma used to start the Plasmatron facility. After starting the plasma on argon gas, with the test sample in place, the test gas is switched to pure nitrogen. The stagnation point of the test sample is placed 445 mm from the torch exit.

The free stream condition is reconstructed in a previous step by using a 25 mm radius copper water-cooled probe, mounting a copper calorimeter in the center of the front face. The calorimeter is used for heat flux measurements in the same fashion as seen for catalysis (Sec. 3.2.2). A water-cooled Pitot probe is used to perform dynamic pressure measurements P_{d}, together with an absolute pressure transducer that measures the static pressure P_{s}. The probes are mounted inside the Plasmatron test chamber at 445 mm distance from the torch exit. The placement ensures that the axis of the probe and the axis of the torch itself coincide. The water-cooled copper calorimeter probe, Pitot probe and TPS material probe are sequentially exposed to the plasma flow.

Measurement techniques. The copper calorimeter, Pitot probe and static pressure transducer all work according to the same principles highlighted in Sec. 3.2.2. The objective in both cases is the same: gather information about the boundary layer edge conditions. For the ablative sample, the measurements of the two-color pyrometer play the same role as for the catalysis studies, it reports the measurements of surface temperatures.

In this case, the two-color pyrometer employs a wide (0.75 - 1.1 μm) and narrow (0.95 - 1.1 μm) spectral bands for the surface temperature T_w determination at 1 Hz adquisition rate (1300 K - 3300 K). It is assumed that emissivity of the char surface is constant over this narrow wavelength range. The set-up followed for the pyrometer is identical to that depicted in Sec. 3.2.2. The instrument is calibrated up to 3300K using a high temperature graphite blackbody.

The two-dimensional ICCD array of the spectrometer set-up, enables spectral measurements across the complete jet diameter of 20 cm, yielding a spatial resolution of 0.195 mm. The 150 grooves/mm grating of the spectrometer is used for these cases to benefit from the wide spectral range. The integration time is set between 40 ms and 150 ms for all tests, allowing to get instantaneous pictures of the flowfield with regard to the test time. A total of 10 frames are averaged within few seconds to increase the signal to noise ratio. The raw data obtained from the spectrometer are in the form of counts. To convert the data into spectral intensities [$\mathrm{W}/(\mathrm{m}^2 \cdot \mathrm{sr} \cdot \mathrm{nm})$] calibration of the whole system, consisting of the light collection mechanism and the spectrometer efficiency between 373 nm and 430 nm, is performed [3]. For each acquisition, the camera recorded a data matrix with wavelength distributed along the horizontal axis and the lateral positions of the observed plasma radius distributed along the vertical axis (see Fig. 3.9).

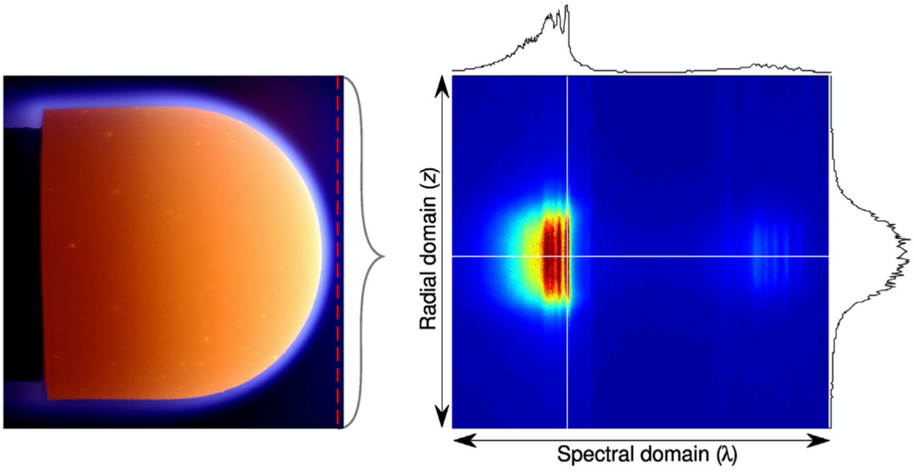

Figure 3.9: *Graphite sample subjected to the subsonic plasma flow undergoing ablation, indicating the radial position of the spectrometer (left). Example of a single data frame taken by the ICCD array illustrating the spectral emission (horizontal line) and radial emission distribution of CN violet maximum (vertical line)(right). Figure from Helber [3].*

As the plasma jet is being observed from the side, the recorded signal is a result of the local emission integrated along the line-of-sight, projected onto the ICCD sensor. If we assume axisymmetry of the jet and an optically thin gas, the inverse Abel transformation provides the local emission coefficient at distance r from the center. Treatment of the experimental spectra is necessary prior to conversion of local emission through the Abel transformation [3]. The local spectral emission at the stagnation region is compared against synthetic spectra to reconstruct the flowfield temperatures at the desired location. The analysis is performed through the minimization of the Root Mean Squared Error (RMSE) between the calibrated Abel-inverted experimental spectrum and the theoretical spectrum. Given that we are dealing with a molecule (CN) and they can store energy in the form of rotation and vibration, the theoretical spectrum is produced as a function of two temperatures which account for the translational-rotational and vibrational-electronic energies. Once the temperatures have been estimated, we can compute the CN density ρ_{CN} at that location in the flowfield. To do so, the local CN violet emission is integrated at radial position r in the spectral range between 375 nm and 390 nm to capture all underlying radiation. This is compared against the simulated integrated emission which takes as inputs the translational, rotational, vibrational, and electronic temperatures, as well as mole fraction of the species of interest, pressure and slab width. Given the previous computation of the rotational and vibrational temperatures, we can now obtain species mole fractions by comparing the experimental and simulated integrated emission intensities. The application of the Abel transformation and experimental CN density determination can be found in more detail in the work of Helber [3].

3.3 Computation of the plasma freestream condition

The computation of the freestream condition plays a radically different role in the inferences we perform for catalysis and ablation. In this case, we refer to the freestream condition as the flow quantities at the edge of the boundary layer at a distance δ from the material surface as depicted in Fig. 3.10. A coupled experimental-numerical methodology is adopted to recover the freestream conditions given a set of measurements with the copper calorimeter, Pitot probe and static pressure transducer. In catalysis testing as well as ablation, this step precedes the measurements on the actual TPS materials and, in most cases, plays an important role on the outcomes of the experimental studies, which then propagates to the model parameters we are trying to estimate.

Having an accurate treatment and assessment of this methodology is crucial for the correct interpretation of results and their uncertainty estimation. As reported in Sec. 3.1 the simulation tools we use to solve for the models considered (Chapter 2) take into account the boundary layer for which the inlet conditions must be specified. If we did not have any more information about our experiments, we would have to assume that all boundary layer edge conditions are unknown and we would have to estimate them along with the model parameters of interest. On closer inspection, the experimental boundary layer is generated by the VKI Plasmatron and its characteristics closely depend on the operating conditions selected for the experiments. Given this information, we can recuperate some boundary layer edge parameters that depend on the facility operating conditions and do not play such an important role in the inferences we want to undertake. This allows us to estimate these parameters and used them as given quantities for the inferences.

The subsonic VKI Plasmatron flowfield, composed by the torch and test chamber, is numerically simulated using an axisymmetric LTE magnetohydrodynamics solver which computes the solution of the Navier-Stokes equations coupled to the Maxwell's equations under certain assumptions (VKI ICP code [141–143]). Initially developed as a standalone tool, the VKI ICP code is nowadays integrated into the Computational Object-Oriented

Library for Fluid Dynamics (COOLFluiD) [144]. The ICP simulation takes the inlet mass flow $\dot{m}$, the power transmitted to the plasma from the coils P_{plasma}, the chamber static pressure P_{s} and the probe geometry as inputs. The power transmitted to the plasma flow is a percentage of the total power injected to the coils P_{el}. This percentage is usually taken as 50% [145].

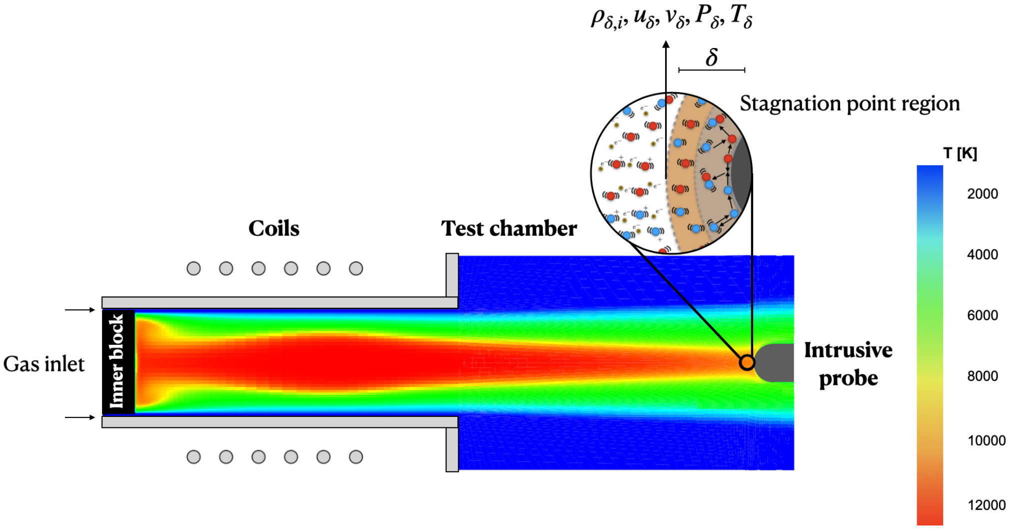

Figure 3.10: *Axisymmetric equilibrium computation of the temperature field inside the Plasmatron torch and test chamber (air, $\dot{m}$ = 16 g/s, P_{s} = 20 hPa, P_{plasma} = 95 kW), with detailed schematic of the stagnation point region.*

The governing equations rely on the MUTATION^{++} library [130] for the computation of the thermodynamic and transport properties of nitrogen and air with five and eleven species mixtures, respectively: $\{\mathrm{N_2}, \mathrm{N_2^+}, \mathrm{N}, \mathrm{N^+}, \mathrm{e^-}\}$, $\{\mathrm{O_2}, \mathrm{N_2}, \mathrm{O_2^+}, \mathrm{N_2^+}, \mathrm{O}, \mathrm{N}, \mathrm{O^+}, \mathrm{N^+}, \mathrm{NO}, \mathrm{NO^+}, \mathrm{e^-}\}$. From the VKI Plasmatron simulations we can obtain the local momentum characteristics at the edge of the boundary layer we are trying to reproduce. For this, we can compute Non-Dimensional Parameters (NDPs) that define the momentum influx and boundary layer thickness δ [145, 146]. These non-dimensional parameters together with the dynamic pressure expression, corrected for viscous effects $P_{\mathrm{d}}/K_{\mathrm{H}} = 1/2\rho_\delta u_\delta^2$ [136], allow us to define a relationship for the inlet velocity components $u_\delta, v_\delta = f(\mathrm{NDPs}, P_{\mathrm{d}}, \rho_\delta)$ or, conversely, for the axial velocity u_δ and the velocity gradient β_δ, depending on the solver and the prescribed inputs (1D boundary layer code in Sec. 3.1.1 or stagnation line code in Sec. 3.1.2). It is important to mention that the variability of the inlet non-dimensional parameters with the operating conditions is small as shown by Panerai [4], and they can be assumed to play a negligible role in the inferences we want to carry out. The fact that they are computed from axisymmetric LTE simulations does not really affect the momentum transfer from the torch to the boundary layer.

This previous step of determining the velocity components, allows us to focus on the reconstruction of the boundary layer edge temperature T_δ as the target of the copper calorimeter experiments for both catalysis and ablation. The general deterministic framework to accomplish such task is highlighted in Chapter 4.

3.4 Sources of uncertainties

One of the critical and defining steps in the scientific method is the objective comparison between theoretical models and experiments. Many steps are required for carrying out this task in a consistent way as reviewed by Oberkampf and Roy [36]. One of the most important ingredients is the proper assessment of the uncertainties that are present in the theoretical model predictions as well as the experimental observations to be compared against. Many question marks can be posed in the modeling assumptions, experimental apparatus, and modeling employed to recover the corresponding physical quantities from the raw measurement data. This work considers the uncertainties related to the mathematical model used to simulate the phenomena in question, and the experimental conditions and measurements. These uncertainties play a defining role in the calibration of model parameters which in itself constitutes an essential part in the objective comparison between models and experiments [147].

In this thesis, numerical errors are not explicitly discussed. For all the simulations run, we impose the conditions of reaching convergence before using the obtained solutions for the inverse problems. Further, surrogate model errors are also kept under a threshold of 1%.

In the following sections, uncertainties are classified into the ones that stem from the modeling and those which stem from the experimental side.

3.4.1 Model uncertainties

When representing natural phenomena with approximate mathematical models we need to question the structure of such models and the values of the input and data parameters. According to our state of knowledge about a particular phenomenon, uncertainties must be identified and treated accordingly [148]. In this work, uncertainties concerning model parameters and boundary conditions are considered. Model form uncertainties are also taken into account [149] for the inverse problem of ablation (Chapter 7).

Generally, boundary conditions are prescribed by experimental data as part of conducting experiments in a controlled environment. In the case of high temperature, dissociated flows in plasma wind tunnel experiments, measuring all quantities needed to simulate a reacting boundary layer is not directly possible, therefore, the conditions of the experiments are not perfectly known. For the few quantities measured, such as pressures and wall temperatures, the uncertainties are considered as inherent variability that comes with the process of measuring. This inherent variability is generally referred to as aleatory uncertainty [150]. It is a kind of randomness that is present due to unknown perturbations in the measurement devices that are not possible to control or reduce. The mathematical framework for treating these aleatory uncertainties consists in prescribing probability distribution functions (PDFs) for the different measured quantities.

The uncertainties associated to model parameters and boundary conditions that are not measured must reflect the fact that there exists a lack of knowledge about those parameters, by contrast with the measured quantities. This type of uncertainty is called epistemic and it can be reduced through experiments, improved numerical approximations, expert opinion, higher fidelity physics modeling, etc. In our case, these uncertainties are implemented as PDFs that represent the degree of belief of the true value as it is defined in a Bayesian setting [151]. Other different ways of treating epistemic uncertainties can be found in the works proposed by Shafer [152] and Zimmermann [153].

Focusing now on the particularities of the theoretical modeling used in this thesis, we should accurately quantify the resulting confidence we have in the computation of all the flowfield variables depicted in Table 2.2. This is a monumental task, given all the closure models (Table 2.3) and boundary conditions that must be assessed along. In particular, epistemic uncertainties range from what phenomena we choose to include in our governing equations, the degree of thermal non-equilibrium assumed and its modeling, the particular values of the model data for kinetic processes, thermodynamics and transport, to the boundary conditions that need definition with no measured counterparts. Further, all of these choices are also coupled to each other. For example, the derivation of boundary conditions from indirect observations, such as boundary layer edge temperatures from heat flux measurements, entails assumptions for the modeling of the whole boundary layer flowfield, which encapsulates all the sources cited here. Apart from this, the material is treated in an approximated way. Additional epistemic uncertainties stem from the phenomena that take place within the material that are not captured in a fully coupled way.

In this thesis, we focus on the most immediate sources of uncertainties that are linked to the problems we study, such as catalysis and ablation model parameters, the boundary conditions of the experiments, and thermodynamics modeling. The particular parameters taken as uncertain are described in more detail in the relevant chapters (Chapters 5-7). The results are therefore conditioned on all the other modeling choices we made in Chapter 2. Even though they represent reasonable and widely accepted assumptions for this kind of experiments, we must still acknowledge the fact that there exists uncertainty around them.

3.4.2 Experimental uncertainties

The role of experiments in this work is to provide information regarding the models we want to calibrate. Some experimental data are direct or indirect measurements of boundary conditions while other observations are quantities of interest that are used along to inform our model parameters and obtain ranges of possible values within a given model structure. We use both sources of information to calibrate boundary conditions and model parameters jointly. In order to have reliable uncertainty estimates on the sought out model parameters, we need accurate quantification of uncertainties on the experimental data. This task is generally carried out by the experimentalists themselves who report their measurements with such estimates which we then use for the calibration of physical models. Nevertheless, the uncertainty characterization techniques used in the aerothermodynamics community for experimental measurements are often poorly suited for their purpose.

There are many different caveats affecting the proper quantification of experimental uncertainties. The raw experimental data, such as voltages measured in time, must be converted into useful physical quantities for the model predictions to be compared against. To do so, a calibration methodology involving some kind of modeling of the experimental apparatus response is required. Aleatory uncertainties stemming from the raw data must be added to epistemic and aleatory uncertainties stemming from the experimental calibration modeling [154]. Both aspects define the final uncertainties on the measured quantities as already discussed in Sec. 1.2. Some measurements techniques are easier to deal with than others. Deriving heat fluxes from differences in water temperatures (Eq. (3.61)) is more straightforward in terms of modeling and assumptions than reconstructing flow temperatures and species concentrations from spectrometer data [3]. Forward and backward uncertainty propagation techniques should be employed to deal with such uncertainty sources. Furthermore, the experiments should be repeated enough times to have reliable statistics on the raw measurements. This point is particularly delicate given how expensive would be to run a plasma wind tunnnel hundreds of times for the same experiment. It is just not feasible. Additionally, special attention should be devoted if the conditions of the measurements differ from the conditions of the calibration [36] which is common to happen in spectrometer measurements [3, 154].

In general, the widely adopted methodology to produce uncertainties (more conveniently defined in this case as error bars) on the experimental data is by performing local Taylor expansions on the quantities of interest that we want to report as measurements, e.g. heat fluxes, flow temperatures, species concentrations, etc. Through these expansions, error bars computed from the raw data for the measured calibrated quantities (water temperatures, surface temperatures, etc) are propagated through the corresponding experimental apparatus models, such as Eq. (3.61), to obtain the error bars on the quantities of interest. The statistical fluctuations of the raw data are based on time series data points where measurements are performed for a given time with a given frequency and the resulting deterministic value is the average over selected points that are considered relevant (e.g. once steady-state is reached in the experiment and there is no evidence of the underlying physics changing). Empirical error bars are also computed on these points.

The final account of error bars does not include any degree of confidence on the different values, and they are solely based on local expansions where the errors are assumed small enough. Further, each measured quantity propagated to some reported quantity of interest, such as a heat flux, is considered to contribute to the error bars only through its direct influence without taking into account higher order interactions among the variables themselves. As we recall from Sec. 1.2, the same methods used for the characterization of uncertainties in physical models should be adopted for the proper characterization of experimental uncertainties. There is not a reason why models and experiments should not be treated on equal footing when it comes to their objective comparison and evaluation of uncertainties. They are both data-generating processes subjected to the same type of uncertainties.

In this thesis, uncertainties related to measured quantities are considered aleatory uncertainties, being mathematically described as probability distribution functions. We use the information reported with the publication of the experimental data, such as error bars and nominal values, and assume a confidence interval for the reported error bars from which we build our distributions. The actual distributions are depicted in the relevant chapters (Chapters 5-7). This is considered a valid assumption given that the experimental devices are well-characterized and the different model parameters involved in their calibrations are considered well-defined (Sec. 3.2.2 & Sec. 3.2.3). This is true when talking about pressure, temperature and heat flux measurements, which are the bulk of the experimental data used in this work. For this reason, the PDFs assigned to the observations are direct reflections of the experimental raw data variabilities alone, as no epistemic uncertainties are considered in the experimental calibration process [3, 4]. Additional experimental data used in the calibration of nitridation efficiencies, such as CN local densities ρ_{CN}, do not have such straightforward measurement process and experimental calibration as seen previously in Sec. 3.2.3. Nevertheless, we model them as aleatory uncertainties, placing a question mark on their prescribed distributions (Chapter 7).

3.5 Summary

In this chapter, we review the data-generating tools. From the numerical codes that practically solve reduced sets of the governing equations exposed in Chapter 2, to the experimental set-ups. The different data-generating processes entail uncertainty sources that must be identified and treated accordingly.

The numerical tools reviewed are oriented to the simulation of reacting flow boundary layers, targeting conditions and geometries typical of the experimental set-ups. The 1D boundary layer code is a very efficient and accurate tool which solves the classical boundary layer equations with catalytic boundary conditions. The equations are presented along with their transformation for the simplification of their solution. Lagrangian and Hermitian polynomials are used for their discretizations to obtain a fourth order accurate solution in step size across the boundary layer. For the closure of the system, the physico-chemical data used are also introduced along with the catalytic boundary condition.

For ablation studies, the numerical tool of choice is the stagnation line code which unlike the 1D boundary layer code, it can handle different physico-chemical models and boundary conditions through the use of the MUTATION^{++} library. In this case, we solve the full set of the Navier-Stokes equations but dimensionally reduced to the one dimensional stagnation line. This enhances the efficiency of obtaining flowfield solutions while keeping a good accuracy, providing a good tool to compare our models to the experiments. The derivation of the DRNSE along with their numerical implementation are first reviewed, followed by the physico-chemical modeling that concerns this work.

The experimental facility and the different set-ups for catalysis and ablation studies are introduced, with particular focus on the measurement techniques. Their calibration and treatment represent important sources of uncertainties. It is relevant for the work of this thesis to understand the complexity behind some of the measurement techniques to be able to have a better assessment on the way experimental uncertainties are commonly prescribed and treat them accordingly. Experimental testing conditions can also be used to determine some free stream parameters with the help of an axisymmetric simulation, linking the operation conditions of the Plasmatron to the inlet of the boundary layer. This provides information to our inference problems in the form of inlet momentum components.

A discussion on the sources of uncertainties stemming from the different data-generating processes closes the chapter. The first step in all uncertainty analyses is the identification of sources and how they can be treated in a stochastic framework. This is discussed in a general way and it is dealt with in more details in the following chapters.

Chapter 4

Inference methods

This chapter opens by referencing deterministic inverse methods and their shortcomings, as well as offering a succinct account of their usage in the atmospheric entry flows community. The chapter follows with a review of the defining features of stochastic inverse problems. In particular, the Bayesian formalism towards inverse problems is reviewed through each of its constitutive steps. The general formulation of the stochastic inverse problem opens the discussion followed by the derivation of the likelihood function in the cases where the noise is additive and multiplicative. The problem of encoding objective prior information in probability distributions is also tackled. Models and methods for the effective exploration of the posterior distribution are presented, as well as the convergence diagnostics tools generally used. Model selection techniques are also highlighted as they are relevant for the set of ablation experiments and models tackled in this thesis. A last section is devoted to the methods used to make the process of solving a statistical inverse problem less burdensome when dealing with complex models. In particular, surrogate modeling by means of Gaussian processes and sensitivity analysis methods are addressed as they constitute important steps in the methodologies developed in this work.

4.1 Classical inverse problems

Inverse problems are defined, as the term itself indicates, as the inverse of direct or forward problems. Consequently, solving inverse problems involves solving the forward problems. Inverse problems are encountered typically in situations where we want to learn about some quantity of interest but we cannot observe it directly. In this case, we perform indirect observations of some other easily accesible quantities and trace them back somehow to the quantity of interest itself through the repeated use of the forward problem. The challenges associated with solving inverse problems amount to the issue of non-locality and non-causality. It is the legacy of Newton, Leibniz and others that laws of nature are often expressed as systems of differential equations. These equations are local in the sense that at a given point they express the dependence of the function and its derivatives on physical conditions at that location. Another typical feature of such laws is the notion of causality, in which later conditions may depend on the previous ones. Locality and causality are features typically associated with direct models. These features are not found in inverse problems, where we cannot rely on locality and causality to estimate some past or far away quantities, which may lead to instabilities in the solution procedure.

In many fields of engineering research it is still common practice to resort to deterministic approaches when it comes to posing and solving inverse problems for the calibration of theoretical models. It is important to stress that this issue not only concerns active parameter fitting procedures but also the resulting *objective* comparisons between model predictions and experiments which drive model validation.

Deterministic inverse problems can come in many flavors. Classical deterministic parameter estimations such as minimization of an error metric with possible regularization terms are by far the most widespread [155–157]. In this case, we are looking for a vector of model parameters $\boldsymbol{c} \in \mathbb{R}^m$ given a set of observations $\boldsymbol{y} \in \mathbb{R}^n$. The two quantities are related through a model $\boldsymbol{y} = f(\boldsymbol{c}, \boldsymbol{p})$, where $\boldsymbol{p} \in \mathbb{R}^l$ is a vector of model parameters that are usually assumed perfectly known and $f : \mathbb{R}^m \times \mathbb{R}^l \rightarrow \mathbb{R}^n$. The process for obtaining the solution to the deterministic inverse problem in the form of the parameters $\boldsymbol{c}$ consists of minimizing some functional that reflects the discrepancy between observations and model predictions while incorporating some prior information in the form of a regularization term $\mathcal{R}(\boldsymbol{c}, \boldsymbol{p})$

$$\arg\min_{\boldsymbol{c}} J(\boldsymbol{p}) = \|\boldsymbol{y} - f(\boldsymbol{c}, \boldsymbol{p})\|^2 + \mathcal{R}(\boldsymbol{c}, \boldsymbol{p}). \tag{4.1}$$

This inference formulation fails at dealing with the uncertainties present in experimental data as well as epistemic uncertainties that stem from the model parameters $\boldsymbol{p}$ that are kept fixed. The results of such inferences are point estimates on $\boldsymbol{c}$ for some conditions.

Let us imagine an example. An engineer is insterested in reconstructing the chemical kinetic parameters of a flow through a porous material at a very high temperature. The forward problem consists of predicting the flow temperature in a three dimensional domain inside a porous medium as a function of the flow conditions at the boundaries, the material properties, and the flowfield kinetic parameters. The inverse problem consists of the even more challenging objective of retrieving the selected chemical kinetic parameters from a few thermocouple readings. Furthermore, the engineer decides to adopt the formulation of Eq. (4.1) which considers other flow kinetic parameters, material properties and boundary conditions to be perfectly known $\boldsymbol{p}$, and the thermocouple readings to be a single number $\boldsymbol{y}$ in each location, as representative of their mean value over a certain adquisition window, or as particular realizations of the measurements. In turn, this engineer would obtain a reasonable estimate of the sought out parameters $\boldsymbol{c}$ but it would not be, by any means, the only possible answer.

Now consider this: in the forward problem, small changes in the known kinetic parameters $\boldsymbol{p}$ can drastically change the temperatures predicted at the thermocouple locations, even when considering the values of the parameters $\boldsymbol{c}$ previously estimated. In turn, a slightly different choice of those parameters $\boldsymbol{p}$ would yield completely different answers to the inverse problem. This issue also extends to the choosing of the values of the experimental data $\boldsymbol{y}$. In sum, the engineer finds that vastly different flowfield and material characteristics may have produced the same thermocouple observations, at least within the accuracy limit of the measurements. This is a serious problem that requires a careful analysis of the data and the methods for inverse analysis.

Moreover, the engineer draws conclusions about her work by only looking at the obtained parameters $\boldsymbol{c}$, trying to derive some physical understanding from such exercise. The conclusions and knowledge derived as well as the values of the parameters themselves are just one possible description of the problem that does not encapsulate the whole picture. One might argue that based on previous studies and experiments, the material characteristics and the other flowfield parameters encapsulated in $\boldsymbol{p}$ are well-known, but the same argument can be posed on how that knowledge was derived in the first place. How is it possible to even define model validation on the basis of these methods? It is straightforward to see why these techniques are ill-equipped to produce reliable model calibrations and validations and why uncertainty is a necessary component that should be modeled in addition to the physical problem of interest.

As we can see from the example, uncertainty naturally arises in situations where insufficient information is provided or some determining factors are not observed. This is the case when we seek to learn from an experimental dataset. Probabilistic models, which represent a probability distribution over random variables, provide a principled and solid framework to resolve problems involving uncertainty. Scientific inference is a learning process where uncertainty must be evaluated at every step and traced back to all possible causes for the observed effects. Incorporating uncertainties in inverse problems to study the plausibility of the experimental data under the hypothesis of a given model requires the overhaul of deterministic inverse techniques. The information content of the solutions to stochastic inverse problems is different from the deterministic ones, and so are the mathematical framework and algorithms needed to solve them.

4.2 General formulation of the stochastic inverse problem

Contrary to deterministic inverse problems, where we need to solve an optimization problem to get a point-estimate, stochastic inverse problems make use of another mathematical framework to enrich the estimation. This framework is probability theory and lays the foundation for statistical inverse problems. The methods to solve inverse problems involving uncertainty can range from computing a sole value for parameters in a probabilistic model that represent a good approximation of the solution, to obtaining the full probability distribution that the sought out parameters follow. The former are commonly refer to as deterministic approximate inference techniques which reasonably approximate the distribution we are after. Some examples are the Laplace approximation where a mode of the distribution is approximated with a Gaussian distribution by the second-order Taylor expansion about the mode, and variational inference where a simpler family of probability distributions are used to find the distribution that is closest to the true one [158]. The literature is rich with other deterministic approximation methods whose aim is to make intractable problems tractable [159].

We are interested in the problems formulated to compute the full parameter distribution which are more commonly referred to as stochastic inverse problems. The general inverse problem we seek to solve would read as follows. Assume we measure the same quantity $\boldsymbol{y}$ in order to get information about another quantity $\boldsymbol{c}$. We have a good candidate model that relates the two quantities with the parameters $\boldsymbol{p}$ now considered unknown to us to some extent. The model may also be inaccurate in its proposed form. Moreover, the quantity observed $\boldsymbol{y}$ is always noisy. Typically we have

$$\boldsymbol{y} = f(\boldsymbol{x}, \boldsymbol{e}), \tag{4.2}$$

where $\boldsymbol{x} \in \mathbb{R}^{m+l}$ is the vector containing all the parameters not known to us $\boldsymbol{x} = \{\boldsymbol{c}, \boldsymbol{p}\}$ and $\boldsymbol{e} \in \mathbb{R}^k$ is the measurement noise. In a statistical setting, all variables are treated as *random variables* and the problem is recast as

$$\boldsymbol{Y} = f(\boldsymbol{X}, \boldsymbol{E}), \tag{4.3}$$

where the corresponding random variables are denoted with capital letters, with their particular realizations in lowercase letters as in Eq. (4.2). The statistical treatment of the inverse problem enriches the solution by providing not only a point-estimate on some regularized quantity $\bar{\boldsymbol{x}}$ that minimizes a given functional but by characterizing the probability of each point $\boldsymbol{x}$ through a computed distribution. This fact allows us to compute different estimates stemming from the obtained distribution and have a more complete picture of the information we have for a particular parameter.

Generally, we possess some a priori information about $\boldsymbol{X}$. In the Bayesian formalism which is proposed for solving statistical inverse problems in this thesis, this prior information can be encoded in a probability distribution $\mathcal{P}(\boldsymbol{x})$ known as the prior density. This term is quite self-explanatory: it expresses what we know about the unknown parameters $\boldsymbol{x}$ before we see the data $\boldsymbol{y}$. A more detailed account on how to propose prior distributions can be found in Sec. 4.4. Solving the inverse problem for $\boldsymbol{X}$ given some noisy experimental data $\boldsymbol{Y} = \boldsymbol{y}_{\text{obs}}$ can be stated as finding the conditional distribution $\mathcal{P}(\boldsymbol{x}|\boldsymbol{y}_{\text{obs}})$ which expresses our information about $\boldsymbol{X}$ after observing the data $\boldsymbol{y}_{\text{obs}}$. According to Bayes' theorem, this conditional distribution is the solution of the following expression

$$\mathcal{P}(\boldsymbol{x}|\boldsymbol{y}_{\text{obs}}) = \frac{\mathcal{P}(\boldsymbol{y}_{\text{obs}}|\boldsymbol{x}) \cdot \mathcal{P}(\boldsymbol{x})}{\mathcal{P}(\boldsymbol{y}_{\text{obs}})}, \tag{4.4}$$

where the conditional distribution $\mathcal{P}(\boldsymbol{y}_{\text{obs}}|\boldsymbol{x})$ is the likelihood function because it expresses the likelihood of different measurement outcomes with $\boldsymbol{X} = \boldsymbol{x}$ given. The denominator term $\mathcal{P}(\boldsymbol{y}_{\text{obs}})$ is the probability of observing the measured data under the considered model. In practical terms, $\mathcal{P}(\boldsymbol{y}_{\text{obs}})$ is the normalization constant of the posterior distribution, expressed as $\mathcal{P}(\boldsymbol{y}_{\text{obs}}) = \int \mathcal{P}(\boldsymbol{y}_{\text{obs}}|\boldsymbol{x})\mathcal{P}(\boldsymbol{x})\mathrm{d}\boldsymbol{x}$, also referred to as marginalized likelihood or evidence. This factor is of little importance for obtaining $\mathcal{P}(\boldsymbol{x}|\boldsymbol{y}_{\text{obs}})$ as long as $\mathcal{P}(\boldsymbol{y}_{\text{obs}}) \neq 0$, which would imply that the underlying model is not consistent with reality. However, it becomes an essential tool for hypothesis testing and model selection problems (Secs. 4.6-4.7). The conditional distribution $\mathcal{P}(\boldsymbol{x}|\boldsymbol{y}_{\text{obs}})$ is referred to as the posterior distribution in contrast to the prior distribution, as it offers updated information on the variable of interest $\boldsymbol{X}$ after observing the data $\boldsymbol{y}_{\text{obs}}$.

The Bayesian inference formalism for statistical inverse problems can be then broken down into three distinct tasks:

1. Find an adequate representation of the likelihood distribution $\mathcal{P}(\boldsymbol{y}_{\text{obs}}|\boldsymbol{x})$ which best captures the interrelation between the noisy observations $\boldsymbol{y}_{\text{obs}}$ and the unknown parameters $\boldsymbol{X}$.

2. Find a prior distribution $\mathcal{P}(\boldsymbol{x})$ that judiciously represents all that is a priori known about $\boldsymbol{X}$.

3. Explore the posterior probability distribution.

The following sections focus on each of these tasks highlighting their challenges and most important features.

4.3 Construction of the likelihood function

The stochastic inverse problem depends on the probabilistic model assigned to the measurement error in the absence of model error. This error model makes its appearance through the parameter $\boldsymbol{E}$ in Eq. (4.3) which considers the distribution used to describe the noise of the experimental data. In general, the likelihood function is the probabilistic model that results from the relationship imposed between the forward model $f(\boldsymbol{X})$, or its variables if they are directly observed, and the noise parameter $\boldsymbol{E}$. Depending on the nature of the experimental data, different likelihood functions are commonly found in the literature [158]. The most common likelihood functions are derived from explicit noise models where the forward model $f(\boldsymbol{X})$ and the noise parameter $\boldsymbol{E}$ are explicitly related. The most common explicit noise relations are additive and multiplicative [160]. Generally, these relations lead to the implementation of Gaussian or log-normal likelihood functions.

In some cases, the likelihood is not based on a model of the type $\boldsymbol{Y} = f(\boldsymbol{X}, \boldsymbol{E})$. Instead, we may know the distribution of the measurement itself, not the error from which the likelihood must be derived in the case of explicit models. Some examples are measurements based on counting events, such as the photon count arriving at a pixel of a camera. The likelihood function would represent a Poisson process for which additional noise could be added as well. In addition to the Poisson distribution, one can encounter other parametric observation models such as beta or gamma models [161].

In this thesis, we use additive and multiplicative explicit error models to deal with data associated to catalysis and ablation and upon which we construct our likelihood functions. They represent good assumptions for the knowledge we have about the experimental data, which normally consist of a representative value and some deviation from it. For such constraints, Gaussian distributions of different flavours (log-normal is included here) reasonably represent our state of knowledge without the need to impose additional assumptions.

The details about the likelihood derivations from the noise distributions and relations to the forward model are given in the following sections.

4.3.1 Likelihood with additive noise

The most common stochastic model in the literature considers the noise of the observations to be additive and independent from the model parameters

$$\boldsymbol{Y} = f(\boldsymbol{X}) + \boldsymbol{E}. \tag{4.5}$$

Assuming that the distribution of the noise $\boldsymbol{E}$ is known or given $\mathcal{P}_{\text{noise}}(\boldsymbol{e})$ we can derive a distribution for the difference between the observed value of $\boldsymbol{Y} = \boldsymbol{y}_{\text{obs}}$ and the forward model $f(\boldsymbol{X})$ as

$$\mathcal{P}(\boldsymbol{y}_{\text{obs}} - f(\boldsymbol{X})) = \mathcal{P}_{\text{noise}}(\boldsymbol{y}_{\text{obs}} - f(\boldsymbol{X})). \tag{4.6}$$

Given the independence of the error model with respect to the model parameters, the resulting distribution of $\boldsymbol{E}$ does not change when conditioned on $\boldsymbol{X} = \boldsymbol{x}$. Based on this, the likelihood distribution reads

$$\mathcal{P}(\boldsymbol{y}_{\text{obs}}|\boldsymbol{x}) = \mathcal{P}_{\text{noise}}(\boldsymbol{y}_{\text{obs}} - f(\boldsymbol{X})). \tag{4.7}$$

In this thesis, when the noise is assumed additive, the error models for the different measured quantities consist of unbiased Gaussian distributions such that the likelihood can be expressed as

$$\mathcal{P}(\boldsymbol{y}_{\text{obs}}|\boldsymbol{x}) \propto \exp\left(-\frac{1}{2\sigma^2} \parallel \boldsymbol{y}_{\text{obs}} - f(\boldsymbol{X}) \parallel^2\right). \tag{4.8}$$

The assumptions behind such error model are that we consider it to be independent from the model parameters $\boldsymbol{X}$, and when having various error sources from multiple measurements we consider the different errors to be independent from each other. These assumptions are justified in case of experimental noise given that each measurement relies on a different apparatus with its own internal modeling and various noise levels. When using synthetic data we also make the same likelihood choice even though now the "measurements" are simulated quantities that are correlated. Nevertheless, this model is adopted as it is representative of the actual experimental scenario.

4.3.2 Likelihood with multiplicative noise

In general, we can have more complicated relations among the forward model, model parameters and error model. Another common noise model, which still assumes it to be independent from the model parameters, is expressed as

$$\boldsymbol{Y} = \boldsymbol{E} f(\boldsymbol{X}), \tag{4.9}$$

which reflects the fact that the noise is proportional to the values of the observations. For this noise model the variable that is now distributed as the noise is

$$\mathcal{P}\left(\frac{\boldsymbol{y}_{\text{obs}}}{f(\boldsymbol{X})}\right) = \mathcal{P}_{\text{noise}}\left(\frac{\boldsymbol{y}_{\text{obs}}}{f(\boldsymbol{X})}\right), \tag{4.10}$$

which leaves the following likelihood [160]

$$\mathcal{P}\left(\boldsymbol{y}_{\text{obs}}|\boldsymbol{x}\right) = \frac{1}{f(\boldsymbol{X})}\mathcal{P}_{\text{noise}}\left(\frac{\boldsymbol{y}_{\text{obs}}}{f(\boldsymbol{X})}\right). \tag{4.11}$$

An example of this likelihood is when the error model is assumed to follow a log-normal distribution, where the log-error is normally distributed

$$\boldsymbol{Y} = 10^{\boldsymbol{E}} f(\boldsymbol{X}), \quad \text{with} \quad \boldsymbol{E} \sim \mathcal{N}(0, \sigma^2), \tag{4.12}$$

which by taking logarithms results in a likelihood that reads

$$\mathcal{P}(\boldsymbol{y}_{\text{obs}}|\boldsymbol{x}) \propto \frac{1}{f(\boldsymbol{X})} \exp\left(-\frac{1}{2\sigma^2} \| \left(\log_{10} \boldsymbol{y}_{\text{obs}} - \log_{10} f(\boldsymbol{X})\right) \|^2\right). \tag{4.13}$$

In this thesis, this is the kind of multiplicative noise model used for the treatment of measurement errors in ablation experiments given the nature of the spectrometer measurements (Chapter 7).

4.4 Assigning prior probabilities

The choice of priors is a defining feature of Bayesian inverse problems. The prior reflects the knowledge we have about the parameters we want to infer before incorporating the experimental data into the analysis. This prior information can come from expert elicitation or from previous data or analyses. In assigning prior probabilities, researchers often struggle to properly find a way to incorporate qualitative knowledge into a quantitative object that is a defined probability distribution. Given the ample scope of how to properly construct priors in the literature, we focus on the route followed in this thesis with references to other relevant methods.

In general, given the kind of statistical inverse problems treated in this thesis, the goal for a prior distribution is not to add dubious information that can bias the results in a considerable way. This is an important feature given the limited nature of the experimental data. In problems with plenty of data to learn from, the choice of priors loses relevance as the problem becomes robust in the posterior sense. The cases studied in this thesis are usually one experiment, taken as one data point, that is studied and incorporated for the calibration of the physical model. A very informative prior based on expert elicitation of subjective belief would have a significant impact on the results. We focus instead on defining objective priors for our model parameters where only objective information is reflected in the prior distribution.

Objective information can also be of different nature. The most common information we have about our parameters are location and/or scale. Location is information regarding the likelihood of the parameters to lay in some particular subset of the parameters space. In general, this information is encoded in bounded uniform distributions where we imply we are certain about a span of values for our parameters, yet we do not have enough information to favour any particular one. When the bounds of the prior information can span several orders of magnitude we must admit being indifferent to the likelihood of the different scales of the parameters in question as well. In this case, our ignorance regarding the parameter scaling is reflected in a bounded log-uniform distribution where any scale is equally likely. This fact is embodied in the derivation of the Jeffreys prior [161, 162]. These particular choices of priors comply with logical consistency rules [161] based on the stated states of knowledge. These prior distributions are the ones chosen in this work for their non-informative properties as well as their reflected degree of knowledge about the different parameters.

In an increasing order of prior objective information, we can find in the literature other methods for proposing prior distributions based on testable information. In the case where previous experiments are available and can be trusted, we may possess additional information about our parameters. This information can be encoded in expected values or variances, among others. In this situation, Jaynes [163] suggested to recast the problem of assigning prior distributions by finding the PDFs with the maximum entropy for the given constraints. Overall, the literature is rich in examples for different plausible scenarios and nature of the inverse problem as thoroughly reviewed by Kaipio and Somersalo [160].

4.5 Computation of the posterior distribution

All the obtained information about the inferred model parameters are contained in the resulting posterior distribution. The prior distribution reflects the information (or ignorance) we have about the parameters before incorporating the information coming from the experimental data encoded in the likelihood function. As seen in Eq. (4.4), the posterior distribution $\mathcal{P}(\boldsymbol{x}|\boldsymbol{y}_{\text{obs}})$ is the result of the likelihood $\mathcal{P}(\boldsymbol{y}_{\text{obs}}|\boldsymbol{x})$ times the prior $\mathcal{P}(\boldsymbol{x})$ divided by a normalization constant $\mathcal{P}(\boldsymbol{y}_{\text{obs}}) = \int \mathcal{P}(\boldsymbol{y}_{\text{obs}}|\boldsymbol{x})\mathcal{P}(\boldsymbol{x})\mathrm{d}\boldsymbol{x}$. This constant is very hard to calculate because the likelihood (or the prior) can have extremely complex structure, with multiple arbitrarily compact modes, arbitrarily positioned in the (presumably high-dimensional) parameter space $\boldsymbol{x}$. In contrast, Eq. (4.4) can also have a straightforward analytical solution if likelihood and prior are of particular types [151]. This is generally not the case for complex high-dimensional problems and assuming so can have far-reaching consequences in the analysis.

Moreover, we may be interested in different estimators or quantities derived from the full joint posterior. Integration for computing expectations, marginalized distributions and confidence intervals, among others, is a vital step to understand all the pieces of information coming from the full posterior. Forward uncertainty propagation might also be important to estimate the impact that a certain parameter posterior has on a simulated quantity. In this case, being able to efficiently draw samples from it is necessary. In sum, we are interested in performing integration and drawing samples from the posterior distribution without having to compute the normalization constant.

In this regard, normalization-insensitive techniques that rely on ratios of the unnormalized posterior distribution are desired. For this purpose, the properties of particular stochastic models, such as Markov chains, can be exploited in a Monte Carlo framework for accomplishing the efficient sampling of arbitrarily complex posterior distributions. The sampling method, known as Markov Chain Monte Carlo (MCMC), has straightforward computational implementation and it is ideal for sampling posteriors in the real situations in which scientists find themselves.

In the literature, other sampling methods are proposed which combine the computation of the unnormalized posterior and the normalization constant by transforming the likelihood function according to the prior density [164]. Nested sampling makes use of this idea to constrain the posterior sampling to high probability regions within an area proportional to the normalization constant. This approach can take many iterations to reach the bulk of a confined posterior, but relatively few to cross it [161]. Only these relatively few are significantly informative about the posterior. If the principal interest is in accurate estimation of the posterior, this imbalance can be wasteful. Furthermore, the numerical implementation of nested sampling algorithms is more complex and not as useful as MCMC algorithms if we are not seeking to compute the normalization constant.

The following sections introduce the basics behind MCMC methods and algorithms used in this work.

4.5.1 The Markov chain stochastic model

Markov chains are ubiquitous stochastic models that can be found across many fields of application. Particularly, in the domain of statistical inverse problems, they are used to sample complex probability distributions by making a series of local changes to an arbitrary initial state.

Consider a sequence of random states $\boldsymbol{x}^{(0)}, ..., \boldsymbol{x}^{(n)}$ defined on a finite space $\mathcal{X}$. This sequence is called a Markov chain if it satisfies the Markov property

$$\mathcal{P}(\boldsymbol{x}^{t+1}|\boldsymbol{x}^{(t)}, ..., \boldsymbol{x}^{(0)}) = \mathcal{P}(\boldsymbol{x}^{(t+1)}|\boldsymbol{x}^{(t)}), \tag{4.14}$$

which is stated often by saying that *the future depends on the past only through the present.* Further, if the form of $\mathcal{P}(\boldsymbol{x}^{(t+1)}|\boldsymbol{x}^{(t)})$, the transition function, does not change with t, we can say that the chain is time-homogeneous.

There are properties associated to time-homogeneous Markov chains that hold for certain transition functions. These properties are enumerated under the ergodic theorem which guarantees, given the specified properties, that Markov chain samples can be used for constructing Monte Carlo estimates with good statistical convergence. These three properties are irreducibility, aperiodicity and stationarity. Given a probability measure π, the transition kernel $\mathcal{P}$ is irreducible with respect to π if for each $\boldsymbol{x}, \boldsymbol{y} \in \mathbb{R}^n$ with $\pi(\boldsymbol{y}) > 0$ there exists an integer k such that $\mathcal{P}^{(k)}(\boldsymbol{x}, \boldsymbol{y}) > 0$, with k being the propagated steps forward in time. Thus, regardless of the starting point, the Markov chain generated by the transition kernel $\mathcal{P}$ visits with a positive probability any set of positive measure. An irreducible transition kernel $\mathcal{P}$ is also periodic if it generates a Markov chain that remains in a periodic loop forever. The opposite is said for aperiodic Markov chains. Finally, the measure π is an invariant or stationary measure of $\mathcal{P}$ if

$$\pi\mathcal{P} = \pi, \tag{4.15}$$

that is, if the distribution of the random variable $\boldsymbol{x}_j$ before the time step $j+1$ is the same as the variable $\boldsymbol{x}_{j+1}$ after the step $j+1$. A way of ensuring invariance is by satisfying the detailed balance equation

$$\pi(\boldsymbol{x})\mathcal{P}(\boldsymbol{x}, \boldsymbol{y}) = \pi(\boldsymbol{y})\mathcal{P}(\boldsymbol{y}, \boldsymbol{x}), \quad \forall \boldsymbol{x}, \boldsymbol{y} \in \mathbb{R}^n, \tag{4.16}$$

which drives the development of algorithms capable of generating this kind of Markov chains. For formal proofs of these statements and their derivations the reader is directed to the work of Liu [165].

Overall, we can find a transition function that defines a Markov chain with the properties described. This allows us to use such chain for directly sampling the equilibrium or stationary distribution $\pi(\boldsymbol{x})$ we are interested in. The formal proposition of the ergodic theorem reads

Proposition 1.1. *Let π be a probability measure in $\mathbb{R}^n$ and $\{\boldsymbol{x}_j\}$ a time-homogeneous Markov chain with a transition kernel $\mathcal{P}$. Assume further that π is an invariant measure of the transition kernel $\mathcal{P}$, and that $\mathcal{P}$ is irreducible and aperiodic. Then for all $\boldsymbol{x} \in \mathbb{R}^n$,*

$$\lim_{n\to\infty} \mathcal{P}^{(n)}(\boldsymbol{x}, \boldsymbol{y}) = \pi(\boldsymbol{y}), \tag{4.17}$$

and for $f \in L^1(\pi(\mathrm{d}\boldsymbol{x}))$

$$\lim_{n\to\infty} \frac{1}{n}\sum_{j=1}^{n} f(\boldsymbol{x}_j) = \int_{\mathbb{R}^n} f(\boldsymbol{x})\pi(\mathrm{d}\boldsymbol{x}), \tag{4.18}$$

almost certainly.

This theorem is the foundation of Markov Chain Monte Carlo (MCMC) methods where one needs to find a transition kernel $\mathcal{P}$ such that it is invariant, irreducible and aperiodic with stationary distribution the posterior distribution we are seeking to sample. Sampling from the posterior is then equivalent to sampling from the transition kernel of the constructed Markov chain until statistical convergence is reached.

4.5.2 Markov Chain Monte Carlo algorithms

The question now is defined as the construction of a transition kernel $\mathcal{P}$ such that the resulting Markov chain has the posterior distribution π as stationary measure. Several algorithms exist in the literature to construct a Markov chain with the desired stationary distribution π which differ in the way they construct the Markov chain. The cornerstone of all Markov Chain Monte Carlo methods is the so-called Metropolis algorithm, proposed by Metropolis, Rosenbluth, Rosenbluth, Teller and Teller in 1953 [166]. In it, they introduced the fundamental idea of evolving a Markov process by rejection sampling to achieve the simulation from the targetted π. This seed algorithm is restricted to transition kernels $\mathcal{P}$ that are symmetric. Nevertheless, it paved the way to a whole class of methods developed to sample from very complex distributions.

Metropolis-Hastings algorithm. A later development by Hastings in 1970 [167], extended the Metropolis algorithm to accommodate non-symmetrical transition kernels. The aim of this algorithm is to construct a transition kernel $\mathcal{P}$ that satisfies the detailed balance equation Eq. (4.16) which guarantees the invariance of the constructed Markov chain. Let $q : \mathbb{R}^n \times \mathbb{R}^n \to \mathbb{R}_+$ be a given function with the property $\int q(\boldsymbol{x}, \boldsymbol{y})\mathrm{d}\boldsymbol{y} = 1$. The kernel q is called the proposal distribution defining a transition kernel $\mathcal{P}(\boldsymbol{x}, A) = \int_A q(\boldsymbol{x}, \boldsymbol{y})\mathrm{d}\boldsymbol{y}$. If q happens to satisfy the detailed balance equation Eq. (4.16) then we simply set $\mathcal{P}(\boldsymbol{x}, \boldsymbol{y}) = q(\boldsymbol{x}, \boldsymbol{y})$, otherwise we correct the kernel by a multiplicative factor α such that

$$\mathcal{P}(\boldsymbol{x}, \boldsymbol{y}) = \alpha(\boldsymbol{x}, \boldsymbol{y})q(\boldsymbol{x}, \boldsymbol{y}). \tag{4.19}$$

Picture the following scenario. For some $\boldsymbol{x}, \boldsymbol{y} \in \mathbb{R}^n$ we have

$$\pi(\boldsymbol{y})q(\boldsymbol{y}, \boldsymbol{x}) < \pi(\boldsymbol{x})q(\boldsymbol{x}, \boldsymbol{y}). \tag{4.20}$$

We can then choose an α parameter that restores the detailed balance

$$\pi(\boldsymbol{y})\alpha(\boldsymbol{y}, \boldsymbol{x})q(\boldsymbol{y}, \boldsymbol{x}) = \pi(\boldsymbol{x})\alpha(\boldsymbol{x}, \boldsymbol{y})q(\boldsymbol{x}, \boldsymbol{y}), \tag{4.21}$$

which is achieved by setting

$$\alpha(\boldsymbol{y}, \boldsymbol{x}) = 1, \qquad \alpha(\boldsymbol{x}, \boldsymbol{y}) = \frac{\pi(\boldsymbol{y})q(\boldsymbol{y}, \boldsymbol{x})}{\pi(\boldsymbol{x})q(\boldsymbol{x}, \boldsymbol{y})} < 1. \tag{4.22}$$

We can see that the kernel $\mathcal{P}$ satisfies Eq. (4.16) if we define

$$\alpha(\boldsymbol{x}, \boldsymbol{y}) = \min\left(1, \frac{\pi(\boldsymbol{y})q(\boldsymbol{y}, \boldsymbol{x})}{\pi(\boldsymbol{x})q(\boldsymbol{x}, \boldsymbol{y})}\right). \tag{4.23}$$

The practical implementation of such algorithm is quite simple

Algorithm 1: Metropolis-Hastings (MH) MCMC algorithm

1. Set the initial value $\boldsymbol{x}_1 \in \mathbb{R}^n$ and start $k = 1$.
2. Draw a candidate $\boldsymbol{y} \in \mathbb{R}^n$ from the proposal distribution $q(\boldsymbol{x}_k, \boldsymbol{y})$ and calculate the acceptance ratio
$$\alpha(\boldsymbol{x}_k, \boldsymbol{y}) = \min\left(1, \frac{\pi(\boldsymbol{y})q(\boldsymbol{y}, \boldsymbol{x}_k)}{\pi(\boldsymbol{x}_k)q(\boldsymbol{x}_k, \boldsymbol{y})}\right).$$
3. Draw $t \in [0, 1]$ from a uniform probability distribution.
4. If $\alpha(\boldsymbol{x}_k, \boldsymbol{y}) \geq t$ set $\boldsymbol{x}_{k+1} = \boldsymbol{y}$, else $\boldsymbol{x}_{k+1} = \boldsymbol{x}_k$.
5. When $k = K$, the desired sample size, stop, else increase $k \to k + 1$ and go to step 2.

Thus, we explore thoroughly areas of high probability and sometimes we accept moves towards lower probability regions. Issues arise when defining the stopping criterion for a well-converged chain, which is a chain that correctly simulates draws from the complex distribution we are trying to sample. To make sure this is the case, we need to employ diagnostics techniques to monitor and reliably assess the chain convergence. These topics are covered in the next section Sec. 4.5.3.

Make it efficient. In general, computational models can be of arbitrary complexity. In the particular case of reacting flows, even in reduced dimensions, the simulations are still costly for achieving a well-converged Markov chain with the barebones MH method based on trial-and-error proposal distributions. Proceeding this way would imply thousands of model calls, slow convergence and poor chain properties. To make the process more efficient we can adopt different strategies. In this work, the proposal distributions considered are of the random walk form

$$\boldsymbol{x}_{k+1} = \boldsymbol{x}_k + \boldsymbol{z}_{k+1}, \quad \text{with} \quad \boldsymbol{z}_{k+1} \sim \mathcal{N}(0, \Sigma_p), \tag{4.24}$$

where the move $\boldsymbol{x}_{k+1}$ is proposed by drawing from a symmetric density of Gaussian form centered around the previous state with proposed covariance matrix Σ_p. In this particular flavour of Metropolis-Hastings algorithm, the question is how to efficiently choose the scaling of the posterior covariance matrix Σ for fast convergence. Too small scaling parameter and the chain will move too slowly, too large and the proposals will usually be rejected. Instead, we must avoid both extremes and find a value which is optimal according to some asymptotic quantity. This quantity is the acceptance rate, the fraction of proposed moves that are accepted. Roberts, Gelman, and Gilks [168], proved the result that as the number of chain samples goes to infinity, the optimal acceptance rate is precisely 0.234 for the very restricted case of targetting homogeneous stationary distributions π. Later, Roberts and Rosenthal [169] showed that the original result of Roberts et al. [168] still holds for inhomogeneous stationary distributions for which it is optimal to have

$$\Sigma_p = s \cdot \Sigma, \tag{4.25}$$

where $s = (2.38)^2/d$ is the scaling parameter obtained by Roberts et al. by theoretical considerations where d is the dimension of the stationary distribution. Given that the covariance of the targetted posterior Σ is not known a priori, it can be progressively estimated from the samples drawn during an initial *burn-in* stage as an empirical covariance matrix [170]. This is known as the Adaptive Metropolis (AM) algorithm [171].

Both the optimal scaling parameter and the adaptation of the proposal covariance matrix are techniques directed at improving the efficiency and chain properties. The literature is rich with algorithms aimed at further improving the efficiency and robustness of such sampling methods [170].

4.5.3 Diagnostics

The Markov chain stochastic model is guaranteed to converge to a given stationary distribution when the number of samples drawn is large enough. This “large enough” number can depend on the algorithm used to generate the samples as adaptive methods tend to converge faster. Two questions come to mind when faced with the task of sampling from a complex distribution: how large is “large enough”?, and how do we know we achieved convergence? To answer these questions we need to take a look at some of the diagnostics methods and tools which help assess the chain convergence and properties. We sample a Gaussian distribution $x \sim \mathcal{N}(\mu, \sigma)$ with hyperparameters $\mu = 5$ and $\sigma = 2$. Even though it is not a complex distribution to sample from, it is a good example for the purpose of illustrating the different MCMC diagnostics techniques and how to tell if our chain is well-converged.

Trace plot. The most simple and straightforward way to assess the convergence of a Markov chain is by plotting the trace of the MCMC samples. The lack of convergence reveals itself by showing a clumsy trace if the proposal covariance is too small. In this case, almost all proposed moves are accepted but they represent small movements and the chain does not mix well. On the other hand, if the proposal covariance is quite large, almost no move is accepted and the chain tends to stay in the same state for long periods. A proposal covariance in between, closer to the actual value, allows a balance of accepted and rejected moves in such a way that the chain mixes well and explores the full stationary distribution support. The three examples are depicted in Fig. 4.1.

Acceptance rate. A simple way to avoid the two extremes of small and large proposal covariances is to actually monitor the acceptance rate. Very high acceptance rate means we are using a small proposal covariance. Conversely, low acceptance rate indicates the use of a large proposal covariance. Ideally, we should remain in an interval between 0.1 and 0.6 for a good and efficient mixing of the chain. For the Gaussian example of Fig. 4.1, we obtain acceptance rates of: 0.977 for the chain with small proposal covariance, 0.479 for the chain with good proposal covariance, and 0.129 for the chain with large proposal covariance.

Autocorrelation function. Another efficient way to verify if a good proposal distribution is chosen is to plot the empirical autocorrelation function at different lags for each component of the input vector [170]. The autocorrelation measures the interdependence of the iterations of the chain. A good value of the proposal covariance would show a fast decay of the autocorrelation function with the lag. Fig. 4.2 shows the corresponding autocorrelation functions (ACF) for the same cases shown for the trace plot.

We can plot the resulting distributions and see how well they compare to the original Gaussian distribution we are trying to sample from. Fig. 4.3 shows the three different results we obtain when using different proposal covariances in the construction of our Markov chains. In a real world case, we would not know how the complex distribution we are trying to sample from should look like so these diagnostics methods are quite reliable in assessing convergence.

There exist other more rigorous diagnostics approaches to assess the MCMC chain convergence such as the ones proposed by Raftery et al. [172] and Cowles et al. [173]. In this thesis, we make use of trace plots combined with estimations of the acceptance rates. Even though the convergence cannot be guaranteed through these diagnostics methods, the combination of several techniques provides good evidence of the asymptotic behavior of the MCMC chains.

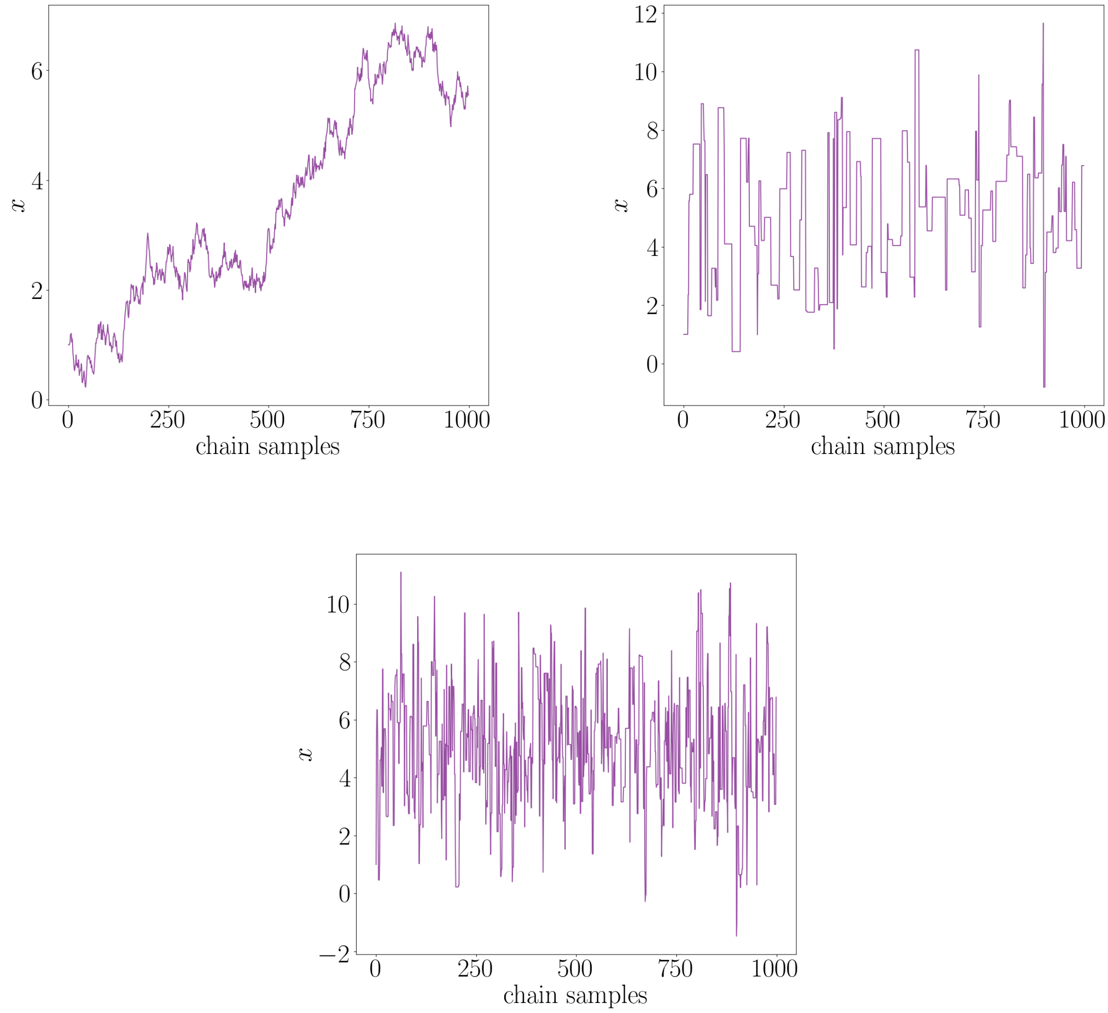

Figure 4.1: *Trace plots of a chain with small proposal covariance (upper left), large proposal covariance (upper right), and good proposal covariance (lower center).*

4.6 Bayesian hypothesis testing

The computation and exploration of Bayesian posterior distributions are aimed at calibrating parameters within the structure of a given model. It can also happen that our ignorance goes beyond the model parameters and can affect the model structure itself. A common problem in this scenario is how to quantify which model is the most suitable for explaining the experimental data or which hypotheses are not supported anymore.

In this thesis, this is particularly relevant given that some hypotheses have to be made about the physico-chemical nature of the reacting flows in the experiments in order to infer other relevant parameters. In some cases, the experimental conditions are well understood and the assumptions are backed by previous experiments and studies in the literature. Nevertheless, there are other conditions for which the thermal behavior of the flow, together with the structure of the wall boundary conditions are not so well understood. It is in these

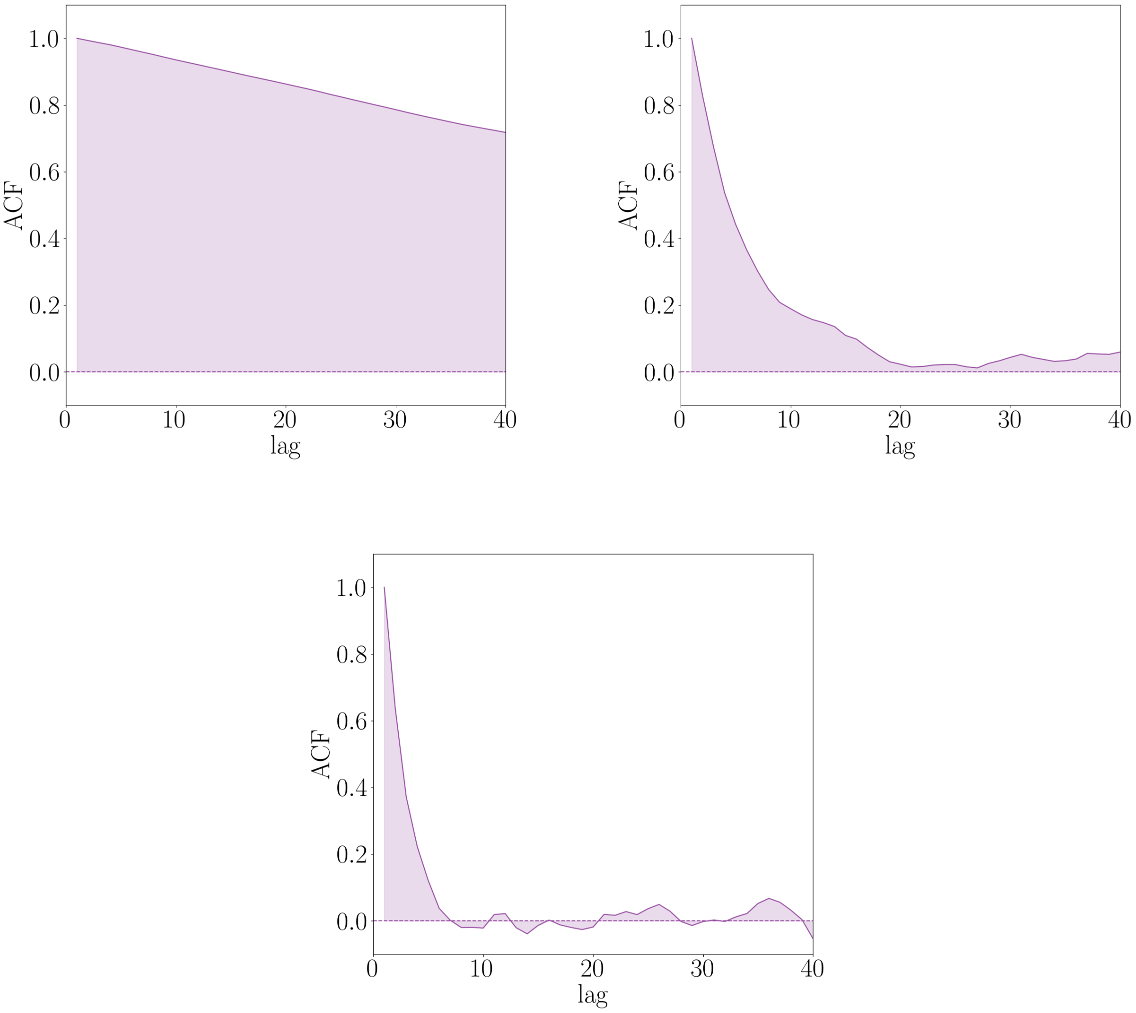

Figure 4.2: *Autocorrelation plots of a chain with small proposal covariance (upper left), large proposal covariance (upper right), and good proposal covariance (lower center).*

selected cases that we have to remain uncertain about our model choices and assess them against each other (Chapter 7).

In the previous sections we have discussed the computation or specification of the different ingredients of the Bayes' rule Eq. (4.4), except the normalization constant. We have shown that its computation is not necessary to achieve the objective of sampling from the posterior distribution for a given model. When different models are to be compared in their predictive capabilities, the normalization constant becomes central.

Performing a hypothesis testing study entails the evaluation of the posterior probabilities of each competing model (or hypothesis in our context). This comparison allows us to weigh the relative merit of each model. At first thought, we might consider the most suitable model to be the one that best fits the data. Difficulties quickly arise as we aim at comparing models of different complexity. More complex models involving the definition of more parameters can generally be more expressive and fit very well the data. In this

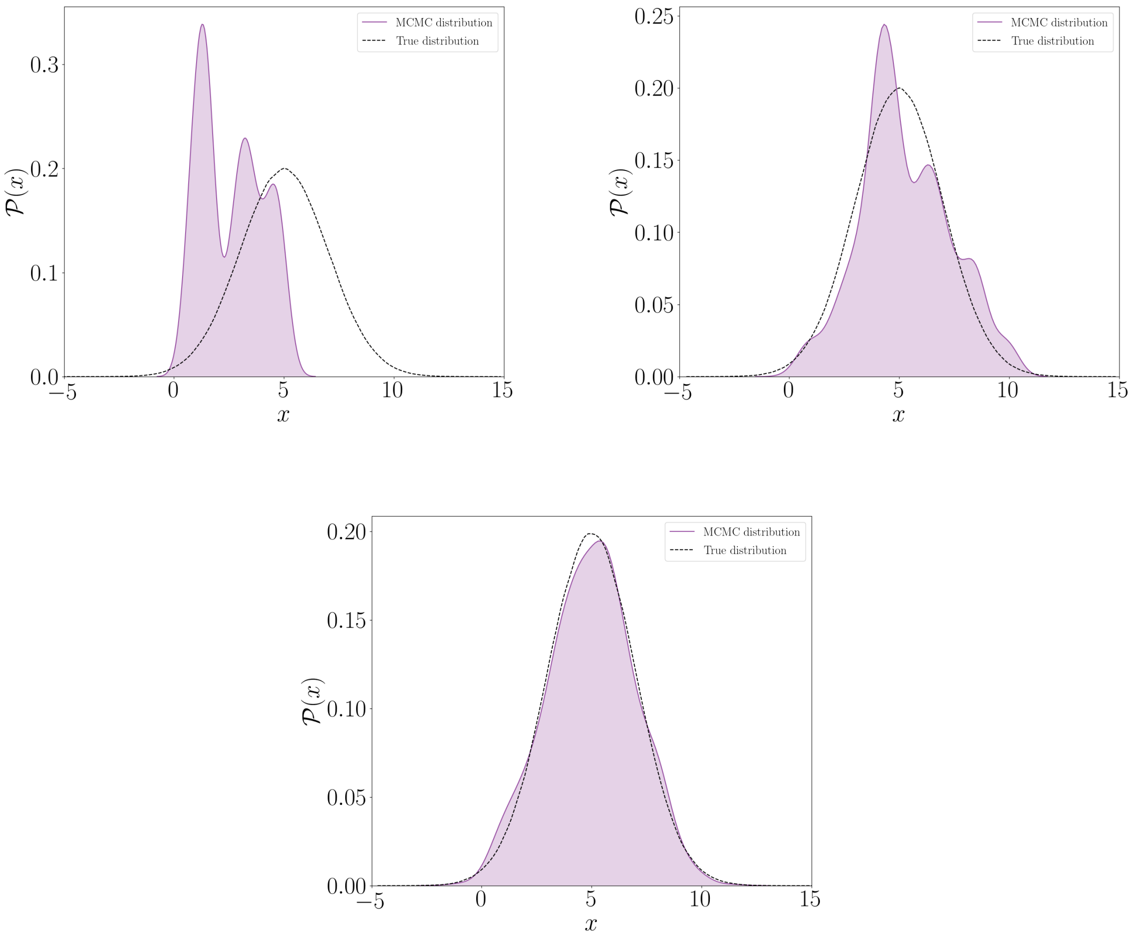

Figure 4.3: *Resulting probability distribution functions produced with a chain with small proposal covariance (upper left), large proposal covariance (upper right), and good proposal covariance (lower center) compared to the true underlying distribution we are trying to simulate.*

case, the results of hypothesis testing studies have the philosophical principle of *Ockham's razor* built in them. This principle embodies the fact that the simplest models that can explain comparatively well the data are the preferred ones.

As said, to perform such assessment we need to compare the posterior distributions for the different models. The comparison is driven through the posterior ratio

$$\frac{\mathcal{P}(\mathcal{M}_1|\boldsymbol{y}_{\text{obs}})}{\mathcal{P}(\mathcal{M}_0|\boldsymbol{y}_{\text{obs}})}, \tag{4.26}$$

where $\mathcal{M}_0$ and $\mathcal{M}_1$ are the two competing models we are considering. If the posterior ratio is very much less than one, we would prefer model $\mathcal{M}_0$ and viceversa. If the ratio is of order unity then the data do not provide enough evidence to preferentially support either model. To analyse the effects of the different components on the model posteriors and the ratio, we can decompose it according to the Bayes' rule

$$\frac{\mathcal{P}(\mathcal{M}_1|\boldsymbol{y}_{\text{obs}})}{\mathcal{P}(\mathcal{M}_0|\boldsymbol{y}_{\text{obs}})} = \frac{\mathcal{P}(\boldsymbol{y}_{\text{obs}}|\mathcal{M}_1)}{\mathcal{P}(\boldsymbol{y}_{\text{obs}}|\mathcal{M}_0)} \times \frac{\mathcal{P}(\mathcal{M}_1)}{\mathcal{P}(\mathcal{M}_0)}, \tag{4.27}$$

where the posterior ratio is expressed as the product of the ratio of the marginalized likelihoods and priors of the different models. The marginalized likelihoods of the different models can also be expressed as the marginalization over each model's parameters prior as

$$\mathcal{P}(\boldsymbol{y}_{\text{obs}}|\mathcal{M}_i) = \int_{\mathcal{X}} \mathcal{P}(\boldsymbol{y}_{\text{obs}}|\boldsymbol{x}_i, \mathcal{M}_i)\mathcal{P}(\boldsymbol{x}_i|\mathcal{M}_i)\mathrm{d}\boldsymbol{x}_i, \quad \forall i \in \{0, 1\}, \tag{4.28}$$

where $\boldsymbol{x}_i$ is the vector of model parameters of each model and $\mathcal{P}(\boldsymbol{x}_i|\mathcal{M}_i)$ is the prior for $\boldsymbol{x}_i$ under model $\mathcal{M}_i$. $\mathcal{P}(\boldsymbol{y}_{\text{obs}}|\mathcal{M}_i)$ is also known as the evidence of the data under model $\mathcal{M}_i$ and it is the factor in the Bayes' rule denominator which is often disregarded as a proportionality constant in parameter inference. The evidence ratio expresses the merit of each model based on two distinct aspects: how well the data is fitted, through the presence of the likelihood $\mathcal{P}(\boldsymbol{y}_{\text{obs}}|\boldsymbol{x}_i, \mathcal{M}_i)$, and how much prior space is given to each model $\mathcal{P}(\boldsymbol{x}_i|\mathcal{M}_i)$. Each evidence is the result of a likelihood average that decreases as the prior space increases, penalizing complex models. The ratio of the evidences is also known as the Bayes factor for $\mathcal{M}_1$ versus $\mathcal{M}_0$

$$BF_{10} = \frac{\mathcal{P}(\boldsymbol{y}_{\text{obs}}|\mathcal{M}_1)}{\mathcal{P}(\boldsymbol{y}_{\text{obs}}|\mathcal{M}_0)}. \tag{4.29}$$

It quantifies the change from prior to posterior model odds brought about by the observations $\boldsymbol{y}_{\text{obs}}$.

In general for this thesis, the prior odds are taken as unity, giving both models the same prior beliefs. The priors ratio can affect the results if we impose strong convictions about a model and the data are not enough to balance the posterior odds towards an objective estimation. In this case, one has to be careful not to bias the results with subjective beliefs. This issue is more widely treated in the relevant literature in which detailed analyses of the benefits and pitfalls of incorporating informative model prior distributions can be found in more detail [174].

4.7 Bayesian model selection and averaging

The comparison of posterior distributions under different models is instrumental to devise techniques that allow us to select among a pool of candidate models when model uncertainty is to be included in the analysis.

An important ingredient in the posteriors ratio introduced in Sec. 4.6 is the Bayes factor expressed as the ratio of the evidences for two different models given the observations. The Bayes factor quantifies the relative strength of the evidence in favor of a model versus the other. In this regard, it is straightforward to see that $BF_{10} = 7$ indicates that the data are 7 times more likely under $\mathcal{M}_1$ than under $\mathcal{M}_0$, whereas $BF_{10} = 0.2$ indicates that the observations are 5 times more likely under $\mathcal{M}_0$ than under $\mathcal{M}_1$.

Given the same prior odds for both models, this is a metric that allows us to quantify the overall best performing model. In general, Bayes factors are expressed in logarithmic scale

$$\log_{10} BF_{10} = \log_{10}\left(\mathcal{P}(\boldsymbol{y}_{\text{obs}}|\mathcal{M}_1)\right) - \log_{10}\left(\mathcal{P}(\boldsymbol{y}_{\text{obs}}|\mathcal{M}_0)\right), \tag{4.30}$$

for which typical thresholds for strong evidence in favor/against a given model are found in the literature by Jeffreys [175] and Kass and Raftery [176].

Apart from Bayes factors, other model selection criteria are commonly used in the literature. One criterion that closely approximates the Bayes factor is the Bayesian Information Criterion (BIC). Developed by Schwarz [177], the BIC serves as an asymptotic approximation to a transformation of the Bayesian posterior probability of a candidate model. The model corresponding to the minimum value of BIC is selected. Similarly, the Akaike Information Criterion (AIC) score rewards models that achieve a high goodness-of-fit score and penalizes them if they become overly complex [178]. The model with the lower AIC score is expected to strike a superior balance. A comprehensive overview of AIC and other popular model selection methods is given by Ding et al. [179].

In this thesis, we focus on computing Bayes factors as the metric used to discard different thermochemical models and ablation boundary conditions (Chapter 7). An issue that arises is the fact that Bayes factor thresholds are not very sharp and there can be a grey area where the prior spaces for both models are comparable as well as their goodness-of-fit ratio. There can also be a trade-off between prior space, or complexity, and goodness-of-fit in such a way that the Bayes factor falls in the grey area. This would indicate that the more complex model manages to overcome the complexity penalization by fitting the data much better than the simpler model. In this case, discarding a given model is not possible on the basis of the data and prior information we possess.

Already Chamberlin [180] advocated the concept of "multiple working hypotheses", implying that there is not a single "right" model; instead, there are several well-supported models that are being entertained. If new experiments are well-designed to maximize their informational content, the results tend to support one or more models while providing less support for others. Repetition of this general approach leads to advances, combining experimental design with comparison of theoretical models. New or more elaborate models are consequently postulated, while models with little empirical support are gradually dropped from consideration.

Acknowledging this fact means incorporating model uncertainty stemming from the existence of more than one plausible model. Given these conditions, we may forego selection, retaining the uncertainty across the model space. In this thesis, we focus on Bayesian Model Averaging (BMA) [174]. The model averaged posterior density for the common model parameters $\boldsymbol{x}_j$ shared between $\mathcal{M}_0$ and $\mathcal{M}_1$ is sought out and reads

$$\mathcal{P}(\boldsymbol{x}_j|\boldsymbol{y}_{\text{obs}}) = \sum_{i\in\{0,1\}} \mathcal{P}(\boldsymbol{x}_j|\boldsymbol{y}_{\text{obs}}, \mathcal{M}_i)\mathcal{P}(\mathcal{M}_i|\boldsymbol{y}_{\text{obs}}). \tag{4.31}$$

Here, the posteriors of $\boldsymbol{x}_j$ under each model are weighted according to their model posteriors. If the prior odds is unity, the differential weighting is due to the differences in the evidences of each model. Fig. 4.4 illustrates a practical example involving the weighted average of two Gaussian posteriors for the common parameter x_0 where the evidences for models $\mathcal{M}_0$ and $\mathcal{M}_1$ change while the prior odds remain as unity.

BMA is important for expressing model uncertainty in a consistent way, thus, avoiding over-confident inferences. Introduced by Roberts [181], who for the first time combined two expert opinions in the statistical literature, BMA has a challenging implementation due to the complex probability distributions it deals with and their integrations. Moreover, assigning prior distributions to each specified model can be a source of caveats when the choice is not obvious.

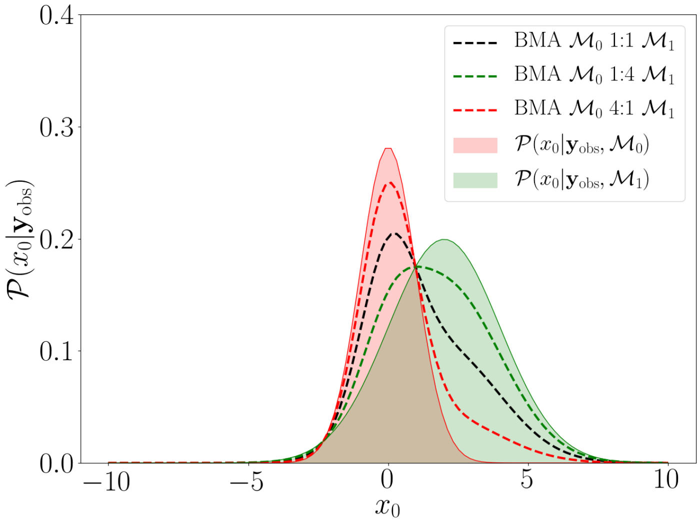

Figure 4.4: *Bayesian model averaging of two Gaussian posterior distributions with different evidence weighting.*

4.8 Making it more efficient

In general, Monte Carlo-based methods, such as MCMC, need a thorough exploration of the distributions to have good statistical convergence. A good exploration of the posterior distribution can, therefore, be very expensive in terms of model evaluations. If those model evaluations are a system of non-linear tightly coupled PDEs with expensive closure models, then MCMC methods can be rendered unfeasible for such task. Nevertheless, there are different ways of aiding MCMC methods attain efficiency for complex models. A straightforward way is by constructing surrogate models to replace the expensive cost of the evaluations [182, 183]. A good surrogate model should be constructed on a limited number of model evaluations and should accurately emulate the underlying model. Generalized regressions are standard surrogate modeling constructions that minimize the squared error between a linear combination of a given functional basis and the true model at selected training points. Examples of functional bases are polynomials and radial basis functions [184, 185]. For high dimensional cases, sparse methods such as lasso or ridge regression allow reducing the number of coefficients by using regularization techniques [186]. Alternatively, neural networks [187] are also gaining interest from the UQ community. Non-parametric approaches such as kriging, also called Gaussian Processes (GP) [188] have become popular for uncertainty quantification problems. In general, selecting a good surrogate model is strongly linked to our knowledge of the shape of the underlying function we are aiming to approximate.

One of the challenges associated with accurately approximating complex models is the fact that a priori we might not be sure about the degree of smoothness of the model outputs with respect to changes in the input quantities. Such is the case when chemical parameters, such as those describing wall catalysis and ablation, are to be included in the surrogate as free varying parameters with wide ranges of values. In this work, we choose Gaussian processes given the possibility of using kernels of varying degree of smoothness and generalization, together with the fact that we only need approximations for low dimensional functions. Overall they present attractive characteristics for our problems.

In the particular case of this thesis, not only do we deal with likelihood functions that are expensive to evaluate but also the experimental procedures consist of multiple steps (Sec. 3.2) which, in turn, require multiple model evaluations for a single likelihood point, adding to the complexity in detriment of the performance of sample-based posterior exploration methods. We are then interested in cutting down the number of different simulations needed to recover gas-surface interaction information from multi-step experiments. In this case, we can benefit from performing sensitivity analyses to assess how important the free parameters in our models are to the variability of the different experimental observations that we are trying to recover. If certain boundary conditions do not play important roles, we do not need to spend model evaluations simulating an additional experimental step exclusively devoted to the determination of such boundary conditions. This is the case for the boundary layer edge temperature in the nitridation experiments (Chapter 7). There, separate measurements on a copper probe are included as part of the experimental dataset to infer the edge temperature of the experiments. If, for example, the edge temperature does not influence recession rates, from which we learn nitridation reaction efficiencies, we do not need to evaluate the model and add to the likelihood function the observation made with the copper probe. The edge temperature can be assumed fixed to a certain value as it does not influence the results of the inverse problem.

Overall, the combination of surrogate modeling and sensitivity analysis of the forward model represent good techniques for making the process of solving the inverse problem more efficient without the need to trade accuracy in the process. The following sections Secs. 4.8.1-4.8.2 introduce Gaussian processes and global sensitivity analysis in detail.

4.8.1 Surrogate modeling: Gaussian process

Gaussian process models have been widely used in uncertainty propagation, sensitivity analysis, optimization and inverse problems [189]. Gaussian processes define distributions over functions. In this sense, a GP can be thought of a function that takes a certain input $\boldsymbol{x}$ to produce as output a realization of a Gaussian distribution with mean μ and variance σ^2. The interesting part is that due to their statistical nature, GPs provide a measure of the uncertainty in the prediction, unlike other traditional deterministic regression methods. This is very useful for informing the approximation on where more points or information is needed such that different learning strategies can be devised. Adopting the notation used by Rasmussen [188] a function described by a GP can be written as

$$f \sim \mathcal{GP}(m(\boldsymbol{x}), C(\boldsymbol{x}, \boldsymbol{x}')), \tag{4.32}$$

where $C(\boldsymbol{x}, \boldsymbol{x}')$ is the covariance function and $m(\boldsymbol{x})$ is the mean function of the GP. Different parametrizations can be used to describe the mean and covariance functions, in particular, different kernels are generally chosen for the parametrization of the covariance function. The choice of kernel and the ensemble of hyperparameters are set a priori by taking into account any information we have about the function to approximate. Useful information is the expected smoothness as this is associated with the correlation length parameter of the kernel. Overall, kernels encode assumptions we have about the function being learned by defining the *similarity* between two points. We can distinguish two categories of kernels: stationary and non-stationary. Stationary kernels only depend on the absolute distance between points, making them invariant to translations in the input space. Non-stationary kernels, on the other hand, depend on the particular values of the points. Further, stationary kernels can be isotropic or anisotropic depending on whether they are invariant to rotations in the input space or not. In this thesis, we choose stationary isotropic kernels of smooth shape as we aim at approximating physical quantities which do not change abruptly within the continuum input space explored. Particularly, we study two different choices of kernels: zero-mean squared-exponential kernel and kernels of the Matérn class [188]

$$C_{\mathrm{SE}}(\boldsymbol{x},\boldsymbol{x}') = \sigma_{\mathrm{GP}}^2 \exp\left(-\frac{1}{2l^2}(\boldsymbol{x}-\boldsymbol{x}')^{\mathrm{T}}(\boldsymbol{x}-\boldsymbol{x}')\right), \tag{4.33}$$

$$C_{\mathrm{M}}(\boldsymbol{x},\boldsymbol{x}') = \sigma_{\mathrm{GP}}^2 \frac{1}{\Gamma(\nu)2^{\nu-1}} \left(\frac{\sqrt{2\nu}}{l}(\boldsymbol{x}-\boldsymbol{x}')^{\mathrm{T}}(\boldsymbol{x}-\boldsymbol{x}')\right)^{\nu} K_\nu \left(\frac{\sqrt{2\nu}}{l}(\boldsymbol{x}-\boldsymbol{x}')^{\mathrm{T}}(\boldsymbol{x}-\boldsymbol{x}')\right), \tag{4.34}$$

where $C_{\mathrm{SE}}(\cdot)$ is the squared-exponential kernel and $C_{\mathrm{M}}(\cdot)$ is the Matérn kernel. The squared-exponential kernel is an infinitely smooth kernel and so is the GP constructed with it. The parameters σ_{GP}, l are positive hyperparameters a priori unknown to be learned from the training data.

The Matérn class of kernels represents intermediately smooth functions with $\sigma_{\mathrm{GP}}, l, \nu$ positive hyperparameters while $K_\nu(\cdot)$ is a modified Bessel function and $\Gamma(\cdot)$ is the gamma function. The regularity of the kernel is related to the ν parameter. Through this parameter the Matérn kernel is a generalized squared-exponential kernel with the former converging to the latter when $\nu \to \infty$. Usually half integer values of ν are selected since the kernel becomes a product of a polynomial and an exponential. The Matérn kernel is initially proposed to account for possible intermediate smoothness in the approximations of the optimal likelihood function (Chapter 5) given the nature of the distance between different optimized solutions. The following Fig. 4.5 shows the type of functions derived from squared-exponential and Matérn kernels in untrained GPs.

Posterior GP. Once the kernel and hyperparameters are specified, we can use the posterior GP to make predictions conditioned on observations or data. We can retrieve the resulting Gaussian distributions for any new input point $\boldsymbol{x}^*$ as the function evaluation $f^*(\boldsymbol{x}^*)$ conditional on the training points $\boldsymbol{y} = (f(\boldsymbol{x}_1), ..., f(\boldsymbol{x}_n))$ such as

$$f^*|\boldsymbol{y} \sim \mathcal{N}\left(\boldsymbol{k}(\boldsymbol{x}^*)^{\mathrm{T}}\boldsymbol{K}^{-1}\boldsymbol{y}, C(\boldsymbol{x}^*,\boldsymbol{x}^*) - \boldsymbol{k}(\boldsymbol{x}^*)^{\mathrm{T}}K^{-1}\boldsymbol{k}(\boldsymbol{x}^*)\right), \tag{4.35}$$

where $C(\boldsymbol{x}^*,\boldsymbol{x}^*)$ is the specified kernel, $\boldsymbol{k}(\boldsymbol{x}^*) = (C(\boldsymbol{x}^*,\boldsymbol{x}_1), ..., C(\boldsymbol{x}^*,\boldsymbol{x}_n))$ and $K_{i,j} = C(\boldsymbol{x}_i,\boldsymbol{x}_j) + \sigma_{\mathrm{e}}\delta_{i,j}$ with $\delta_{i,j}$ being the Kronecker symbol and σ_{e} the error on the estimation of $\boldsymbol{y}$. From this we can easily identify the new mean and covariance of any new prediction $f(\boldsymbol{x}^*)$ at an unseen point $\boldsymbol{x}^*$

$$\mu(\boldsymbol{x}^*) = \boldsymbol{k}^{\mathrm{T}}(\boldsymbol{x}^*)\boldsymbol{K}^{-1}\boldsymbol{y}, \tag{4.36}$$

$$\sigma^2(\boldsymbol{x}^*) = C(\boldsymbol{x}^*,\boldsymbol{x}^*) - \boldsymbol{k}^{\mathrm{T}}(\boldsymbol{x}^*)\boldsymbol{K}^{-1}\boldsymbol{k}(\boldsymbol{x}^*). \tag{4.37}$$

As $\sigma_{\mathrm{e}} \to 0$ the variance σ^2 on the training points vanishes. This hyperparameter is usually

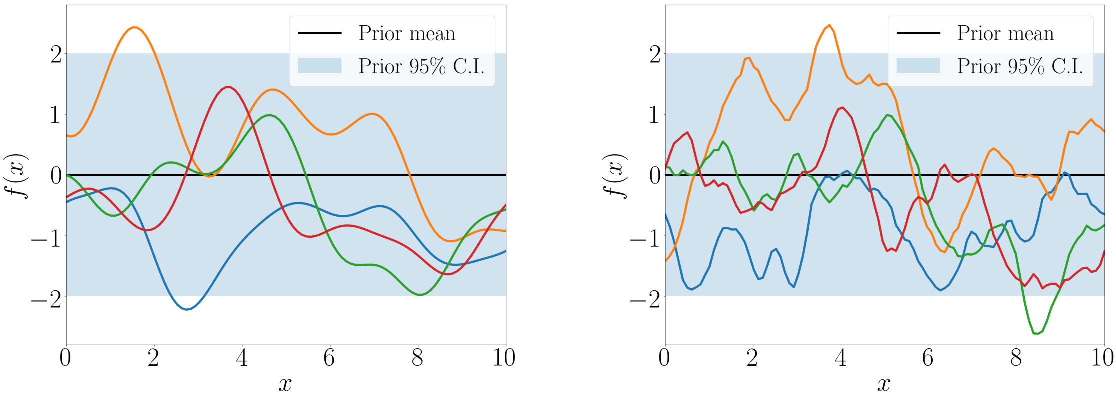

Figure 4.5: *Functions drawn from GPs with squared-exponential kernel (left) with* $l = 1$*, and Matérn kernel (right) with* $l = 1$ *and* $\nu = 3/2$*. The variance of the processes is* $\sigma_{\text{GP}} = 1$ *for both.*

included when the training points consist of noisy observations, being σ_{e} the level of noise. In our case, the parameter σ_{e} is set to a small but non-zero value to ensure that the matrix $\boldsymbol{K}$ is invertible.

Training a GP. A kernel and its hyperparameters chosen a priori are not likely to represent accurately our real function. Constructing a trained GP, where the hyperparameters are tuned to fit the training data best according to some metric, requires executing an optimization exercise. The prior set of kernel hyperparameters, in light of the observations or training points, is updated through a likelihood function

$$L = \log(\mathcal{P}(\boldsymbol{y}|\boldsymbol{x}, \boldsymbol{\lambda})) = -\frac{1}{2}\log|\boldsymbol{K}| - \frac{1}{2}(\boldsymbol{y} - \boldsymbol{\mu})^{\text{T}}\boldsymbol{K}^{-1}(\boldsymbol{y} - \boldsymbol{\mu}) - \frac{n}{2}\log(2\pi), \tag{4.38}$$

where $\boldsymbol{K}$ and $\boldsymbol{\mu} = (\mu(x_1), ..., \mu(x_n))$ are dependent on the set of points $\boldsymbol{x} = (\boldsymbol{x}_1, ..., \boldsymbol{x}_n)$. Eq. (4.38) represents the log-likelihood function of a set of observations $\boldsymbol{y}$ for given $\boldsymbol{x}$ and hyperparameters $\boldsymbol{\lambda} = (\lambda_1, ..., \lambda_p)$, where p is the number of hyperparameters of the chosen kernel. L is also known as the log marginal likelihood [190] and the hyperparameters chosen are the ones that maximize this quantity. Fig. 4.6 shows different stages of the training of a GP to approximate the benchmark function $f(x) = x\sin(x)$. Starting with the prior mean and 95% confidence interval bounds, the hyperparameters get updated by optimizing the log marginal likelihood with increasing number of training points. The increase of training points generates a more accurate posterior GP.

Different strategies can be adopted as Design of Experiments (DoE) for GP regression [191]. In this work, we employ what it is known as model-free DoE which does not rely on model evaluations as an active learning strategy would require [192]. Model-free DoEs are concerned with optimizing the exploration of the input space with a finite set of points. In this case, we build a uniform grid for the optimal log-likelihood approximation (Chapter 5) and use a Latin Hypercube Sampling (LHS) algorithm, introduced by McKay et al. [193], for the problems of ablation (Chapter 7). The LHS sampling algorithm presents the advan-

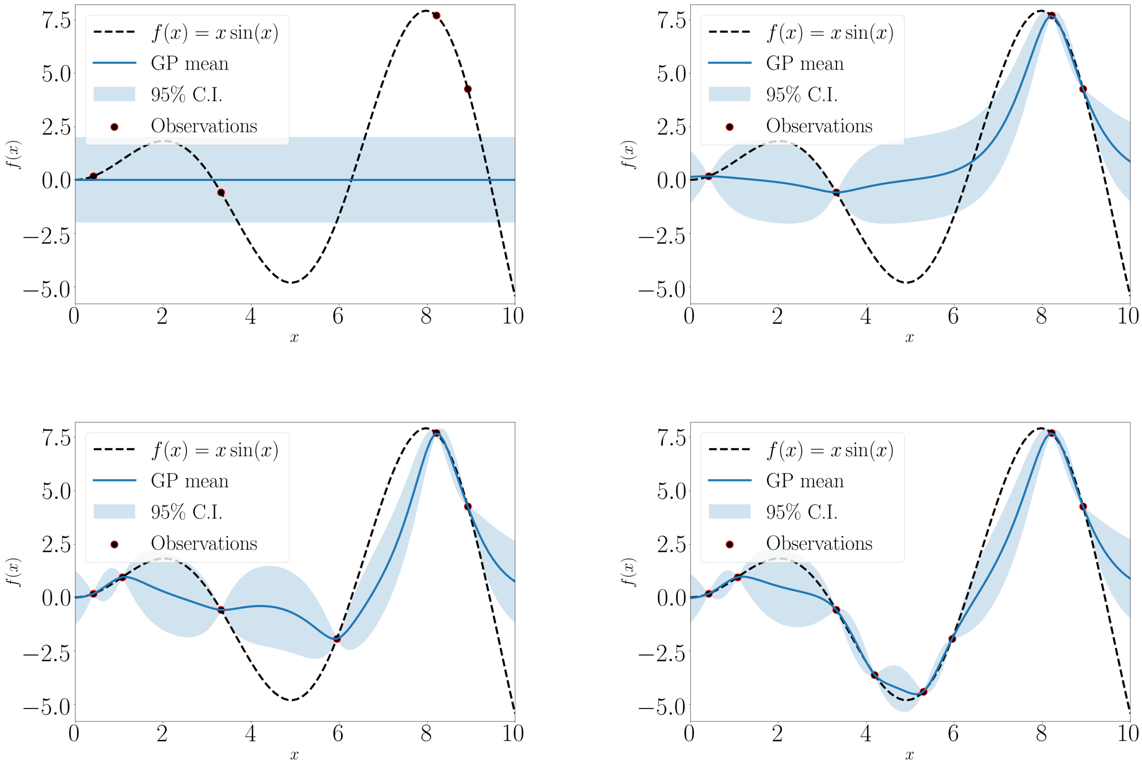

Figure 4.6: *Training a GP with increasing number of data points.*

tage of allowing us to survey the input space by devising a space filling strategy adapted to the inputs probability distributions. This strategy consists of dividing the range of each variable into n equally probable intervals in which sampling is performed at random in our case.

4.8.2 Global sensitivity analysis

In contrast with deterministic approaches, stochastic formulations of inference problems have the capability of relaxing assumptions to represent our true state of knowledge. However, this advantage comes with a drawback: the dimensionality of the problem escalates as parameters are now considered uncertain. Sensitivity analysis comes in handy when we want to study the dependencies of our model and discard possible irrelevant quantities to the variability of the solution. We recall that in this thesis, global sensitivity analysis is used to reduce the number of observations needed for the inference of nitridation rates, given that the simulation of such observations is an expensive task. If the observations we question do not contain information about the parameter to be inferred, we can disregard them, simplifying the problem greatly as well as the experimental procedure. In a way, performing sensitivity analyses is getting to know your model and its most important sources of information. As Fürbringer put it rhetorically in 1996 while highlighting the need to look into the model black box: *"Sensitivity Analysis for Modelers: Would you go to an orthopedist who did not use X-Ray?"*.

The literature behind sensitivity analysis took off with the so-called local analyses. These are deterministic methods which estimate the impact of each input variable on the model output as the effects of small deviations from the chosen input values through the computation of partial derivatives. To overcome some of their limitations such as locality, linearity and normality assumptions, global sensitivity analyses were brought forth. They can take into account the whole domain of input variables and their interactions in a statistical framework, without relying on partial derivatives on specified nominal points. Different techniques for global sensitivity analysis were developed and are in use today. Iooss et al. [194] and Borgonovo et al. [195] give complete and comprehensive reviews on local and global sensitivity analysis methods ranging from screening methods [196], where one can identify non-influential inputs with a small number of model calls, to moment-independent methods. The latter assesses the changes in the full output distributions with respect to the variability of the inputs by computation of some chosen metric [197, 198]. In between these two extremes, we focus on variance-based sensitivity methods [199]. This group of methods can assess the importance of the various inputs on the variability of the output through their contribution to the total output variance. Their advantage and usefulness for this work reside on the fact that they can be used to analyze non-linear and non-monotonic functions along with a measure of the importance of interactions between inputs. The latter point is used to have a full picture of the influence of a given input on the desired output. The sensitivity indices computed along these lines are the Sobol' indices [200]. Sobol' defined a product measure which entails independence among model inputs. These sensitivity indices are based on a functional decomposition of the output with respect to its variance called ANOVA (Analysis Of Variances) decomposition [200]. Computing Sobol' indices comes down to performing high dimensional integrals, which can be tackled by using simple Monte Carlo or Quasi Monte Carlo methods [200]. In this context, surrogate models become important for such a task when the full model we are trying to analyze has expensive evaluations. This option is proposed in this work to tackle the problem of performing global sensitivity analysis through the computation of Sobol' indices with Monte Carlo estimators.

It is important to underline the fact that ranking parameters by using the output variance as metric is an approximation that holds well for symmetric outputs for which higher order statistics, such as skewness and kurtosis, are not needed for their description and analysis. Other methods that mimic the ANOVA decomposition while taking into account higher order statistics can be found in the literature [201]. In the remainder part of this section, we introduce the variance decomposition and computation of sensitivity indices in detail.

Variance decomposition. The model of interest can be expressed as a function $f(\boldsymbol{x})$ whose input $\boldsymbol{x} = (x_1, ..., x_n)$ is a vector in n-dimensional space and whose output is a scalar y. For practical purposes, the n-dimensional space can be considered canonical where all components of the input $\boldsymbol{x} \in [0, 1]$. This leads to the designation of the unit hypercube I^n as the input space to explore for the global sensitivity analysis. It is also important to link the inputs $\boldsymbol{x}$ to the random vector $\boldsymbol{X} = \{x_1, ..., x_n\}$ with a joint probability density function (PDF) $\mathcal{P}(\boldsymbol{x})$ defined in the probability space $(\mathbb{R}^n, \mathcal{B}_n, \mathcal{P})$ where $\mathcal{B}_n$ is the n-dimensional Borel space of all σ-algebras with distributions $\mathcal{P}$. The assumption of uncorrelated input variables allows to express $\mathcal{P}(\boldsymbol{x}) = \prod_{i=1}^{n} \mathcal{P}(x_i)$, where $\mathcal{P}(x_i)$ is the marginal PDF of x_i.

We can represent $f(\boldsymbol{x})$ in I^n in the following form

$$\begin{aligned}f(\boldsymbol{x}) = f_0 + \sum_{s=1}^{n} \sum_{i_1<\cdots<i_s}^{n} f_{i_1\cdots i_s}(x_{i_1},\cdots,x_{i_s}) = \\ = f_0 + \sum_{i=1}^{n} f_i(x_i) + \sum_{1\leq i<j\leq n}^{n} f_{ij}(x_i,x_j) + \cdots + f_{1,\dots,n}(x_1,\dots,x_n).\end{aligned} \tag{4.39}$$

Eq. (4.39) is known as the ANOVA decomposition and was first introduced by Sobol' [199, 200] when the following condition holds

$$\int_0^1 f_{i_1\cdots i_s}(x_{i_1},\dots,x_{i_s})\mathcal{P}(x_{i_1},\dots,x_{i_s})\mathrm{d}x_k = 0, \quad \text{for } k = i_1,\dots,i_s. \tag{4.40}$$

The condition expressed in Eq. (4.40) implies that all of the terms in the ANOVA decomposition are orthogonal and that the expectation of $f(\boldsymbol{x})$ is f_0. The original model $f(\boldsymbol{x})$ is decomposed into orthogonal lower-dimensional sub-models.

To be able to link this formulation to the sought out analysis of variances, we need to impose that $f(\boldsymbol{x})$ is square integrable, leading to square integrable sub-functions $f_{i_1\cdots i_s}$. Squaring Eq. (4.39) and integrating over the unit hypercube I^n we get the following expression

$$\int_0^1 f^2(\boldsymbol{x})\mathcal{P}(\boldsymbol{x})\mathrm{d}\boldsymbol{x} - f_0^2 = \sum_{s=1}^{n} \sum_{i_1<\cdots<i_s}^{n} \int_0^1 f_{i_1\cdots i_s}^2 \mathcal{P}(x_{i_1},\dots,x_{i_s})\mathrm{d}x_{i_1}\cdots\mathrm{d}x_{i_s}, \tag{4.41}$$

through which we can define the conditional variances for each component of the function

$$D_{i_1\cdots i_s} = \mathbb{V}[f_{i_1\cdots i_s}] = \int_0^1 f_{i_1\cdots i_s}^2 \mathcal{P}(x_{i_1},\dots,x_{i_s})\mathrm{d}x_{i_1}\cdots\mathrm{d}x_{i_s}, \tag{4.42}$$

where $\mathcal{P}(x_{i_1},\dots,x_{i_s})$ is the joint PDF of the set of variables $x_{i_1},\dots,x_{i_s}$. From Eq. (4.42) follows the relation

$$D = \sum_{s=1}^{n} \sum_{i_1<\cdots<i_s}^{n} D_{i_1\cdots i_s}, \tag{4.43}$$

which states that the total variance can be decomposed into the different conditional variances of every function of the corresponding ANOVA decomposition.

Computation of Sobol' indices. Building on the variance decomposition, Sobol' [199] defined a set of indices that can be used to quantify the sensitivity of the output to the different inputs for non-linear functions with uncorrelated inputs. The indices are defined through the ratios

$$S_{i_1\cdots i_s} = \frac{D_{i_1\cdots i_s}}{D}, \tag{4.44}$$

which express the contribution to the total variance D of $f(\boldsymbol{x})$ of the different conditional variances $D_{i_1\cdots i_s}$ with the subscript s defining the order of such interaction. All the indices $S_{i_1\cdots i_s}$ are non-negative and comply with

$$\sum_{s=1}^{n}\sum_{i_1<\cdots<i_s}^{n} S_{i_1\cdots i_s} = 1. \tag{4.45}$$

From these definitions is straightforward to see that the indices accounting for the contribution of only one variable S_{i_1} are first order indices. Indices of higher order quantify the variability of the output due to the interactions among different inputs.

Another useful index is the total Sobol index which accounts for a given input's global effect on the variability of the output. It is a combination of first order plus higher order indices involving a given input

$$S_{\mathrm{T}_i} = \sum_{\boldsymbol{s}_j \ni i} S_{\boldsymbol{s}_j}, \tag{4.46}$$

where $\boldsymbol{s}_j$ denotes a multi-index associated with the $i_1, ..., i_s$ input indices. In words, the total order indices are the result of a sum over all possible distinct sets of first and higher order indices which include the input for which the total index is computed. First and total indices are used together to assess the impact of a given input on the variability of the solution. If the first order index is large enough, the input is influential in itself. If both first and total order indices are negligible, such input can be ignored by fixing it to a prescribed value in our subsequent computations. If first order and total order are similar, the input affects the output mainly through direct interactions. If all the inputs have similar first and total order indices, then the model can be said to be additive.

In practicality, computing Sobol' indices amount to solving high dimensional integrals. This can be tackled by means of Monte Carlo methods. In this work, we opt to solve for Quasi Monte Carlo estimators to approximate such integrals. We can define two different subsets of inputs ξ and η. The variance due to the subset ξ, D_ξ, and related interactions is expressed as

$$D_\xi = \int_0^1 f(\boldsymbol{x}) f(\xi, \eta') \mathrm{d}\boldsymbol{x} \mathrm{d}\eta' - f_0^2, \tag{4.47}$$

Similarly, we can define a conditional variance for the subset η, D_η, as

$$D_\eta = \int_0^1 f(\boldsymbol{x}) f(\xi', \eta) \mathrm{d}\boldsymbol{x} \mathrm{d}\xi' - f_0^2, \tag{4.48}$$

thus for obtaining S_ξ and $S_{\mathrm{T}_\xi} = 1 - S_\eta$ one has to compute four integrals for the expectation of $f(\boldsymbol{x})$, the variance and the conditional variances for the two distinct input subsets ξ and η

$$\begin{aligned} f_0 &= \int_0^1 f(\boldsymbol{x}) \mathcal{P}(\boldsymbol{x}) \mathrm{d}\boldsymbol{x},\ D + f_0^2 = \int_0^1 f^2(\boldsymbol{x}) \mathcal{P}(\boldsymbol{x}) \mathrm{d}\boldsymbol{x}, \\ D_\xi + f_0^2 &= \int_0^1 f(\boldsymbol{x}) f(\xi, \eta') \mathcal{P}(\boldsymbol{x}) \mathcal{P}(\eta') \mathrm{d}\boldsymbol{x} \mathrm{d}\eta', \\ D_\eta + f_0^2 &= \int_0^1 f(\boldsymbol{x}) f(\xi', \eta) \mathcal{P}(\boldsymbol{x}) \mathcal{P}(\xi') \mathrm{d}\boldsymbol{x} \mathrm{d}\xi', \end{aligned} \tag{4.49}$$

where $\mathcal{P}(\eta')$ and $\mathcal{P}(\xi')$ are the marginal PDFs for the ξ and η subsets. We can then defined the Monte Carlo estimators for such integrals

$$\begin{aligned}
&\frac{1}{N}\sum_{i=1}^{N} f(\boldsymbol{x}_i) \xrightarrow{\mathcal{P}} f_0, \quad \frac{1}{N}\sum_{i=1}^{N} f^2(\boldsymbol{x}_i) \xrightarrow{\mathcal{P}} D + f_0, \\
&\frac{1}{N}\sum_{i=1}^{N} f(\boldsymbol{x}_i) f(\xi_i, \eta_i') \xrightarrow{\mathcal{P}} D_\xi + f_0^2, \quad \frac{1}{N}\sum_{i=1}^{N} f(\boldsymbol{x}_i) f(\xi_i', \eta_i) \xrightarrow{\mathcal{P}} D_\eta + f_0^2,
\end{aligned} \tag{4.50}$$

with N the number of points used for the estimation, (ξ, η) and (ξ', η') two independent sets of points randomly sampled from the joint distribution of the inputs $\mathcal{P}(\boldsymbol{x})$. The Monte Carlo estimators for S_ξ and S_{T_ξ} require three model evaluations for each point $f(\boldsymbol{x}), f(\xi', \eta)$ and $f(\xi, \eta')$ which can be very expensive if we want to achieve high accuracy. In this work, each model evaluation consists on solving a set of tightly coupled PDEs and a range of auxiliary problems to obtain the closure data for the physico-chemical models. Therefore, performing a sensitivity analysis via Monte Carlo estimators translates into a very expensive task. A way of increasing the efficiency while still keeping the general Monte Carlo approach is by using surrogate models.

The use of surrogate models for sensitivity analysis is not new and can be found in numerous works in the literature. From Iooss et al. [202] who used a response surface function to approximate the real model to Marseguerra et al. [203] who relied on neural networks, passing by Marrel et al. [204] with Gaussian process surrogates.

4.9 Summary

This chapter introduces the fundamentals of statistical inverse analysis by means of Bayesian methods. The different constitutive steps of comprehensive Bayesian inference analyses are reviewed in light of the needs addressed in this thesis.

First, the formulation of general stochastic inverse problems is introduced, highlighting the fundamental differences with deterministic approaches. The introduction of statistical distributions to characterize variables leads to a whole new problem that must be solved to retrieve uncertain model parameters in a consistent manner when accounting for different sources of information. Given that we want to incorporate any a priori information we have about the model parameters to be inferred, the statistical inverse problem is formulated using the Bayesian formalism.

Generally, Bayesian inference problems can be broken down into three distinct tasks and each of them poses challenges unfaced when dealing with deterministic inverse problems. We introduce the construction of the likelihood function and how the noise of the observations is incorporated into the problem to encode the information coming from the experimental data. The other source of information in Bayesian inference is the one coming from any prior source that has not seen the data. In this chapter, we tackle the issue of encoding objective prior information, particularly when this information is related to bounds or scale of the parameters involved in the inference. The final task consists of thoroughly exploring the posterior distribution to be able to derive useful estimators and other relevant quantities.

Regarding the exploration of the Bayesian posterior, we introduce the Markov chain stochastic model as a way of sampling complex distributions. This is achieved by building the chain whose stationary distribution is the sought out posterior. Markov chains with certain properties are guaranteed to have a stationary distribution from which sampling is equivalent to sampling from a transition function an infinite number of times. In order to build a chain with such properties, a detailed balance equation involving the stationary distribution and transition function must be satisfied.

Different Markov chain Monte Carlo algorithms relevant to this work are also introduced. They concern the practical implementation of building a Markov chain with the sought properties. The built chain generates samples from the posterior distribution. To monitor convergence and properties of the chain as it is being built, some diagnostics methods are also discussed with emphasis on trace plots and acceptance rates.

Very often, the lack of knowledge in inverse problems can also affect the model used to infer its parameters. When the model structure is also considered uncertain among different choices, we are dealing with a model selection problem. Model selection problems are rooted on Bayesian inference as they evaluate different posterior distributions in light of some available experimental data. Given the nature of the flow equations and their tight coupling, the choosing of different closure models or boundary conditions can have an impact on the model parameters we want to infer. It is for this reason that we must remain uncertain regarding different model structures available to explain our experimental data.

Two different methods relevant to the choosing of competing models are introduced. Hypothesis testing represents a way of using the model posterior information to select or, alternatively, leave out the model (or hypothesis) for which the data offer very small evidence. In computing the evidence of the different models, the complexity inherent to each model is also weighted in, giving an indication of the overall performance of fitting the data and being a complex model. Given that the threshold for such task is quite diffused, it often happens that the data are not enough to discard any given model. For this case, we present the topic of Bayesian model averaging where the posteriors retrieved by the different models are weighted by the model posterior as computed for hypothesis testing. In doing so, we can express model uncertainty in a consistent way, avoiding over-confident inferences.

Finally, we also introduce two different methods to lighten the burden of performing a Bayesian inference analysis with expensive model evaluations. Surrogate models in the form of Gaussian processes are introduced. GPs are used throughout this work to build approximations of the different model outputs and likelihood functions. On the other hand, global sensitivity analysis is also discussed as it helps to reduce the complexity of the inferences by reducing the number of observations needed. This is important as each observation in this thesis is associated with different models that should be run independently, therefore making the process more time consuming.

Chapter 5

Bayesian framework for the inference of catalytic recombination

This chapter deals with the inference of catalytic recombination parameters from plasma wind tunnel experiments for reusable thermal protection materials. The main objective of this chapter is to develop a dedicated Bayesian framework that allows us to infer catalytic parameter values. The developed framework accounts for uncertainties involved in the model definition and incorporates all measured variables with their respective uncertainties. Furthermore, we propose an optimization procedure built on the construction of the likelihood function to improve the quality of the inference. We substitute the optimal likelihood of the experimental measurements with a surrogate model to make the inference procedure both faster and more robust.

5.1 Motivation and problem definition

The interaction between a dissociated plasma flow and a reusable thermal protection system is governed by the material behavior which acts as a catalyst for recombination reactions of the atomic species in the surrounding gas mixture [205]. The determination of the catalytic properties of thermal protection materials is a complex task subjected to experimental and model uncertainties, and the design and performance of reusable atmospheric entry vehicles must account for these uncertain characterizations.

Not only catalytic recombination is relevant for the design of re-usable systems but also its inference is important for the production of high-quality wind tunnel data. As the number of model parameters that need definition increases with complexity (as seen in Chapter 2), the experimental data are too often pretty scarce for proper validation studies. Assuming values for model parameters becomes a common exercise when simulating experimental conditions against which to compare our models, potentially biasing the obtained results with partial understanding of the problem. Producing specifically tailored calibration data to inform some of such parameters is becoming increasingly important in validation tasks [40]. Catalytic recombination is very ubiquitous in ground testing where typical TPS materials as well as other standard testing probes have catalytic properties that must be quantified to understand the experimental data. Stochastic calibration of

---

The contents of this chapter have been published in

- A. del Val, O. P. Le Maître, O. Chazot, T. E. Magin and P. M.Congedo, **A surrogate-based optimal likelihood function for the Bayesian calibration of catalytic recombination in atmospheric entry protection materials**, *Applied Mathematical Modelling (In press).*

such models can then compute objective uncertainty levels on the calibrated parameters, producing better and more reliable predictions.

In the present chapter, we explore the possibility of exploiting experimental data resulting from measurements reported by Panerai and Chazot [19] for the purpose of inferring catalytic recombination efficiencies. The inference focuses on a Bayesian approach that has the advantage of providing a complete characterization of the parameters' uncertainty through their resulting posterior distribution. While conceptually simple, performing a Bayesian inference raises several computational and practical difficulties at every one of its constitutive steps, from expensive model evaluations to limited data [206–208]. The main issue in our problem is related to the appearance of nuisance parameters within the model, such as pressures, wall temperatures and the boundary layer edge enthalpy. These parameters are needed to perform the inference but we are not explicitly interested in getting their distributions, nor we can measure all of them. Traditional Bayesian approaches deal with this problem by prescribing prior distributions on such parameters at the expense of some of the observations consumed to evaluate these nuisance parameter posteriors. Consequently, it is important to remark their impact on the quality of the inference [209].

In the following sections we first present a review of previous experimental works and inverse problems for catalysis determination found in the relevant literature. An analysis of the BL code in the context of the simulation of our experiments is presented next in Sec 5.3. Sections 5.4-5.5 describe the developed Bayesian framework and all its components. The chapter ends with the presentation of results and discussion.

5.2 Review of previous works

The catalytic activity on a material surface cannot be measured directly. We need models and simulations to bypass that lack of knowledge and use other measurable quantities to rebuild the model parameters we are seeking. Numerical simulations can accomplish this task by using experiments and models intertwined in a complex fashion. The literature offers a compelling account of works carried out by various research groups in different facilities to reconstruct catalytic properties. In the next sections, we make the distinction between different experimental approaches that rely on the same deterministic rebuilding principles and stochastic methods applied to existing experimental approaches.

5.2.1 Experimental efforts and deterministic inverse approaches

Two different families of experiments are highlighted. Such families constitute the main core of experimental research regarding catalysis. Experiments in plasma wind tunnels, such as inductively-coupled plasma facilities and arc-jets, rely on heat flux measurements to assess the catalytic activity of materials. On the other hand, diffusion reactors and flow tubes, operate on different principles, estimating the catalytic efficiencies through the measurement of species concentrations in the vicinity of the stagnation point of a given material.

Plasma wind tunnels. The main catalysis experiments performed in ICP wind tunnels are from Kolesnikov et al. [14] at the Institute for Problems in Mechanics (IPM) in Moscow, Pidan et al. [15] and Schüßler et al. [16] at the Institute of Space Systems (IRS) in Stuttgart, and Conte et al. [17] at the CORIA Lab in Rouen. In the Aerodynamic Heating Facility

(AHF), the arc-jet at NASA Ames Research Center, recent works on surface catalysis determination were performed by Stewart et al. [18] for the Space Shuttle tiles coating. The common thread in all of them is the fact that they measured the heat fluxes in oxidized copper as well as the TPS material in question. The oxidized copper wall was assumed fully catalytic in all cases. Comparing both measured heat fluxes allows them to estimate the TPS catalytic activity sought out. This rebuilding method is plagued with assumptions regarding the behavior of oxidized copper surfaces which, apart from being considered perfectly known, their catalytic behavior was also assumed independent from the flow conditions. The state of the plasma flow was considered in equilibrium in all cases.

Closer to home, the experimental work on which this chapter builds was performed by Panerai and Chazot [19] in the VKI Plasmatron. In that work, the assumption of the catalytic parameters being independent from the flow conditions was questioned and recombination coefficients were rebuilt for different chamber pressure conditions. The value of the catalytic parameter for the copper probe was no longer assumed constant but dependent on the chamber pressure conditions according to the available literature. A subsequent experimental work by Viladegut and Chazot [20], set the basis for the determination of copper catalysis for different testing conditions with the premise of relaxing the assumption of perfectly knowing the catalytic response of copper surfaces even when considered as function of chamber pressure. The experimental methodology relied on the catalytic behavior of yet two other reference materials (silver and quartz) from which plausible upper and lower bounds for the catalytic response of copper could be obtained. Adding more probes to the experiment increases its information content without necessarily incurring in new major assumptions.

Diffusion reactors. Contrary to plasma wind tunnel testing where the aim is reproducing the reacting boundary layer, diffusion reactors can produce more direct measurements of the surface chemistry. They can do so by "turning off" the thermal and chemical processes in the flow, such as temperature gradients for thermal diffusion, and gas phase chemistry. In turn, the measurements in diffusion reactors only depend on surface recombination and oxidation. An important technique used for the determination of surface recombination efficiencies in such facilities is actinometry. Actinometrical techniques introduce a low amount of a known gas, such as argon, and measure the evolution of the intensity ratio of an oxygen line (for atomic oxygen) to an argon line along the reactor's discharge zone. Relevant works in these facilities include the rebuilding of recombination coefficients for silicon carbides SiC, SiC + SiO_2 and sintered Al_2O_3 by Balat et al. [210]. The same author also produced an extensive database for surface recombination on SiO_2 (β-cristobalite and quartz) [211] used by Bedra et al. [212] for the validation of a catalytic model. More catalysis data on sintered Al_2O_3 can be found in [213]. Laser Induced Fluorescence (LIF) techniques are also used in diffusion reactors, such as the NASA Ames side-arm reactor. LIF techniques rely on exciting specific atomic energy levels using a laser beam and detecting the emitted energy during the relaxation process. The efficacy of the technique was demonstrated by Pallix et al. [214]. Stewart [215] combined diffusion type facilities with arc-jet measurements to produce recombination efficiencies for a wide range of surface temperatures. Sepka et al. [216] studied surface reactions in CO mixtures for Martian entries. Marschall et al. [217, 218] are estimating recombination coefficients by fitting the experimental concentration profiles with CFD results based on a 2D-axisymmetric reaction-diffusion model.

5.2.2 Statistical inverse approaches

The previous section evidences a clear tendency in empirical work in the aerothermodynamics community. Part of the data released by experimentalists also include reconstructed data such as surface recombination efficiencies which are already loaded with assumptions buried in the reconstruction work. It is difficult, from the user perspective, to have an estimation of how much we can trust such data. It is recalled from the introduction to this thesis as well as Chapter 4 that scientific inferences can carry deep assumptions about a given problem, its chosen mathematical representation, and our level of knowledge when it comes to the understanding of the experimental conditions. It is imperative, for the proper validation of models, that we start assessing such issues in a consistent and rigorous manner.

The research in statistical inverse approaches for catalysis determination is still in the early stages. It is a recently started effort within the aerothermodynamics community for which a whole set of mathematical background is needed to tackle such a challenge. The first related works start with Tryoen et al. [46] and Cortesi et al. [219] in which the authors attempted to reconstruct free stream conditions from flight data. Tryoen et al. acknowledged the epistemic uncertainties stemming from the catalytic response of the protection material. Nevertheless, the complexity of the inverse problem when including the catalytic parameter prevented them from estimating it in the inverse problem as a quantity of interest. They concluded that adding the heat flux as an observation from which to effectively learn catalytic parameters requires the development of novel methods. They kept the value of the catalytic parameter fixed in the formulation of the inverse problem. Cortesi et al. followed in this line of work and developed new techniques to deal with measured heat fluxes from which the catalytic parameter could be learned. Even though the data were not informative enough concerning catalysis, the result did not depend on the chosen value for the catalytic parameter, avoiding biasing the result in this way.

More down to Earth, first efforts on stochastic catalysis determination come from Sanson et al. [220]. In this precursor work, the authors solved a forward uncertainty problem through conventional propagation of error bars as well as using a more general approach through non-intrusive generalized polynomial chaos expansions. The inverse problem was built deterministically and they propagated the uncertainties from the observations to the model parameters through realizations of a polynomial chaos model. Sanson et al. used different values for the catalytic parameter of the reference material to assess its importance in the obtained model parameters. In a subsequent work, Sanson et al. [5] recognized the need for objective uncertainty estimates when it comes to catalysis, proposing to actually learn the catalytic parameters from VKI Plasmatron data. This work represents a departure from the state of the art at the time, in which the reconstruction method no longer had to make assumptions about the reference material used and both catalytic properties could be learned jointly, in addition, the observations were also assumed to be subjected to uncertainties. However, the results showed the difficulties faced with such a methodology, since the authors claimed that the experimental data were not informative enough to learn both catalytic parameters.

5.3 On the boundary layer model

To identify the TPS catalytic properties γ_{TPS}, we simulate the chemically reacting boundary layers in the vicinity of the probe stagnation points with the Boundary Layer code reviewed in Sec. 3.1.1. The objective of such simulations is the prediction of the wall heat fluxes on the reference and material probes which are then compared to the experimental data for the model calibration.

Overall, for given local flow conditions, the wall heat flux contribution to the hydrodynamic equations computed by the BL code amounts to (see Sec. 2.2.2 for transport properties)

$$q_{\text{w}} = \lambda_{\text{w}}^{\text{tot}} \nabla T_{\text{w}} + \sum_i \rho_{\text{w},i} V_{\text{w},i} h_{\text{w},i}, \forall i \in \mathcal{S}, \tag{5.1}$$

where $h_{\text{w},i}$ is the enthalpy at the wall for species i, and $\lambda_{\text{w}}^{\text{tot}}$ is the mixture thermal conductivity at the wall. Eq. (5.1) shows the different contributions to the overall wall heat flux due to Fourier conduction and Dufour diffusion of enthalpy. Note that the dependency on the catalytic parameter γ is implicit in the species densities term at the wall $\rho_{\text{w},i}$ through the catalytic mass balance equation Eq. (2.99) in Sec. 2.3.2.

For the momentum equation, we impose a no slip condition at the wall, and a wall temperature for the energy flux. In depth details about the derivation, coordinate transformations and numerical implementation of the BL code are available in Sec. 3.1.1.

In summary, the predictive quantity of the code is the wall heat flux which can be expressed through a relationship with the hydrodynamic parameters needed to close the flow equations. These parameters are proxies for the coefficients that appear in Eq. (5.1) through the thermodynamic and transport closure models, and surface mass balances (Secs. 2.2.1-2.2.2,2.3.2).

$$q_{\text{w}} = q_{\text{w}} \left(\gamma, T_{\text{w}}, P_\delta, H_\delta, \delta, \left.\frac{\partial u}{\partial x}\right|_\delta, v_\delta \frac{\partial}{\partial y} \left(\frac{\partial u}{\partial x} \right) \Big|_\delta \right). \tag{5.2}$$

The free stream parameters are denoted with subscript δ which refers to the boundary layer thickness. The coordinates x and y denote the radial and axial directions along the stagnation line, respectively. The last two arguments are the velocity gradient at location δ, which controls the local chemistry by imposing the residence time of the flow around the stagnation point, and the axial velocity times the derivative of the velocity gradient at location δ, respectively. This last quantity is included in the formulation to account for the fact that the free stream flow is highly viscous, unlike in classical boundary layer formulations. To match the outer flow solution to the boundary layer solution, the last argument in Eq. (5.2) has to be imposed to account for the extrapolation to the wall of the external flow pressure gradient in the axial momentum equation [106].

If we did not have any more information about our experiments, we would have to assume that all boundary layer edge conditions are unknown and we would have to estimate them along with the model parameters of interest. On closer inspection, the experimental boundary layer is generated by the VKI Plasmatron and its characteristics closely depend on the operating conditions selected for the experiments as recalled from Sec. 3.3. Given the electric power, injected mass flow, static pressure and probe geometry, we can recuperate some boundary layer edge parameters. From the subsonic VKI Plasmatron flowfield simulation depicted in Sec. 3.3, non-dimensional parameters for the boundary layer thickness δ, the velocity gradient $(\partial u/\partial x)\big|_\delta$, and the axial gradient of the velocity gradient $(\partial\left(\partial u/\partial x\right)/\partial y)\big|_\delta$, are defined [145, 146]. The dynamic pressure, corrected for viscous effects $P_\mathrm{d}/K_\mathrm{H} = 1/2\rho_\delta v_\delta^2$ with K_H as Homman's correction factor [136], is used as a convenient proxy for the axial velocity v_δ in Eq. (5.2) given that it is a measured quantity [135]. As we are assuming a boundary layer edge in chemical equilibrium, the density ρ_δ in the dynamic pressure expression is defined by the enthalpy H_δ and pressure P_δ. The variability of the non-dimensional parameters with the operating conditions is small as shown by Panerai [4], therefore they can be considered known constants for each experiment [220]. Finally, for given VKI Plasmatron operating conditions, the predictions we are seeking to match the experimental data are now recast as

$$q_\mathrm{w} = q_\mathrm{w}\left(\gamma, T_\mathrm{w}, P_\delta, H_\delta, P_\mathrm{d}\right), \tag{5.3}$$

where P_δ is taken as the chamber static pressure P_s, and the momentum boundary layer edge conditions have been replaced by the dynamic pressure, given that the non-dimensional parameters are taken as constants.

5.4 Proposed framework for the calibration of catalytic parameters

In this section, the Bayesian formulation of the inference problem is derived in detail. Fig. 5.1 shows a schematic representation of all the steps included to obtain the catalytic parameters posterior. The proposed formulation uses all available measurements of heat fluxes $q_\mathrm{w}^\mathrm{ref}, q_\mathrm{w}^\mathrm{TPS}$, surface temperatures $T_\mathrm{w}^\mathrm{ref}, T_\mathrm{w}^\mathrm{TPS}$, and static and dynamic pressures $P_\mathrm{s}, P_\mathrm{d}$ on the reference and testing probes to jointly infer their catalytic parameters $\gamma_\mathrm{ref}, \gamma_\mathrm{TPS}$ assuming the same degree of prior uncertainty on both. We recall from Sec. 3.2.2 that the experiments consist of different steps. First, the copper calorimeter referred to as "ref" is subjected to the plasma flow and the heat flux to its surface is measured. Subsequently, the probe with the TPS sample is subjected to the same plasma flow. The installation allows switching probes without interrupting the plasma discharge. For this reason, the responses of both probes are tied to the same plasma flow free stream condition, characteristic that we exploit in the derivation of this framework.

The proposed formulation involves a particular treatment of the nuisance parameters which are the inputs to the boundary layer code excluding the catalytic parameters we are interested in calibrating. The effect of their uncertainties is reduced by solving an auxiliary maximum likelihood problem to derive an optimal likelihood function $\mathcal{P}^\mathrm{opt}(\boldsymbol{y}_\mathrm{obs}|\boldsymbol{\gamma}(\boldsymbol{\xi}))$, where the variable $\boldsymbol{\xi}$ is the canonical transformation of the variable $\boldsymbol{\gamma}$. This maximum likelihood problem alleviates the need to sample the nuisance parameters, and can then improve the computational efficiency of the inference, providing more consistent and accurate posterior distributions. Solving this auxiliary problem and sampling the posterior distribution is expensive, as it requires multiple evaluations of the boundary layer equations. To mitigate this issue, we use a surrogate model $Y(\boldsymbol{\xi})$ of the optimal log-likelihood function, making the whole inference process faster and allowing for extensive exploration of the posterior distribution. The posterior is sampled using the Metropolis-Hastings MCMC algorithm [160, 221]. We choose this algorithm given its straightforward computational implementation and the fact that most of the work to make the sampling of the posterior more efficient has been already carried out upstream with the construction of a surrogate model.

The use of this methodology leads to an improved exploitation of the experimental measurements with, as a result, a better estimation of the catalytic parameters for a wide range of conditions.

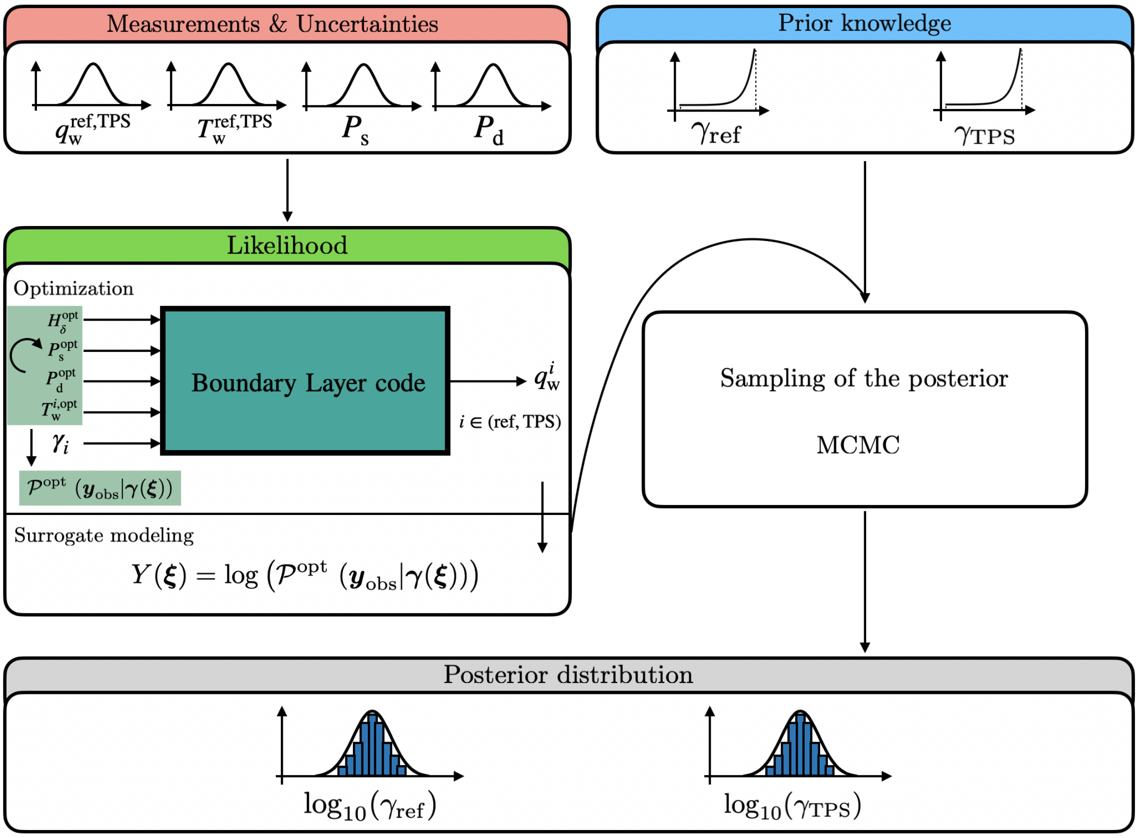

Figure 5.1: *Bayesian inference framework in a nutshell.*

First, the likelihood function and prior distributions are defined, followed by the definition of the GP surrogate model used to approximate the optimal likelihood function.

5.4.1 Bayesian formulation of the inverse problem

The inference of the model parameters uses the Bayes formula which can be generically formulated as

$$\mathcal{P}(\boldsymbol{q}|\boldsymbol{y}_{\mathrm{obs}}) = \frac{\mathcal{P}(\boldsymbol{y}_{\mathrm{obs}}|\boldsymbol{q})\ \mathcal{P}(\boldsymbol{q})}{\int_\Omega \mathcal{P}(\boldsymbol{y}_{\mathrm{obs}}|\boldsymbol{q})\ \mathcal{P}(\boldsymbol{q}) d\boldsymbol{q}}. \tag{5.4}$$

In (5.4), we denote $\boldsymbol{q} = (\gamma_{\mathrm{ref}}, \gamma_{\mathrm{TPS}}, T_w^{\mathrm{ref}}, T_w^{\mathrm{TPS}}, P_s, H_\delta, P_d)$ the vector of model parameters to be inferred, $\boldsymbol{y}_{\mathrm{obs}} = (q_w^{\mathrm{ref,meas}}, q_w^{\mathrm{TPS,meas}}, T_w^{\mathrm{ref,meas}}, T_w^{\mathrm{TPS,meas}}, P_s^{\mathrm{meas}}, P_d^{\mathrm{meas}})$ the vector of measurements or observations, $\mathcal{P}(\boldsymbol{q})$ the prior distribution of the parameters, $\mathcal{P}(\boldsymbol{y}_{\mathrm{obs}}|\boldsymbol{q})$ the likelihood of the measurements, $\mathcal{P}(\boldsymbol{q}|\boldsymbol{y}_{\mathrm{obs}})$ the posterior distribution of $\boldsymbol{q}$, and $\int_\Omega \mathcal{P}(\boldsymbol{y}_{\mathrm{obs}}|\boldsymbol{q})\ \mathcal{P}(\boldsymbol{q}) d\boldsymbol{q}$ the evidence or marginal likelihood. The issue here is that the model predictions are not just functions of the catalytic coefficients $\boldsymbol{\gamma} = (\gamma_{\mathrm{ref}}, \gamma_{\mathrm{TPS}})$, but also depend on all the inputs of the BL code: the wall temperatures $T_w^{\mathrm{ref}}, T_w^{\mathrm{TPS}}$, the pressures P_s, P_d and the boundary layer edge enthalpy H_δ. The pressures and wall temperatures are measured in the experiment, but only with limited precision, while the enthalpy H_δ is simply not known. Consequently, there may be zero, or multiple, boundary layer edge conditions consistent with the measurements. Since the boundary layer edge conditions can not be completely characterized, the remaining uncertainty should be accounted for when inferring the test probe catalytic coefficients.

One possibility to handle this issue is to consider the whole set of uncertain quantities, not just the quantities of interest γ_ref and γ_TPS, but also the so-called nuisance parameters included in $\boldsymbol{q}$. The introduction of the nuisance parameters induces several difficulties related to the necessity to specify their prior distributions, the increased dimensionality of the inference space, and the consumption of information for the inference of the nuisance parameters. This last issue is detrimental to learning the parameters of interest. In [5], non-informative priors were used for all the nuisance parameters. This approach only approximates the posterior of $\boldsymbol{q}$ including the nuisance parameters, and the influence of the (unknown) prior densities of these parameters is unclear. Not only that but the ability to effectively learn from these experimental data is lost. In the following, we derive an alternative formulation for the joint inference of the two catalytic coefficients $\boldsymbol{\gamma} = (\gamma_\mathrm{ref}, \gamma_\mathrm{TPS})$. Specifically, we consider the following Bayes formula

$$\mathcal{P}(\boldsymbol{\gamma}|\boldsymbol{y}_\mathrm{obs}) = \frac{\mathcal{P}(\boldsymbol{y}_\mathrm{obs}|\boldsymbol{\gamma})\ \mathcal{P}(\boldsymbol{\gamma})}{\int_\Omega \mathcal{P}(\boldsymbol{y}_\mathrm{obs}|\boldsymbol{\gamma})\ \mathcal{P}(\boldsymbol{\gamma}) d\boldsymbol{\gamma}}, \tag{5.5}$$

as before, $\mathcal{P}(\boldsymbol{y}_\mathrm{obs}|\boldsymbol{\gamma})$ refers to the likelihood of the measurements in $\boldsymbol{y}_\mathrm{obs}$. This formulation only depends on the two catalytic coefficients $(\gamma_\mathrm{ref}, \gamma_\mathrm{TPS})$ and not on the other nuisance parameters. As a result, only the prior $\mathcal{P}(\boldsymbol{\gamma})$ is needed.

5.4.2 Optimal likelihood function

Our objective is to design a reduced likelihood function which does not involve any nuisance parameters. As stated before, the prediction of the heat fluxes involves not only the catalytic coefficients $\gamma_\mathrm{ref}, \gamma_\mathrm{TPS}$, but also $T_\mathrm{w}^\mathrm{ref}, T_\mathrm{w}^\mathrm{TPS}, P_\mathrm{s}, H_\delta$ and P_d. Assuming independent unbiased Gaussian measurement errors, with magnitude σ, the full likelihood of $\boldsymbol{y}_\mathrm{obs}$ with the nuisance parameters would read as

$$\begin{aligned}\mathcal{P}(\boldsymbol{y}_\mathrm{obs}|\boldsymbol{q}) \propto{}& \exp\left[-\frac{(P_\mathrm{s}^\mathrm{meas}-P_\mathrm{s})^2}{2\sigma_{P_\mathrm{s}}^2}\right] \times \exp\left[-\frac{(P_\mathrm{d}^\mathrm{meas}-P_\mathrm{d})^2}{2\sigma_{P_\mathrm{d}}^2}\right] \times \\ & \times \prod_{i\in\{\mathrm{ref},\mathrm{TPS}\}} \exp\left[-\frac{\left(q_\mathrm{w}^{i,\mathrm{meas}} - q_\mathrm{w}^i(\gamma_i, T_\mathrm{w}^i, P_\mathrm{s}, H_\delta, P_\mathrm{d})\right)^2}{2\sigma_{q_\mathrm{w}}^2} - \frac{\left(T_\mathrm{w}^{i,\mathrm{meas}} - T_\mathrm{w}^i\right)^2}{2\sigma_{T_\mathrm{w}}^2}\right],\end{aligned} \tag{5.6}$$

where the variables with the “meas” superscript refer to the measured quantities, σ_{P_s}, σ_{P_d}, σ_{q_w} and σ_{T_w} are the standard deviations associated with each measurement, and γ_ref, γ_TPS, $T_\mathrm{w}^\mathrm{ref}$, $T_\mathrm{w}^\mathrm{TPS}$, P_s, H_δ and P_d are the components of $\boldsymbol{q}$. The two probes differ in their measurements of heat flux $q_\mathrm{w}^\mathrm{ref,meas}$ and $q_\mathrm{w}^\mathrm{TPS,meas}$, and wall temperatures $T_\mathrm{w}^\mathrm{ref,meas}$ and $T_\mathrm{w}^\mathrm{TPS,meas}$. In this likelihood, the dependencies on γ_ref and γ_TPS are implicitly contained in the heat flux terms. To reduce the dependencies of the likelihood to just the parameter $\boldsymbol{\gamma}$, we propose to set the nuisance parameters $\boldsymbol{q} \setminus \boldsymbol{\gamma}$ to the values that maximize the likelihood (5.6). In the following, we denote $T_{\mathrm{w}}^{i,\mathrm{opt}}, P_{\mathrm{s}}^{\mathrm{opt}}, H_{\delta}^{\mathrm{opt}}, P_{\mathrm{d}}^{\mathrm{opt}}$, the maximizers of (5.6). Note that these maximizers are functions of the catalytic coefficients. We shall also denote $q_{\mathrm{w}}^{i,\mathrm{opt}}(\boldsymbol{\gamma})$ the corresponding model predictions of the heat fluxes for each probe. With these values for the nuisance parameters, we define the optimal likelihood as

$$\begin{aligned}\mathcal{P}^{\mathrm{opt}}(\boldsymbol{y}_{\mathrm{obs}}|\boldsymbol{\gamma}) \propto \exp\left[-\frac{\left(P_{\mathrm{s}}^{\mathrm{meas}} - P_{\mathrm{s}}^{\mathrm{opt}}(\boldsymbol{\gamma})\right)^2}{2\sigma_{P_{\mathrm{s}}}^2}\right] \exp\left[-\frac{\left(P_{\mathrm{d}}^{\mathrm{meas}} - P_{\mathrm{d}}^{\mathrm{opt}}(\boldsymbol{\gamma})\right)^2}{2\sigma_{P_{\mathrm{d}}}^2}\right] \times \\ \times \prod_{i\in\{\mathrm{ref},\mathrm{TPS}\}} \exp\left[-\frac{\left(q_{\mathrm{w}}^{i,\mathrm{meas}} - q_{\mathrm{w}}^{i,\mathrm{opt}}(\boldsymbol{\gamma})\right)^2}{2\sigma_{q_{\mathrm{w}}}^2} - \frac{\left(T_{\mathrm{w}}^{i,\mathrm{meas}} - T_{\mathrm{w}}^{i,\mathrm{opt}}(\boldsymbol{\gamma})\right)^2}{2\sigma_{T_{\mathrm{w}}}^2}\right],\end{aligned} \tag{5.7}$$

where the dependence of the nuisance parameters on the two material properties has been made explicit for clarity.

Given $\boldsymbol{y}_{\mathrm{obs}}$ and a value for the couple of catalytic coefficients, the optimal nuisance parameters and associated heat fluxes are determined using the BL code. The procedure for this optimization is the Nelder-Mead algorithm [222], which is a gradient-free method requiring only evaluations of the BL model solution. Typically, a few hundreds resolutions of the BL model are needed to converge to the optimum of (5.6). The computational cost of the optimization prevents us from using directly this approach to draw samples of $\boldsymbol{\gamma}$ from their posterior distribution, and this fact motivates the approximation of the optimal (log) likelihood in (5.7).

5.4.3 Prior distributions

To complete the Bayesian formulation, we now discuss the selection of the prior for the catalytic coefficients $\boldsymbol{\gamma}$. We start by observing that, although it was assumed that the reference probe is well characterized when designing the experiments, the expression of the likelihood in Eq. (5.7) does not make any additional assumptions concerning γ_{ref} that would bias the resulting possible values taken by the function. γ_{ref} is a free parameter of the problem as it is γ_{TPS}. In fact, the observations should contribute to learn about both material properties. In other words, the differences in the knowledge of $\boldsymbol{\gamma}$ should be reflected by their distinct priors and not in the design of the likelihood. Therefore, it is important to select priors that fairly account for the initial beliefs in the values of the catalytic coefficients. In this case, we have to be cautious with our choice. Considering first the catalytic property of the reference calorimeter, previous works [223–232] show that the a priori knowledge of γ_{ref} is actually quite poor: values proposed in literature vary significantly from one experiment to another. Furthermore, γ_{ref} has been reported for a limited number of conditions, leaving us with large prior uncertainties since in our experiment the boundary layer edge conditions are unknown too. Similarly, the initial knowledge of γ_{TPS} is poor. For instance, previous works (*e.g.* [19]) show that the value of γ_{TPS} can span two orders of magnitude depending on the testing conditions. To conclude, constructing a sharp prior distribution for γ_{TPS} on the basis of previous works is difficult, while assuming a better knowledge of γ_{ref} is not realistic. For all these reasons, we decided in this work to consider independent priors with initial ranges spanning few orders of magnitude, stating bounds on plausible values:

$$10^{-4} \leq \gamma_{\text{ref}}, \gamma_{\text{TPS}} \leq 1.$$

The lower and upper bounds were set to encompass values proposed in the literature and to ensure that they contain the values to be inferred. Based on the proposed bounds, the last step to derive the prior consists in specifying the distribution within the range. Here, instead of using a non-informative prior where any value is as likely as any other (*i.e.*, a uniform prior), we decided to go for log-uniform distributions,

$$\log_{10}(\gamma_{\text{TPS}}), \log_{10}(\gamma_{\text{ref}}) \sim \mathcal{U}(-4, 1),$$

which express our prior ignorance more accurately when the a priori possible $\boldsymbol{\gamma}$ values range over several orders of magnitude [161].

The theoretical models describing the chemically reacting boundary layer, together with the experimental data available are integrated in the Bayesian framework for the inference of $\boldsymbol{\gamma}$. In the next section, we describe how we reduce the computational complexity inherent to the sampling of the posterior. Specifically, we rely on a surrogate model for the log-likelihood function to alleviate most of the computational burden.

5.5 Surrogate modeling

The likelihood function must be evaluated multiple times when sampling the posterior distribution using MCMC methods. Since an evaluation of the likelihood requires many resolutions of the reacting boundary layer model to determine the optimum boundary layer edge conditions, direct sampling strategies based on the full model would be too costly. To overcome this issue, the logarithm of the likelihood function in Eq. (5.7) is approximated by a surrogate model whose evaluations are computationally cheap. In particular, it is very common to proceed with the log-likelihood function instead of the likelihood as it is smoother and it ensures the positivity of the approximation while keeping the same relative structure in the parameter space (e.g. the same parameter values are favoured in both cases).

To construct the surrogate model, we first introduce new canonical random variables, $\boldsymbol{\xi} = (\xi_1, \xi_2)$, for the parametrization of the catalytic coefficients. We set $\boldsymbol{\xi}$ to be uniformly distributed over the unit square: $\boldsymbol{\xi} \sim \mathcal{U}[0, 1]^2$. The uniform grid is chosen for its capability to survey the input space evenly. This is particularly important when dealing with chemical parameters such as $\boldsymbol{\gamma}$ which generally can cause irregular behavior of the simulated quantities. Another concern is the fact that we are dealing with the approximation of an optimal function which can also present high variability for neighbouring points. Given these issues and the fact that a priori we do not know the exact behavior of the function to be approximated, we propose a uniform grid which could potentially be enriched with additional points if the approximation is not good enough. The parameters $\boldsymbol{\gamma}$ are then expressed as functions of the canonical variables $\boldsymbol{\xi}$, for this we fix $\gamma_{\text{TPS}}(\xi_1) = 10^{-4\xi_1}$ and $\gamma_{\text{ref}}(\xi_2) = 10^{-4\xi_2}$, such that $\gamma_{\text{TPS}}(\boldsymbol{\xi})$ and $\gamma_{\text{ref}}(\boldsymbol{\xi})$ are independent, identically distributed, and follow log-uniform distributions with range $[10^{-4}, 1]$. The Bayesian inference problem can finally be recast in terms of the canonical random variables, leading to

$$\mathcal{P}(\boldsymbol{\xi}|\boldsymbol{y}_{\text{obs}}) \propto \mathcal{P}^{\text{opt}}(\boldsymbol{y}_{\text{obs}}|\gamma(\boldsymbol{\xi}))\mathcal{P}(\boldsymbol{\xi}), \quad \mathcal{P}(\boldsymbol{\xi}) = \begin{cases} 1, & \boldsymbol{\xi} \in [0,1]^2, \\ 0, & \text{otherwise}. \end{cases} \tag{5.8}$$

We seek to construct a surrogate of the optimal log-likelihood $\log \mathcal{P}^{\text{opt}}(\boldsymbol{y}_{\text{obs}}|\gamma(\boldsymbol{\xi}))$ with this parametrization. More precisely, we aim for a surrogate model of $Y(\boldsymbol{\xi})$ defined by

$$Y(\boldsymbol{\xi}) \doteq \log\left(\mathcal{P}^{\text{opt}}(\boldsymbol{y}_{\text{obs}}|\gamma(\boldsymbol{\xi}))\right).$$

We then use a GP model to approximate $Y(\boldsymbol{\xi})$. The realization of a Gaussian process is characterized by its mean $\mu(\boldsymbol{\xi})$ and two-point covariance $C_{\text{GP}}(\boldsymbol{\xi},\boldsymbol{\xi}')$ function which expresses the mathematical relationship between two points in the domain $\boldsymbol{\xi}$ and $\boldsymbol{\xi}'$. Given the observation of the function values $Y^{(i)}$ at the sample points $\boldsymbol{\xi}^{(i)}$, one can derive the posterior distribution of the GP model, and evaluate the GP mean and variance at any new point $\boldsymbol{\xi}$. The selection of the prior of the GP model is a crucial step. In this work we tested several zero-mean, stationary processes with covariance functions from the Matern's class [233]; we found that the log-likelihood function is well approximated using the standard isotropic squared exponential kernel, given that both catalytic parameters play the same role in the likelihood. The covariance function then reads

$$C_{\text{GP}}(\boldsymbol{\xi},\boldsymbol{\xi}') = \sigma_{\text{GP}}^2 \exp\left(-\frac{1}{2L_{\text{GP}}^2}(\boldsymbol{\xi}-\boldsymbol{\xi}')^{\text{T}}(\boldsymbol{\xi}-\boldsymbol{\xi}')\right), \tag{5.9}$$

where L_{GP} and σ_{GP}^2 are the a priori correlation length and variance of the GP. All results presented hereafter use the covariance function in (5.9). Denoting $\boldsymbol{Y} = (Y^{(1)} \cdots Y^{(p)})^{\text{T}}$ the vector of observations, we recall that the posterior mean of the GP model, or the best prediction of $Y(\boldsymbol{\xi})$ is

$$\mathbb{E}\left[Y_{\text{GP}}(\boldsymbol{\xi})\right] = \boldsymbol{k}^{\text{T}}(\boldsymbol{\xi})\boldsymbol{K}^{-1}\boldsymbol{Y}, \tag{5.10}$$

where the vector $\boldsymbol{k}(\boldsymbol{\xi})$ and matrix $\boldsymbol{K}$ are given by

$$\boldsymbol{k}_i(\boldsymbol{\xi}) = C_{\text{GP}}(\boldsymbol{\xi},\boldsymbol{\xi}^{(i)}), \quad \boldsymbol{K}_{i,j} = C_{\text{GP}}(\boldsymbol{\xi}^{(i)},\boldsymbol{\xi}^{(j)}) + \sigma_\epsilon^2\delta_{i,j},$$

where $\delta_{i,j}$ is the Kronecker symbol. The variance of the prediction is

$$\mathbb{V}\left[Y_{\text{GP}}(\boldsymbol{\xi})\right] = C_{\text{GP}}(\boldsymbol{\xi},\boldsymbol{\xi}) - \boldsymbol{k}^{\text{T}}(\boldsymbol{\xi})\boldsymbol{K}^{-1}\boldsymbol{k}(\boldsymbol{\xi}),$$

which can be used to inform additional training points to improve the approximation.

5.6 Results on a case study

The methodology presented in the previous sections is used for a real case of plasma wind tunnel testing. This case is used to assess the validity and possible shortcomings of the approach.

5.6.1 Experimental data and associated uncertainties

The experimental run used for this case study is depicted in Table 5.1. As we recall from the introduction to this chapter, this dataset was obtained by Panerai and Chazot [19].

The uncertainties related to this experimental condition are reported in [5] and taken as the 3σ level of confidence. The errors associated with the different experimental quantities are modeled as random variables following unbiased independent Gaussian distributions with zero mean and standard deviation σ. It is important to remark that $q_{\mathrm{w}}^{\mathrm{TPS}}$ is derived from the measurement of the material emissivity as already explained in Sec. 3.2.2.

Table 5.1: *Experimental data and uncertainties considered in our case study.*

Experiment S_1	$q_{\mathrm{w}}^{\mathrm{ref}}$ [kW/m^2]	$T_{\mathrm{w}}^{\mathrm{ref}}$ [K]	P_{s} [Pa]	P_{d} [Pa]	$q_{\mathrm{w}}^{\mathrm{TPS}}$ [kW/m^2]	$T_{\mathrm{w}}^{\mathrm{TPS}}$ [K]
Reported value	195	350	1300	75	91.7	1200
Error std deviation (σ)	6.5	11.7	1.3	1.5	3.05	40

5.6.2 Log-likelihood approximation

We run the optimization algorithm in a uniform grid of 176 points on the space of the $\log_{10}(\gamma_{\mathrm{ref}})$ and $\log_{10}(\gamma_{\mathrm{TPS}})$ variables. This uniform grid is chosen slightly asymmetric, 11x16 points, repectively. This choice for an initial grid gives us better refinement on the $\log_{10}(\gamma_{\mathrm{TPS}})$ direction. From physical considerations, we expect the variability of this parameter to be greater on the posterior than $\log_{10}(\gamma_{\mathrm{ref}})$. Therefore, providing a more refined grid on $\log_{10}(\gamma_{\mathrm{TPS}})$ could produce better approximations for less cost than a squared grid of that size. Fig. 5.2 shows the log-likelihood function evaluated at these grid points. These evaluations are then used to construct the surrogate approximation by transforming the physical variables $\log_{10}(\gamma_{\mathrm{ref}})$ and $\log_{10}(\gamma_{\mathrm{TPS}})$ into their respective canonical counterparts $\boldsymbol{\xi}$.

Overall, the shape of the log-likelihood function falls from the compatibility of the given pair of γ_{ref} and γ_{TPS} with the observed quantities measured in the plasma wind tunnel. In general, for large values of γ_{ref}, log-likelihood values tend to be larger. The same happens with γ_{TPS} for low values. This is already hinting at the fact that higher catalytic activity is expected for the reference material than for the protection material in question, for the given boundary layer edge conditions. On top of that, there is a range of values for γ_{ref} and γ_{TPS} that represent the best agreement with the experimental data. This set of values have to be interpreted jointly: for high γ_{ref} values, γ_{TPS} can only take values in a narrow range placed at the middle of its spectrum. For low values of γ_{ref} (mid-spectrum), γ_{TPS} can take down to the minimum value of 10^{-4}. For large values of γ_{ref} and low values for γ_{TPS}, the heat flux, which is the quantity in the likelihood sensitive to our choice of catalytic parameters, is not sensitive enough to changes in those specific ranges.

As already mentioned previously in Sec. 5.5, we need to properly capture all these features of the log-likelihood with a surrogate model. Fig. 5.3 shows the normalized L_2 error norm for the GP surrogate on a validation set with 10% of the available points plotted against a varying number of training points used to infer the GP hyperparameters of correlation length L_{GP} and standard deviation σ_{GP}. We carry out this procedure 1,000 times with different validation sets each time. The results show the mean and the 95% confidence interval of the computed error. The approximation falls below a 1% error on the validation set as the number of training points gets closer to 160. In practice, we use all model evaluations (176) to construct our GP, knowing that the approximation is

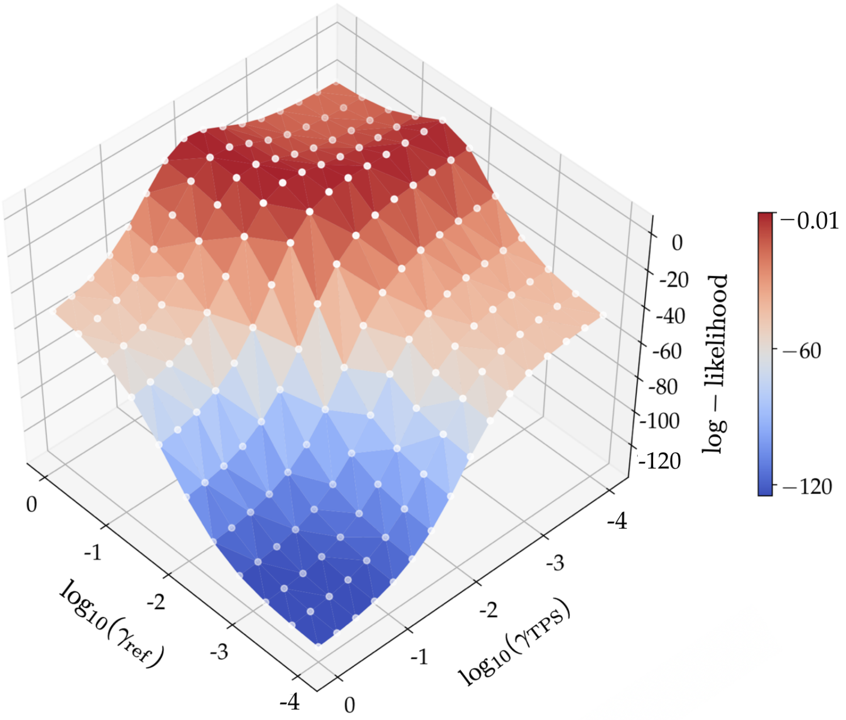

Figure 5.2: *Log-likelihood function evaluated on the chosen* $\gamma_{\text{ref}}, \gamma_{\text{TPS}}$ *grid.*

already good enough. Furthermore, this approximation obtained has a maximum predictive standard deviation of 1%. Fig. 5.4 shows the apparent good agreement between the mean value predicted by the GP and the data points computed for the log-likelihood in Fig. 5.2.

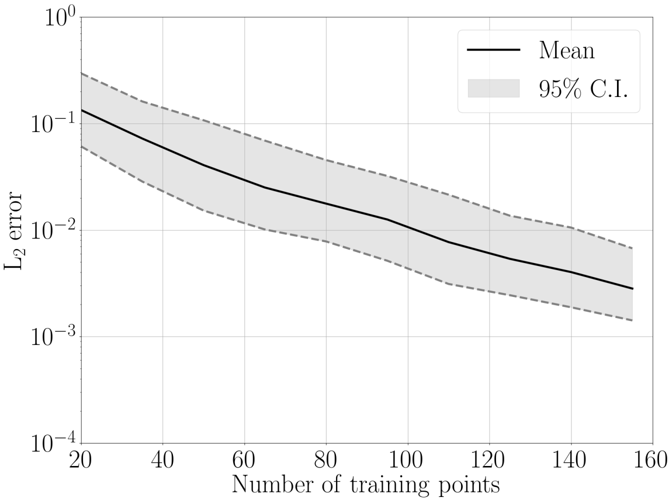

Figure 5.3: *Normalized* L_2 *error norm of the GP approximation with varying number of training points.*

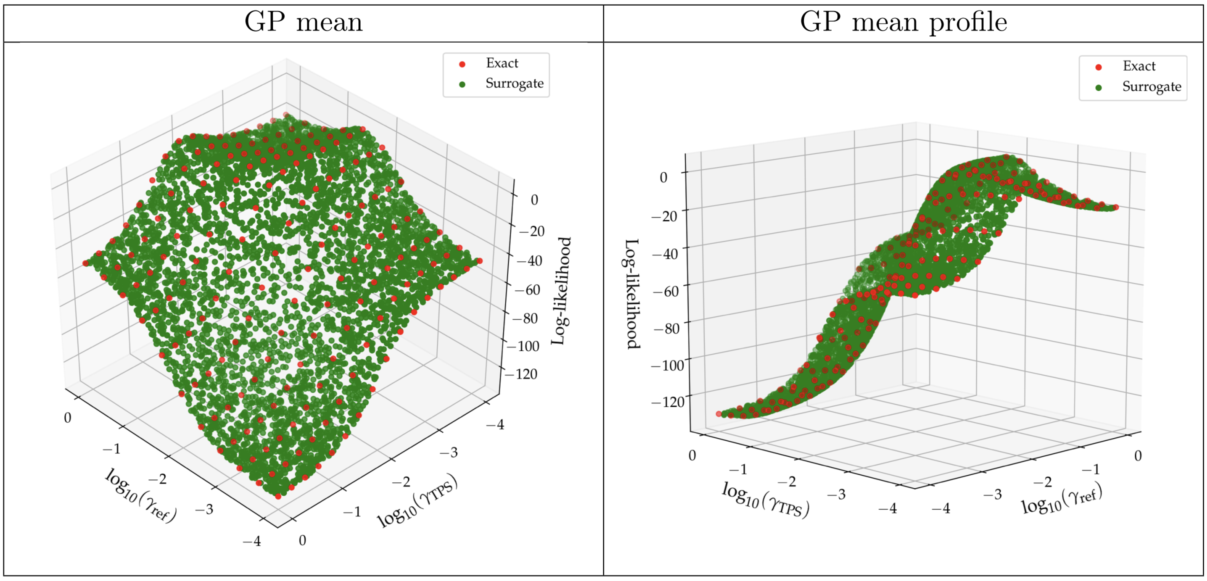
GP mean

GP mean profile

Figure 5.4: *GP surrogate comparison with the exact log-likelihood values in logarithmic variables.*

5.6.3 Sampling of the posterior distribution

We perform a MCMC sampling for the choice of GP surrogate. The chains obtained are depicted in Fig. 5.5. We can see that the chains present no long-term correlation and mix well.

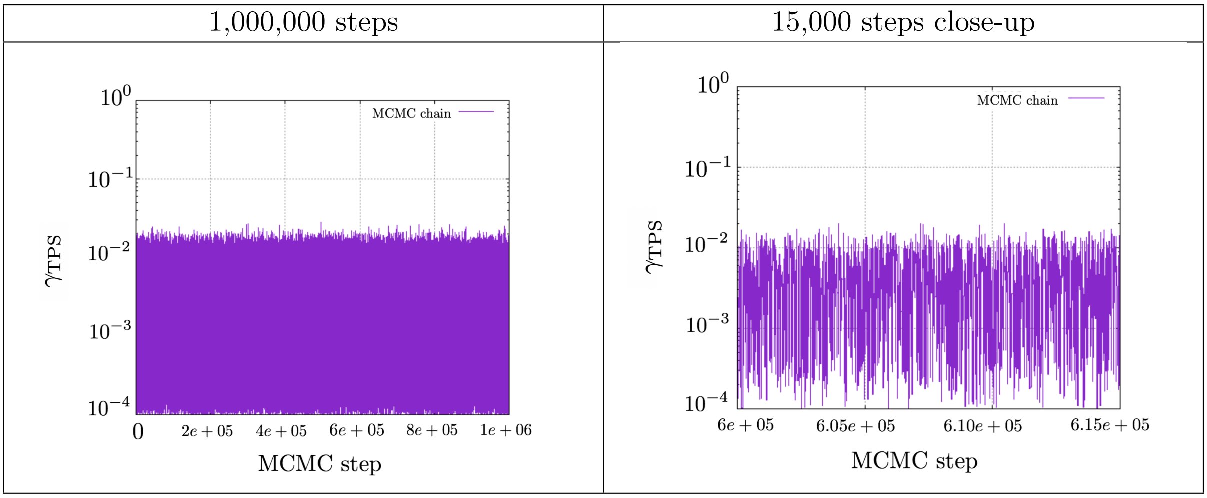
1,000,000 steps

15,000 steps close-up

Figure 5.5: *Chain obtained with 1,000,000 steps and 15,000 steps (right).*

The posterior samples obtained are shown in Fig. 5.6. In general, the tendency of the samples is to remain in a narrow area of the γ_{TPS} space when γ_{ref} takes large values. Once γ_{ref} starts moving towards lower values this tendency is reversed and γ_{TPS} can take values in a wider range while γ_{ref} is confined in a narrow region. This joint behavior falls from the inference framework. The key variable here is the boundary layer edge enthalpy H_δ which is shared between both materials tested (reference and TPS). When the model takes up large values for γ_{ref}, a large amount of the observed heat flux for the reference material is explained in the model through the magnitude of this parameter, setting low the influence of the enthalpy H_δ. Low enthalpy needs larger γ_{TPS} values to account for the observed heat flux on the protection material surface. The same happens for low values of γ_{ref} and γ_{TPS}. In this case, the values that lay interior to the shape defined by the posterior samples are not in agreement with observations for the reason just explained: large γ_{ref} needs large γ_{TPS}. The fact that "large" and "low" are also defined within a range (e.g not more than $\sim 10^{-1.8}$ for γ_{TPS} and not less than $\sim 10^{-2}$ for γ_{ref}) is not imposed by the inference problem setting but by the physics-based model which makes some assumptions regarding the chemical nature of the flow. Some values of γ_{ref} and γ_{TPS} could not explain, under the same H_δ, the observations. Overall, this behavior will naturally reflect on the marginal posterior distributions depicted in the next section.

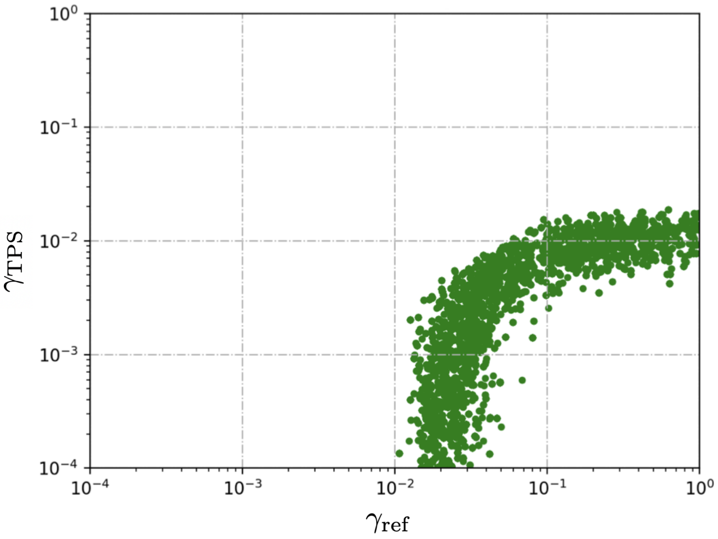

Figure 5.6: *Joint posterior samples of the MCMC algorithm.*

5.6.4 Discussion on the posterior distribution

The posterior marginals are reported below in Fig. 5.7. We can observe that the distributions of both γ_{ref} and γ_{TPS} drop to small values at both ends of the spectrum, reducing the support from the prior distributions proposed. This satisfying behavior can be explained by the proposed likelihood form, which uses all the available measurements to access the fitness of the model predictions. As a result, the formulation predicts that the values of H_δ^{opt} that could explain the whole set of measured fluxes, temperatures and pressures, are actually far away from the maximum likelihood points when $\gamma_{\text{ref}} \ll 1$ and γ_{TPS} reaches large values. It is also important to notice that both distributions have well-defined peaks for $\gamma_{\text{ref}} \simeq 0.016$ and $\gamma_{\text{TPS}} \simeq 0.01$. The ranges of values observed in our calibration for both gammas fit perfectly with the model previously assumed by the experimentalists where the reference parameter takes higher values than the catalytic parameter of the protection material. It is also important to emphasize the fact that in this framework no assumptions are made concerning γ_{ref}, which is estimated along with the protection material parameter with no differences in their prior knowledge. It can be suggested that a deeper experimental study can provide more insights to the behavior of the reference material and a different prior can be defined for the same analysis where differences in knowledge between the two probes can be then accounted for.

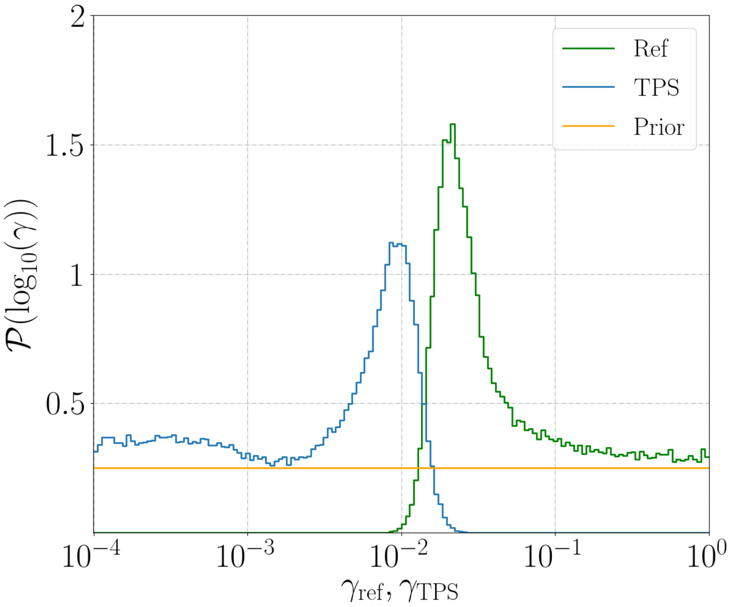

Figure 5.7: *Posterior marginals obtained for* γ_{ref} *and* γ_{TPS}.

The statistics associated with these distributions are gathered in Table 5.2, where MAP refers to the Maximum A Posteriori and CV to the Coefficient of Variation. The differences between these results and the outcomes of [5] are clear when looking at the values in the table and the shapes of the distribution functions obtained. A reduction of almost 20% of the standard deviation and 40% of the CV for the catalytic parameter of the reference material is observed. There is no reporting of the posterior statistics for γ_{TPS} in [5]. The capability of learning γ_{TPS} from experimental data is lost without any particular treatment of the nuisance parameters in the formulation of the inference problem. In contrast, the results of this work show that it is possible to learn γ_{TPS} from this experiment through the optimal likelihood framework.

Table 5.2: *Comparison of the posterior statistics for experiment* S_1 *with the work of [5].*

Experiment S_1	Mean (μ)	Std dev. (σ)	MAP	CV [σ/μ]
γ_{ref}	0.060	0.078	0.022	1.3
γ_{TPS}	0.0034	0.0047	0.008	1.4
Experiment S_1 from [5]				
γ_{ref}	0.042	0.095	0.018	2.3
γ_{TPS}	-	-	-	-

The distributions of the optimal parameters are also computed. For each of these quantities, a GP surrogate is computed on the same $\gamma_{\text{ref}}, \gamma_{\text{TPS}}$ grid than the log-likelihood. The resulting posterior samples of γ_{ref} and γ_{TPS} are used as input for these surrogates, obtaining the distributions of the optimal parameters shown in Fig. 5.8. A bimodal distribution is obtained for the enthalpy H_δ^{opt}. The shape of this distribution is a direct result from the optimization algorithm that computes the H_δ^{opt}, where many of its best points ("best" meaning the ones which maximize the likelihood) fall into two different groups of values, decreasing the probability density between them. The physical system, represented by the BL code, computes the quantity $q_{\mathrm{w}} = q_{\mathrm{w}}(\gamma, T_{\mathrm{w}}, P_{\mathrm{s}}, H_\delta, P_{\mathrm{d}})$. For each $T_{\mathrm{w}}, P_{\mathrm{s}}, P_{\mathrm{d}}$ and q_{w}, the system relates the enthalpy H_δ and the catalytic parameter γ through an S-shaped curve (see Fig.5.9). During the optimization, the physics allow the S-shaped curves to move when different parameters change. The pressure quantities play a minor role due to their small uncertainties and the fact that both curves move together when these quantities change, being common for both materials. It is also important to take into account that we have information about all the nuisance parameters but the enthalpy H_δ which is not measured, therefore, all the other nuisance parameters try to be close to their measured values as a result of the optimization. The lack of information about H_δ gives more uncertainty in the resulting H_δ^{opt}. In turn, we can think of the optimization algorithm as looking for the optimal H_δ while keeping the other nuisance parameters very close to their measured values (within their prescribed standard deviation).

Fig. 5.10 shows the optimization procedure at work and how it finds a common enthalpy H_δ^{opt} that maximizes the likelihood function while reaching a trade-off among the other quantities with respect to their measured values. The thick solid lines represent the S-shaped curves for the reference and TPS material when taking the measured values of all the nuisance parameters and the heat flux. The dashed lines represent a change of heat flux from the values of the thick solid lines. The thin solid lines represent the final optimal solution for the given γ_{ref} and γ_{TPS} (vertical dashed lines) for which a change of wall temperature T_{w} is added to the change of heat flux q_{w}, transforming the original curves (thick solid lines) to the final optimal curves (thin solid ones). At the pair of γ_{ref} and γ_{TPS} where the two thick S-shaped curves have the same H_δ, the algorithm finds the model to agree perfectly with the experiments. For the pair of γ_{ref} and γ_{TPS} given in Fig. 5.10 as an example, the reference and TPS material do not share the same H_δ for their corresponding measured values (thick S-shaped curves). The optimization algorithm finds an optimum H_δ^{opt} which represents a trade-off between the deviations in wall temperatures T_{w} and heat fluxes q_{w} with respect to their measured values over their uncertainty range σ. As the deviation needed to find a common H_δ point for both curves increases, the value of $\log\left(\mathcal{P}^{\mathrm{opt}}(\boldsymbol{y}_{\mathrm{obs}}|\boldsymbol{\gamma}(\boldsymbol{\xi}))\right)$ decreases. In turn, the algorithm performs this for every pair of γ_{ref} and γ_{TPS} in our grid, defining the most likely values for the catalytic parameters in light of the experimental data.

As a result, the points sampled by the MCMC algorithm are shown hereafter in Fig. 5.11. We can appreciate how the points which maximize the likelihood are the ones falling in the range where both S-shaped curves coincide in enthalpy levels. These points represent the best agreement of the system response with respect to the experimental data. This logic explains the bimodal distribution for the enthalpy and the rest of the optimal parameters.

It is an important exercise to put these results in perspective. We are able to relax some assumptions in our model and propose a new functional relationship through the use of the optimal likelihood function. Still, there are other assumptions that remain highly uncertain in within the model. One contributor to such uncertainty is the chemistry of the gas. Specifically, the speed of the different reactions considered can play a role in the

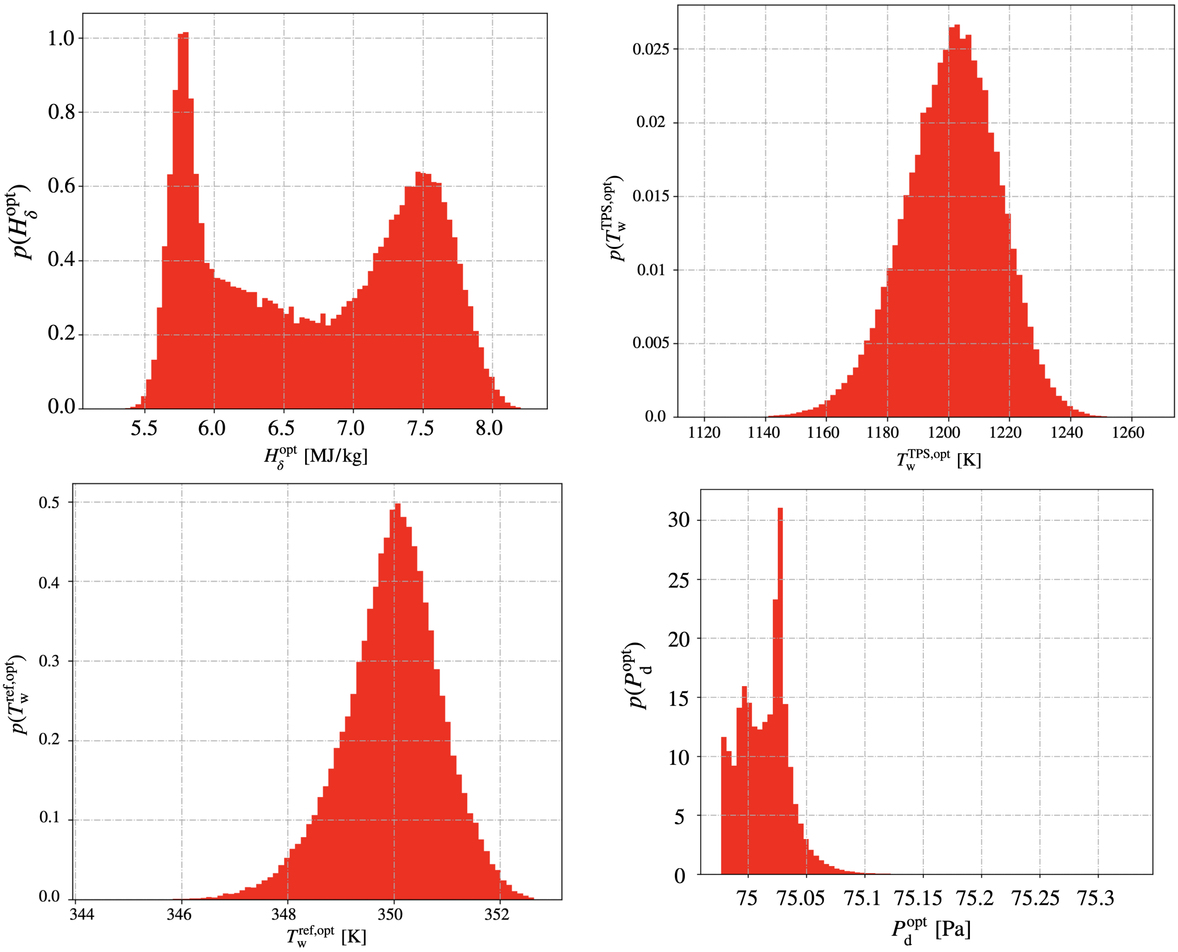

Figure 5.8: *Distributions of the optimal nuisance parameters after propagating the posterior of* γ_{ref} *and* γ_{TPS}.

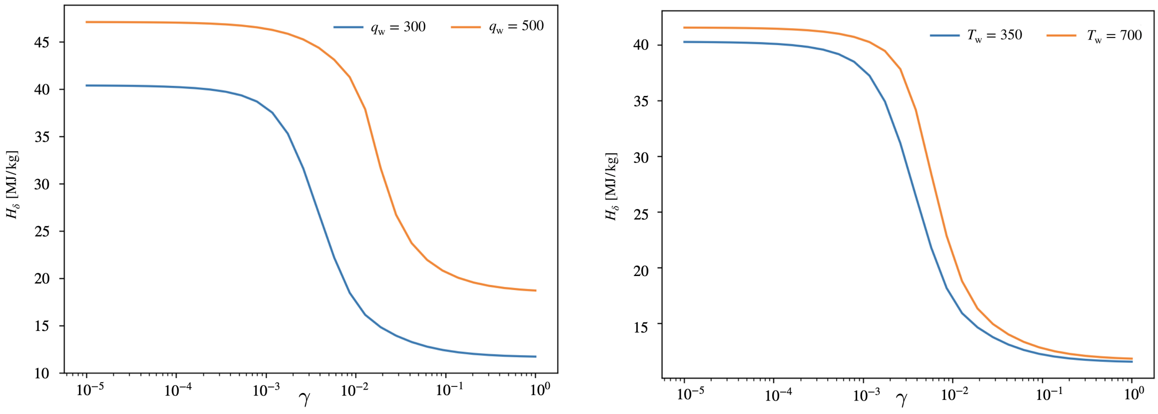

Figure 5.9: *Change on the S-shaped curves positions due to changes in heat flux* (q_w) *or wall temperature* (T_w).

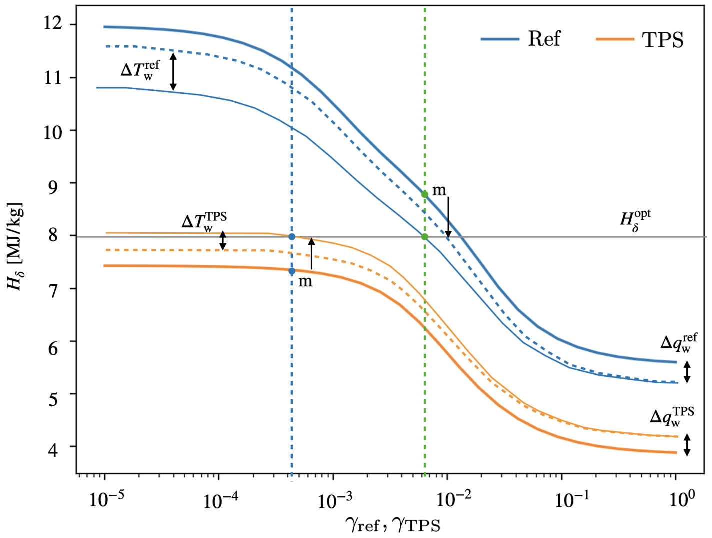

Figure 5.10: *Schematic of the optimization algorithm at work and how it finds a common enthalpy H_δ^{opt} while modifying the S-shaped curves.*

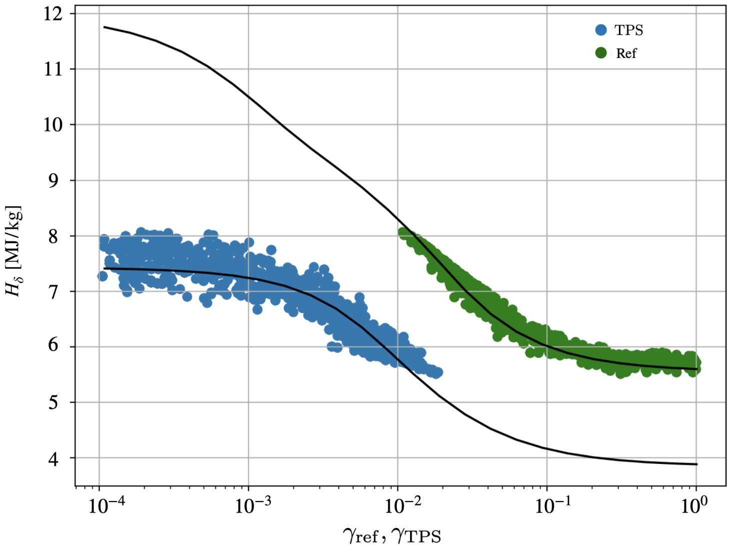

Figure 5.11: *Posterior samples along the S-shaped curves.*

inference, given that a flow in chemical equilibrium or frozen can produce very different heat fluxes under the same edge conditions. The chemistry should be calibrated in dedicated experiments to obtain reliable predictions in the future, as it can impact whether or not the chosen model can explain the experimental data, and this, in turn, influences the calibrated γ_{TPS} obtained.

Another uncertain assumption is the thermodynamic state of the gas. Even though this assumption has been validated using spectroscopic measurements [57] for the test conditions considered, recent numerical investigations [234] suggest that LTE may not hold under different conditions (e.g. lower mass flows). A more extensive use of this framework with dedicated experimental campaigns can help shed light on these issues in the future.

5.7 Summary

In this chapter, we propose a novel Bayesian inference formulation for the calibration of the catalytic parameters of reusable thermal protection materials. The calibration gives estimates of the material catalytic parameter through its posterior probability distribution which can be disseminated for uncertainty propagation analyses. In plasma wind tunnel experiments, the characterization of the reference material behavior plays an important role. In this dedicated framework we relax the assumption of having a well-characterized reference material, as proven to be in conflict with the respective literature in many cases. The Bayesian approach allows for the simultaneous computation of both materials in the inference process which proves to be more accurate than the conventional sequential approach as already shown by Sanson et al.

Our main contribution is the methodology itself. We derive a likelihood function by considering an optimization problem in the nuisance parameters space, reducing the dimensionality of the likelihood to just the quantities of interest $\gamma_{\text{ref}}, \gamma_{\text{TPS}}$. To cope with this computationally demanding likelihood, we propose the use of a surrogate model. GP works quite well for this problem yielding good results with low standard deviations on the chain samples. In addition, the approach is robust, in the sense that the MCMC sampling method works smoothly for any given conditions. Overall, the optimization formulation presented has the impact of improving considerably the inference results by giving more consistent and accurate posterior distributions of the catalytic parameters when compared to the results of Sanson et al. The main differences being the reduced support, with a decrease of 20% in the standard deviation, and well-defined peaks of the respective marginal posteriors. Subsequently, it is possible to say that the catalytic parameters can be effectively learned from the experimental conditions and under the considered model assumptions.

In the next chapter, dedicated experimental campaigns benefit from this work by exploiting the experimental data more thoroughly and adopting a more informative testing methodology.

Chapter 6

Experimental methodology for accurate CMC catalysis calibration

The main objective of this chapter is to develop a dedicated experimental methodology that allows for a better characterization of catalytic recombination parameters for reusable CMC materials when having uncertain measurements and model parameters. First, a synthetic dataset is proposed to test whether or not an already existing experimental approach with three different materials brings any advantages in terms of uncertainty reduction on the sought out parameters. The evaluation is done through the use of the Bayesian framework presented in Chapter 5. The experimental methodology is then adapted for testing ceramic matrix composites with the choice of quartz as a low catalytic reference material. Measurements are then used to jointly infer the catalytic parameters of the three materials, together with the boundary layer edge conditions of the experiments. The testing methodology proves to be a more reliable approach for characterizing these materials while reducing the uncertainty on the calibrated catalytic efficiencies by more than 50 %. An account of the posteriors summary statistics is provided to enrich the current state-of-the-art experimental databases.

6.1 Motivation and problem definition

In Chapter 5, we present a Bayesian framework able to exploit more thoroughly plasma wind tunnel data for catalysis determination. The framework is proven to give accurate uncertainty estimates on the catalytic parameters while considering the observations and some model assumptions to be uncertain. As it was recalled in the previous chapter, the existing experimental databases available in the literature for catalysis in reusable TPS materials have various delicate assumptions built in them (Sec. 5.2.1). Further, there are not reliable (if any) estimations on the bounds for different levels of confidence in the parameters reported. Assuming that the reconstruction of catalytic properties from experimental data is a defined process with well-known characteristics makes the following question not

---

Parts of this chapter have been published in

1. A. del Val, O. P. Le Maître, O. Chazot, T. E. Magin and P. M.Congedo, **A surrogate-based optimal likelihood function for the Bayesian calibration of catalytic recombination in atmospheric entry protection materials**, *Applied Mathematical Modelling (In press).*
2. D. Luís, A. del Val and O. Chazot, **Characterization under Uncertainty of Catalytic Phenomena in Ceramic Matrix Composites Materials for Spacecraft Thermal Protection Systems**, *8th European Conference for Aeronautics and Aerospace Sciences (EUCASS),* Madrid, June 2019, DOI: 10.13009/EUCASS2019-257

worth asking: how should we perform experiments in order to get the most information regarding catalytic coefficients under uncertain observations and model parameters?

The identification of uncertainty sources and how to deal with them unveils a new set of issues, namely, how well we can learn the catalytic parameters we are after and how to improve such estimation by acting on our experimental methodologies. The previously trivial question now acquires central relevance if we want to move forward in the quest for predictive models. The more informative our experiments get, the more useful are the data to increase the confidence in our models or, conversely, invalidate them.

The objectives of this chapter are twofold: first, to show how the *rules of the game* for catalysis testing have changed when introducing uncertain hypotheses and observations. Second, to provide a first database of catalytic parameters for CMC materials and their corresponding testing boundary conditions with associated probability distributions and confidence levels.

The chapter is organized as follows. First, we assess different aspects of existing experimental methodologies, namely the role of different reference materials, and the gains (reduction of uncertainty), or otherwise, of using two reference materials jointly with the TPS material in question. This last idea was developed by Viladegut and Chazot [20] to have a better estimation of the catalytic properties of copper under different plasma flow conditions. Based on the results of both assessments, we propose to adapt the existing 3-probes methodology for the testing of TPS materials by choosing adequate reference materials. Two sets of results are subsequently analysed: synthetic cases for the proposed set-up and the actual Plasmatron test cases for which the catalytic efficiencies are recovered through the stochastic methods developed in Chapter 5. Interpretation of results and computation of summary statistics of the parameters' posterior distributions follow.

6.2 Assessment of experimental methodologies

The developed inference methodology in Chapter 5 can help underpin the important characteristics of testing for catalytic TPS, namely, the conditions and/or configurations that can give the most information by decreasing the uncertainty to a minimum. In particular, we first assess the role of the reference material used for testing. As extending the testing methodology to include three different materials is already a possibility [20], we study the information gain with this methodology with synthetic data. In this section, we discuss how choosing different reference materials and performing experiments with more probes impact the outcome of the inference.

6.2.1 Influence of the reference testing material

Apart from the different testing conditions that can be set for a given experiment (power of the facility, static pressure in the testing chamber, mass flow and probe geometry), we also have the freedom of choosing a reference material with which to gather information about the boundary layer edge conditions.

As it is recalled from the introduction to this chapter, one fundamental uncertainty in the way of rebuilding the TPS catalytic behavior is the fact that the boundary layer edge conditions cannot be estimated accurately if the reference material behavior is not a priori well-known. We explore an assessment of this argument by assuming a high catalytic material (more than the conventional reference of copper) which resembles the catalytic response of a hypothetical probe made with silver [20]. We devise synthetic data where the resulting heat flux to the proposed reference material is higher than the previously considered copper, while still keeping the same wall temperature. The only variable that changes from the case of copper to this synthetic case is the catalytic activity at the proposed reference material surface. Table 6.1 shows the data used to simulate this particular case. Results from the inference are depicted in Fig. 6.1 with the marginal posterior distributions of the case study of Chapter 5 with copper as reference material and the results obtained for the synthetic case. The distributions show the same features than the case study with reduced support and well-defined peaks. We can appreciate that both the supports of the synthetic silver and the TPS are further reduced from the one with copper, giving a slightly better characterization of these properties.

Table 6.1: *Synthetic data and uncertainties.*

Experiment $\mathrm{S_{Ag}}$	$q_{\mathrm{w}}^{\mathrm{Ag}}$ [kW/m^2]	$T_{\mathrm{w}}^{\mathrm{Ag}}$ [K]	P_{s} [Pa]	P_{d} [Pa]	$T_{\mathrm{w}}^{\mathrm{TPS}}$ [K]	$q_{\mathrm{w}}^{\mathrm{TPS}}$ [kW/m^2]
Reported value	232	350	1300	75	1200	91.7
Error std deviation (σ)	7.7	11.7	1.3	1.5	40	3.05

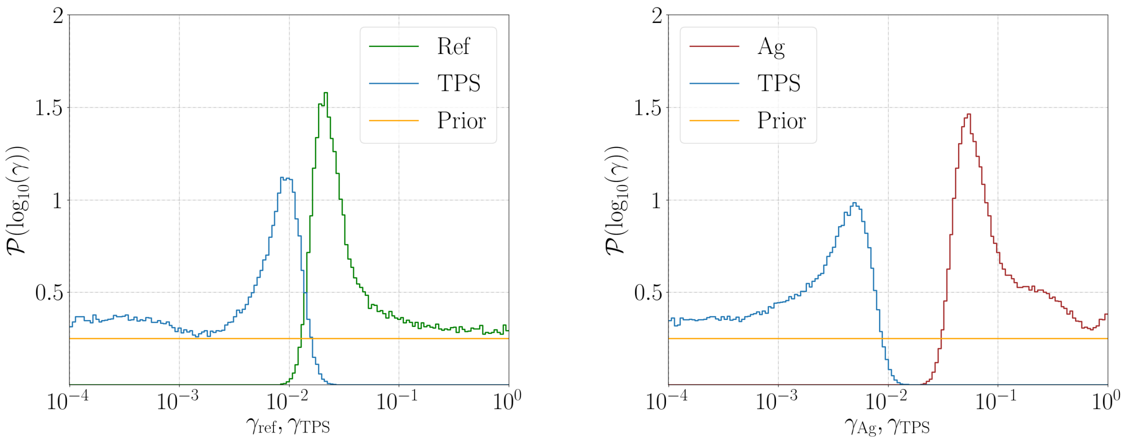

Figure 6.1: *Marginal posteriors obtained in Chapter 5 for the case study with copper (left) and marginal posteriors obtained for the TPS material and synthetic silver (right).*

To assess the information gain with this particular testing configuration, we need to turn to the enthalpy of the plasma flow and see if we manage to capture this information better with synthetic silver. Fig. 6.2 shows the distribution of the optimal enthalpy for both the case study in Chapter 5 and the synthetic case. It is easy to spot the benefits of changing the reference material to a higher catalytic one. The support is greatly reduced when comparing the resulting enthalpies recovered. In turn, the boundary layer edge conditions obtained would be less uncertain in the latter case. More information is contained in that experiment than in our case study. Still the characterization of the boundary layer edge conditions could be further improved as we try to recover a more defined unimodal distribution.

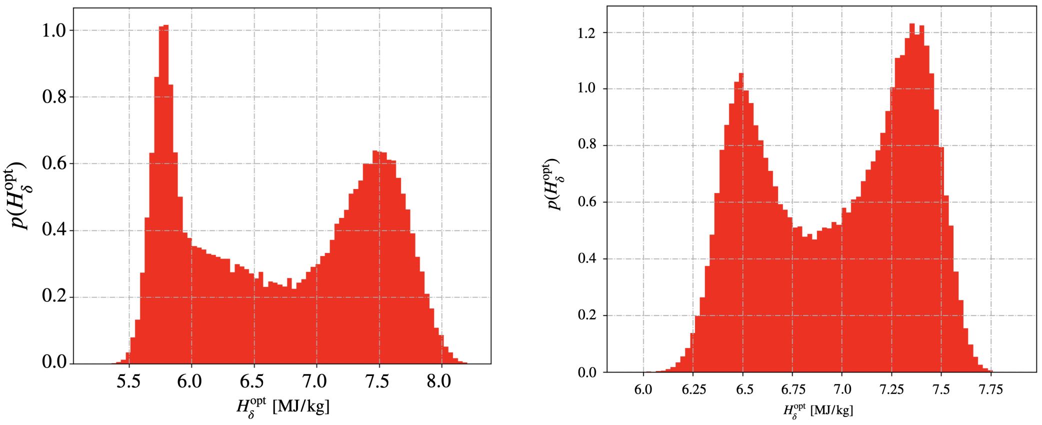

Figure 6.2: *Optimal enthalpy H_δ^{opt} distribution obtained for the case study in Chapter 5 (left) and the synthetic case (right).*

6.2.2 Influence of testing with an additional reference material

The characterization of catalytic parameters can be further studied with a testing methodology that uses two reference materials instead of one [20]. The information brought by this additional probe is expected to improve the characterization of the boundary layer edge conditions. For the following case study S^*_{Ag}, all the three probes seen so far, copper ref, TPS and synthetic silver, are used jointly under the same boundary layer edge conditions as the case study in Chapter 5 for comparison. In this case, we imagine an experiment where the three materials are sequentially exposed to the same plasma flow and the heat fluxes they experience are recorded. The inference uses now all measurements on the three materials to assess their catalytic properties as well as the boundary layer edge conditions jointly. For this, the synthetic dataset of Table 6.1 is enriched with the data from the copper reference material in Table 5.1, given that they are all subjected to the same free stream. This synthetic case allows us to test the benefits of this methodology with the potential of reducing the uncertainty on the characterization of γ_{TPS} if adding an additional material and measurements is informative enough.

Fig. 6.3 shows the marginal posterior distributions obtained. We can observe that both the TPS and synthetic silver distributions are left almost unchanged from the case where they were tested together (Fig. 6.1), although the tail of the synthetic silver distribution shows some growth compared to the previous case. The most notable difference is the posterior distribution of the copper reference material. The presence of a higher catalytic material increases the information obtained for higher values of the catalytic parameters, reducing, as a consequence, the support for high catalytic values of the copper probe.

Table 6.2 depicts the summary statistics of the reference copper and TPS parameters for the case study considered in this chapter and the case study of Chapter 5. We can see that the mean value for the reference probe is moved towards lower catalytic values as well as the mean for the TPS. The standard deviation is decreased significantly for the reference probe (-80%) and for the TPS probe (-45%) while the MAP values have suffered overall less change.

Turning now to the optimal enthalpy, we can see in Fig. 6.4 that the resulting support is comparable to the one obtained with just the TPS material and synthetic silver (Fig. 6.2). We can appreciate a slight shift of the modes due to the fact that the error on the mea-

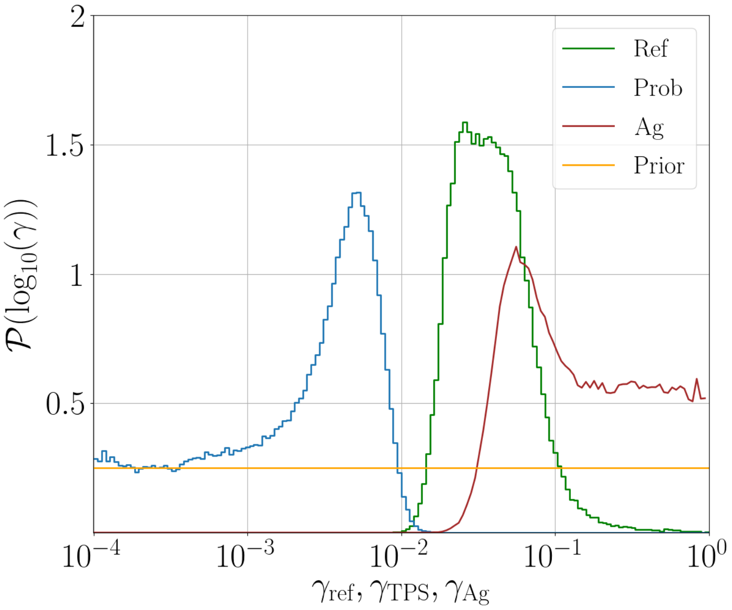

Figure 6.3: *Marginal posteriors obtained for the TPS material, reference material and synthetic silver.*

Table 6.2: *Posterior statistics for the synthetic experiment* $\mathrm{S}^*_{\mathrm{Ag}}$ *and the case study of Chapter 5* S_1.

Experiment $\mathrm{S}^*_{\mathrm{Ag}}$	Mean (μ)	Std dev. (σ)	MAP	CV [σ/μ]
γ_{ref}	0.041	0.015	0.025	0.36
γ_{TPS}	0.0027	0.0026	0.005	0.96
Experiment S_1				
γ_{ref}	0.060	0.078	0.022	1.3
γ_{TPS}	0.0034	0.0047	0.008	1.4

surements of the additional probe weighs in to build the optimized log-likelihood, bringing the optimal enthalpy values closer to the lower plateau where both synthetic silver and copper lay closely together as seen in Fig. 6.5. We recall from Chapter 5 that the S-shaped curves are the resulting possible relationships between the parameters of the model that are not directly observed, such as the edge enthalpy and catalytic efficiency, for given measurements. The amount of information contained in this test case, with three different materials and the previous case with TPS material and synthetic silver is the same and the same support for the optimal enthalpy is retrieved. The materials laying in the extremes of the catalytic spectrum are the ones carrying the information about the boundary layer edge conditions. A closer look at Fig. 6.3 when compared to Fig. 6.1 reveals the fact that the material with a catalytic behavior in between the other two is the best characterized using this methodology.

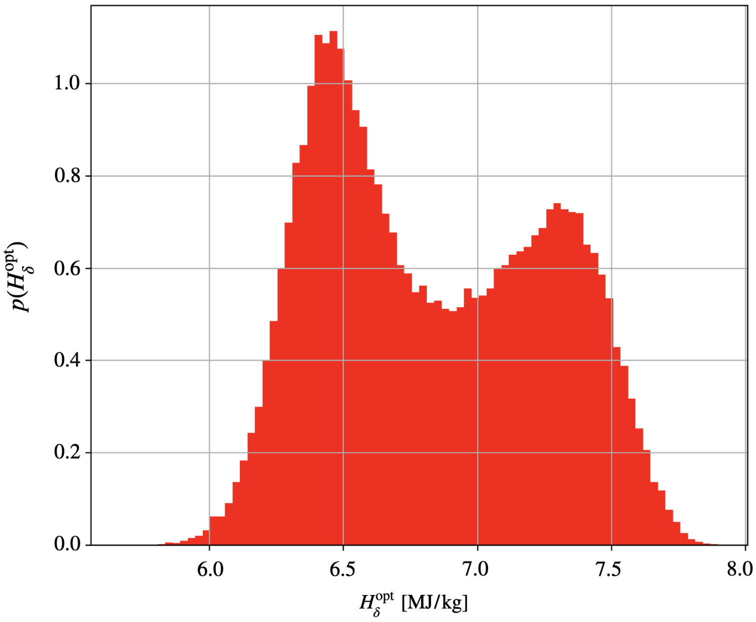

Figure 6.4: *Optimal enthalpy* H_δ^{opt} *distribution obtained by propagating the catalytic parameters posterior of the TPS material, reference material and synthetic silver.*

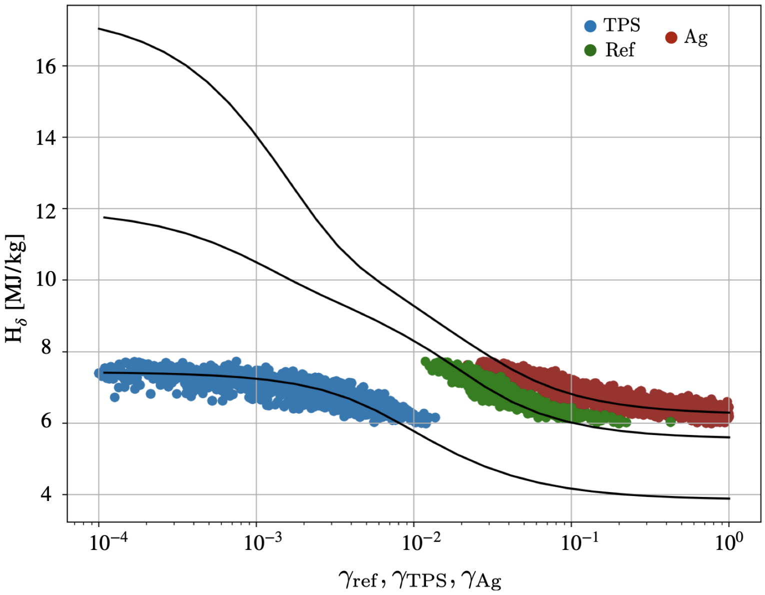

Figure 6.5: *Posterior samples on the S-shaped curves for the three tested materials.*

6.3 Proposed experimental methodology

As we recall from the introduction to this chapter, new questions arise in how to devise experiments once we accept and have to deal with uncertainty sources. As it has been highlighted throughout this thesis, the state-of-the-art catalysis reconstruction assumes the fact that we are able to perfectly characterize the environment under which a TPS material is being tested, namely, all the fluid variables at the boundary layer inlet. In accepting this premise, we can then trace back the heat flux on the TPS sample to the catalytic activity under a prescribed thermal and chemical state of the flow if the surface temperature is measured along. When acknowledging the facts that we can only get noisy observations from the tests and that the assumptions about the edge conditions/reference material are quite uncertain, we need to propose experiments that better inform the sought out catalytic parameters in the presence of such uncertainties.

In this section, we introduce the experimental set-up installed in the Plasmatron facility, together with a brief description of the intrusive/non-intrusive measurement techniques used.

6.3.1 Plasmatron set-up and methods

Based on the analysis of the case study presented in Sec. 6.2.2, the chosen set-up uses two different reference materials. We refer to this general set-up as 3-probes testing methodology given that we test two different reference materials along with the TPS sample in question. Although the 3-probes testing methodology was already devised by Viladegut and Chazot [20] in a different context, the novelty introduced here is the choice of the reference materials that accompany the testing of the CMC samples as well as the fact that the 3-probes testing methodology has not been used before for better characterization of TPS materials. Apart from the novelties in the set-up itself, there is also novelty in the way we arrive at the proposed set-up by strictly performing stochastic analyses on synthetic data. In other words, by finding constraints on the model parameters sought out through a devised experimental set-up.

In this context, our aim is to perform tests where the CMC surface catalysis can be framed between a lower and upper limits of catalytic recombination embodied in reference materials which are the ones carrying the information about the boundary layer edge conditions. The upper catalytic material is an obvious choice, being copper the most studied material for this kind of testing. Conversely, the lower catalytic material is more challenging due to the nature of TPS materials, designed to purposefully be of low surface catalysis. Furthermore, evidence of oxidation of the SiC coating of CMC materials can also impact the catalytic activity on such TPS surfaces [4]. Nevertheless, we find a good option in quartz from the experimental results of Viladegut and Chazot [20] when compared to the tests of Panerai and Chazot [19] for CMC materials under similar conditions. This choice is first tested on synthetic data (Sec. 6.4.1) to corroborate the good choice before attempting the real experiments. The major hurdle in the way of the proposed set-up is that for achieving the full potential of the 3-probes methodology, the TPS material and quartz should have catalytic responses that differ significantly. If the CMC material responds similarly to quartz, adding quartz to the tests would not bring any new information. The results with the proposed methodology would effectively be as 2-probes testing cases in terms of uncertainties on the CMC catalytic parameters, giving out similar results as the case study of Chapter 5. Even though the oxidation of the SiC coating on the TPS material surface causes SiO_2 (quartz) to form, the differences in wall temperatures can make the TPS and quartz catalytic responses differ enough to achieve good characterizations. Furthermore, microscopic considerations on the oxidized TPS layer could also prevent both catalytic responses from being very similar. The ceramic matrix composite material is pyrolized carbon-fiber-reinforced polymer (CFRP) coated with silicon carbide SiC manufactured by MT Aerospace (MTA) in Germany.

Fig. 6.6 presents the experimental set-up proposed for this study. Copper, TPS and quartz samples are mounted on probe holders and are sequentially exposed to the same plasma flow. In these experiments, "standard" ESA geometry probes (also known as Euromodel) for typical non-equilibrium boundary layers, with a radius of 25 mm, are used.

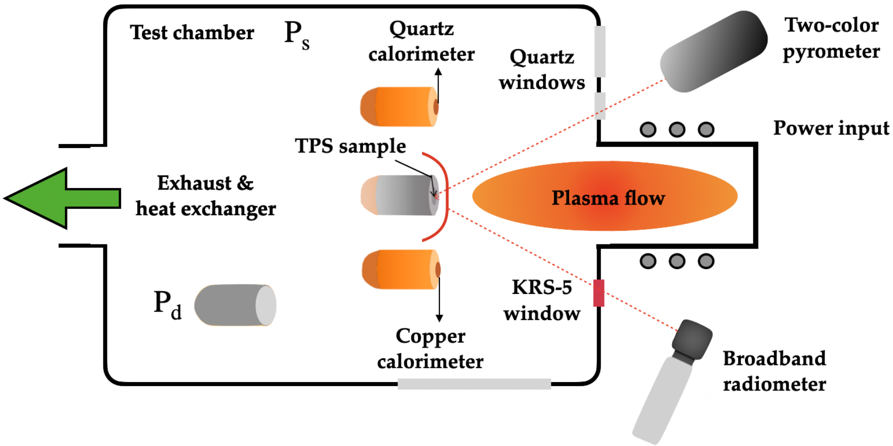

Figure 6.6: *Schematic of the experimental set-up (seen from top, not to scale) with pyrometer and radiometer optical paths in front of the TPS material sample.*

To calibrate the plasma flow conditions, we use two water-cooled 14 mm (sensing area) copper and quartz calorimeters. They measure the cold wall heat flux at the stagnation point ($T_{\mathrm{w}}^{\mathrm{Cu}} \approx 350\mathrm{K}$ and $T_{\mathrm{w}}^{\mathrm{Qz}} \approx 750\mathrm{K}$, respectively). These heat fluxes are determined by the water mass flow ($\dot{m}$), which is controlled by a calibrated rotameter, and the temperature difference ($T_{\mathrm{out}}^{i} - T_{\mathrm{in}}^{i}$) in the cooling water supply. Thus, the heat flux for the cold wall probes (q_{w}^{i}) is given by the expression

$$q_{\mathrm{w}}^{i} = \frac{\dot{m} c_{\mathrm{p}} (T_{\mathrm{out}}^{i} - T_{\mathrm{in}}^{i})}{A}, \qquad \forall i \in \mathrm{Cu}, \mathrm{Qz}, \tag{6.1}$$

where c_{p} is the water specific heat and A the area of the surface of the probe. The cold wall heat flux probes are injected into the plasma flow once the air mass flow and chamber pressure are stabilized. The dynamic pressure (P_{d}) is measured using a Valydine differential pressure transducer and the static pressure (P_{s}) in the Plasmatron chamber is measured by an absolute pressure transducer (Memberanovac DM 12, Leybold Vacuum, OC Oerlikon Corporation AG). As the Plasmatron only has three probe holders, the dynamic pressure is recorded during a different test case, where the copper heat flux and pressures of the first experimental run are duplicated.

To analyse the surface temperature and emissivity of the TPS material, a two-colour pyrometer and an infrared radiometer are used. As previously mentioned, cold wall heat flux and pressure probes are used for jet calibration. The optical instruments (pyrometer and radiometer) are calibrated with the aid of a black-body (BB) source (LANDCAL R1500T, LAND Instruments International), which provides a reference temperature spot with an emissivity value close to 1.

A two-colour Raytek Marathon Series MR1S-C infrared pyrometer with an operating range between 1000 and 3000 °C is used. Optical access to the testing chamber is offered through a 1 cm thick quartz window, placed at ~ 1 m distance to the probe, with an orientation of 35° with respect to the stagnation line. To record the surface radiance, a broadband infrared radiometer (KT19, HEITRON-ICS Infrarot Messtechnik GmbH) is used. This instrument is located at 47° angle relative to the surface normal in front of a 1.8 cm thick KRS-5 window, which offers ~ 70 % optical transparency [4] in the whole infrared range of the instrument ($0.6 - 39\mu$m). Its temperature range is between 0 and 3000° C and the acquisition frequency is set to 1 Hz. The output provided is the integrated thermal radiation over the spectral range, converted into equivalent temperature through an adjustable emissivity value which, in the context of the Plasmatron facility, is set to one. As the range between $0.6 - 39\mu$m contains the highest percentage of thermal radiation at the operation temperatures of the Plasmatron [4], the actual radiance and emissivity can be computed with the Stefann-Boltzmann law. Being $T_{\mathrm{w}}^{\mathrm{pyro}}$ the real surface temperature acquired by the pyrometer and $T_{\mathrm{w}}^{\mathrm{radio}}$ the equivalent temperature measured by the radiometer, the total emissivity can be determined as

$$\varepsilon = \frac{(T_{\mathrm{w}}^{\mathrm{radio}})^4}{(T_{\mathrm{w}}^{\mathrm{pyro}})^4}. \tag{6.2}$$

Emissivity being estimated from the measurements of the pyrometer and radiometer, we can now estimate the actual heat flux to the TPS sample by assuming radiative equilibrium as

$$q_{\mathrm{w}}^{\mathrm{TPS}} = \sigma\varepsilon\,(T_{\mathrm{w}}^{\mathrm{pyro}})^4\,, \tag{6.3}$$

where σ is the Stefan-Boltzmann constant and $T_{\mathrm{w}}^{\mathrm{pyro}}$ is the actual TPS material temperature measured with the pyrometer and referred to as $T_{\mathrm{w}}^{\mathrm{TPS}}$ in the remaining of this work.

All the measured quantities here described present inherent uncertainties. These uncertainties are due to the limited precision of the measuring devices as well as statistical deviations due to the finite number of possible repetitions of such measurements to derive a proper statistical distribution. In the case of the measurements described previously in this section, the measurement uncertainty model is taken as independent unbiased Gaussian distributions. Mean values represent the most likely outcome of the measurement while standard deviations reflect the precision and statistical fluctuations. It is important to take into account the fact that the measured quantities are not the raw experimental measurements but calibrated and post-processed quantities. A forward propagation of uncertainties is needed to estimate properly the uncertainty levels (standard deviations of the Gaussian distributions) of the different post-processed quantities. In the limit case where properties of the experimental apparatus (specific heat of water c_{p} and area A used in Eq. (3.61), for example) are not perfectly known, preliminary measurements may be needed to calibrate the unknowns of the measurement chain through a Bayesian inference framework. The calibrated coefficients of the system together with the raw experimental data should then be forwardly propagated to obtain accurate uncertainty estimates on the measured quantities.

The focus of this contribution is not to properly define the experimental uncertainties involved in the set-up measurement chains. That would entail the development of a whole set of frameworks for each measurement technique, involving calibration data. The objective of the chapter is centered around the possible improvement of the characterization of catalytic efficiencies for TPS materials through experimental design alone, given experimental uncertainties consistent with the current state-of-the-art Plasmatron testing for comparison. In this case, the uncertainty estimates considered here are computed in agreement with the methodologies followed in the available literature for experiments in the

Plasmatron facility [3, 4]. The distributions associated to the static pressure P_s, dynamic pressure P_d, wall heat fluxes q_w^Cu, q_w^Qz and $q_\mathrm{w}^\mathrm{TPS}$, and surface temperatures T_w^Cu, T_w^Qz and $T_\mathrm{w}^\mathrm{TPS}$ are given in Sec. 6.4.2.

6.3.2 On the dynamic pressure measurements

The experiments are performed with three sample probes (copper, TPS and quartz) which is the maximum number of available probes to test in a single run in the Plasmatron facility. Apart from the heat fluxes to the three materials of choice, we need a probe to mount the pressure transducer which measures the dynamic pressure P_d. For each defined testing case, a second experimental run is performed for the recording of the dynamic pressure. Together with the pressure transducer probe, the water-cooled copper calorimeter is also tested to give a reference for the testing conditions by looking at the resulting copper heat flux measurement.

A correlation is established between heat flux and Pitot measurements [119], and linear regressions for given static pressure and mass flow conditions are obtained with the copper heat fluxes and dynamic pressures measured in the calibration run. The actual value of the dynamic pressure in the first run is computed through the linear regressions for the copper heat flux measured in the first run.

More details and additional experimental results can be found in Appendix C.

6.4 Results

In this section, we first perform a study of synthetic data. The study allows us to gauge the viability of the methodology in terms of well defined posteriors for the TPS catalytic parameters which is what we are looking for in defining these experiments.

Consequently, we apply the methodology previously discussed to real tests performed in the Plasmatron facility. A brief discussion on the testing conditions selected is followed by the analyses of the results.

6.4.1 Test cases based on synthetic data

As a proof of concept, the 3-probes testing methodology works well when the materials tested have a range of different catalytic responses to the incoming flow (Sec. 6.2.2). We could devise a synthetic case with the BL code where the catalytic parameters of copper, quartz and TPS get assigned values consistent with the literature. The corresponding synthetic observations such as heat fluxes and pressures can be corrupted by noise also consistent with the measuring devices. From these synthetic observations we could check if we could infer the catalytic parameters initially assigned and study the quality of the posterior distributions. The problem with this common approach in our case is that the catalytic parameter values consistent with the literature are already compromised based on a priori knowledge about the corresponding reference materials. Our synthetic case would not be representative of the actual Plasmatron tests we want to perform if we cannot have a priori an accurate assessment of the catalytic response of quartz with respect to the TPS material.

For this reason, we devise two synthetic cases from different existing experimental data. On one hand, Panerai and Chazot [19] tested the TPS material we are interested in and obtained measurements of its surface temperature under conditions we can consider. On the other hand, Viladegut and Chazot [20] tested quartz and copper calorimeters together under similar conditions to Panerai and Chazot. The cases we are after concern the testing of quartz, copper and TPS under the same incoming flow conditions. Panerai and Chazot, and Viladegut and Chazot tested under the same static pressure which allows us to produce accurate linear regressions for $q_\mathrm{w}^\mathrm{TPS}$ and $T_\mathrm{w}^\mathrm{TPS}$ with increasing reference heat fluxes q_w^Cu. We use Viladegut and Chazot's measured reference heat fluxes to then retrieve the equivalent $q_\mathrm{w}^\mathrm{TPS}$ and $T_\mathrm{w}^\mathrm{TPS}$ for Viladegut and Chazot's testing conditions. The actual data from Panerai and Chazot, and Viladegut and Chazot used to define our two synthetic cases as well as the different linear regressions can be found in Appendix C.

Table 6.3 shows the resulting synthetic cases. Two static pressures, 15 mbar and 50 mbar, are selected from the tests of Panerai and Chazot, and Viladegut and Chazot. One of the interesting aspects of this exercise is to see how sensitive the results are to different testing conditions, especially static pressures.

Table 6.3: *Experimental data and uncertainties considered in our synthetic data study.*

Experiment MTAs1	P_s [hPa]	q_w^Cu [kW/m^2]	T_w^Cu [K]	q_w^Qz [kW/m^2]	T_w^Qz [K]	P_d [Pa]	$q_\mathrm{w}^\mathrm{TPS}$ [kW/m^2]	$T_\mathrm{w}^\mathrm{TPS}$ [K]
Reported value	15	700	350	234	750	164	298	1561
Error std deviation (σ)	0.075	35	17.5	11.7	37.5	16.2	9.6	7.8
Experiment MTAs2	P_s [hPa]	q_w^Cu [kW/m^2]	T_w^Cu [K]	q_w^Qz [kW/m^2]	T_w^Qz [K]	P_d [Pa]	$q_\mathrm{w}^\mathrm{TPS}$ [kW/m^2]	$T_\mathrm{w}^\mathrm{TPS}$ [K]
Reported value	50	700	350	223	750	45	334	1600
Error std deviation (σ)	0.25	35	17.5	11.1	37.5	4.5	11.4	8

Fig. 6.7 shows the results for the two cases. The priors selected for these cases follow the same considerations as the case study of Chapter 5 given that we want to remain as agnostic as possible about the material behaviors in order not to introduce biasing issues. Thus, log-uniform distributions of range $\log\mathcal{U}[-4,0]$ are used for all three materials in each case. In retrospective, more refined priors could be introduced for quartz for which its catalytic properties are better characterized in the literature, nevertheless we choose to stick to our previous analyses for consistency.

The marginal posterior distributions for the three catalytic parameters are what we were looking for with this experimental methodology. Copper and quartz lay well at the extremes of the catalytic parameter space, leaving the TPS marginal posteriors with significantly reduced supports and well-defined peaks. The accuracy of these results over Chapter 5's case study, and even over the one presented in Sec. 6.2.2, clearly justifies the use of the proposed methodology. We continue forward and perform the real experiments.

6.4.2 Plasmatron testing conditions

The experimental test cases are chosen to study the impact of changing the heat flux for the same pressure (similar chemistry in the gas, higher TPS wall temperatures). Hence, heat fluxes of 500, 700 and 900 kW/m^2 are tested. Additionally, a higher static pressure (100 mbar) is tested for the same heat fluxes (where the gas is closer to chemical equilibrium). Thereafter, we compare the impact of changing heat fluxes and pressures in the posterior analysis. These cases are representative of material behaviors of copper and quartz as

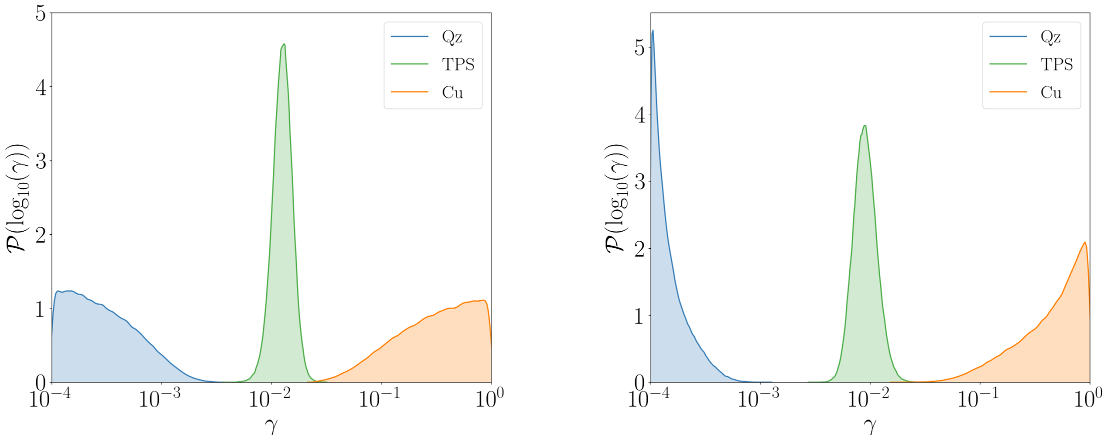

Figure 6.7: *Marginal posterior distributions of the three catalytic parameters for MTAs1 (left) and MTAs2 (right).*

discussed in [20], yielding good posterior distributions for the TPS material. Therefore, we choose them for a first comprehensive study with the proposed set-up. A case with an intermediate static pressure of 50 mbar is also proposed as it was used in the synthetic case study of the previous Sec. 6.4.1.

To proceed with the experiments, the Plasmatron is switched on and the air mass flow is set with a calibrated rotameter. The vacuum pumps are then regulated until the target static pressure is reached inside the chamber. After that, the probe with the copper calorimeter is injected into the plasma and the power is regulated according to the target heat flux being measured, displayed and recorded in real time. Once the calorimeter reaches a steady-state signal under the imposed conditions, the probe is removed from the plasma jet and the one holding the quartz calorimeter is introduced. The heat flux is measured and the injection/ejection process is repeated for the TPS sample. Tables 6.4 and 6.5 summarize the experimental testing conditions and associated uncertainties. The uncertainty levels are obtained following the same procedures as Viladegut [119], Panerai [4] and Helber [3], adopting consistent error values for the different measurements.

Table 6.4: *Plasmatron testing conditions (15, 50 and 100 mbar, atmospheric air) for* $\dot{m} = 16$ *g/s: targetted cold wall heat flux* $q_{\mathrm{w}}^{\mathrm{Cu}}$*, dynamic pressure* P_{d}*, mean wall heat fluxes* $q_{\mathrm{w}}^{\mathrm{Qz}}$ *and* $q_{\mathrm{w}}^{\mathrm{TPS}}$*, and mean surface temperatures* $T_{\mathrm{w}}^{\mathrm{Cu}}$*,* $T_{\mathrm{w}}^{\mathrm{Qz}}$ *and* $T_{\mathrm{w}}^{\mathrm{TPS}}$*.*

Experiment ID	P_{s} [hPa]	$q_{\mathrm{w}}^{\mathrm{Cu}}$ [kW/m^2]	$T_{\mathrm{w}}^{\mathrm{Cu}}$ [K]	$q_{\mathrm{w}}^{\mathrm{Qz}}$ [kW/m^2]	$T_{\mathrm{w}}^{\mathrm{Qz}}$ [K]	P_{d} [Pa]	$q_{\mathrm{w}}^{\mathrm{TPS}}$ [kW/m^2]	$T_{\mathrm{w}}^{\mathrm{TPS}}$ [K]
MTAt1	15	500	350	219.3	750	121.5	227.8	1462.9
MTAt2	15	700	350	317.9	750	160.3	346.5	1631.0
MTAt3	15	900	350	374.1	750	196.6	417.2	1698.4
MTAt4	50	700	350	258.2	750	37.4	324.7	1585.6
MTAt5	100	500	350	251.0	750	13.6	302.5	1566.5
MTAt6	100	700	350	277.4	750	16.6	381.9	1655.8
MTAt7	100	900	350	337.0	750	19.6	470.4	1741.4

Table 6.5: *Experimental uncertainties for 2σ level of confidence.*

Experiment ID	P_s [hPa]	$2\sigma_{P_\mathrm{s}}$ [hPa]	$2\sigma_{q_\mathrm{w}^\mathrm{Cu}}$ [kW/m^2]	$2\sigma_{T_\mathrm{w}^\mathrm{Cu}}$ [K]	$2\sigma_{q_\mathrm{w}^\mathrm{Qz}}$ [kW/m^2]	$2\sigma_{T_\mathrm{w}^\mathrm{Qz}}$ [K]	$2\sigma_{P_\mathrm{d}}$ [Pa]	$2\sigma_{q_\mathrm{w}^\mathrm{TPS}}$ [kW/m^2]	$2\sigma_{T_\mathrm{w}^\mathrm{TPS}}$ [K]
MTAt1	15	0.15	43.9	35	19.4	75	2.3	21.4	21.9
MTAt2	15	0.15	62.6	35	28.4	75	2.5	32.5	24.5
MTAt3	15	0.15	79.8	35	33.3	75	2.4	39.1	25.5
MTAt4	50	0.50	61.2	35	22.9	75	2.6	30.5	23.8
MTAt5	100	1.0	43.5	35	22.2	75	2.5	28.4	23.5
MTAt6	100	1.0	61.0	35	24.6	75	2.5	35.8	24.8
MTAt7	100	1.0	79.1	35	29.9	75	2.6	44.1	26.1

In the next sections, the cases are divided according to the static pressure of the tests given that similar pressures produce similar trends in the results.

6.4.3 15 mbar cases

The γ_TPS marginal posterior distributions for MTAt2-3 present similar morphologies with bimodal distributions and values centered around $\gamma_\mathrm{TPS} \approx 10^{-2}$ (Fig. 6.8). The results for MTAt1 are different in that the distribution for γ_TPS presents a single peak, although the support is similar to MTAt2-3 and the distribution is also centered around $\gamma_\mathrm{TPS} \approx 10^{-2}$. The marginal posterior distributions for the reference materials are also similar among them, favouring the extreme values of the catalytic parameter space. Even though the information of the relative catalytic efficiencies among materials is not given in the form of priors to the Bayesian analysis, the calibration ends up giving us this information from experimental data alone.

The results seem to indicate that the experimental set-up is useful for obtaining peaky distributions and reducing the uncertainty on the posterior of γ_TPS when compared to the work of the previous Chapter 5. Nevertheless, we still need to perform a careful assessment of the quality of the results. In particular, it is important to verify whether or not the calibration achieved can, in turn, predict the experimental data. It is not a trivial question, even for cases used for the calibration itself. Bayesian inference always gives some posterior distribution around the maximum likelihood estimate (in the case of non-informative priors, like the present study). It does not take into account the fact that the model might not be able to reproduce the experimental data for some combination of the parameters and the maximum estimate is just the best the model can do to reproduce the experimental data, but not enough. Through careful scrutiny, we can pinpoint successful cases and formulate new hypotheses for the cases that are not well calibrated, giving a way forward. Also this analysis can help gain more insight into the results.

The best way to visualize the quality of the inference is through the computation of the S-shaped curves. They represent the model output for the relationship between the boundary layer edge enthalpy H_δ and the catalytic efficiency parameter γ for given measurements $P_\mathrm{s}, P_\mathrm{d}, q_\mathrm{w}, T_\mathrm{w}$. In other words, they relate the possible values of the enthalpy H_δ and γ so that the prescribed measurements $P_\mathrm{s}, P_\mathrm{d}, q_\mathrm{w}, T_\mathrm{w}$ are predicted by the chosen model. Propagating the uncertainty of the measurements on these S-shaped functions gives us the boundaries of the allowed space where the curves should live if the model was a good description of the experiments. Comparing the prescribed boundaries with the γ_TPS pos-

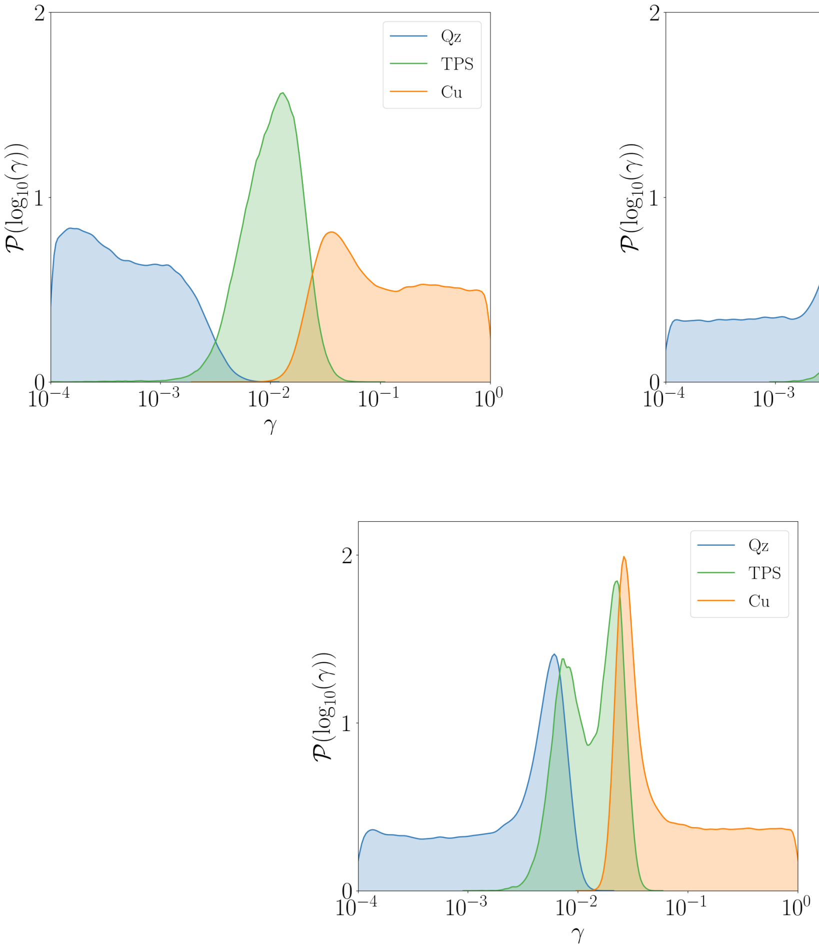

Figure 6.8: *Marginal posterior distributions for the recombination parameters of the three materials for MTAt1 (upper left), MTAt2 (upper right) and MTAt3 (lower center).*

terior and H_δ^{opt} resulting distribution gives us an assessment of the quality of the inference and its deviation from the experimental data. Fig. 6.9 depicts the three S-shaped curves for each testing condition and the points drawn from the posterior distribution of $\gamma_{\text{Cu}}, \gamma_{\text{Ag}}$ and γ_{TPS}, and propagated to obtain H_δ^{opt}. As it can be seen, for the three cases considered under low pressure conditions, the calibrated $\gamma_{\text{Cu}}, \gamma_{\text{Ag}}$, and γ_{TPS} can successfully reproduce the experimental data.

6.4.4 50-100 mbar cases

The γ_{TPS} marginal posterior distributions for these cases present similar morphologies with a well-defined peak and a reduced support compared to the previous low pressure cases (Fig. 6.10). Testing under higher pressures (50 and 100 mbar) give the most precise catalytic efficiencies while relatively high heat fluxes and low pressure cases give more uncertain outcomes. In low pressure conditions, the chemistry does not play such an important role as in the higher pressure cases. The gas phase Damköhler number, defined

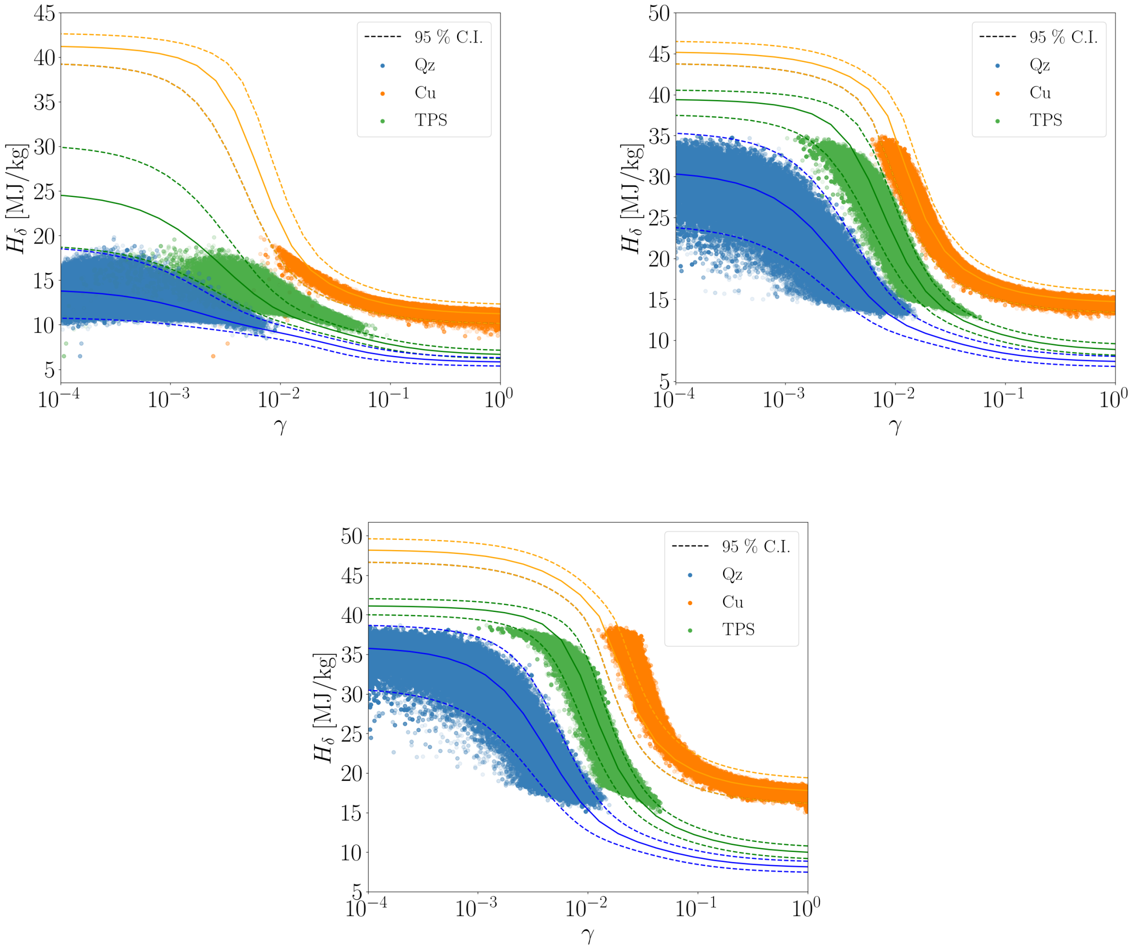

Figure 6.9: $\gamma_{\mathrm{Cu}}, \gamma_{\mathrm{Ag}}$, γ_{TPS} *and* H_δ^{opt} *distributions projected onto S-shaped curves and their* 2σ *confidence intervals for MTAt1 (upper left), MTAt2 (upper right) and MTAt3 (lower center).*

as the ratio between the characteristic diffusion time and the chemical relaxation time $Da = \tau_{\mathrm{diff}}/\tau_{\mathrm{chem}}$, is small ($\mathcal{O}(10^2)$) for low pressure cases. This indicates that we are in a reaction limited regime [99] and that the heat flux measured can be explained by widely different combinations of catalytic activity at the surface and edge conditions. Given fast diffusion time scales, catalytic activity at the surface becomes important as it modulates a considerable amount of diffusive flux. In these cases, convective and diffusive heat fluxes can be traded by modifying the recombination efficiencies, giving the same total heat flux measured. High pressure cases, on the other hand, tend to be in a diffusion limited regime (Damköhler number of the gas large, $\mathcal{O}(10^6)$) and the modulation achieved by the recombination efficiency parameters is not so important, setting the diffusive flux to within certain values for which only a handful of edge conditions suffice to match the total heat flux measured. This reduction of the uncertainty that is case-dependent works better if the materials have very different catalytic behaviors.

Fig. 6.11 depicts the S-shaped curves for each testing condition. As it can be seen, for

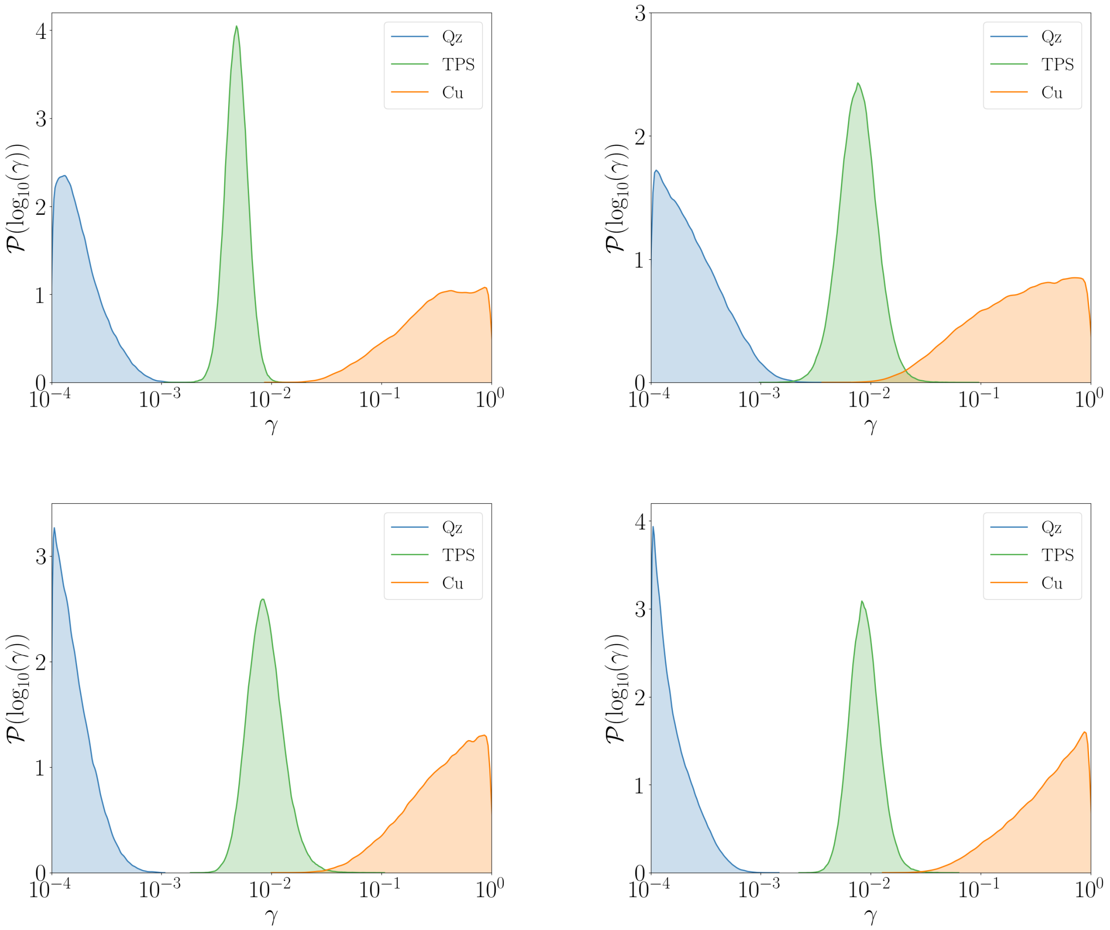

Figure 6.10: *Marginal posterior distributions for the recombination parameters of the three materials for MTAt4 (upper left), MTAt5 (upper right), MTAt6 (lower left) and MTAt7 (lower right).*

some of the cases considered under high pressure conditions, the calibrated $\gamma_{\mathrm{Cu}}, \gamma_{\mathrm{Qz}}, \gamma_{\mathrm{TPS}}$ cannot successfully reproduce the experimental data. Particularly, the posterior distributions of γ_{Qz}, γ_{Cu} and γ_{TPS} for cases MTAt6-7 cannot quite explain the experimental data measured in the Plasmatron. The resulting deviations are beyond the 3σ level of confidence. In other words, the model fails to simulate our experiments if there is not a single edge condition that can explain the different heat fluxes and surface temperatures observed. Looking at it in reverse, the model cannot predict all three heat fluxes under the requisite of a common edge condition. Therefore, in a follow-up analysis, we must highlight problematic assumptions beyond the ones considered here and properly assess our knowledge about them. There might be aspects of the system that are not known precisely in addition to the unknowns considered in this work (edge conditions and catalytic efficiency of all three materials).

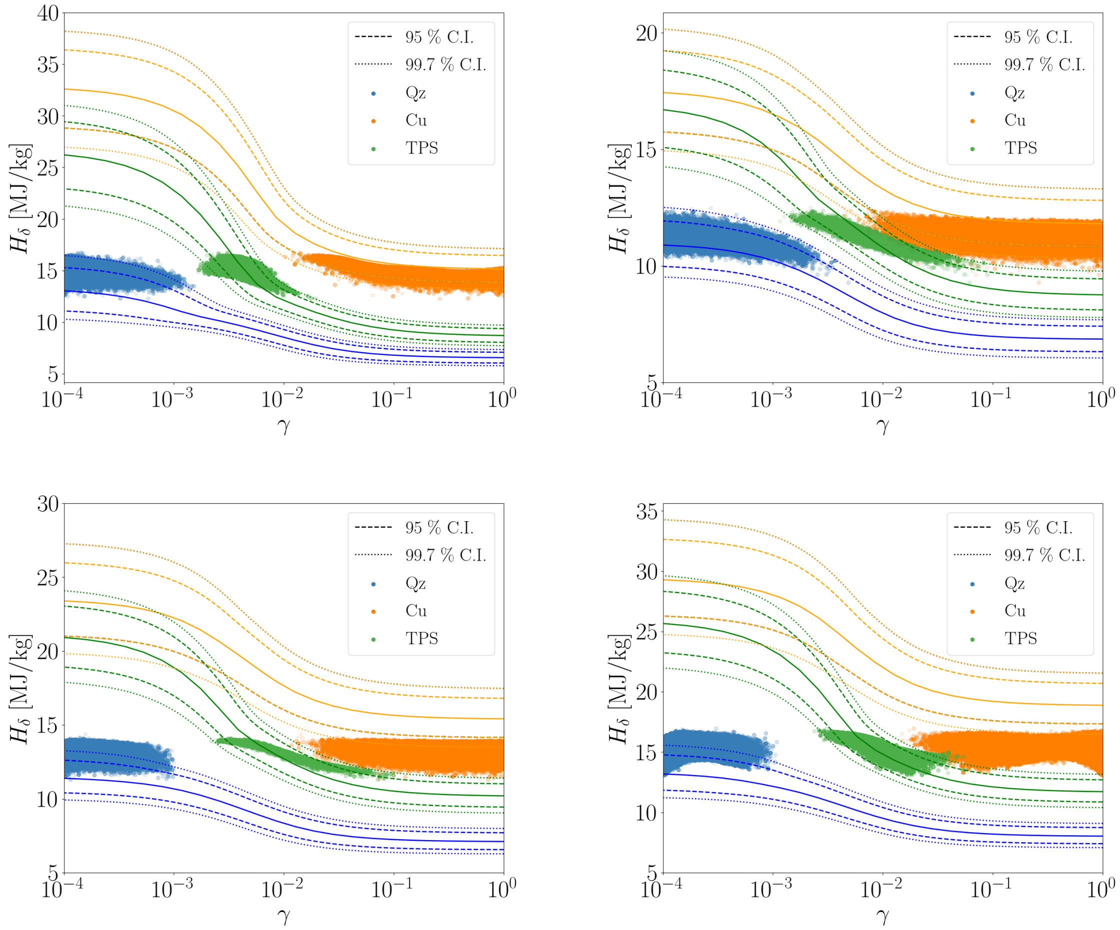

Figure 6.11: *$\gamma_{\text{Cu}}, \gamma_{\text{Ag}}, \gamma_{\text{TPS}}$ and H_δ^{opt} distributions projected onto S-shaped curves and their 2σ and 3σ confidence intervals for MTAt4 (upper left), MTAt5 (upper right), MTAt6 (lower left) and MTAt7 (lower right).*

6.4.5 Interpretation of results and summary statistics

The main outcomes of the analyses are the γ_{TPS} marginal posterior distributions for the different test cases. The objective being to obtain well defined probability distributions for the catalytic parameters of the CMC material. A larger experimental study built on this methodology could calibrate this parameter in different regimes, allowing to probe the fundamental physics behind it.

15 mbar cases. It is seen that as the heat flux gets higher for the same pressure conditions, the sensitivity of the problem to γ is also higher (steeper S-shaped curves), broadening the span of possible solutions. Higher heat fluxes for the same pressure involves a higher degree of dissociation at the boundary layer edge as a consequence of the edge temperature increase. For a flow in a reaction limited regime (Damköhler number in the gas small), this higher dissociation degree means more sensitivity to surface reactions of the wall heat flux. Overall, higher heat fluxes produce wider supports for the reference materials (MTAt2-3) and two equally probable values of γ_{TPS} in the form of bimodal distributions. The lower γ_{TPS} peak corresponds to low values of γ_{Qz} and γ_{Cu}, while the opposite is observed for the upper γ_{TPS} peak. The obtained bimodal distributions for γ_{TPS} can be explained due to the fact that the priors assign the same probability to the different plausible values of the various decades of catalytic parameters. This issue, coupled with the high sensitivity of the problem to catalytic recombination at low pressures, produces two distinct favoured values in the posterior distributions. As can be seen in Fig. 6.9 most of the obtained posterior samples for MTAt2-t3 fall on one of the two plateaus of the optimal enthalpy with respect to the catalytic parameter γ. These two plateaus accummulate solutions for a certain range of catalytic parameters while favouring mainly two different values of the optimal edge enthalpy. Conversely, these two favoured values of the free stream also favour upper and lower limits on the γ_{TPS}. Both solutions are equally likely and more information is needed in either the priors or the experimental data to be able to pinpoint a more precise distribution.

From only looking at the marginal distributions it may seem that γ_{Qz} and γ_{TPS} both share simultaneous support for some values. As already mentioned, when γ_{TPS} values are taken from the lower peak (support shared with γ_{Qz}), the possible values for γ_{Qz} are the ones in the tail of the corresponding distribution. Due to the wall temperature differences, the model chosen can only consider low γ_{TPS} values for high boundary layer edge enthalpies. Conversely, for quartz, the γ_{Qz} values shared with γ_{TPS} can only be considered for substantially lower boundary layer edge enthalpies given the low wall temperature of the quartz probe. In other words, γ_{Qz} and γ_{TPS} cannot both have the same values simultaneously (which could be expected if an oxide layer of quartz forms on the TPS material surface). To actually gauge the importance of TPS oxidation on the determination of γ_{TPS} and how it actually compares to γ_{Qz}, evidence of formation of a stable oxide layer and microscopic analyses of the structure could be pursued.

50-100 mbar cases. It is seen that for some of the cases considered under high pressure conditions, the calibrated $\gamma_{\text{Cu}}, \gamma_{\text{Qz}}, \gamma_{\text{TPS}}$ cannot successfully reproduce the experimental data. Due to the complexity of the involved physics, we acknowledge that there might be aspects of the system that are not known precisely in addition to the unknowns considered in this chapter. One candidate for such unknown is the chemistry of the gas. The chemical state of the gas poses epistemic uncertainties given that different models exist in the literature and are widely used. Specifically, the speed of the different reactions considered can play a role in the inference, given that a flow in chemical equilibrium or frozen can produce very different heat fluxes under the same edge conditions. Catalytic activity can also be relegated to be non-influential in the heat flux experienced by the material if the gas chemistry has already consumed all the available energy contained in the dissociated flow, and this is likely to occur under high pressure conditions. A numerical experiment and a priori forward propagation of uncertainty can show if the effects of an uncertain gas chemistry would have an impact on the possible solutions for high pressure cases such as MTAt6 and MTAt7. The proposed exercise would indicate whether further analysis in that direction would be needed in the future. A numerical experiment is a good exercise to explore the models at hand while knowing exactly which assumption is not correctly considered in a synthetic reconstruction of simulated data. It is something not possible to achieve with experimental data due to the large number of unknowns involved, making difficult to have a definitive assessment of the effects some assumptions have. The following exercise highlights the impact of the adequacy of the gas phase chemistry model on the possible calibrated solutions. The results indicate that a model that overestimates the speed of chemical reactions in the flow can fail to reproduce the experimental data, while the opposite scenario would extend the uncertainty on the resulting calibrated parameters.

The numerical experiment is as follows. We simulate a boundary layer to which two different materials of high ($\gamma_{\mathrm{H}} = 1$) and low ($\gamma_{\mathrm{L}} = 10^{-4}$) catalytic efficiencies are subjected. The chosen conditions are similar to the experiments of this work and under the chemistry model of Gupta et al. [235]. This model considers the reactions to be slower than the alternative models of Park [88] and Dunn and Kang [118]. We choose the static pressure of such numerical experiment to be $P_{\mathrm{s}} = 100$ hPa, while the edge velocity is chosen so that we obtain a dynamic pressure $P_{\mathrm{d}} = 16.6$ Pa for an edge temperature of $T_{\delta} = 5500$ K, and Barker effect correction coefficient $K_{\mathrm{H}} = 1.1$ [136]. We impose the temperature at the wall for the high catalytic material to be $T_{\mathrm{w}}^{\mathrm{H}} = 350$ K while the low catalytic material has a wall temperature of $T_{\mathrm{w}}^{\mathrm{L}} = 750$ K similar to our copper and quartz probes. We also take the non-dimensional parameters (Sec. 3.3) to be the same as the case MTAt6 which would be equivalent to a Plasmatron power of 191 W and mass flow of 16 g/s. The uncertainties on all the considered measured quantities are consistent with the values reported in the literature for Plasmatron and in this work. The simulated heat fluxes are then taken as measurements from this numerical experiment with a ±10% uncertainty level for a 2σ confidence interval. We then compute the S-shaped curves from the simulated heat fluxes with their true chemistry in Fig. 6.12 (Gupta et al. model, continuous lines) and a faster chemistry model (Park, dashed lines). It can be appreciated that using a faster chemistry model when the heat fluxes correspond to a simulation with a slower gas chemistry model can result in S-shaped curves distancing away (or the opposite if the model used to reconstruct the simulated data uses a slower chemistry model than the original simulation). This issue can be evidence that in the high pressure experiments S-shaped curves do not overlap because the chosen model overestimates the speed of the chemical reactions in the gas phase.

Fig. 6.12 shows the line corresponding to the edge conditions of the numerical experiment which touches each S-shaped curve at the limits of their γ values as chosen for each material. In Fig. 6.12, it can also be seen that low catalytic efficiencies need lower enthalpies to produce the same heat flux with a faster chemistry model than with a slower one. Enthalpies for large catalytic efficiencies do not change under gas chemistry models. This effect can be traced to the diffusive regime at the wall. The Damköhler number at the wall for large recombination efficiencies (fast wall chemistry) is large, meaning that we are in a diffusion limited regime. Different chemical models in the gas do not have an impact on the diffusive fluxes at the wall, setting the same outer edge conditions for all cases. On the other hand, reaction limited walls are more susceptible to the gas chemical models. Slower chemistry produces smaller concentration gradients which are easily overcome by species diffusion. This tendency produces smaller diffusion fluxes for the same pressure, which has to be compensated by larger temperature gradients across the boundary layer. As a result, higher enthalpies at the edge are required for the same heat flux in the case of slower chemistry at small wall Dankӧhler numbers. It is equivalent to changing the Damköhler number of the flow to smaller values as the chemistry gets slower, while the diffusion time scale stays the same.

The right side of Fig. 6.12 shows the two S-shaped curves obtained with the Park chemistry model and their associated confidence intervals when considering only the measurements as uncertain. In this scenario, an assumption of faster gas chemistry is considered where the actual data comes from a flow with slower chemistry. In this case, not even including the measurements uncertainties can give any solutions, or common edge conditions. The shaded grey area represents the added uncertainty when also the chemistry is assumed uncertain. The uncertainty on the chemistry is bounded by the slowest and fastest models that can be assumed for the problem, Gupta et al. and Park, respectively. This changes the picture by enabling possible solutions. Nonetheless, it can be observed that more than 50% of the resulting uncertainty for low catalytic values is due to the chemistry alone. The take away from this exercise is that the chemistry should be calibrated in dedicated experiments to obtain reliable predictions in the future, as it is shown to impact whether or not the chosen model can explain the experimental data, and this, in turn, influences the calibrated γ_{TPS} obtained. This issue was already studied by Viladegut et al. [99] from a different perspective. They studied different diffusion regimes while maintaining the same chemistry models and showed that the coupling between diffusion and chemistry in the flow has an impact on the computed values for catalytic efficiencies from experiments.

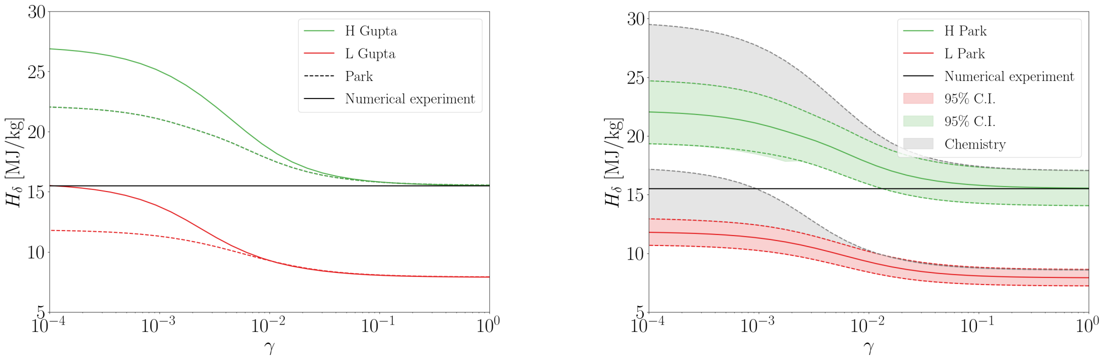

Figure 6.12: *S-shaped curves for the chosen boundary layer simulation with slow and fast chemistry (left). Propagated uncertainty on the S-shaped curves of the numerical experiment, including uncertain chemistry models (right).*

This issue does not influence the main outcomes of this study. If the adequacy of the chemical models are case-dependent, then for the same cases the proposed experimental methodology still should perform better under equal chemical model epistemic uncertainties. The major impact would be related to the final calibrated values and how those are affected by these epistemic uncertainties.

It is important to remark that the highlighted issues with the modeling of the gas phase chemistry are just one hypothesis given to explain the discrepancies observed in the results for high pressures. The likely real scenario might be a mix of different model inadequacies in various closures and assumptions, such as assumed elemental fractions at the boundary layer edge, thermal state of the gas, etc. The relevance of the numerical exercise rests on the capability to define new research avenues and identify further model issues.

Summary statistics. The resulting summary statistics for the different γ_{TPS} parameters are shown in Table 6.6. The resulting statistics for H_δ^{opt} after propagation of the calibrated parameters are shown in Table 6.7. Only the cases with successful inferences are shown.

Table 6.6: γ_{TPS} *marginal posterior distributions: mean, Maximum A Posteriori and 95% C. I. values.*

Experiment ID	P_{s} [hPa]	Mean (μ) γ_{TPS}	MAP γ_{TPS}	95% C.I. γ_{TPS}
MTAt1	15	0.01	0.012	[0.0029, 0.0276]
MTAt2	15	0.011	0.019	[0.0036, 0.0289]
MTAt3	15	0.013	0.023	[0.0044, 0.0303]
MTAt4	50	0.0048	0.0048	[0.0030, 0.0076]
MTAt5	100	0.0077	0.0076	[0.0035, 0.0167]

Table 6.7: $H_{\delta}^{\mathrm{opt}}$ *distributions: mean, Maximum A Posteriori and 95% C. I. values.*

Experiment ID	P_{s} [hPa]	Mean (μ) $H_{\delta}^{\mathrm{opt}}$ [MJ/kg]	MAP $H_{\delta}^{\mathrm{opt}}$ [MJ/kg]	95% C.I. $H_{\delta}^{\mathrm{opt}}$ [MJ/kg]
MTAt1	15	12.6	11.5	[10.8, 15.7]
MTAt2	15	21.1	15	[14.3, 31.7]
MTAt3	15	26.0	17.8	[17.3, 36.7]
MTAt4	50	14.7	14.7	[13.9, 15.5]
MTAt5	100	11.2	11.2	[10.7, 11.7]

6.5 Summary

In this chapter, we extend the contribution of Chapter 5 by proposing a more informative experimental methodology and performing stochastic analyses on the resulting plasma wind tunnel data, enriching current catalysis databases.

First, we study the choice of reference material with respect to the information that it brings about the free stream. As the difference between the catalytic responses of the materials tested grows, so does the information we can obtain about the free stream conditions in the wind tunnel. On these lines, we also perform a study of a 3-probes testing methodology and show an overall improvement on the characterization of copper catalysis up to 80% with respect to the results of Chapter 5. The 3-probes testing methodology case study reveals that the ideal possible testing scenario is with three materials where a good characterization is achieved for the one in the middle of the catalytic parameter space.

Following these preliminary studies, we propose an experimental set-up for the accurate calibration of catalytic efficiencies of CMC materials. The proposed 3-probes testing methodology proves to be a good experimental approach due to the fact that the surface catalytic activity of the TPS material lays in between the catalytic activity of the two reference materials chosen (copper and quartz). This conclusion is first reached by performing a synthetic case study which combines data from two different experimental campaigns available in the literature. The results of this synthetic study increases our confidence in the proposed methodology with which real experiments are performed in the VKI Plasmatron by Luís et al. [236] for the context of this study.

A set of seven test cases is proposed under different static pressures and heat fluxes to study their influence on the results. The results show two different classes of characterizations achieved. First, for low pressures of 15 mbar, we show an improvement of 50 % over previous analyses. Even though it is still an improvement, we can appreciate a considerable support for the TPS material marginal distribution and a tendency towards following bimodal distributions.

In contrast, higher pressure cases such as 50 and 100 mbar, yield very precise parameters. Nevertheless, we should not lose sense of the fact that the gas chemistry is considered well-known. The diffusive fluxes in these cases are set in within some limits due to the chemistry being most likely in equilibrium, leaving little room for the outer edge enthalpy values which, in turn, are heavily conditioned. In this regard, a well characterized and precise TPS catalytic parameter can be obtained. The reduction of the uncertainty in this case is 30-50 % with respect to the previous 15 mbar cases and it relies solely on the chosen testing conditions. Nevertheless, not all the inferred parameters can be trusted. The model is found not to be a good representation of the experiments for two of the cases. Alternative explanations such as the uncertainty on the chemical state of the gas could lead to an improvement.

In the future, dedicated experimental campaigns, including spectroscopic measurements, can benefit from this work by exploiting the experimental data more thoroughly and incorporating additional knowledge and uncertainties in terms of the gas phase chemistry.

Chapter 7

Calibration of graphite ablation models for nitrogen flows

In this chapter, we study the problem of carbon ablation when subjected to high temperature nitrogen flows. In this context, we seek to infer nitrogen ablation model parameters combining different experimental measurements and various flow model assumptions. First, the dependencies of the proposed stagnation line forward model are studied to establish the influence of the different parameters on the available observations. The model calibrations are performed taking into account the relevant observations for the unknown parameters such as boundary layer edge and wall conditions, and nitrogen ablation parameters. We compare the results of the various inferences performed for which different relevant observations are considered. The comparisons allow us to test the consistency of the given observations. Using only the trustworthy experimental data, a calibration of the Arrhenius law parameters for nitridation efficiencies is performed taking into account all available experimental conditions jointly. Finally, we test different flow modeling choices against the same experimental data for which we define hypotheses testing scenarios. Based on the successful models we build model averages on the common inferred nitridation parameters to capture the epistemic uncertainties due to the thermal state of the flow as well as the heterogeneous chemistry at the surface. The resulting summary statistics of the averaged parameter posteriors are given.

7.1 Motivation and problem definition

Characterizing ablation phenomena for different atmospheric and material compositions is quite challenging. It is important to understand the coupling mechanisms between material surface properties and the resulting ablation rates which in turn are coupled to the flowfield computations [237]. A key element of the modeling behind these phenomena is the surface chemical processes that are taken into account to explain the experiments. It is not always straightforward, from an a priori point of view, to know which chemical processes underpin the macroscopic effects we see in thermal protection materials subjected to reactive flow environments. Through dedicated experiments which manage to isolate and identify different chemical mechanisms, we are now in the position to fill in the knowledge of the selected model parameters with experimental data.

Parts of this chapter have been published in

- A. del Val, O. P. Le Maître, O. Chazot, P. M. Congedo and T. E. Magin, **Inference methods for gas/surface interaction models: from deterministic approaches to Bayesian techniques**, *Uncertainty Quantification & Optimization 2020 conference proceedings.*

The nitridation reaction $C_s + N \rightarrow CN + 0.34eV$ on a solid (s) carbon surface is still weakly understood. There have been experimental efforts to characterize it [21, 44, 139] but the different methods used to rebuild nitridation efficiencies from experimental data give out results that differ by several orders of magnitude. Even though the low exothermic energy of the nitridation reaction does not directly have a significant influence on the wall heating rate, it can indirectly affect exothermic recombination reactions at the wall. In recent works, Helber et al. [22] determined the nitridation reaction efficiency of graphite at surface temperatures up to 2,575 K with a coupled deterministic experimental-numerical approach. For the reconstruction of the nitridation efficiency parameter, they used recession rate measurements, while assuming negligible the recombination of nitrogen at the wall. The proposed methodology was validated with the experiments by comparing the predicted CN species densities in the boundary layer with the CN densities experimentally derived from the recorded CN violet emission.

In the present chapter, we explore the possibility of exploiting such experimental data for the purpose of inferring nitridation reaction efficiencies in a statistical setting by means of a Bayesian approach. We first conduct an a priori analysis of the forward model, a thermal equilibrium stagnation line flow with nitridation as the only surface mechanism. We can assess the sensitivity of the model to each input parameter by propagating a priori uncertainty ranges. To lighten the computational burden of the propagation, we construct different GP surrogates for the model outputs. This a priori exploration of the model leads to the simplification of the inference problem by prescribing the important experimental observations for nitridation efficiencies determination. Recession rates and local CN densities are used, together with static pressures, dynamic pressures and wall temperatures, to infer all parameters needed to define the flow solutions: boundary conditions and constitutive relation parameters, where we include the nitridation reaction efficiencies. When used independently, measured recession rates and CN densities each give information about nitridation reactions. As they are both part of the same experiments, one model should be capable of explaining both observations at once. Checking for this consistency with the available data has the potential of improving the characterization of nitridation mechanisms and signaling issues with the model and/or the experiments. We make use of the surrogate models built previously for the sensitivity analysis to make the problem of the inference computationally efficient when sampling the posterior distribution. Further, we also propose to combine all available measurements for the calibration of a stochastic Arrhenius law, extending the computation of nitridation efficiencies to a broader span of surface temperatures for which there are no reliable experimental data.

Lastly, the assumption of a thermal equilibrium model with only nitridation as surface process is questioned. Hypothesis testing scenarios are proposed to gauge the evidence in the available experimental data towards different modeling assumptions considering thermal non-equilibrium in the flow, as well as the importance of nitrogen surface recombination. The final parameter posterior distributions obtained under each successful model are weighted and summed using Bayesian model averaging to account for the epistemic uncertainties stemming from these different modeling assumptions. We find weak evidence for thermal non-equilibrium at the wall, and are able to set a plausible upper limit for nitrogen surface recombination.

This chapter is structured as follows. First, we include a literature review of nitridation experiments and estimations to discuss and highlight the state-of-the-art results. A detailed study of the stagnation line model follows, where we discuss the assumptions considered in the baseline forward model, and what are the parameters that need estimation from the experimental data. We then perform an a priori study of this model where a sensitivity analysis of its inputs with respect to its outputs is carried out by means of surrogate models. The developed Bayesian methodology and results for the baseline model are included next. Finally, we discuss the methods and results of the model assessments and averaging.

7.2 Review of previous works

In general, nitridation reaction efficiencies result from elaborated processes that combine models and experiments. In the next sections, we show a summary of experimental methods and how nitridation efficiencies are derived from them. This review includes traditional deterministic estimations usually carried out by the experimentalists themselves as well as state-of-the-art statistical approaches.

7.2.1 Experimental efforts and deterministic inverse approaches

In the literature, there exist multiple experimental ways of testing for carbon nitridation efficiencies, from ICP wind tunnels to molecular beams. Except for the case of the molecular beam, not a single experiment has a straightforward interpretation for the derivation of nitridation efficiencies. They require several layers of assumptions about the experimental apparatus and its theoretical modeling that could render the obtained parameters dubious. Molecular beam experiments, on the other hand, can directly measure reaction probabilities through the products scattering dynamics. Nevertheless, it is difficult to relate hypersonic boundary layer conditions to those recreated with the beam which are limited to low pressure conditions.

Microwave discharges. The experimental work of Goldstein in 1964 [238] was the first in which the nitridation reaction was carefully assessed as function of the surface temperature. The microwave-activated nitrogen would react with the exposed carbon surface and cause it to lose mass through heterogeneous chemistry reactions. By measuring the concentration of products of such interactions and the concentration of nitrogen atoms at the inlet, Goldstein was able to pinpoint the ratio of cyanogen products to active nitrogen available. Zhang et al. [44] studied the problem experimentally with similar methods to the ones used by Goldstein. They employed a furnace-heated quartz flow tube coupled to a microwave discharge. The N-atom concentrations entering and exiting the furnace were measured by chemical titration as done previously by Goldstein. The missing piece was the atom concentration at the graphite sample location. For that, they used a simple reactive-flow model with which they interpolated the atomic nitrogen concentrations measured in the inlet and outlet. The reaction efficiency for graphite nitridation was derived from the interpolated N-atom concentration and the measured graphite mass loss for a given test time.

Shock tubes. Park and Bogdanoff [239] decided to extract nitridation reaction efficiencies from shock tube experiments at the NASA Ames Electric Arc Shock-Tube (EAST) for lower surface temperatures. They placed a grid of metal wire coated with carbon downstream the discharge of the shock tube. The observations were based entirely on the radiative signature of the gas cyanogen (CN) present in the wake of the flow after passing through the exposed grid. From the intensity of the radiation detected, they could determine CN concentrations by using a radiation model based on Boltzmann populations of the internal energy levels of the participating particles. A flow model was used to obtain predictions of the nitrogen atom concentrations in the freestream. The concentration of CN in the wake compared to that of N in the impinging stream gives out the fraction of atoms that actually reacted to create CN, defining the reaction rate coefficient.

Plasma wind tunnels. Suzuki et al. [21] in 2008 were the first ones to derive nitridation reaction efficiencies from ICP wind tunnels. They heated a graphite rod subjected to a high-temperature nitrogen flow in the test section of the wind tunnel. The amount of mass loss and the surface temperature of the graphite rod were measured during the experiments. The value of the atomic nitrogen number density striking onto the graphite rod was estimated by calculating the flowfield around the graphite rod without accounting for nitridation at the surface. Nitridation reaction efficiencies were deduced from the amount of mass loss rate, the surface temperature, and the atomic nitrogen number density computed. The results obtained differed significantly from the ones derived by Park and Bogdanoff which sparked more contributions to the topic. In 2010, Suzuki et al. [240] provided new data and inferred nitridation reaction efficiencies for lower surface temperatures following the same methodology. More recently, Helber et al. [22] performed experiments in the VKI Plasmatron to determine nitridation reaction efficiencies. They pushed the boundaries of the state of the art with respect to the work of Suzuki et al. [21] for higher surface temperatures. They did so by including nitridation in the computation of atomic nitrogen wall concentration as well as adding optical emission spectroscopy measurements of the CN radiative signature in the flowfield in front of the graphite sample. The more accurate modeling, together with an additional independent measurement sensitive to CN production allowed them to compute an updated Arrhenius law for nitridation reaction efficiencies backed-up by the validation with the spectroscopy measurements.

All the above experimental techniques and methods to retrieve nitridation reaction efficiencies rely on modeled components such as the atomic nitrogen concentrations at the sample locations. Depending on the nature of the experimental facility, different assumptions are made about the flow and the physical models used. Park and Bogdanoff's estimations are two orders of magnitude above the other researchers. Their choice to rely on radiation models adds complexity and, therefore, assumptions to their inference problem. Plasma wind tunnels and microwave discharges data also differ substantially from each other.

Molecular beams. In the last couple of years, molecular beam experiments at lower pressures were performed by Murray and Minton [29] for the study of ablation in hypersonic flight. A pulsed molecular beam containing atomic and molecular nitrogen was directed at a vitreous carbon surface held at temperatures relevant to hypersonic flight. They measured the scattering products at different angles and their Time Of Flight (TOF). The scattering dynamics of CN in such environment indicated that it was formed through a mechanism in thermal equilibrium with the surface. They also computed the activation energy of nitridation reaction efficiencies following an Arrhenius rate law with the surface temperature. More recently, Murray et al. [30] produced another set of molecular beam data with a continuous beam to address some of the assumptions and uncertainties of the previous work. The experiments had relatively modest incident velocities with high atom fluxes and roughened and disordered surfaces to make the exposure conditions similar to those of actual hypersonic flights. Consequently, Prata et al. [241] built an air-carbon ablation model for hypersonic flight which includes nitridation based on such data. Most of the parameters of the finite-rate chemistry model were physically motivated a priori or fitted from different experiments. Their aim was to identify pressure dependent characteristics in the proposed finite-rate air ablation model by deterministically comparing their predictions to the available data in the literature at high and low pressures. While the molecular beam experiments manage to get a direct estimation of nitridation reaction efficiencies without the need to introduce many assumptions, the extrapolation of the beam experimental conditions to actual duplication of hypersonic reacting boundary layers is very much subjected to additional uncertainties. The more detailed surface chemical mechanism and generalization of the model to different pressures need to be leveraged with proper stochastic approaches to really see how much far ahead we can see.

7.2.2 Statistical inverse approaches

The only account of stochastic approaches for the inference of nitridation reaction efficiencies is found in the work of Upadhyay et al. [43]. In their work, the authors re-formulated the inference problem performed by Zhang et al. [44] as a statistical inverse problem, which they solved using the Bayesian formalism. They formulated four different model classes that differ in the physical model itself and the parameters considered uncertain. They were able to calibrate power laws for each model class for the dependence of nitridation reaction efficiencies with surface temperatures.

It is difficult to derive definite conclusions from this work given the fact that they compared the different model classes by only looking at the marginal posteriors of the different parameters. A proper hypothesis testing study is lacking to really assess the evidence of each model for such experimental data. Even though the parameters to be calibrated are the same for the two physical models proposed, the more detailed model can achieve so by considering some of its parameters as perfectly known which might not be the case. Extra parameters can make the detailed model perform poorly compared to the simpler one on the basis of complexity in a hypothesis testing study. Further, the physical models used were built on many assumptions which also prevents us from deriving consistent takeaways from this work. Moreover, the final calibrated power law does not capture any of the additional nitridation data reported in the literature.

7.3 On the stagnation line model

The stagnation line code reviewed in Sec. 3.1.2 is used to perform efficient simulations of the reacting boundary layers in front of the graphite samples with ablative wall conditions.

The inlet boundary condition imposed for the simulations of such reacting flows comprises species densities ρ_i, temperature T, and velocity components u, v, while the surface conditions are temperature at the wall T_{w}, which closes the energy equation; we assume no slip condition, which closes the momentum equations, and we define surface mass balances for the species mass equations. These mass balances need the chemical mechanism at the surface to be specified and we also need to give values to the different parameters. The information needed to prescribe the boundary condition at the free stream pertains to a supersonic inlet even though we want to carry out subsonic simulations. This methodology has been investigated and discussed in [123], where it was verified that the solution of the Riemann problem at the boundary interface automatically screens the information needed from the inlet.

All in all, we intend to find the flow solutions that are compatible with our experimental observations under the considered model. This means that from the observations reported by Helber et al. [22], we want to infer the inlet conditions and the wall conditions in such a way that we are left with a population of possible flow solutions. As we work with a mixture of 9 species: $\mathcal{S} = \{\mathrm{e}^-, \mathrm{C}^+, \mathrm{C}_2, \mathrm{C}_3, \mathrm{CN}, \mathrm{C}, \mathrm{N}, \mathrm{N}^+, \mathrm{N}_2\}$, we are left with a 14-dimensional problem if we only consider nitridation at the wall. The predictive quantities $\dot{s}$ and ρ_{CN} we are after would read

$$\dot{s} = \dot{s}\left(\rho_{\delta,i}, u_\delta, v_\delta, T_\delta, T_{\mathrm{w}}, \gamma_{\mathrm{N}}^{\mathrm{CN}}\right), \quad \forall i \in \mathcal{S}, \tag{7.1}$$

$$\rho_{\mathrm{CN}} = \rho_{\mathrm{CN}}\left(\rho_{\delta,i}, u_\delta, v_\delta, T_\delta, T_{\mathrm{w}}, \gamma_{\mathrm{N}}^{\mathrm{CN}}\right), \quad \forall i \in \mathcal{S}, \tag{7.2}$$

where the subscript δ defines the boundary layer edge conditions. The terms u_δ and v_δ refer to the radial and axial stagnation line velocities, respectively. The fact that we carry out one dimensional simulations and we need to specify two velocity components falls from the assumed ansatz for the derivation of the dimensionally-reduced Navier-Stokes equations (Sec. 3.1.2). The velocity components should be set to comply with the velocity gradient and dynamic pressure we want to impose at the inlet. As can be appreciated, not all the unknown parameters are of interest for us given that we are only interested in learning the nitridation parameter $\gamma_{\mathrm{N}}^{\mathrm{CN}}$. Nevertheless, these nuisance parameters must be included in the inference as they constitute unknowns of the problem and they are needed to carry out the flow simulations.

We can reduce the dimensionality of the problem by taking into account some physical relationships. As we recall, for the VKI Plasmatron, given the electric power, injected mass flow, static pressure and probe geometry, we can recuperate some boundary layer edge parameters. The radial velocity u_δ can be expressed as a linear relationship with v_δ through the velocity gradient $(\partial u/\partial x)\big|_\delta = (u_\delta + v_\delta)/R_0$ [61], where x is spatial coordinate for the radial direction and R_0 is the equivalent spherical radius of the probe. From the subsonic VKI Plasmatron flowfield simulation depicted in Sec. 3.3, non-dimensional parameters (NDPs) for the boundary layer thickness δ, the velocity gradient, and the axial gradient of the velocity gradient, both at location δ, can be defined [145, 146]. The dynamic pressure, corrected for viscous effects $P_{\mathrm{d}}/K_{\mathrm{H}} = 1/2\rho_\delta v_\delta^2$ with K_{H} as Homman's correction factor [136], is used as a convenient proxy for the axial velocity v_δ. Together, the non-dimensional parameters and the dynamic pressure define the inlet velocities imposed by the experimental conditions. As we are assuming a boundary layer edge in chemical equilibrium, the density ρ_δ in the dynamic pressure expression, as well as $\rho_{\delta,i}$ are defined by the temperature T_δ and pressure P_δ for a fixed elemental composition. In sum, the following functional relationships are introduced as valid additional relations of the boundary layer edge conditions to some characteristics of the experimental set-up

$$\rho_{\delta,i} = \rho_{\delta,i}(T_\delta, P_\delta), \tag{7.3}$$

$$u_\delta = u_\delta(\mathrm{NDPs}, P_{\mathrm{d}}, T_\delta, P_\delta), \tag{7.4}$$

$$v_\delta = v_\delta(\mathrm{NDPs}, P_\mathrm{d}, T_\delta, P_\delta). \tag{7.5}$$

It is possible to test these assumptions by getting rid of the additional structure in our model, considering species densities and different thermal bath temperatures as unknowns of the inference problem. At the end of the analysis, for given Plasmatron operating conditions, we are left with the expressions

$$\dot{s} = \dot{s}\left(P_\mathrm{d}, T_\delta, P_\delta, T_\mathrm{w}, \gamma_\mathrm{N}^\mathrm{CN}\right), \tag{7.6}$$

$$\rho_\mathrm{CN} = \rho_\mathrm{CN}\left(P_\mathrm{d}, T_\delta, P_\delta, T_\mathrm{w}, \gamma_\mathrm{N}^\mathrm{CN}\right), \tag{7.7}$$

where the momentum boundary layer edge parameters u_δ, v_δ have been replaced by the dynamic pressure P_d, given that the non-dimensional parameters are taken as constant. These expressions constitute the dependencies of the forward model.

Apart from the dedicated nitridation measurements, Helber et al. performed another set of tests aimed at recovering the free stream conditions T_δ for each case by using a water-cooled copper calorimeter [22] (see Sec. 3.2.2). In this chapter, we evaluate how important is the information about the free stream conditions in the inference of $\gamma_\mathrm{N}^\mathrm{CN}$. For this purpose, we only depict here the additional pressure measurements which are a priori included in the inference proposed. A water-cooled Pitot probe measures the dynamic pressure P_d within the plasma jet, and an absolute pressure transducer records the static pressure P_s in the Plasmatron chamber.

7.4 A priori analysis of the forward model

This section explores the different dependencies of the forward model and builds a hierarchy of influential parameters on the predictive quantities. This helps us understand what parameters are the drivers of the inference and what observations are relevant to consider.

The forward model depicted in Sec. 7.3 depends on a set of nuisance parameters and quantities of interest. We are concerned with the capabilities of learning $\gamma_\mathrm{N}^\mathrm{CN}$ from the experimental data of Helber et al. [22]. For this purpose, we first perform an uncertainty propagation by assuming a priori uncertainty ranges on the input parameters. We then perform a variance-based sensitivity analysis and derive sensitivity indices for the dependencies of the model.

Non-intrusive uncertainty propagation involves multiple evaluations of the forward model. This step can be very expensive and burdensome as each individual evaluation should also have good convergence properties. We decide to lighten the burden by building surrogates on the predictive quantities $\dot{s}$ and ρ_CN. These surrogate models are also used later in the inference.

7.4.1 Surrogate modeling

To construct the surrogates, we first introduce new canonical random variables for the 5 parameters upon which $\dot{s}$ and ρ_CN depend, $\boldsymbol{\xi} = (\xi_{P_\mathrm{d}}, \xi_{T_\delta}, \xi_{P_\delta}, \xi_{T_\mathrm{w}}, \xi_{\gamma_\mathrm{N}^\mathrm{CN}})$. We set $\boldsymbol{\xi}$ to be defined over the unit hypercube: $\boldsymbol{\xi} \in [0,1]^5$ in order to simplify the training and use of the surrogate models. We then fix the a priori ranges in the physical variables to be $P_\mathrm{d}(\xi_{P_\mathrm{d}}) = 200 + \xi_{P_\mathrm{d}}160$, $T_\delta(\xi_{T_\delta}) = 9000 + \xi_{T_\delta}4000$, $P_\delta(\xi_{P_\delta}) = 1200 + \xi_{P_\delta}500$, $T_\mathrm{w}(\xi_{T_\mathrm{w}}) =$

$2000 + \xi_{T_\mathrm{w}}2000$, and $\gamma_\mathrm{N}^\mathrm{CN}(\xi_{\gamma_\mathrm{N}^\mathrm{CN}}) = 10^{-4\xi_{\gamma_\mathrm{N}^\mathrm{CN}}}$, such that they all have canonical range 1. The ranges are chosen large enough to acommodate possible parameter values under the experimental conditions considered.

We seek to construct surrogates of the $\dot{s}$ and ρ_CN with this parametrization. In particular, we decide to proceed with the log of $\dot{s}$ and ρ_CN (from now on referred to as log variables) instead of the natural variables as it ensures the positivity of the approximation. More precisely, we aim for surrogate models of $Y_{\dot{s}}(\boldsymbol{\xi})$ and $Y_{\rho_\mathrm{CN}}(\boldsymbol{\xi})$ defined by

$$Y_{\dot{s}}(\boldsymbol{\xi}) \doteq \log\left(\dot{s}(\boldsymbol{\xi})\right), \tag{7.8}$$

$$Y_{\rho_\mathrm{CN}}(\boldsymbol{\xi}) \doteq \log\left(\rho_\mathrm{CN}(\boldsymbol{\xi})\right). \tag{7.9}$$

We propose to use Gaussian process models to approximate these functions (Sec. 4.8.1).

The surrogate models are built on an initial 600 points grid where Latin Hypercube Sampling (LHS) is chosen due to its capability to explore all the unit hypercube evenly. This is particularly important when dealing with chemical parameters such as $\gamma_\mathrm{N}^\mathrm{CN}$ which generally can cause irregular behavior of the simulated quantities, especially if the surface temperature T_w can also vary from point to point. An extra 600 points are added in a Monte Carlo fashion to enrich the approximation around the areas with largest variance of the GP prediction if needed. Fig. 7.1 shows the normalized L_2 norms of the errors of the surrogate approximations for both log variables. The L_2 norms are changing as we increase the number of points used to train the surrogates while keeping the same validation sets to compute the errors (10% of all available points). This process is done 1,000 times with different validation sets to produce the 95% confidence intervals depicted in Fig. 7.1. The normalized errors drop fairly quickly below 1%.

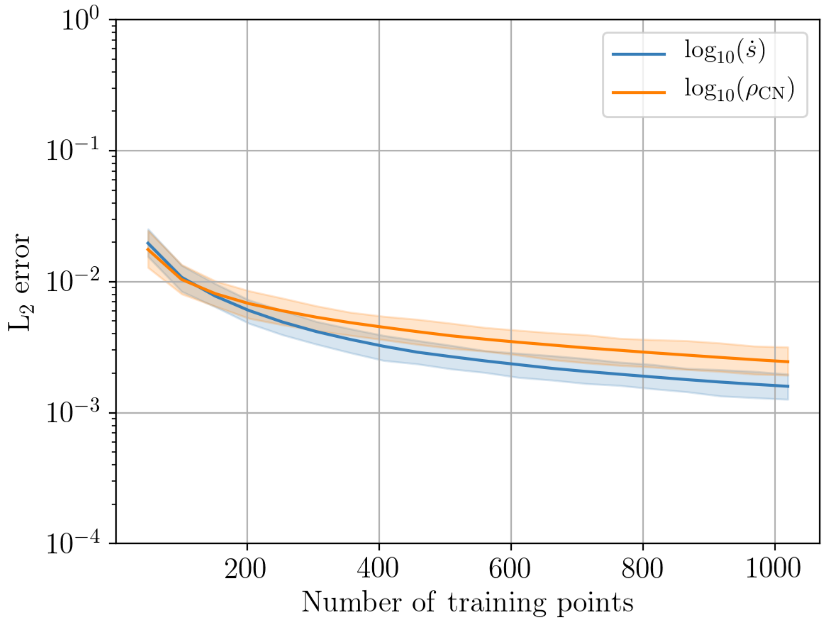

Figure 7.1: *Normalized* L_2*-error norms of the log variables approximations.*

7.4.2 Sensitivity analysis

Once we have built the surrogate models, we can propagate the uncertainty from the inputs and model parameters to the outputs. Particularly, we are interested in knowing if the uncertainty on the free stream information T_δ is important for the variability of recession rates $\dot{s}$ and CN densities ρ_{CN}. If those two observed quantities are not sensitive enough to the variation of temperature T_δ, we would not need to add the additional experimental data to our inference as it would not bring any useful information for $\gamma_{\mathrm{N}}^{\mathrm{CN}}$. Furthermore, the treatment of the measurements for free stream determination entails additional models and computations, increasing the complexity of the inference for no gain.

We propagate the input distributions depicted in Table 7.1. In this case, we only perform this analysis for one of the experimental cases as the modeling and experimental data remain consistent for all. Whenever possible, the ranges and distributions of the input variables are taken directly from the available measurements. When no experimental counterpart is available, the same ranges as the ones prescribed for the construction of the surrogates are used. This is the case for the boundary layer edge temperature T_δ and the nitridation reaction efficiency $\gamma_{\mathrm{N}}^{\mathrm{CN}}$. The pressure at the edge of the boundary layer P_δ is taken as the chamber static pressure P_{s}, therefore its uncertainty is taken as the corresponding experimental uncertainty associated with P_{s}.

Table 7.1: *Input uncertainties for the a priori forward model analysis.*

Experiment **ID**	P_{d} [Pa]	T_{w} [K]	P_δ [Pa]	T_δ [K]	$\gamma_{\mathrm{N}}^{\mathrm{CN}}$ -
G5	$\mathcal{N}(268, 2.68)$	$\mathcal{N}(2410, 12.05)$	$\mathcal{N}(1500, 22.5)$	$\mathcal{U}[9000, 13000]$	$\log \mathcal{U}[-4, 0]$

The values in the table are normalized within the ranges prescribed for building the surrogates. We then obtain the corresponding uncertainty distributions for the canonical variables $\boldsymbol{\xi}$ from which to input the GP surrogate models and perform the propagation. Fig. 7.2 shows the values of $\dot{s}$ and ρ_{CN} for the propagated canonical inputs $\boldsymbol{\xi}$. This exercise clearly shows which parameter dominates the variability of each predicted quantity $\dot{s}$ and ρ_{CN}. Under the considered testing conditions (and also for the other test cases), $\gamma_{\mathrm{N}}^{\mathrm{CN}}$ is the most important parameter for the variability of recession rates and CN densities. None of the other parameters play a substantial role. We can appreciate a small influence of T_δ on the variability of ρ_{CN} but qualitatively seems very negligible compared to the effect of $\gamma_{\mathrm{N}}^{\mathrm{CN}}$.

Quantitatively, we can compute the associated first and total order Sobol' indices (see Sec. 4.8.2) to establish a hierarchy among the variables and reliably assess the influence of the uncertainty of T_δ on $\dot{s}$ and ρ_{CN}. Fig. 7.3 shows the outcome of the Sobol' indices computation. The result shows almost two orders of magnitude difference in the influence of the uncertainty of $\gamma_{\mathrm{N}}^{\mathrm{CN}}$ over the uncertainty of T_δ on ρ_{CN} and even more for $\dot{s}$. A red arrow is placed to highlight the indices associated with $\gamma_{\mathrm{N}}^{\mathrm{CN}}$. This shows the fact that good knowledge of the boundary layer edge conditions does not play a significant role in the inference of $\gamma_{\mathrm{N}}^{\mathrm{CN}}$ from recession rates and/or CN densities when the other variables are known to the prescribed degree of uncertainty. We can now safely ignore the rest of the experimental data gathered by Helber et al. (no depicted in this work, see [22]).

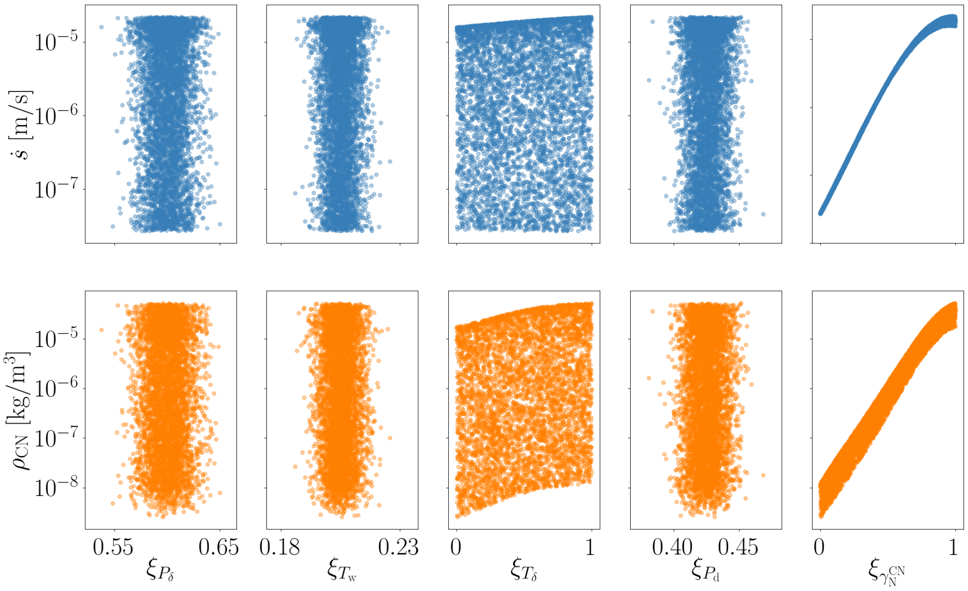

Figure 7.2: *Resulting recession rates and CN densities for the propagated a priori uncertainty distributions of the canonical variables* $\boldsymbol{\xi}$.

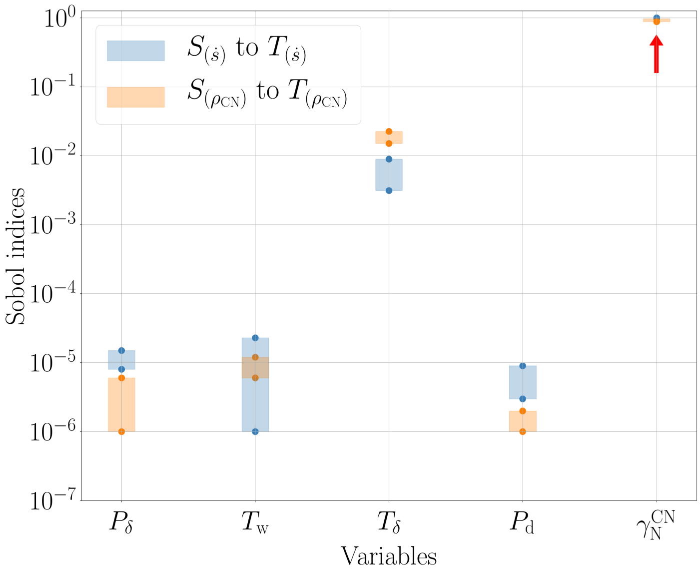

Figure 7.3: *First and total order partial variance decompositions for* $\dot{s}$ *and* ρ_{CN}. *The rectangles represent the change from first to total order sensitivity indices.*

7.5 Bayesian inference methodology

In this section, the Bayesian framework is presented in detail. First, the formulation of the inverse problem is reviewed for the inference of nitridation reaction efficiencies. The likelihood function and prior distributions are highlighted next.

7.5.1 Bayesian formulation of the inverse problem

The inference of model parameters uses the Bayes formula which can be generically formulated as

$$\mathcal{P}(\boldsymbol{q}|\boldsymbol{y}_{\text{obs}}) = \frac{\mathcal{P}(\boldsymbol{y}_{\text{obs}}|\boldsymbol{q})\ \mathcal{P}(\boldsymbol{q})}{\int_{\Omega} \mathcal{P}(\boldsymbol{y}_{\text{obs}}|\boldsymbol{q})\ \mathcal{P}(\boldsymbol{q}) d\boldsymbol{q}}, \tag{7.10}$$

where $\boldsymbol{q} = (P_{\text{d}}, T_{\delta}, P_{\delta}, T_{\text{w}}, \gamma_{\text{N}}^{\text{CN}})$ is the generic vector of parameters, having for components the parameters of the analysis. The vector $\boldsymbol{q}$ results from the stagnation line modeling and physical considerations presented in Sec. 7.3. The term $\boldsymbol{y}_{\text{obs}} = (P_{\text{d}}^{\text{meas}}$, $P_{\text{s}}^{\text{meas}}$, $T_{\text{w}}^{\text{meas}}$, $\dot{s}^{\text{meas}}$, $\rho_{\text{CN}}^{\text{meas}})$ is the vector of the measured quantities used for the analysis. For compact notation, we split the observations and parameters to be inferred in two distinct subsets. The subset $\boldsymbol{q}' = (P_{\text{d}}, P_{\delta}, T_{\text{w}})$ whose parameters have direct measured counterparts, and the subset $\boldsymbol{q}'' = \left(T_{\delta}, \gamma_{\text{N}}^{\text{CN}}\right)$ whose parameters appear implicitly in the model outputs dependencies such that $\boldsymbol{q} = (\boldsymbol{q}', \boldsymbol{q}'')$. Similar subsets are defined for the observations set. The subset $\boldsymbol{y}'_{\text{obs}} = (P_{\text{d}}^{\text{meas}}, P_{\text{s}}^{\text{meas}}, T_{\text{w}}^{\text{meas}})$, and the subset $\boldsymbol{y}''_{\text{obs}} = (\dot{s}^{\text{meas}}, \rho_{\text{CN}}^{\text{meas}})$ are defined such that $\boldsymbol{y}_{\text{obs}} = (\boldsymbol{y}'_{\text{obs}}, \boldsymbol{y}''_{\text{obs}})$. We denote $\mathcal{P}(\boldsymbol{q})$ the prior probability distribution of the parameters.

We recall that usually the posterior distribution in Eq. (7.10) is not known in a closed form due to the complexity of the mapping $\boldsymbol{q} \to M(\boldsymbol{q})$ where $M(\boldsymbol{q})$ is the vector of model predictions using the forward model. The noise and error models can also complicate calculations. Therefore, sampling strategies, such as MCMC methods (Sec. 4.5.2), are used to estimate the statistics of the posterior distribution of $\boldsymbol{q}$ (e.g., mean, moments, median, and mode). In this chapter, we use the Metropolis-Hastings (MH) algorithm (Sec. 4.5.2), adapting the proposal covariance matrix using previously sampled points in a burn-in stage [160]. The scaling factor is selected to ensure an acceptance rate varying between 20 and 50% following Roberts et al [221], and ensure a sufficiently fast decorrelation of the chain. The starting point for the MCMC algorithm is also important. In this context, we shall also consider the computation of the the Maximum A Posteriori (MAP) point, $\boldsymbol{q}_{\text{MAP}}$, defined by

$$\boldsymbol{q}_{\text{MAP}} = \arg\max_{\boldsymbol{q}}\ \mathcal{P}(\boldsymbol{q}|\boldsymbol{y}_{\text{obs}}). \tag{7.11}$$

The MAP can be estimated by solving Eq. (7.11) with a dedicated optimization procedure. To calculate the MAP, we rely on the Nelder-Mead algorithm which is robust enough as it does not make use of gradients [222]. The main drawback of both the MCMC and optimization approaches is that they require a large number of evaluations of the forward model $M(\boldsymbol{q})$. In our case, this means solving a system of coupled PDEs in one dimension with auxiliary problems for the closure terms at least thousands of times. As a result, the approach would be computationally intractable. Instead, we use a surrogate model $\hat{M}(\boldsymbol{q})$, with low evaluation cost and good accuracy, that can be used in place of the original model $M(\boldsymbol{q})$ in the likelihood, as proposed in other works such as [242]. If the surrogate model can be constructed at a reasonable computational cost, the sampling of the posterior distribution can be orders of magnitude faster and cheaper than the direct sampling using the full forward problem. Moreover, we can use sampling algorithms that have a straightforward implementation, such as MH, given that most of the work to make the process more efficient has been done upstream with a surrogate model.

Lastly, we recall that the integral under the denominator in Eq. (7.10) extends to the space of $\boldsymbol{q}$, denoted here with the Greek letter Ω. In practical terms, this integral is called the evidence and it is a single number. It usually does not mean anything by itself, but becomes useful when we compare one evidence with another evidence. Formally, the evidence is a likelihood function. Specifically, it is the completely marginalized likelihood function. It is therefore sometimes denoted $\mathcal{P}(\boldsymbol{y}_{\text{obs}})$ with no $\boldsymbol{q}$ dependence. It can be thought as the probability that the measurements are obtained under the considered model.

7.5.2 Likelihood function and prior distributions

In Sec. 7.3 we referenced the model used to simulate the reacting boundary layer encountered in the experiments. Specifically, we can predict recession rates and CN densities which we can then compare to the observations. As already mentioned, without further modeling assumptions, we would have to infer 15 parameters, all nuisance except for the one $\gamma_{\text{N}}^{\text{CN}}$ we are interested in. Further reasonable physical assumptions often adopted in the literature let us reduce the problem to a 5-dimensional inference where the most influential parameter is our quantity of interest $\gamma_{\text{N}}^{\text{CN}}$. Having our different sets of measurements and parameters defined, for each experimental case we propose a general likelihood of the form

$$\mathcal{P}(\boldsymbol{y}_{\text{obs}}|\boldsymbol{q}(\boldsymbol{\xi})) \propto \prod_{i=1}^{N'} \exp\left[-\frac{|y'_{\text{obs},i} - q'_i(\xi'_i)|^2}{2\sigma^2_{y'_{\text{obs},i}}}\right] \times \prod_{j=1}^{N''} \exp\left[-\frac{|y''_{\text{obs},j} - Y_j(\boldsymbol{\xi})|^2}{2\sigma^2_{y''_{\text{obs},j}}}\right], \qquad (7.12)$$

where $q'_i, y'_{\text{obs},i}$ represent the ith elements of the $\boldsymbol{q}', \boldsymbol{y}'_{\text{obs}}$ sets, while $y''_{\text{obs},j}$ is the jth element of the $\boldsymbol{y}''_{\text{obs}}$ set. The terms N' and N'' refer to the number of elements in the prime $\boldsymbol{q}', \boldsymbol{y}'_{\text{obs}}$ sets, and the observations double prime $\boldsymbol{y}''_{\text{obs}}$ set, respectively. The dependency of the quantities q'_i with ξ'_i has been made explicit for clarity. In this case, ξ'_i denotes the canonical variables associated to the variables in $\boldsymbol{q}'$. As we recall from Sec. 7.4.1, the surrogates for recession rate and CN density $\boldsymbol{Y} = \left(10^{Y_{\dot{s}}}, 10^{Y_{\rho_{\text{CN}}}}\right)$ are built on their logarithms to ensure the positivity of the approximation. The term $Y_j(\boldsymbol{\xi})$ is the jth element of the surrogates $\boldsymbol{Y}$ set already converted to natural scale. The standard deviations of the elements in both sets of measurements are expressed as $\sigma_{y'_{\text{obs}},i}$ and $\sigma_{y''_{\text{obs}},j}$.

As can be appreciated, in this likelihood, the measurement noise is assumed to follow independent Gaussian distributions with standard deviations σ. It is worth mentioning than in the first formulation of the dependencies of $\dot{s}$ and ρ_{CN} (Eqs (7.1),(7.2)) we have an explicit relation with the velocity components u_δ, v_δ. In the formulation of Eq. (7.12), the set $\boldsymbol{q}$ does not contain the velocity components but the dynamic pressure P_{d}. Even though we carry out the inference on the variable P_{d} instead of the velocity components, the relationship between them is computed externally and the velocity components are fed to the model to output $\dot{s}$ and ρ_{CN}. It is simpler to keep the original inputs to the solver which would let us use this framework as it is to assess possible discrepancies due to the assumptions embedded in the freestream computations, thereby having to include the velocities in the inference problem in the future.

Besides the likelihood function, we need to define prior distributions for all the parameters in $\boldsymbol{q}$. In the available literature for tests in the VKI Plasmatron and stagnation line plasma flows [3, 4, 110, 119] we can only establish some bounds a priori. In a maximum entropy set-up [161] with this a priori information, the resulting prior distributions are uniform over the prescribed range (Sec. 4.4). The priors of $P_\mathrm{d}, P_\mathrm{s}$ and T_w are not going to be very relevant as we have direct measured counterparts for these parameters which will dominate in the final posterior. In this regard, we are not concerned with imposing a tight prior for these parameters when compared to the literature. We have to be more careful with T_δ and $\gamma_\mathrm{N}^\mathrm{CN}$. Even though the influence of the uncertainty on T_δ on $\dot{s}$ and ρ_CN is very small compared to $\gamma_\mathrm{N}^\mathrm{CN}$, we have to take into account that when performing an inference from $\dot{s}$ and ρ_CN jointly, we might run into inconsistencies among measurements and T_δ might become important for the model to attain predictability for these cases as the second most influential parameter. For this reason, the priors for T_δ and $\gamma_\mathrm{N}^\mathrm{CN}$ are chosen conservatively wide. Table 7.2 shows the precise chosen prior distributions.

Table 7.2: *Prior distributions for the inference parameters.*

P_d [Pa]	T_δ [K]	P_s [Pa]	T_w [K]	$\gamma_\mathrm{N}^\mathrm{CN}$
$\mathcal{U}[200, 360]$	$\mathcal{U}[9000, 13000]$	$\mathcal{U}[1200, 1700]$	$\mathcal{U}[2000, 4000]$	$\log\mathcal{U}[-4, 0]$

7.6 Results on the baseline model

We apply the developed methodology to real experimental cases. The objectives are to compute reliable and accurate nitridation reactions efficiencies with uncertainty estimates as well as extend such estimation to a broader span of surface temperatures. In the following sections, the experimental data with their respective uncertainties are presented. Different inferences are then performed using the various available measurements and compared against each other. Inconsistent data are identified and left out for the calibration of an Arrhenius law that encompasses all consistent experimental data under the available conditions and their associated uncertainties.

7.6.1 Experimental conditions and associated uncertainties

The different cases comprise a set of experimental conditions with high heating and high surface temperatures. High heating helps dissociating the molecular nitrogen, creating a higher concentration of atomic nitrogen which enables more nitridation activity at the wall. The high surface temperatures play the same role in promoting nitridation reactions at the wall, enhancing the phenomenon we want to observe. The following tables summarize the different measurements and uncertainties used. In Table 7.3 the measured quantities are the dynamic pressure P_d, the wall temperature T_w, the chamber static pressure P_s, the recession rate $\dot{s}$, and the CN densities ρ_CN estimated from spectra measurements locally resolved. Each experimental case represents one data point for the given Plasmatron conditions.

The experimental uncertainties in Table 7.4 are assumed independently distributed Gaussian distributions with the standard deviations σ taken considering the bounds given on the measurements as 2σ levels of confidence [3].

Table 7.3: *Experimental data.*

Experiment ID	P_d [Pa]	T_w [K]	P_s [Pa]	$\dot{s}$ [μm/s]	ρ_CN [μg/m^3]
G4	231	2225	1500	1.41	385
G5	268	2410	1500	1.64	800
G6	312	2535	1500	2.60	1850
G7	330	2575	1500	2.51	1050

Table 7.4: *Experimental uncertainties.*

Experiment ID	P_d [Pa]	T_w [K]	P_s [Pa]	$\dot{s}$ [μm/s]	ρ_CN [μg/m^3]
G4	$\mathcal{N}(231, 2.31)$	$\mathcal{N}(2225, 11.12)$	$\mathcal{N}(1500, 22.5)$	$\mathcal{N}(1.41, 0.26)$	$\mathcal{N}(385, 52)$
G5	$\mathcal{N}(268, 2.68)$	$\mathcal{N}(2410, 12.05)$	$\mathcal{N}(1500, 22.5)$	$\mathcal{N}(1.64, 0.27)$	$\mathcal{N}(800, 100)$
G6	$\mathcal{N}(312, 3.12)$	$\mathcal{N}(2535, 12.67)$	$\mathcal{N}(1500, 22.5)$	$\mathcal{N}(2.60, 0.27)$	$\mathcal{N}(1850, 250)$
G7	$\mathcal{N}(330, 3.3)$	$\mathcal{N}(2575, 12.87)$	$\mathcal{N}(1500, 22.5)$	$\mathcal{N}(2.51, 0.25)$	$\mathcal{N}(1050, 162)$

Our inference analyses are carried out from different sources of information to potentially unveil some inconsistency issues with the model chosen and/or the measurements. The latter could be due to a bad reconstruction of the corresponding physical quantities from the raw data. Helber et al. [22] used the experimental data for two different tasks. They used recession rates to rebuild nitridation reaction efficiencies, and CN densities for validation of their rebuilding methodology. Recession rates are well understood and the transition from raw data to the physical quantity itself is rather straightforward. On the other hand, CN densities are the result of an elaborated rebuilding procedure with intermediate steps and modeling choices [243]. Unless a very careful uncertainty analysis was carried out upstream, from the raw data to the reduced model parameters of the ICCD sensor of the spectrograph and on to the gas temperatures and CN densities, we cannot be confident in the bounds given for the CN densities or even the nominal values reported. Therefore, it is not fair for the model in question to be validated against dubious experimental data. Cross-validating this way sources of information is useful for detecting inconsistencies stemming from inappropriate experimental data treatment and/or modeling choices. The key for this task is that nitridation influences both recession rates and CN densities and we can then compare their information on $\gamma_\mathrm{N}^\mathrm{CN}$ in an objective Bayesian inference scenario.

The next sections contain results and discussions on the inferences from different measurements on a one by one basis and also when combined all together in a single analysis. We recall that each experimental condition is treated separately and nitridation reaction efficiencies are computed for each case independently. Conversely, for the calibration of an Arrhenius law, the measurements from all cases are combined together.

7.6.2 Inference from recession rates

For the case of using only recession rates, pressures and wall temperatures, the likelihood formulated reads

$$\mathcal{P}(\dot{s}^{\text{meas}}|\boldsymbol{q}(\boldsymbol{\xi})) \propto \prod_{i=1}^{N'} \exp\left[-\frac{|y'_{\text{obs},i} - q'_i(\xi'_i)|^2}{2\sigma^2_{y'_{\text{obs},i}}}\right] \times \exp\left[-\frac{|\dot{s}^{\text{meas}} - 10^{Y_{\dot{s}}(\boldsymbol{\xi})}|^2}{2\sigma^2_{\dot{s}^{\text{meas}}}}\right]. \tag{7.13}$$

Results are depicted in Fig. 7.4 where we can see that the marginal posterior distributions obtained for $\gamma_{\text{N}}^{\text{CN}}$ are well defined with a very reduced support. If we take a look at the experimental conditions, we would expect to see a tendency where $\gamma_{\text{N}}^{\text{CN}}$ increases as a function of the temperature at the wall, which is what is seen in these results (Fig. 7.5). Compared to the deterministic rebuilding performed by Helber et al., our results show agreement and consistency. This is due to the strong dependency of the recession rate with the nitridation reaction efficiency and their quasi-linear relationship as seen in Fig. 7.2. We can also notice in Fig. 7.5 that the distribution on the measured wall temperatures are recovered after the model calibration.

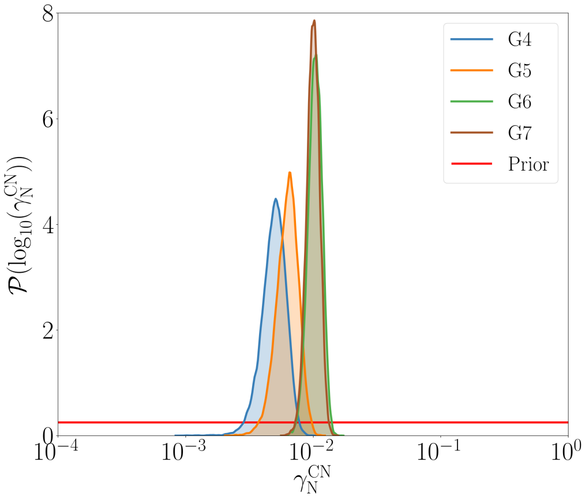

Figure 7.4: *Posterior marginal distributions of* $\gamma_{\text{N}}^{\text{CN}}$ *from recession rates.*

7.6.3 Inference from CN densities

If the chosen model can explain the experiments and the treatment of the raw experimental data is fully consistent with the workings of the experimental apparatus, one can expect the inference from different sources of information to give us consistent answers. In this regard, we explore the possibility of learning nitridation efficiencies from CN densities estimated from spectra measurements of the CN violet system. This measurement is plagued with assumptions about the nature of the CN radiative signature in these experiments. The fact that recession rates give us enough information about nitridation helps us assess the quality and assumptions on the spectra measurements. In the case of the inference from ρ_{CN}, the likelihood considered in this case reads

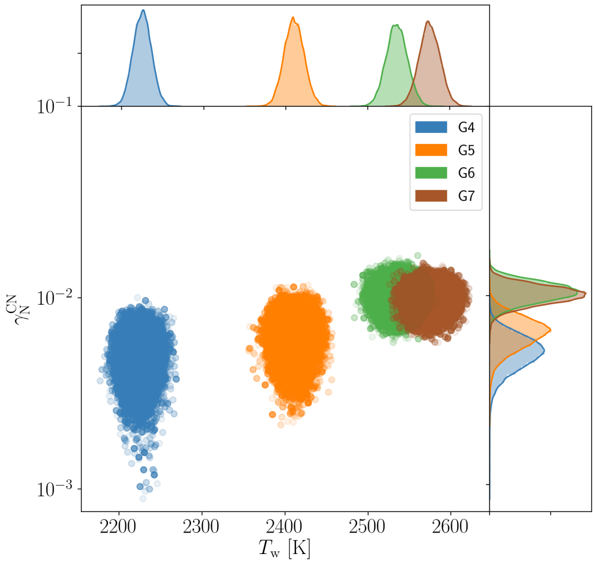

Figure 7.5: *Joint posterior distribution of $\gamma_{\mathrm{N}}^{\mathrm{CN}}$ and T_{w} from recession rates.*

$$\mathcal{P}(\rho_{\mathrm{CN}}^{\mathrm{meas}}|\boldsymbol{q}(\boldsymbol{\xi})) \propto \prod_{i=1}^{N'} \exp\left[-\frac{|y'_{\mathrm{obs},i} - q'_i(\xi'_i)|^2}{2\sigma^2_{y'_{\mathrm{obs},i}}}\right] \times \exp\left[-\frac{|\rho_{\mathrm{CN}}^{\mathrm{meas}} - 10^{Y_{\rho_{\mathrm{CN}}}(\boldsymbol{\xi})}|^2}{2\sigma^2_{\rho_{\mathrm{CN}}^{\mathrm{meas}}}}\right]. \qquad (7.14)$$

Fig. 7.6 shows the inference performed from CN densities, pressures and wall temperatures. The results are visibly different from Fig. 7.4 but the tendency of $\gamma_{\mathrm{N}}^{\mathrm{CN}}$ increasing with wall temperatures is also observed (Fig. 7.7), even though G6 seems to infer a quite higher $\gamma_{\mathrm{N}}^{\mathrm{CN}}$ than that from recession rates in order to match a ρ_{CN} that is larger than any of the other cases. We can notice as well that the support is larger compared to the support from recession rates in Fig. 7.4, meaning that CN density is a less precise measurement and also more sensitive to other parameters than recession rates. We can also see that there are two orders of magnitude of difference between the calibrated $\gamma_{\mathrm{N}}^{\mathrm{CN}}$ for G4 and G6, while for recession rates results were more clustered around 10^{-2}. Overall, there is less information content in this set of measurements than the previous inference with $\dot{s}^{\mathrm{meas}}$.

Even though we do not take into account the details of how the CN densities are rebuilt from spectrometer measurements, we could already signal inconsistencies with this measurement for the different cases here considered. This can trigger a more detailed spectra rebuilding in the future that can potentially enhance the information obtained for $\gamma_{\mathrm{N}}^{\mathrm{CN}}$ with this set of experimental data. In addition, signalling these problems help with the validation of the model when the data considered are the ones coming from the spectrometer. A more thorough treatment and uncertainty propagation would make the validation process more fair for the model when including this set of measurements.

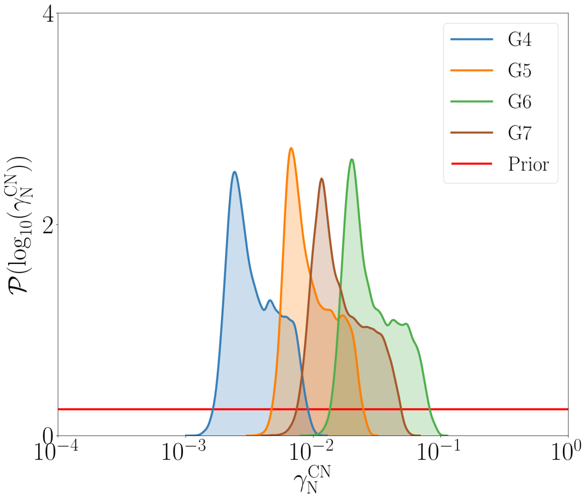

Figure 7.6: *Posterior marginal distributions of* γ_N^{CN} *from CN densities.*

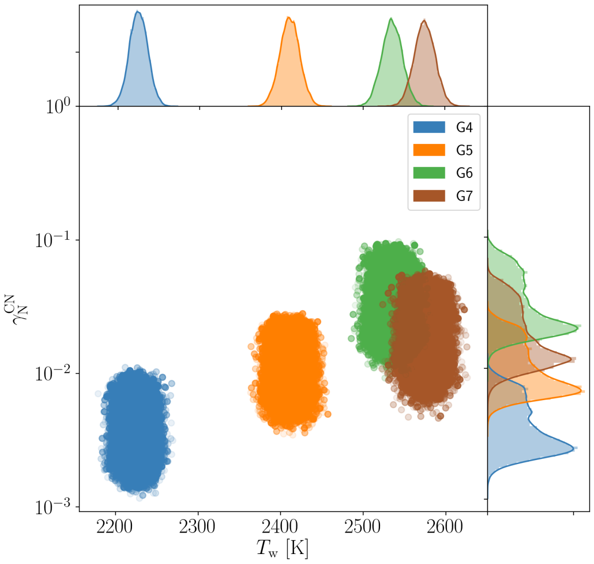

Figure 7.7: *Joint posterior distribution of* γ_N^{CN} *and* T_w *from CN densities.*

7.6.4 Inference from all available measurements

We could expect to learn better γ_N^{CN} if we use all sources of available information. This would be true if we assume that the model error is zero and that the raw data is correctly transformed into meaningful physical quantities. If somehow the model chosen to simulate our experiments is inadequate and there are some missing modeled components, we can probably expect to see a depart of the calibrated distributions obtained independently from each other. In turn, this tension among measurements under the chosen model will find a trade-off distribution when all measurements are used together in the inference but the predictive capabilities might be lost. We would also expect to see the marginal posteriors of $\gamma_{\mathrm{N}}^{\mathrm{CN}}$ from $\dot{s}^{\mathrm{meas}}$ and $\rho_{\mathrm{CN}}^{\mathrm{meas}}$ to share supports with each other. We can expect this overlapping fraction of the $\gamma_{\mathrm{N}}^{\mathrm{CN}}$ posterior marginals to explain all measurements with a reduced support and information gain on the calibrated $\gamma_{\mathrm{N}}^{\mathrm{CN}}$. In this regard, the likelihood now includes all measurements following Eq. (7.12).

We can see in Fig. 7.8 the different inferences that we carried out when using each piece of information independently and jointly. Overall, we can see that the calibration seems consistent, the support of the distributions obtained with all measurements is contained in within the support of each of the parts and one can see some information gain (reduced support compared to either of the parts'). Overall, good agreement seems to be found, although we can clearly see that as the wall temperature increases, there seems to be an over prediction of ρ_{CN} that is not fully consistent with the measurements of recession rates. This is reflected on the calibration of $\gamma_{\mathrm{N}}^{\mathrm{CN}}$ as both measurements are directly and greatly affected by it. If we pay attention to case G6 (lower left), we can see that the overlap of support is very small and the distribution that contains the information of both measurements does not share most of its support with the calibration obtained by using only CN densities. It is clear that, in this case, the results represent a trade-off between the two measurements and this case must be studied further.

The inconsistencies with the measurements of G6 are likely to signal an issue with the measurements. The fact that things look good for all cases but G6 makes it unlikely for the chosen physico-chemical model to only fail at the conditions under which G6 is recorded, given that the testing conditions were steadily changed from one case to the next, always under the same static pressure. The testing conditions reach top values for G7, for which the inferences do not present any inconsistencies. For this reason, we are led to consider this issue to be related to the measurements. Based on the work of Helber et al., no dedicated uncertainty propagation was carried out on the spectra measurement chain. This is particularly important given the intertwined and complex rebuilding to get from the integrated line-of-sight spectrum to local CN densities. We therefore base our attempt at explaining these results on the inadequacy of the uncertainty levels given by Helber et al. on the CN densities.

7.6.5 Inference with experimental uncertainty unknown

In this section, we include the uncertainty on $\rho_{\mathrm{CN}}^{\mathrm{meas}}$ as an additional parameter in the inference with all available measurements. We are interested in retrieving the values of $\sigma_{\rho_{\mathrm{CN}}^{\mathrm{meas}}}$ that would make the cases (specially G6) consistent across all measurements. Introducing an additional parameter in our inferences implies defining a prior distribution for such parameter and its role in the likelihood function. The latter issue is straightforward as the parameter introduced is a standard deviation which does not need to pass through any physical model or alter our likelihood formulation a priori.

We need to specify an objective prior for the standard deviation of a Gaussian distribution. For this, we prescribe a Jeffrey's prior [162] for $\sigma_{\rho_{\mathrm{CN}}^{\mathrm{meas}}}$ for each experimental case. We recall from Sec. 4.4, that the family of Jeffrey's priors are able to objectively capture our ignorance regarding parameter scaling which is what the standard deviation of a Gaussian distribution represents. The $\sigma_{\rho_{\mathrm{CN}}^{\mathrm{meas}}}$ prior for each experimental case is defined as follows

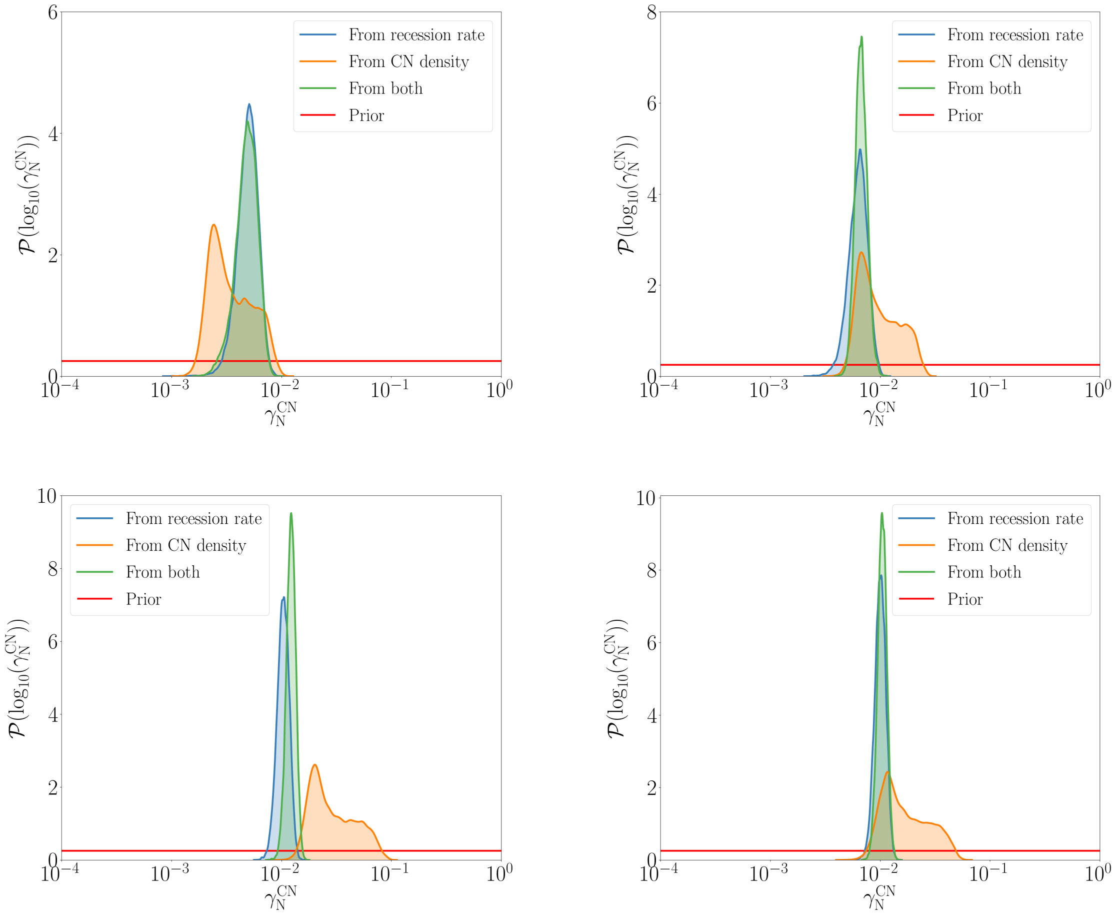

Figure 7.8: *Posterior marginal distributions of* $\gamma_{\mathrm{N}}^{\mathrm{CN}}$ *from recession rates, CN densities and both measurements for G4 (upper left), G5 (upper right), G6 (lower left) and G7 (lower right).*

$$\mathcal{P}(\sigma_{\rho_{\mathrm{CN}}^{\mathrm{meas}}}) = \begin{cases} \dfrac{1}{\sigma_{\rho_{\mathrm{CN}}^{\mathrm{meas}}}} & \sigma_{\rho_{\mathrm{CN}}^{\mathrm{meas}}} \geq \sigma^{*}_{\rho_{\mathrm{CN}}^{\mathrm{meas}}}, \\ 0 & \text{otherwise.} \end{cases} \tag{7.15}$$

with $\sigma^{*}_{\rho_{\mathrm{CN}}^{\mathrm{meas}}}$ being the originally prescribed $\sigma_{\rho_{\mathrm{CN}}^{\mathrm{meas}}}$ by Helber et al. We are implicitly assuming that the actual uncertainty on the CN density experimental estimation is larger than what was originally computed, given the assumptions that go into it and not taken into account in the uncertainty computation.

The problem is now reduced to jointly infer $\boldsymbol{q}$ and $\sigma_{\rho_{\mathrm{CN}}^{\mathrm{meas}}}$ from all the available observations $\boldsymbol{y}_{\mathrm{obs}}$ for each experimental case. We proceed by using the full likelihood depicted in Eq. (7.12) together with the priors defined in Table 7.2 and Eq. (7.15). We want to analyse the results and, particularly, the marginal posteriors for $\sigma_{\rho_{\mathrm{CN}}^{\mathrm{meas}}}$ for each experimental case. We also recall from Table 7.4 that the value of $\sigma^{*}_{\rho_{\mathrm{CN}}^{\mathrm{meas}}}$ is dependant on each experimental case.

Fig. 7.9 shows the calibrated $\sigma_{\rho_{\mathrm{CN}}^{\mathrm{meas}}}$ for each case, as well as the transformed distribution for the logarithmic increment of $\sigma_{\rho_{\mathrm{CN}}^{\mathrm{meas}}}$ with respect to each case's $\sigma^*_{\rho_{\mathrm{CN}}^{\mathrm{meas}}}$. On the left plot of Fig. 7.9, we can see the different marginal posteriors for which their lower bounds coincide with their respective $\sigma^*_{\rho_{\mathrm{CN}}^{\mathrm{meas}}}$ which are dependent on each case (vertical lines), reason why they appear slightly shifted from each other. Overall, we retrieve the same kind of posteriors for all cases but G6, as expected. On the right plot of Fig. 7.9, while all the other cases posteriors still support their respective $\sigma^*_{\rho_{\mathrm{CN}}^{\mathrm{meas}}}$ values (zero), G6 practically gives no chance to its initially prescribed standard deviation in order to be able to support the experimental data with the chosen model.

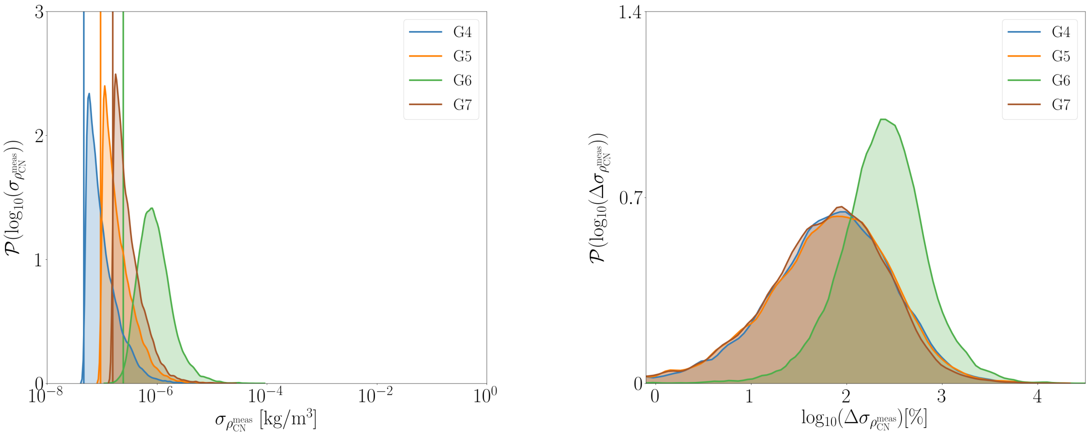

Figure 7.9: *Left: posterior marginal distributions of* $\sigma_{\rho_{\mathrm{CN}}^{\mathrm{meas}}}$. *The vertical lines signal* $\sigma^*_{\rho_{\mathrm{CN}}^{\mathrm{meas}}}$ *for each case. Right: Their transformed logarithmic increment distributions with respect to the given values of* $\sigma^*_{\rho_{\mathrm{CN}}^{\mathrm{meas}}}$ *for each case.*

A minimum of a 10% increment on G6's $\sigma^*_{\rho_{\mathrm{CN}}^{\mathrm{meas}}}$ could already be enough to attain consistency and produce compatible results, although the optimal for G6 would be between one and ten times its $\sigma^*_{\rho_{\mathrm{CN}}^{\mathrm{meas}}}$ (100% and 1000% increment, respectively). A 10% increment is certainly a possibility. Twice the prescribed value of G6's $\sigma^*_{\rho_{\mathrm{CN}}^{\mathrm{meas}}}$ would not be a large stretch either, given the complexity of the densities rebuilding from the measured spectrum and all the parameters uncertainties that should be involved and are not yet. Even though from this procedure we have no way to actually prove that this is the reason why we observe inconsistencies in the inferences under G6 conditions, we can already prescribe the repetition of measurements and an adequate treatment of the raw data and associated uncertainties. In any case, this analysis can already rule out the possibility of learning from G6's $\rho_{\mathrm{CN}}^{\mathrm{meas}}$ to obtain a useful calibrated model given that the data cannot be fully trusted.

We also show in Fig. 7.10 the resulting posterior marginals for $\gamma_{\mathrm{N}}^{\mathrm{CN}}$ with $\sigma_{\rho_{\mathrm{CN}}^{\mathrm{meas}}}$ unknown. We can appreciate how we retrieve consistent posteriors across the different measurements. It is also important to notice that as we let $\sigma_{\rho_{\mathrm{CN}}^{\mathrm{meas}}}$ be calibrated, it will, in general, be larger than each $\sigma^*_{\rho_{\mathrm{CN}}^{\mathrm{meas}}}$ thus, in the inference, the recession rate $\dot{s}^{\mathrm{meas}}$ is the measurement driving the calibration of $\gamma_{\mathrm{N}}^{\mathrm{CN}}$. As the certainty in the measurement of $\rho_{\mathrm{CN}}^{\mathrm{meas}}$ decreases (larger values of $\sigma_{\rho_{\mathrm{CN}}^{\mathrm{meas}}}$), the posterior marginals of $\gamma_{\mathrm{N}}^{\mathrm{CN}}$ when using all available measurements are exactly the posterior marginals when using only $\dot{s}^{\mathrm{meas}}$.

The new parametrization of this inference problem is not free of caveats. As we let $\sigma_{\rho_{\mathrm{CN}}^{\mathrm{meas}}}$

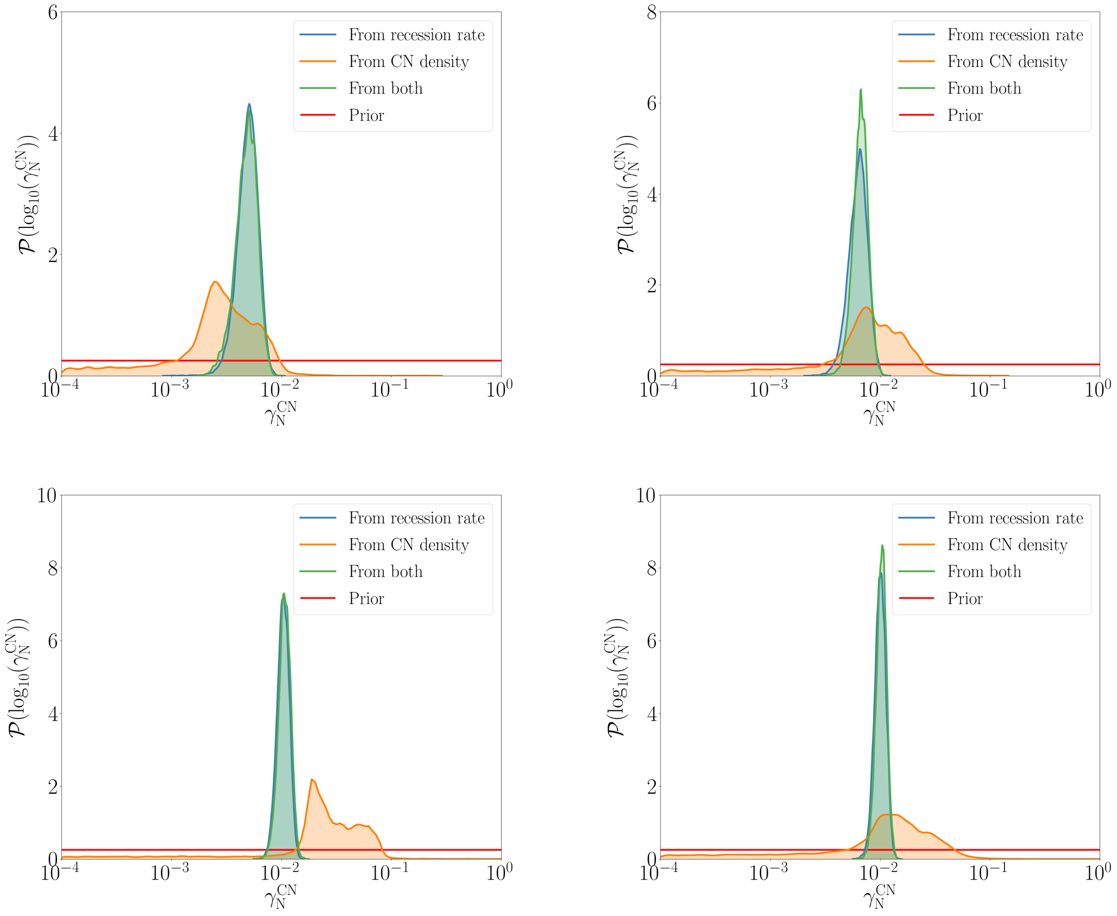

Figure 7.10: *Posterior marginal distributions of* $\gamma_{\mathrm{N}}^{\mathrm{CN}}$ *from recession rates, CN densities and both measurements for G4 (upper left), G5 (upper right), G6 (lower left) and G7 (lower right) with* $\sigma_{\rho_{\mathrm{CN}}}$ *unknown.*

vary freely without any upper bound, the resulting distributions for the measurement error of $\rho_{\mathrm{CN}}^{\mathrm{meas}}$ can lead to possible negative values which is not physical. For this reason, we also consider a log-normal statistical model [244] for the measurement error of $\rho_{\mathrm{CN}}^{\mathrm{meas}}$ for which the resulting possible values are always kept positive. We propose the same Jeffrey's prior for the log-normal standard deviation but in this case, the values $\sigma^*_{\rho_{\mathrm{CN}}^{\mathrm{meas}}}$ are taken as the logarithm of the $\sigma_{\rho_{\mathrm{CN}}^{\mathrm{meas}}}$ originally prescribed by Helber et al. (see Table 7.4). The likelihood proposed in this case is structured as follows

$$\begin{aligned}\mathcal{P}(\boldsymbol{y}_{\mathrm{obs}}|\boldsymbol{q}(\boldsymbol{\xi})) \propto \prod_{i=1}^{N'} \exp\left[-\frac{|y'_{\mathrm{obs},i}-q'_i(\xi'_i)|^2}{2\sigma^2_{y'_{\mathrm{obs},i}}}\right] \exp\left[-\frac{|\dot{s}^{\mathrm{meas}}-10^{Y_{\dot{s}}(\boldsymbol{\xi})}|^2}{2\sigma^2_{\dot{s}^{\mathrm{meas}}}}\right]\times \\ \times \frac{1}{10^{Y_{\rho_{\mathrm{CN}}}(\boldsymbol{\xi})}\sqrt{2\pi\sigma^2_{\rho^{\mathrm{meas}}_{\mathrm{CN}}}}} \exp\left[-\frac{|\log_{10}\rho^{\mathrm{meas}}_{\mathrm{CN}} - Y_{\rho_{\mathrm{CN}}}(\boldsymbol{\xi})|^2}{2\sigma^2_{\rho^{\mathrm{meas}}_{\mathrm{CN}}}}\right].\end{aligned} \tag{7.16}$$

The results of the inference for this error model are shown in Fig. 7.11. Here, $\sigma_{\rho_{\mathrm{CN}}^{\mathrm{meas}}}$ is taken in decades. We can already observe the same tendency as with the previous error model. All cases have now an equivalent $\sigma^*_{\rho_{\mathrm{CN}}^{\mathrm{meas}}}$ in the log-normal distribution around 0.1 decades which makes the posterior marginals start from roughly the same values in all cases. The posterior marginals for $\gamma_{\mathrm{N}}^{\mathrm{CN}}$ do not present visible changes for the inference performed with all measurements (Fig. 7.12). On the other hand, the resulting posterior marginals for $\gamma_{\mathrm{N}}^{\mathrm{CN}}$ when considering only $\rho_{\mathrm{CN}}^{\mathrm{meas}}$ are quite different. This is due to the appearance of an additional term in the likelihood function. For a log-normal likelihood we have to take into account an additional term as the inverse of the density ρ_{CN}, which is transformed as the negative value of the log of ρ_{CN} when considering the log-likelihood function for the MCMC sampling. This additional term favours smaller ρ_{CN} over larger ones, giving as a consequence preference to smaller $\gamma_{\mathrm{N}}^{\mathrm{CN}}$ values in the calibration as seen in Fig. 7.12. Overall, we can draw the same conclusions regarding the data from G6.

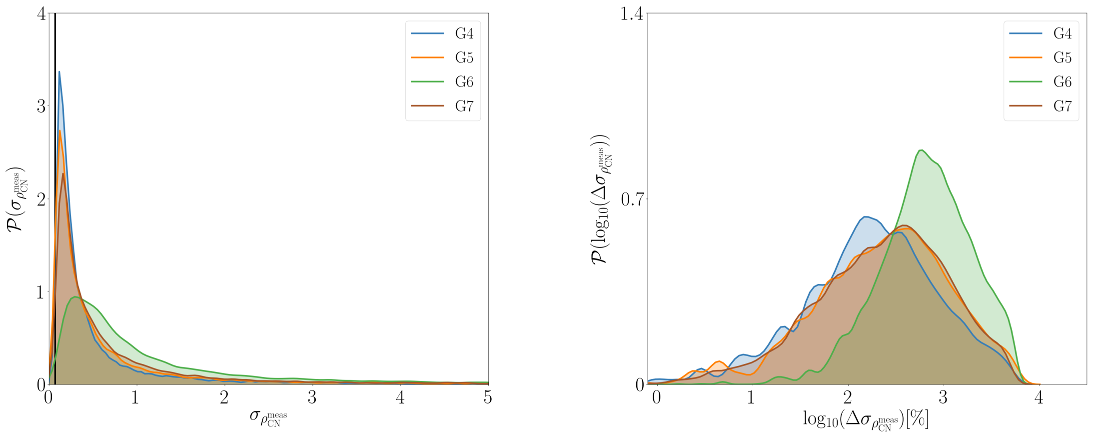

Figure 7.11: *Posterior marginal distributions of $\sigma_{\rho_{\mathrm{CN}}}$ and their transformed logarithmic increment distributions with respect to the equivalent $\sigma^*_{\rho_{\mathrm{CN}}}$ from all measurements.*

7.6.6 Calibration of an Arrhenius law

The scrutiny of the different sources of information for $\gamma_{\mathrm{N}}^{\mathrm{CN}}$ allows us to build a calibrated Arrhenius model with the remaining consistent experimental data. In theory, we could propose any mathematical form for the relationship between $\gamma_{\mathrm{N}}^{\mathrm{CN}}$ and surface temperatures T_{w}. An Arrhenius law of the form

$$\gamma_{\mathrm{N}}^{\mathrm{CN}} = A \exp\left(\frac{-T_{\mathrm{a}}}{T_{\mathrm{w}}}\right), \tag{7.17}$$

with the pre-exponential factor A, and the activation energy (given in temperature units) T_{a}, is a familiar model in the state-of-the-art nitridation modeling [22, 240]. Apart from the possibility of producing direct comparisons between the models derived in this chapter and in the relevant literature, an Arrhenius law model also captures some of the underlying macroscopic physics through its parameters [71].

For this analysis, we aim at calibrating the pre-exponential factor A and the activation energy T_{a} which are the same for all cases. Along with the Arrhenius parameters, we

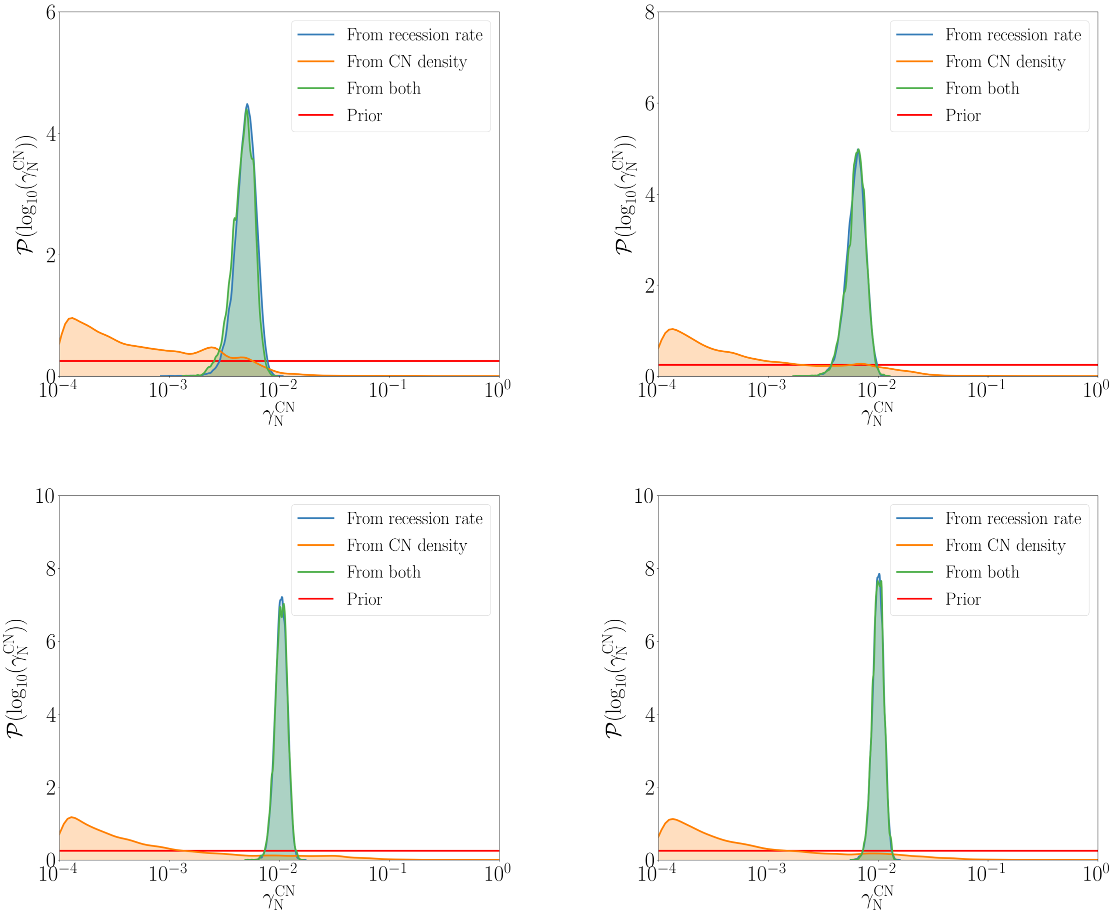

Figure 7.12: *Posterior marginal distributions of* $\gamma_{\mathrm{N}}^{\mathrm{CN}}$ *from recession rates, CN densities and both measurements for G4 (upper left), G5 (upper right), G6 (lower left) and G7 (lower right) with the log-normal* $\sigma_{\rho_{\mathrm{CN}}}$ *unknown.*

need to add all the nuisance parameters to the calibrations. In this case, each nuisance is represented as a different variable for each experimental case. The compact notation is as follows. For each case (i) in $\mathbf{G} = (\mathrm{G}_4, \mathrm{G}_5, \mathrm{G}_6, \mathrm{G}_7)$, we define the set of parameters to be inferred as $\boldsymbol{q}^{(i)} = (\boldsymbol{q}'^{(i)}, \boldsymbol{q}''^{(i)})$, and the set of observations from which we infer $\boldsymbol{y}_{\mathrm{obs}}^{(i)} = (\boldsymbol{y}_{\mathrm{obs}}'^{(i)}, \boldsymbol{y}_{\mathrm{obs}}''^{(i)})$. While the sets of observations remain the same as in the previous sections, the set of parameters to be inferred is now changed to $\boldsymbol{q}^{(i)} = (P_{\mathrm{d}}^{(i)}, T_{\delta}^{(i)}, P_{\delta}^{(i)}, T_{\mathrm{w}}^{(i)}, A, T_{\mathrm{a}})$, where A and T_{a} do not depend on the experimental conditions and they are the same for all cases. The split for the set $\boldsymbol{q}^{(i)}$ is now $\boldsymbol{q}'^{(i)} = (P_{\mathrm{d}}^{(i)}, P_{\delta}^{(i)}, T_{\mathrm{w}}^{(i)})$, and $\boldsymbol{q}''^{(i)} = (T_{\delta}^{(i)}, A, T_{\mathrm{a}})$.

For this new inference problem we need to define a new parametrization in the form of likelihood and prior parameters. We propose the following likelihood

$$\mathcal{P}(\boldsymbol{y}_{\mathrm{obs}}|\boldsymbol{q}(\boldsymbol{\xi})) \doteq \prod_{i \in \mathbf{G}} \mathcal{P}(\boldsymbol{y}_{\mathrm{obs}}^{(i)}|\boldsymbol{q}^{(i)}(\boldsymbol{\xi})), \tag{7.18}$$

with

$$\mathcal{P}(\boldsymbol{y}_{\text{obs}}^{(i)}|\boldsymbol{q}^{(i)}(\boldsymbol{\xi})) \propto \prod_{j=1}^{N'} \exp\left[-\frac{|y_{\text{obs},j}^{\prime(i)} - q_j^{\prime(i)}(\xi_j')|^2}{2\sigma^2_{y_{\text{obs},j}^{\prime(i)}}}\right] \times \prod_{k=1}^{N''} \exp\left[-\frac{|y_{\text{obs},k}^{\prime\prime(i)} - Y_k(\boldsymbol{\xi})|^2}{2\sigma^2_{y_{\text{obs},k}^{\prime\prime(i)}}}\right]. \tag{7.19}$$

We use this formulation to compare the results of the inferences when using only recession rates to the ones obtained when using all consistent data jointly. We recall that in the case of conditions G6, only the measured recession rate is used.

We perform the different inferences with 18 parameters to be calibrated. The prior distribution is taken as independent priors on all parameters, already specified in Sec. 7.5.2. For A we prescribe the same prior as for $\gamma_{\text{N}}^{\text{CN}}$ as it is an equivalent parameter, in this case, $A \sim \log\mathcal{U}[-4, 0]$. The prior on T_{a} is chosen wide enough with the same lower bound as the prior on T_{w}, given that we expect the activation energy to be at least as low as the a priori possible lowest T_{w}. It is not easy to prescribe a good upper bound as there is not so much literature on this particular reaction parameter. We choose the upper bound conservatively large based on the results of Suzuki et al. [240] and Helber et al. [22], having $T_{\text{a}} \sim \mathcal{U}[2000, 10000]$.

The results of these inferences are shown in Fig. 7.13. The plot on the left is the calibrated Arrhenius law that results from using all available measurements except G6's $\rho_{\text{CN}}^{\text{meas}}$, while the right plot contains the calibrated Arrhenius law when using only recession rates from all cases. The up-close plots show the two dimensional joint probability density functions of $\gamma_{\text{N}}^{\text{CN}}$ and T_{w} as the result of each individual inference for comparison with the Arrhenius bounds obtained. The calibrated laws are represented by their mean and 95% confidence interval bounds. We can see that there is a reduction of the law parameters uncertainty when using all available information compared to using just recession rates. From recession rates we can learn $A = 0.26^{+0.22}_{-0.22}$ and $T_{\text{a}} = 8027.4^{+1899.6}_{-3832.3}$ to that precision, while incorporating all measurements gives us different estimations $A = 0.28^{+0.22}_{-0.21}$ and $T_{\text{a}} = 8337.8^{+1608.2}_{-3308.3}$. The major uncertainty reduction is in the activation energy T_{a} and it mainly comes from the combined measurements of G5. We already saw a reduction of the $\gamma_{\text{N}}^{\text{CN}}$ posterior marginal uncertainty for G5 when using all measurements. This is also the case for the Arrhenius parameters. For G4 and G7, we saw that the posterior marginals of $\gamma_{\text{N}}^{\text{CN}}$ changed little or nothing when using recession rates or all measurements, while for G5 the combination of $\dot{s}^{\text{meas}}$ and $\rho_{\text{CN}}{}^{\text{meas}}$ saw a more prominent reduction of the support than for any one measurement alone. The data used for G6 is the same in both cases as we cannot trust the CN density reported. Both results contain the fit produced by Helber et al. in their posterior. The major discrepancy is seen in the low temperature region for which our inferences do not use any experimental data, unlike Helber et al., who included in their fit some selected cases in the lower temperature region.

It is interesting to show the results that are obtained if the measured CN density of case G6 is taken into account. Fig. 7.14 shows the obtained calibrated Arrhenius model, as well as a close-up plot of the two dimensional joint posteriors for the different cases. From the close-up plot, we can observe that the case G6 has more weight in the inverse problem, considerably deviating upward the general trend followed by the other cases captured in the Arrhenius laws of Fig. 7.13. Consequently, the resulting law is significantly modified for the upper and lower values of wall temperatures. The upper surface temperature region leaves completely out the estimation by Helber et al., while for lower surface temperatures, the calibrated law encompasses Helber et al.'s estimation at the very limit of the confidence

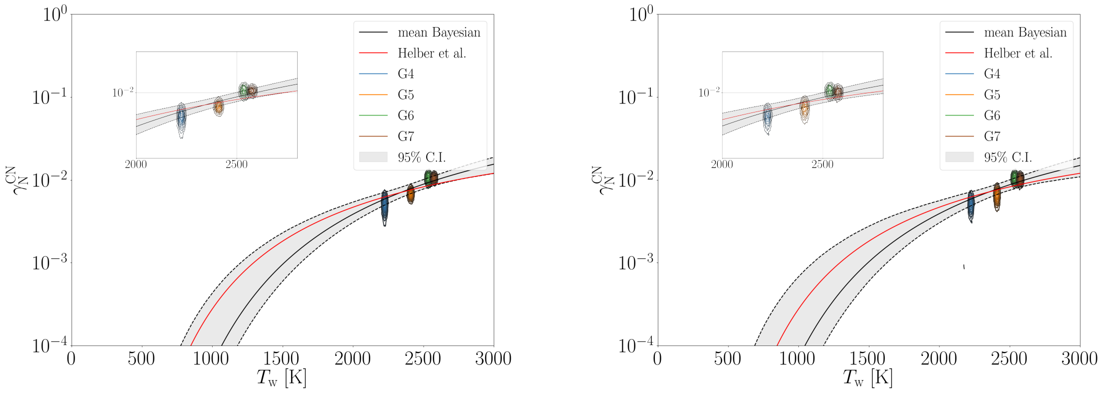

Figure 7.13: *Calibrated Arrhenius laws from the data used in this chapter. Left: resulting law using all consistent measurements. Right: resulting law using only recession rates.*

interval. There is a substantial modification of the resulting uncertainty levels in the lower surface temperatures region for which no additional experimental data are taken into account. In turn, this result falsely decreases the uncertainty levels in the range of lower surface temperatures.

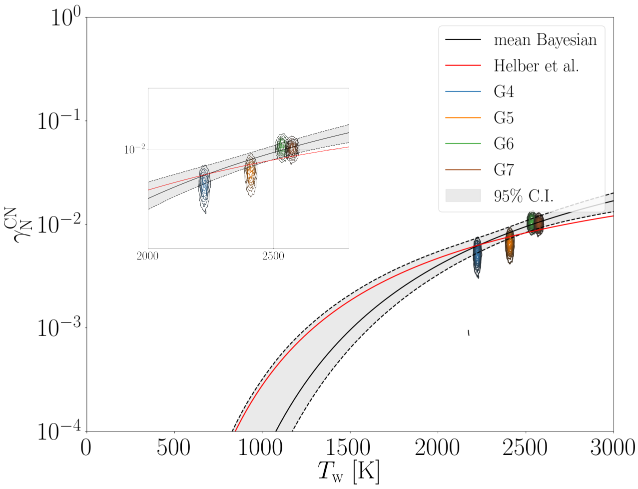

Figure 7.14: *Calibrated Arrhenius law from all the available measurements, including the measured CN density of case G6.*

7.7 Assessment of models and averaging

Several model assumptions stand at the basis of the previous analyses. The flow is assumed in thermochemical equillibrium and the ablative wall conditions amount to only nitridation reactions. Furthermore, measuring the surface temperature also allows us to test ablation energy balance models. In the available literature regarding experimental studies for nitridation, flow simulations are a needed component to compute atomic nitrogen concentrations at probe locations. The resulting nitridation reaction efficiencies rely heavily on such computations which are full of assumptions about the flow and material behaviors. Suzuki et al. [21, 240] used flow simulations that did not account for nitridation at the surface. Helber et al. [22] showed that the atomic nitrogen concentration profile along the stagnation line of the boundary layer is significantly different (∼10%) when nitridation is turned on/off. Suzuki et al. underestimated nitridation reaction efficiencies this way.

The thermal estate of the gas is not expected to impact the previous estimations of nitridation reaction efficiencies given that the recession rates and surface temperatures are accurately measured. Nevertheless, this set of experimental data presents a great opportunity to study the evidence for thermal non-equilibrium and surface energy balance models. The fact that the material tested is graphite in a pure nitrogen flow gives us an unprecedented window for testing hypotheses concerning the flow and wall states without having to add important uncertainties stemming from other physical processes such as pyrolysis and oxidation. Together with the thermodynamics and energy wall conditions, nitrogen recombination reactions are added to our models. As recombination reactions compete with nitridation reactions for the available atomic nitrogen, it is important to evaluate their impact in our calibrations. Moreover, we are also interested in learning about nitrogen recombination from these experiments.

Overall, four different model scenarios of additive physical richness are presented:

- $\mathcal{M}_0$: This is the baseline model used in the previous analyses. It is a one temperature model with no recombination at the surface for which the surface temperature is imposed.
- $\mathcal{M}_1$: This model accounts for nitrogen recombination at the surface by introducing an extra parameter $\gamma_{\mathrm{N}}^{\mathrm{N}_2}$. It considers the flow to be in thermal equilibrium and imposes the surface temperature.
- $\mathcal{M}_2$: In this model the thermal state is considered in equilibrium, surface recombination is taken into account, and the surface temperature is now a prediction of the model through a Surface Energy Balance (SEB) as seen in Sec. 2.3.3.
- $\mathcal{M}_3$: This model assumes thermal non-equilibrium by considering two different thermal baths for the translational-rotational and vibrational-electronic-electron temperatures. Furthermore, it is also agnostic about the wall surface energy condition by allowing it to be in non-equilibrium (Sec. 2.3.1). Surface recombination reactions are also included.

The main characteristics of each modeling scenario are depicted in the following Table 7.5

Table 7.5: *Modeling scenarios considered in this chapter.*

Modeling assumptions	$\mathcal{M}_0$	$\mathcal{M}_1$	$\mathcal{M}_2$	$\mathcal{M}_3$
Thermal non-equilibrium	No	No	No	Yes
Surface energy balance	No	No	Yes	Yes
Surface recombination $\gamma_{\mathrm{N}}^{\mathrm{N}_2}$	No	Yes	Yes	Yes

A hypothesis testing study is performed to compare the resulting evidences under the different models with each other. The baseline model $\mathcal{M}_0$ is used as reference (or null hypothesis) for the comparisons.

As it is recalled from Sec. 4.7, we need to evaluate the posterior probabilities of each competing model (or hypotheses in our context). This comparison allows us to weigh the relative merit of each model. The comparison is driven through the posterior ratio

$$\frac{\mathcal{P}(\mathcal{M}_i|\boldsymbol{y}_{\text{obs}})}{\mathcal{P}(\mathcal{M}_0|\boldsymbol{y}_{\text{obs}})}, \quad \forall i \in \{1, ..., 3\}, \tag{7.20}$$

for which $\mathcal{M}_0$ is used as reference in the denominator. The comparison is performed at the order of magnitude level. If the posterior of the baseline model is several orders of magnitude below the competing model, we would prefer the competing model and viceversa. If both posteriors are of similar orders of magnitude, the data does not provide enough evidence to preferentially support either model.

The posterior ratio can be decomposed according to the Bayes' rule

$$\frac{\mathcal{P}(\mathcal{M}_i|\boldsymbol{y}_{\text{obs}})}{\mathcal{P}(\mathcal{M}_0|\boldsymbol{y}_{\text{obs}})} = \frac{\mathcal{P}(\boldsymbol{y}_{\text{obs}}|\mathcal{M}_i)}{\mathcal{P}(\boldsymbol{y}_{\text{obs}}|\mathcal{M}_0)} \times \frac{\mathcal{P}(\mathcal{M}_i)}{\mathcal{P}(\mathcal{M}_0)}, \quad \forall i \in \{1, ..., 3\}, \tag{7.21}$$

where the posterior ratio is expressed as the product of the ratio of the marginalized likelihoods and priors of the different models. The marginalized likelihood of the data under the assumptions of each model is expressed as follows

$$\mathcal{P}(\boldsymbol{y}_{\text{obs}}|\mathcal{M}_i) = \int_{\Omega} \mathcal{P}(\boldsymbol{y}_{\text{obs}}|\boldsymbol{q}, \mathcal{M}_i)\mathcal{P}(\boldsymbol{q})\mathrm{d}\boldsymbol{q}, \quad \forall i \in \{0, ..., 3\}, \tag{7.22}$$

where the term $\mathcal{P}(\boldsymbol{y}_{\text{obs}}|\boldsymbol{q}, \mathcal{M}_i)$ is the likelihood $\mathcal{P}(\boldsymbol{y}_{\text{obs}}|\boldsymbol{q})$ in Eq. (7.10) for the different models under consideration. $\mathcal{P}(\boldsymbol{q})$ is the prior of the parameters $\boldsymbol{q}$. The marginallized likelihood is also the normalization constant of the posterior $\mathcal{P}(\boldsymbol{q}|\boldsymbol{y}_{\text{obs}})$ under each model. The normalization factor does not play a role in inference problems but it is the defining characteristic of hypothesis testing studies.

The prior ratio $\mathcal{P}(\mathcal{M}_i)/\mathcal{P}(\mathcal{M}_0)$ is taken as unity in this case. We consider all models to be equally likely to explain the experiments a priori. The results from the hypothesis testing study is entirely based on how well each model fits the data (values of the likelihood $\mathcal{P}(\boldsymbol{y}_{\text{obs}}|\boldsymbol{q}, \mathcal{M}_i)$), and how complex each model is regarding the number and ignorance about each model parameter (dimensionality of the integral in Eq. (7.22) and overall support of the priors of $\boldsymbol{q}$).

Following the hypothesis testing study, we use the models whose posteriors compare similarly or better than the baseline to weigh the marginal posterior of nitridation reaction efficiencies with their respective evidences for each experimental case (Sec. 4.7)

$$\mathcal{P}(\gamma_{\text{N}}^{\text{CN}}|\boldsymbol{y}_{\text{obs}}) = \sum_{i \in \{0, ..., 3\}} \mathcal{P}(\gamma_{\text{N}}^{\text{CN}}|\boldsymbol{y}_{\text{obs}}, \mathcal{M}_i)\mathcal{P}(\mathcal{M}_i|\boldsymbol{y}_{\text{obs}}). \tag{7.23}$$

The result is an overall marginal posterior which gathers the information on nitridation efficiencies provided by each valid model, incorporating this way model form uncertainties in the calibration of $\gamma_{\text{N}}^{\text{CN}}$.

7.7.1 Hypothesis testing results and discussion

The vector of parameters $\boldsymbol{q}$ has to be redefined for each model under consideration. The following Table 7.6 details the parameters that are calibrated for each modeling scenario.

Table 7.6: *Parameters to be calibrated and their priors for the different modeling scenarios.*

Inference parameter	$\mathcal{M}_0$	$\mathcal{M}_1$	$\mathcal{M}_2$	$\mathcal{M}_3$	Prior
Dynamic pressure P_d	Yes	Yes	Yes	Yes	$\mathcal{U}[200, 360]$
Edge translational temperature T_δ	Yes	Yes	Yes	Yes	$\mathcal{U}[9000, 13000]$
Static pressure P_s	Yes	Yes	Yes	Yes	$\mathcal{U}[1200, 1700]$
Surface temperature T_w	Yes	Yes	No	No	$\mathcal{U}[2000, 4000]$
Nitridation efficiency $\gamma_\mathrm{N}^\mathrm{CN}$	Yes	Yes	Yes	Yes	$\log\mathcal{U}[-4, 0]$
Recombination efficiency $\gamma_\mathrm{N}^{\mathrm{N}_2}$	No	Yes	Yes	Yes	$\log\mathcal{U}[-4, 0]$
Emissivity ϵ	No	No	Yes	Yes	$\mathcal{U}[0.5, 1]$
Energy acommodation coefficient β	No	No	No	Yes	$\mathcal{U}[-1, 1]$
Collisional efficiency α	No	No	No	Yes	$\mathcal{U}[0, 1]$

It is straightforward to see that the null hypothesis $\mathcal{M}_0$ is the simplest model in terms of model parameters, while $\mathcal{M}_3$ is the most complex one. For $\mathcal{M}_0$ to be definitely invalidated by the experimental evidence, its predictions must be way worse than the ones produced by any other model. We have to consider this assessment with care. We already know that the experimental data can be reasonably well explained with $\mathcal{M}_0$, and the fact that a competing model does much better is reason enough to abandon the hypotheses behind $\mathcal{M}_0$, or at least modify them. If $\mathcal{M}_0$ was not good enough to begin with, we would not have any reason to consider it in the first place for our hypothesis testing study.

We then compute the evidences $\mathcal{P}(\boldsymbol{y}_\mathrm{obs}|\mathcal{M}_i)$ for each model and experimental case (see Table 7.7). The objective of such study is the comparison of competing hypotheses for the experimental data.

Table 7.7: *Evidences or marginalized likelihoods $\mathcal{P}(\boldsymbol{y}_\mathrm{obs}|\mathcal{M}_i)$ of the different models for the given experimental conditions.*

Experiment ID	$\mathcal{M}_0$	$\mathcal{M}_1$	$\mathcal{M}_2$	$\mathcal{M}_3$
G4	1.12×10^{11}	5.6×10^{10}	6.0×10^{7}	6.64×10^{7}
G5	7.31×10^{10}	6.76×10^{10}	2.85×10^{5}	7.73×10^{6}
G6	5.1×10^{4}	5.08×10^{4}	3.45×10^{1}	4.43×10^{1}
G7	3.7×10^{10}	3.76×10^{10}	5.0×10^{5}	3.7×10^{6}

Typically, the evidences are compared through the Bayes factor (Sec. 4.6)

$$BF = \frac{\mathcal{P}(\boldsymbol{y}_\mathrm{obs}|\mathcal{M}_i)}{\mathcal{P}(\boldsymbol{y}_\mathrm{obs}|\mathcal{M}_0)}, \quad \forall i \in \{1, ..., 3\}, \tag{7.24}$$

where BF is the Bayes factor which is generally expressed in logarithmic scale as

$$\log_{10} BF = \log_{10}(\mathcal{P}(\boldsymbol{y}_\mathrm{obs}|\mathcal{M}_i)) - \log_{10}(\mathcal{P}(\boldsymbol{y}_\mathrm{obs}|\mathcal{M}_0)), \quad \forall i \in \{1, ..., 3\}. \tag{7.25}$$

For strong evidences in favour or against a certain hypothesis, the Bayes factor should be above a threshold of $|\log_{10} BF| = 8$, which indicates that as long as the evidences for each model remain in within some orders of magnitude, we cannot conclude anything from the data. Table 7.8 shows the results of the hypothesis testing study. Overall weak evidence is found against any given model compared to $\mathcal{M}_0$. On the other hand, it means that the SEB model does not perform too poorly compared to imposing the measured surface temperature directly, giving us some confidence in such models for ablative surfaces under the considered Plasmatron conditions. The baseline model $\mathcal{M}_0$ does pretty well compared against the other models for which the larger number of parameters to be inferred penalize the resulting evidence. In the case of model $\mathcal{M}_2$, the offset of the temperature prediction is what lowers its evidence given that $\mathcal{M}_0$ and $\mathcal{M}_2$ have the same number of parameters $\boldsymbol{q}$. $\mathcal{M}_2$ also replaces T_w, which is a well-defined parameter within its experimental uncertainty for $\mathcal{M}_0$, with the emissivity ϵ which does not have a measured counterpart in these cases, also contributing to the lowering of $\mathcal{M}_2$'s evidence. Model $\mathcal{M}_2$ needs a perfect prediction of T_w to amount to the evidence of $\mathcal{M}_0$ which is not achieved, although the deviation is small to still consider the model good enough compared to the baseline. It is important to recall that in the case G6 the models are compared on the basis of predicting the recession rate and surface temperature measured. The CN density measurement was deemed untrustworthy in the previous analyses, therefore, it is not used in the context of this study.

Table 7.8: *Bayes factors of the different models against the baseline model $\mathcal{M}_0$ for each experimental condition.*

Experiment ID	$\mathcal{M}_1$	$\mathcal{M}_2$	$\mathcal{M}_3$
G4	-0.3	-3.27	-3.22
G5	-0.034	-5.4	-4.0
G6	-0.0024	-3.17	-3.06
G7	0.01	-4.87	-4.0

The results depicted in Table 7.8 show no definitive evidence against the baseline model which considers thermal equilibrium and nitridation reactions as the only wall reactions. Nevertheless, this study does not conclude that this is the truth but rather that the experimental data is consistent with the baseline model as well as the other models. If the true flow was in non-equilibrium, other measurements would be needed in order to find the relevant evidence and truly invalidate the baseline model of thermal equilibrium. The same is applicable to the presence of recombination reactions. Concentrations of N_2 in the vicinity of the material surface that cannot be explained by the baseline model could definitely give evidence of recombination reactions and their relative importance. So far, the calibrations of the different models with this particular set of experimental data do not provide enough information about recombination reactions. Fig. 7.15 depicts the marginal posteriors for $\gamma_\mathrm{N}^{\mathrm{N}_2}$ under the different models that include such parameter. Almost flat posteriors with the same support as the priors are recovered except for the 1T SEB model $\mathcal{M}_2$ where the posterior support is reduced. In order for $\mathcal{M}_2$ to be able to explain the experimental obbservations, recombination reaction efficiencies cannot surpass a certain upper limit. Going over such limit would probaly throw off the prediction of the surface temperature. Given that the other models have more parameters to control the surface temperature prediction, model $\mathcal{M}_2$ is able to place more constraints on $\gamma_{\mathrm{N}}^{\mathrm{N}_2}$. It can also be appreciated that as the wall temperature measured decreases the posterior support for $\gamma_{\mathrm{N}}^{\mathrm{N}_2}$ shrinks toward lower values.

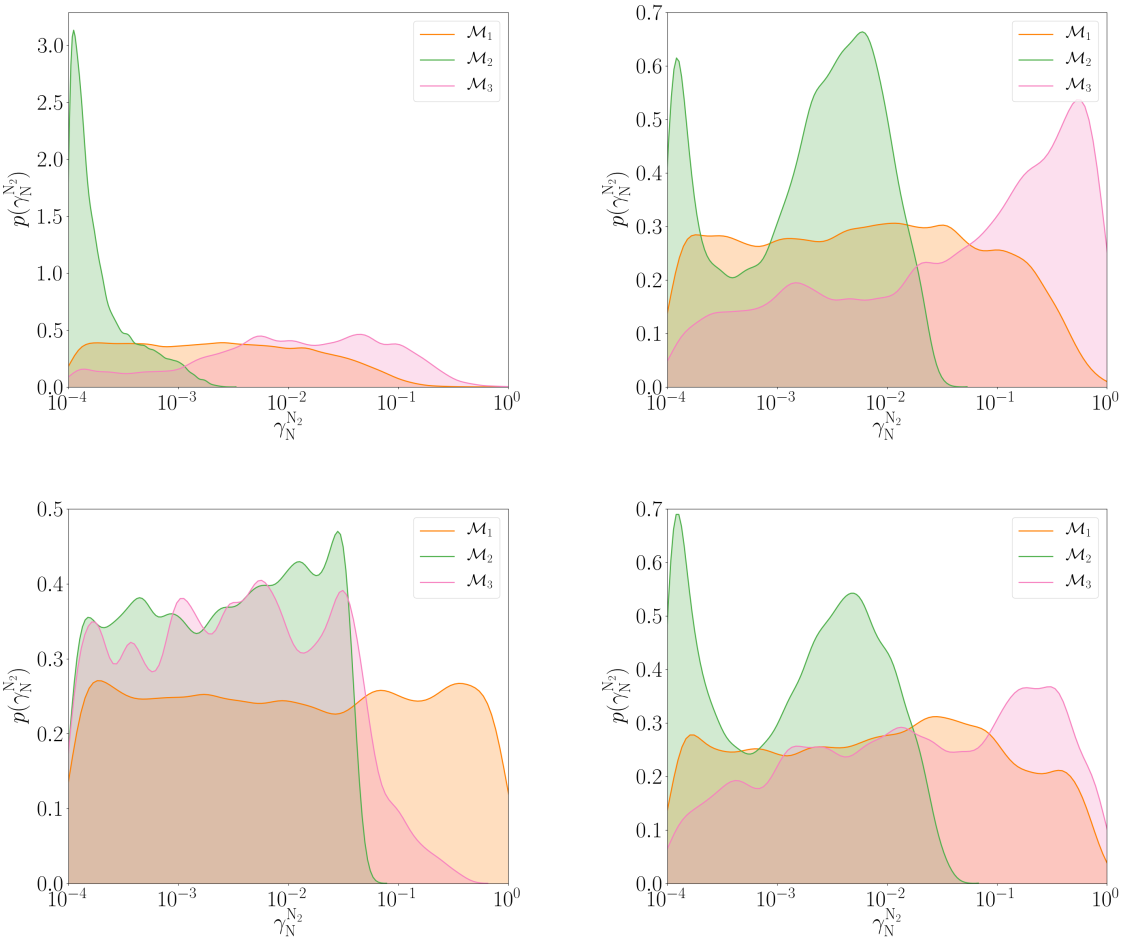

Figure 7.15: *Posterior marginal distributions of $\gamma_{\mathrm{N}}^{\mathrm{N}_2}$ under the different modeling scenarios for G4 (upper left), G5 (upper right), G6 (lower left) and G7 (lower right).*

For more insight about model performance, we can look at the resulting residuals of the statistical inverse problem for the measured quantities. We recall that the inverse problem we are solving every time we perform an inference amounts to solving the equation

$$\boldsymbol{y}_{\mathrm{obs}} = \boldsymbol{Y}(\boldsymbol{q}(\boldsymbol{\xi})) + \boldsymbol{E}, \tag{7.26}$$

where the stagnation line model evaluations are replaced by accurate GP surrogates $\boldsymbol{Y}$ for the predictions of recession rates $\dot{s}$, CN densities ρ_{CN}, and surface temperatures T_{w}. The error model is chosen as unbiased Gaussian distributions for which we prescribe the different standard deviations σ for each measurement. Once the model is calibrated and we have posteriors on the parameters $\boldsymbol{q}$, we propagate them through the model to generate the resulting distribution of $\boldsymbol{y}_{\mathrm{obs}} - \boldsymbol{Y}(\boldsymbol{q}(\boldsymbol{\xi}))$. This distribution is what we call the residual and it should match the error model distribution $\boldsymbol{E}$ initially prescribed for each measurement.

Fig. 7.16 shows the residuals for case G5 for recession rate $\dot{s}^{\text{meas}}$, CN density $\rho_{\text{CN}}^{\text{meas}}$ and surface temperature $T_{\text{w}}^{\text{meas}}$ under the different modeling scenarios. The rest of the results for the other experimental cases can be found in Appendix D. Overall all models retrieve the noise of recession rate and CN density. Model $\mathcal{M}_2$ shows the largest deviations in the predictions which are still quite small. The 1T SEB model tends to over predict recession rates and under predict CN densities in the flowfield. The surface temperature is perfectly captured by the 2T SEB model $\mathcal{M}_3$ while the 1T SEB model $\mathcal{M}_2$ shows some deviation towards higher surface temperatures. The deviation is $\sim$ 25 K which is rather small compared to the range of surface temperatures we deal with in this problem ($>$ 2,000 K).

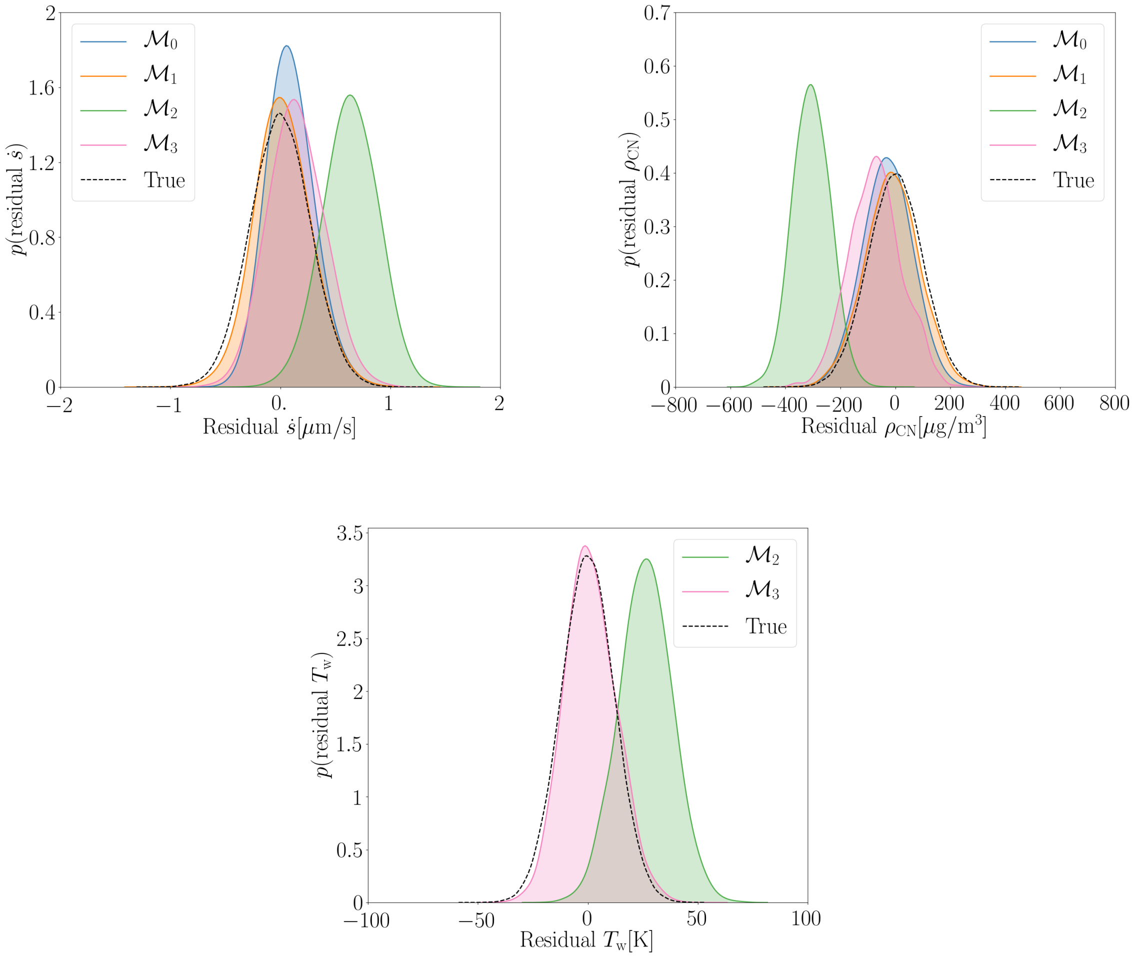

Figure 7.16: *Residuals of recession rate* $\dot{s}^{\text{meas}}$*, CN density* $\rho_{\text{CN}}^{\text{meas}}$ *and surface temperature* $T_{\text{w}}^{\text{meas}}$ *for the different models under conditions G5.*

It is interesting to reflect on how the 2T SEB model manages to achieve a lower prediction of the recession rate and surface temperature, and yet perfectly recuperate the error of the CN density. The only possibility for this to happen is through available thermal non-equilibrium mechanisms which are not considered in the 1T SEB model. The 2T surface energy balance in Eq. (2.95) contains an additional term for the conductive contribution of the internal energy to the total energy balance. Through this mechanism, the 2T SEB model finds the combination of collisional efficiency α and energy acommodation factor β so that the internal energy contribution cools off the surface. Fig. 7.17 shows the resulting marginal posterior distributions as well as samples from the joint distribution of the α and β parameters. The collisional efficiency α is quite constrained by the experimental data to low values, while the energy accommodation coefficient β keeps all the prior support. The resulting distributions are shifted towards values that favour thermal non-equilibrium $(\alpha < 1, \beta < 1)$.

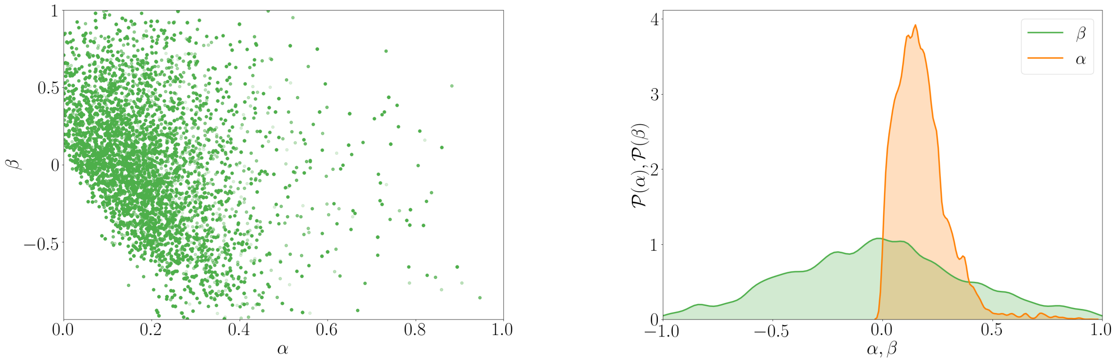

Figure 7.17: *Left: 100,000 samples from the joint posterior distribution of α and β. Right: posterior marginal distributions of α and β under conditions G5.*

Fig. 7.18 shows the propagated posterior solutions of the stagnation line model for both the 1T SEB and 2T SEB models with their corresponding confidence intervals. Promoting strong thermal non-equilibrium, as seen in the temperature profiles in Fig. 7.18, makes the surface excite the internal energy modes, consequently lowering the resulting translational surface temperature to match perfectly the experimental data. This feature of the 2T SEB model can easily decouple the surface temperature prediction from the rest of the temperature profile in the flowfield. The result is an overall increment of the flowfield temperatures with respect to the 1T SEB model.

The fact that this change in the temperature profiles can also alter the chemical composition in the flowfield to match the observed ρ_{CN} (Fig. 7.19) brings forth the importance of another set of assumptions: the gas phase chemistry. In particular, the resulting overall depleition and creation of CN differs between the two models in such a way that a higher CN density is achieved at the spectrometer location for the same concentration of CN at the wall, dictated primarily by the recession rates predicted (schematic representation can be found in Fig. 7.20). Additional experiments for the proper calibration of the gas phase chemistry would be needed to have a realistic assessment on the evidence of thermal non-equilibrium at the wall.

Still, considering the same chemical mechanism and reaction rates, we could also propose new experimental avenues to find strong evidence, or lack thereof, of thermal non-equilibrium at the wall. In particular, the differences in the CN mole fraction profiles could be exploited further by considering the addition of a spectrometer measurement in a different location along the stagnation line. Such measurement could be performed downstream the current spectrometer measurement, although the accuracy and uncertainty estimation of the resulting CN concentration should be carefully addressed to be able to tell the two

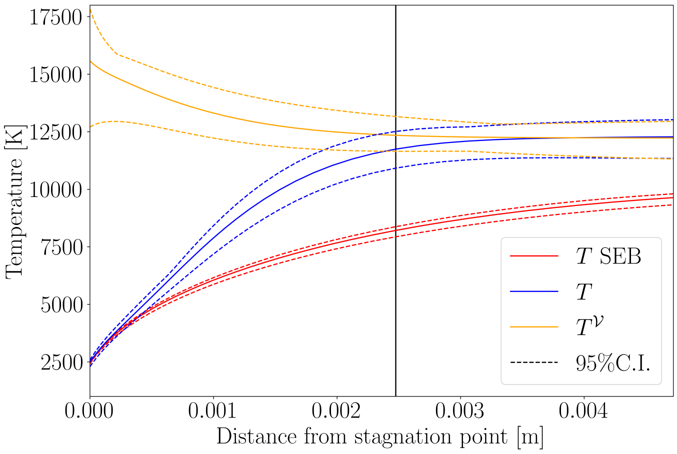

Figure 7.18: *Propagated temperature profiles for the 1T SEB ($\mathcal{M}_2$) and 2T SEB ($\mathcal{M}_3$) models with their respective confidence intervals. The vertical black line represents the position of the spectrometer measurement.*

models apart. Upstream, the radiative signal would lose intensity and the observation would become more noisy. In any case, it represents a challenge to find stronger evidence in favour of thermal equilibrium or non-equilibrium at the wall.

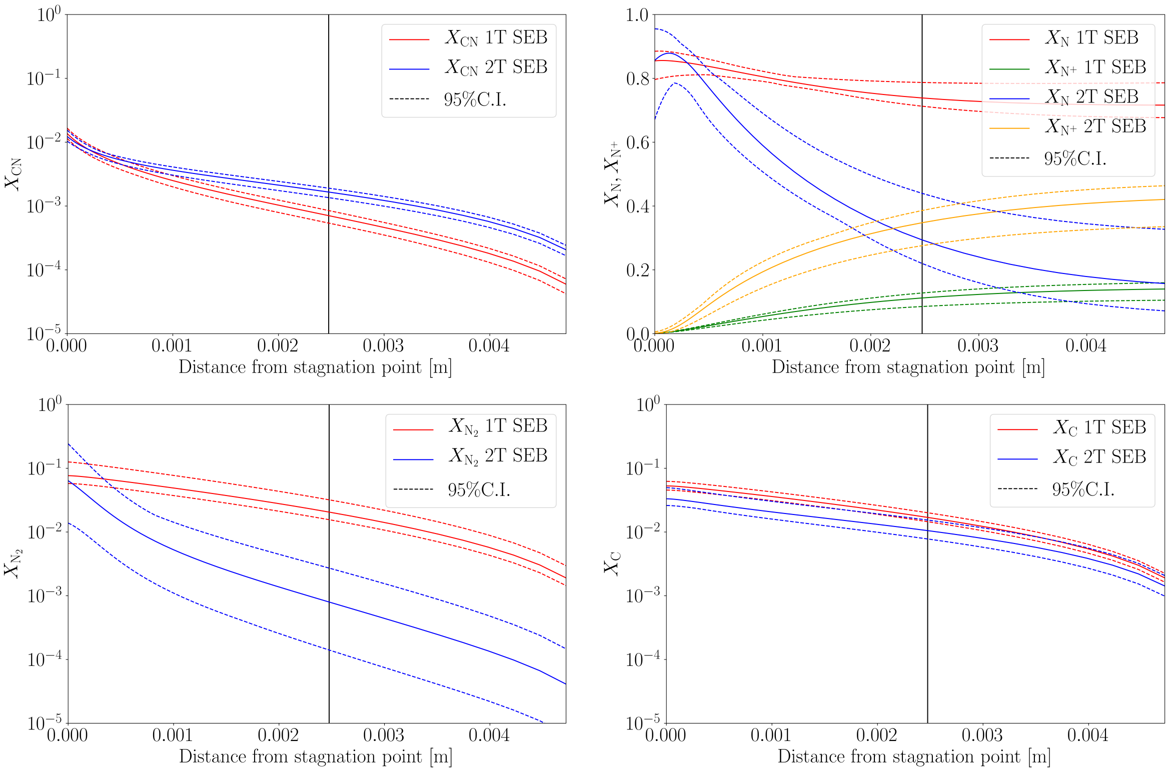

Figure 7.19: *Propagated mole fraction profiles for the 1T SEB ($\mathcal{M}_2$) and 2T SEB ($\mathcal{M}_3$) models with their respective confidence intervals. The vertical black lines represent the position of the spectrometer measurement.*

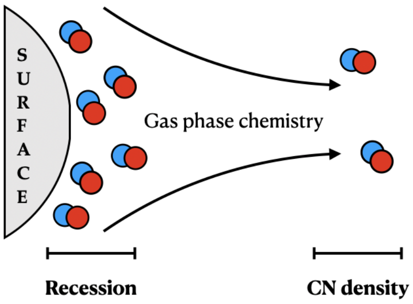

Figure 7.20: *Schematic representation of the modulating effect of the gas phase chemistry in the calibration of the different stagnation line models. The CN concentration at the wall is dominated by the recession rate while the CN density at the spectrometer location is a combined result of the recession rate and the gas phase chemistry.*

7.7.2 Model averaging results

All the modeling scenarios presented are so far consistent with the experimental data. We want to incorporate the uncertainty of these multiple modeling choices into the resulting calibrated nitridation reaction efficiencies $\gamma_{\mathrm{N}}^{\mathrm{CN}}$. We recall the model assumptions for which we remain uncertain. The baseline model $\mathcal{M}_0$ considers a flow in thermal equilibrium for which only one temperature is defined. As heterogeneous chemistry mechanism at the wall it only considers nitridation. Model $\mathcal{M}_1$ introduces the possibility of having nitrogen recombination reactions at the surface. Models $\mathcal{M}_2$ and $\mathcal{M}_3$ incorporate a surface energy balance model for the prediction of surface temperatures which are not imposed in these cases. Further, model $\mathcal{M}_3$ assumes the flow to be in a state of thermal non-equilibrium by assuming two distinct thermal baths.

Fig. 7.21 shows the resulting $\gamma_{\mathrm{N}}^{\mathrm{CN}}$ marginal posteriors under the different modeling scenarios. The resulting weighted average posterior is labelled as BMA. Overall, all the posteriors share supports and are consistent with each other. This is to be expected as $\gamma_{\mathrm{N}}^{\mathrm{CN}}$ is dominated by the recession rate and surface temperature measurements which are quite accurate in all cases and are not substantially affected by the differential features of the models. We notice a broader support for the thermal equilibrium model with recombination $\gamma_{\mathrm{N}}^{\mathrm{N}_2}$ in it $\mathcal{M}_1$. As a competing mechanism, recombination reactions allow nitridation reactions to have higher efficiencies for the same observed recession rates. The atomic nitrogen available at the surface is more scarce for nitridation reactions when competing with recombination reactions. Higher nitridation efficiencies would still produce the same observed recession rates. The wider support is also extended to the averaged posterior given that model $\mathcal{M}_1$ has similar weight as all the other models, consequently widening the support for $\gamma_{\mathrm{N}}^{\mathrm{CN}}$. The models with the tightest supports are the baseline $\mathcal{M}_0$ and the 1T SEB $\mathcal{M}_2$ models. They are also the models with the least number of parameters to be inferred, producing more defined peaks and less uncertainty for $\gamma_{\mathrm{N}}^{\mathrm{CN}}$.

The most relevant summary statistics for the resulting BMA distributions are gathered in Table 7.9.

Given that we have different $\gamma_{\mathrm{N}}^{\mathrm{CN}}$ calibrations under the various models, we can expect the calibrated Arrhenius law to also be slightly different for the variety of models. In this context, the calibration of an Arrhenius law of the same structure as the one in Sec. 7.6.6

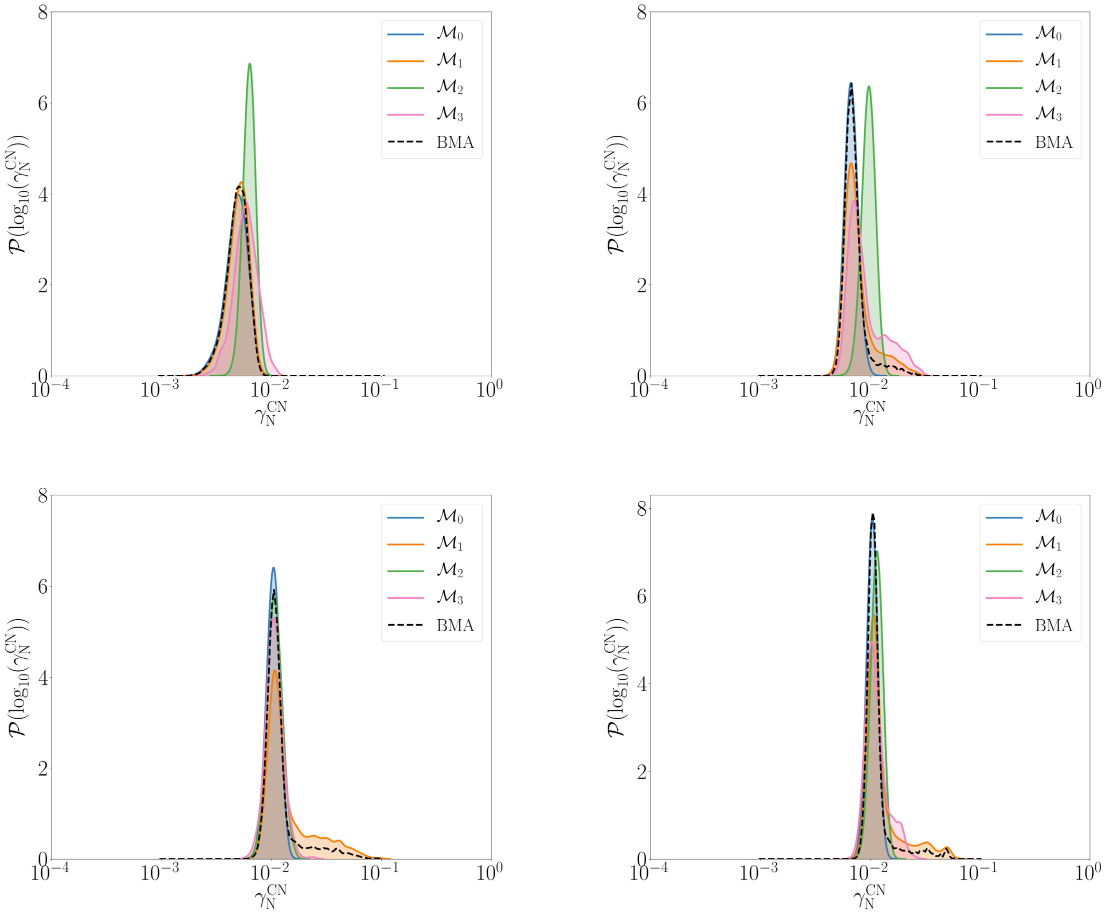

Figure 7.21: *Posterior marginal distributions of* γ_N^{CN} *under the different modeling scenarios and the resulting averaged posteriors for G4 (upper left), G5 (upper right), G6 (lower left) and G7 (lower right).*

Table 7.9: γ_N^{CN} *posterior statistics of the resulting BMA distributions for the different experimental cases.*

Experiment ID	Mean	95% C. I.	MAP
G4	0.005	[0.003, 0.007]	0.005
G5	0.007	[0.005, 0.013]	0.007
G6	0.012	[0.008, 0.026]	0.010
G7	0.012	[0.009, 0.024]	0.010

is performed for all the models proposed. The results of the Arrhenius parameter marginal posteriors can be seen in Fig. 7.22. Overall there is good agreement in their support and the resulting BMA distributions follow closely the posterior obtained with the baseline model $\mathcal{M}_0$. The summary statistics are gathered in Table 7.10.

Propagating the pre-exponential factor and activation energy posteriors we get an estimation of the variation of the nitridation parameter γ_N^{CN} with the surface temperature

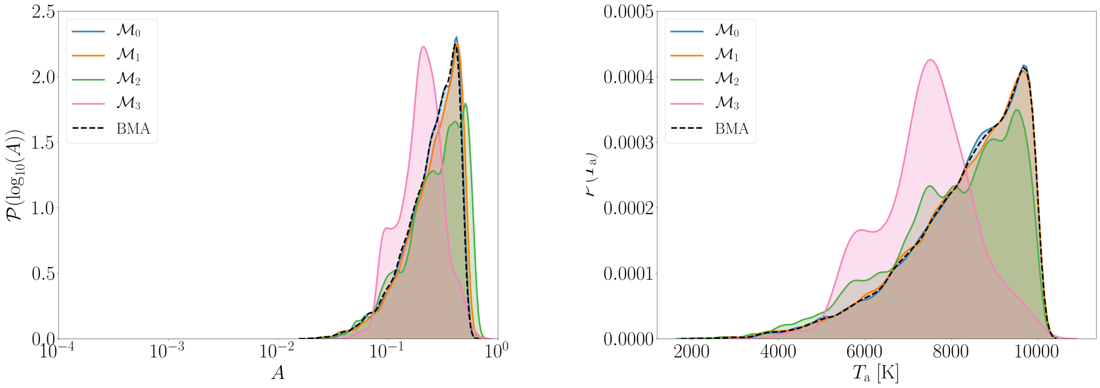

Figure 7.22: *Calibrated Arrhenius parameters and their weighted average for the different models considered.*

Table 7.10: *Posterior statistics of the resulting BMA distributions for the Arrhenius parameters.*

Arrhenius parameter	Mean	95% C. I.	MAP
A	0.253	[0.065, 0.502]	0.42
T_a [K]	8328.7	[4996.1, 9944.2]	9669

T_w. Fig. 7.23 shows the different Arrhenius laws and the BMA with the 95% confidence intervals. The right plot of Fig. 7.23 shows the obtained calibrated laws plotted against the available experimental data. Even though the resulting laws are calibrated with the data from Helber et al., we can project accurate confidence intervals to lower surface temperatures, where the experimental data available differ by several orders of magnitude. The data of Helber et al. are consistent with the experiments from Zhang et al. for lower surface temperatures as well as Suzuki et al.'s data. This apparent agreement enhances our confidence in the tools developed and the analyses performed.

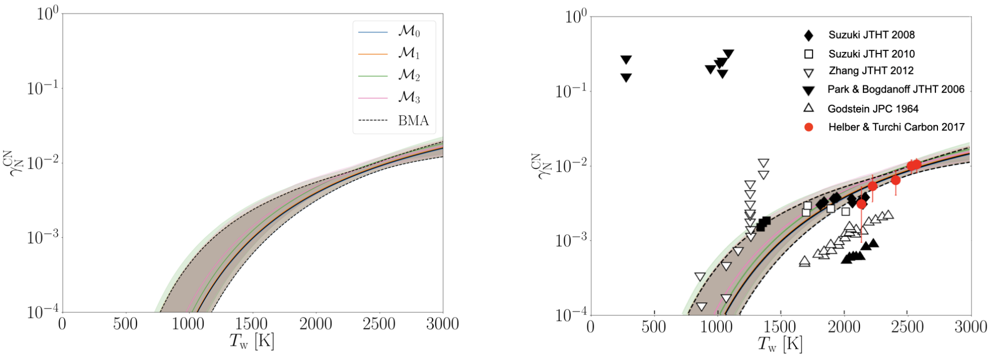

Figure 7.23: *Calibrated Arrhennius laws and their weighted average for the different models considered (left). The Arrhenius laws are compared against the available experimental data (right).*

7.8 Summary

The aim of this chapter is to infer nitridation reaction efficiencies from plasma wind tunnel experiments. We propose an a priori study of the chosen 1D thermal equilibrium stagnation line forward model to discard some experimental data which are not important to the phenomenon we want to study. To do so, we propagate a priori uncertainty levels on all the input and model parameters and derive variance-based sensitivity indices. This procedure shows that information of the boundary layer edge conditions does not play a role in the inference we want to carry out. Consequently, we can drop some experimental data that would otherwise complicate the inference by adding other models and computations to the likelihood estimation. This result also informs the experimental procedures about which data are informative for ablation processes, potentially allowing the simplification of future experimental campaigns. To carry out the a priori analysis, we propose to use Gaussian processes as surrogate models for the predicted quantities. The surrogate models are also used for the inference procedure.

The inference is splitted in terms of the experimental data used. We want to gauge the different levels of information that recession rates and CN densities bring to the inference of nitridation efficiencies. By comparing and combining them we check for consistency issues in the experimental data and/or the model. Overall the calibrations seem consistent, the supports of the distributions obtained with all the measurements are generally contained in within the support of each of the parts and one can see some uncertainty reduction. We conclude that the spectrometer measurements for the case G6 present inconsistencies which are likely to stem from the lack of uncertainty treatment in the complex rebuilding chain from the line-of-sight spectra to local CN densities. We follow up the analysis by including in the inference the uncertainty on the measured CN densities. Apart from the initially adopted Gaussian measurement error model, we also adopt a log-normal error for the CN density measurements. For both cases the conclusion about G6 is the same. We recommend that the measurements are repeated and carefully analysed.

Gathering the consistent data from all the experimental conditions allows us to infer Arrhenius law parameters, relating the nitridation efficiencies to different wall temperatures. For this task, we compare the results when combining all consistent measurements and when using only recession rates. The results differ mainly on the uncertainty levels obtained for the activation energy. Most of the difference is due to the information given by the combination of recession rates and CN densities for the case G5.

The final part of this contribution is devoted to model selection and averaging. The model choice presented in the first part of the analyses is based on flow thermal equilibrium assumptions which may not hold for such low static pressures. The heterogeneous chemical mechanism is also ignoring the fact that nitrogen recombination might be important. We consider three additional modeling scenarios which account for nitrogen recombination, surface energy balances and thermal non-equilibrium in the flow and the wall. All these modeling choices are assessed in a hypothesis testing study. Overall no strong evidence is found against the baseline model and none of the considered models can be discarded. The calibrations of models with surface recombination can define an upper limit for this parameter at best. The calibrated solutions of the thermal non-equilibrium model point to strong thermal non-equilibrium at the wall, although the evidence is weak. Model averaging is performed for the nitridation efficiencies and Arrhenius laws obtained under each model. Complete and accurate characterization of their posterior uncertainties is provided to update the current state-of-the-art databases.

The outcomes of this chapter direct our research efforts in this field towards two different aspects. First, the spectrometer measurements should be studied in depth and proper uncertainty propagation methods should be used to go from raw data to the parameters of the reduced models of the apparatus and forward to flow temperatures and species concentrations. In doing so, the inference of physical model parameters with the derived measured quantities can improve and be more reliable when calibrating new models. Second, new data and experiments are needed to be able to rule out some models and find definitive evidence of thermal non-equilibrium and learn surface recombination.

Chapter 8

Conclusions and future outlook

The process of scientific inference has been a subject of study and debate for centuries. As the mathematical models and experimental apparatus escalate in complexity, deterministic methods for model calibration and validation are being replaced by statistical methods in all disciplines of science and engineering. It happens often that these methods are so deeply ingrained in the way we do science that not many questions are posed on them.

Aerothermodynamic models, particularly those concerning gas-surface interaction but also kinetic models in general, have largely undefined uncertainty levels in their constitutive parameters and, consequently, in their predictions. This is due to the fact that model calibration in aerothermodynamics is largely based on single-point estimates, which, to date, constitutes the standard approach in the state-of-the-art methodologies. This issue limits the extent to which we can confidently validate our models and, consequently, attain predictive performance. It is only in the last decade that an influx of research works have started to pave the way for stochastic methodologies to settle in within the aerothermodynamics community.

Predictive models and simulations represent the cornerstone for future Space exploration missions. Since atmospheric conditions and physical phenomena of planetary entry flights are so varied, it is practically impossible to test all aspects of flight as they would happen during entry. Consequently, we have to rely on models and simulations to give us confidence in our design choices. To estimate accurate confidence levels in our predictions and databases, we need to introduce rigorous model calibration techniques which can handle sources of uncertainties in our models and data.

As we recall from Chapter 1, we identified two overall objectives for this thesis. The first one concerned the **accurate inference of catalytic parameters for reusable TPS**, and the second was the **calibration and assessment of graphite ablation models for nitrogen flows**. In the next section, we first summarize the contributions to each specific objective in detail. We then discuss the broader perspective of such contributions to the research in the aerothermodynamics community.

8.1 Contributions of this work

It is essential to highlight that this work was confined to the experimental data of the Plasmatron facility at VKI. As such, a series of experimental and model assumptions were taken into account as valid representations of the selected experiments used in this thesis. In this context, using 1D boundary layer simulations for the reproduction of stagnation region quantities allowed us to perform the comparisons with the experimental data, which also concerned stagnation region quantities. Further, phenomenological gas-surface interaction models were more suitable for the task of learning from Plasmatron data.

8.1.1 Contributions to the specific objectives

A detailed account on how the objectives of this thesis were achieved is given. Both objectives we set out for were further divided into two distinct tasks. The introdution of each specific task is highlighted in bold. The objectives are presented in chronological order as they appear in the thesis.

Objective 1: Accurate inference of catalytic parameters for reusable TPS

The accuracy of the inferred catalytic parameters is tightly coupled to the information we have about the flow free stream (enthalpy). Deterministic methods tend to infuse the calibration process with a set of delicate assumptions. Relaxing those assumptions and including uncertainties reveal that a poor characterization of the enthalpy leads to large uncertainties on the calibrated catalytic parameters. The conductive and diffusive heat flux components can exchange values easily while giving out the observed wall heat flux. This is the main caveat we dealt with to accomplish this first objective. Overcoming the challenge required the development of inference and experimental methodologies.

First, a novel Bayesian inference formulation was proposed. The calibration gave estimates of the material catalytic parameter through its posterior probability distribution. The Bayesian approach allowed for the simultaneous computation of the catalytic parameters of the reference and Thermal Protection System (TPS) materials, which was already proven to be more accurate than the conventional sequential approach. The improvement of the methodology stemmed from the proposed likelihood function. An optimization problem in the nuisance parameters space was built on the likelihood definition, reducing its dimensionality to just the quantities of interest $\gamma_{\text{ref}}, \gamma_{\text{TPS}}$. To cope with this computationally demanding likelihood, we proposed the use of a surrogate model. Gaussian Processes (GP) worked quite well for this problem yielding good results with low standard deviations on the chain samples. In addition, the approach was robust, in the sense that the Markov Chain Monte Carlo (MCMC) sampling method worked smoothly for any given conditions. Overall, the optimization formulation presented has the impact of improving considerably the inference results by giving more consistent and accurate posterior distributions of the catalytic parameters when compared to the existing literature. The main differences being the reduced support, with a decrease of 20% in the standard deviation, and well-defined peaks of the respective posteriors. Subsequently, it is possible to say that the catalytic parameters can be effectively learned from the experimental conditions and under the considered model assumptions.

Having developed an efficient and effective inference methodology, we then **defined an experimental methodology** that could take the results further in accuracy. A set of seven test cases was proposed under different static pressures and heat fluxes to study their influence on the results. The results showed two different classes of characterizations achieved. First, for low pressures of 15 mbar, we showed an improvement of 50 % over previous analyses. Even though it is still an improvement, we can appreciate a considerable support for the TPS material marginal distribution and a tendency towards following bimodal distributions. In contrast, higher pressure cases such as 50 and 100 mbar, yielded very precise parameters. The reduction of the uncertainty in this case was 30-50 % with respect to the previous 15 mbar cases and it relied solely on the chosen testing conditions. Nevertheless, not all the inferred parameters could be trusted. The model was not found to be a good representation of the experiments for two of the cases. Alternative explanations such as the uncertainty on the chemical state of the gas could lead to an improvement.

Objective 2: Calibration and assessment of graphite ablation models for nitrogen flows

In general, nitridation reaction efficiencies result from elaborated processes that combine models and experiments. The experimental techniques and methods used to retrieve nitridation reaction efficiencies in the literature rely on modeled components such as the atomic nitrogen concentrations at the sample locations. Depending on the nature of the experimental facility, different assumptions are made about the flow and the physical models used. Generally, the estimations from the different facilities and models encountered in the literature differ substantially from each other.

This second objective is accomplished by using state-of-the-art physico-chemical models to represent the gas phase with also different surface mechanisms such as nitridation and recombination, experimental data including radiation measurements which also provide information about ablation, and stochastic methods to deal with uncertainties stemming from the data and model definition.

First, the calibration is splitted in terms of the experimental data used. We wanted to gauge the different levels of information that recession rates and CN densities bring to the inference of nitridation efficiencies. By comparing and combining them we check for consistency issues in the experimental data and/or the model. We concluded that the spectrometer measurements presented inconsistencies for only one case. They were likely to stem from the lack of uncertainty treatment in the complex rebuilding chain from the line-of-sight spectra to local CN densities. Gathering the consistent data from all the experimental conditions allowed us to infer Arrhenius law parameters, relating the nitridation efficiencies to different wall temperatures.

The **second** part of this contribution was devoted to **model selection and averaging**. The base model presented in the first part of the analyses was based on flow thermal equilibrium assumptions which may not have been adequate for such low static pressures. The heterogeneous chemical mechanism was also ignoring the fact that nitrogen recombination might have been important. We considered three additional modeling scenarios which accounted for nitrogen recombination, surface energy balances and thermal non-equilibrium in the flow and the wall. All these modeling choices were assessed in a hypothesis testing study. Overall no strong evidence was found against the baseline model and none of the considered models could be discarded. The calibrations of models with surface recombination could define an upper limit for this parameter at best. The calibrated solutions of the thermal non-equilibrium model pointed to strong thermal non-equilibrium at the wall, although the evidence was weak. Model averaging was performed for the nitridation efficiencies and Arrhenius laws obtained under each model. Complete and accurate characterization of their posterior uncertainties was provided to update the current state-of-the-art databases.

8.1.2 General contributions

In a broader perspective, this thesis contributes to the general need in aerothermodynamics of implementing model calibration methodologies from experimental data for future model validation in a statistical setting. In this section, we discuss the aspects of the specific contributions outlined in Sec. 8.1.1 that also have an impact beyond the VKI Plasmatron facility and its experimental techniques, as well as the choice of modeling used in this work.

Overall, three general contributions are outlined: 1) development of calibration methodologies applicable to plasma wind tunnels and common ground-testing experimental data, 2) computation of accurate uncertainty estimates for catalysis and ablation experimental databases, and 3) application of general hypothesis testing techniques to assess flow models and surface mechanisms in light of experimental data.

First, the inference methodologies developed for catalysis and ablation parameters can also be applied to different classes of plasma wind tunnels, such as arcjets, where experiments on reusable materials are largely based on heat flux measurements in similar environments, and ablation is assessed through the measurements of recession rates and radiative signatures of the flow. Further, the work developed for the calibration of nitridation reaction efficiencies allows us to compare results obtained with different independent measurements. Apart from obtaining uncertainty reductions on the marginal posteriors, the comparisons allowed us to check for consistency in our experimental dataset as well as in model assumptions across the experimental conditions. We know from the literature that the quality and accuracy of the reported measurements represent the foundations on which inference methods stand. So far, there is not a standard and reliable way of checking the quality of experimental data. We have to either rely on the information passed on by the experimentalists or assumed the standard deviation of the measurement errors to be unknown. Independent measurements that give information about the same phenomenon also allow for the accurate model calibration and model cross-validation.

Second, the Bayesian inference methodologies developed can be used as tools for optimal experimental design where the most informative experiments can be proposed. Accurate calibration and experimental design can lead to a large improvement of future gas-surface interaction experimental databases. We have shown the potential of such approaches through an experimental methodology capable of significantly improving current catalysis estimations. Further, when epistemic uncertainties are recognised, such as the ones stemming from the thermal state of the flow or the role of nitrogen recombination in the experiments, we have shown how we can include them in our analyses by using Bayesian model averaging. Overall, the resulting distributions for catalysis and ablation parameters are available for use in CFD codes to propagate their uncertainties and assess their impact on different model predictions.

Third, we have shown how hypothesis testing techniques can be used in aerothermodynamics to gauge the evidence for different flow models and surface mechanisms. These techniques do not rely on single-point estimates such as traditional comparisons between model predictions and experiments in the state-of-the-art, but rather take into account the full posterior distributions obtained from the calibrations. Moreover, the complexity of each model is also taken into account through the extent of their parameter spaces. For similar quality of their predictions, simple models are favoured over more complex ones. Through these methods we were able to show that the presence of strong thermal non-equilibrium at the wall is compatible with the ablation experimental data considered in this thesis. Still, the baseline model of thermal equilibrium could not be discarded based on the data alone, which indicates that more research is needed in that direction. Further, we could find maximum values for nitrogen recombination efficiencies in the experiments considered. These newly found insights are relevant for improving the overall understanding of suitable boundary conditions for typical aerothermodynamic flows in plasma wind tunnels or in equivalent environments in real flight conditions.

8.2 Future work and perspectives

We now present perspectives which build on this work. Some of them take advantage of the novelties introduced in this work while others improve some of the weak points highlighted. Given the multidisciplinary nature of the contributions, future work recommendations are given in two groups: related to the physics/models/experiments (application oriented), and to the methods here used (methodology oriented).

Application oriented

- The experimental datasets for catalysis studies only rely on one type of measurement technique to carry the information on the catalytic parameters. Another independent source of information may be studied in the future. For instance, spectrometer measurements of molecules spectra that result from catalytic recombination may be of interest. Not only could this additional measurement reduce the uncertainty levels on our estimations but also help with the calibration of the gas phase chemistry. Anfuso et al. [245] have recently started an effort in this direction where they aim at using numerical simulations to determine what to look for in the experiments in order to get the most information about the chemistry and wall catalysis.

- The experimental methodology presented in Chapter 6 could be used to find the optimal experimental conditions for obtaining the most informative experiments, and produce a more extensive catalysis database. This methodology is also able to identify the limits of the baseline model used in this thesis. Defining and understanding the experimental conditions for which the baseline model can explain the data is important for accurate flight extrapolation and for the generation of reliable calibration and validation data.

- Following the thread with experimental studies, it was shown in Chapter 7 that reported spectrometer measurements might not be trustworthy. This issue is largely due to the fact that physical quantities derived from spectrometer measurements, such as CN concentrations, are the results of an elaborated measurement chain. As such, proper propagation of uncertainties from the raw data to the physical quantities should be carried out. Further, some intermediate steps, such as deriving flow temperatures from radiative intensities, represent an additional inverse problem. Overall, forward and backward uncertainty propagation techniques should be adopted for the rigorous derivation of physical quantities from raw experimental data.

- In Chapter 7, we found some evidence of possible thermal non-equilibrium at the wall. Given that the results are also conditioned on the gas phase chemistry, additional measurements could be added to the experimental dataset to calibrate the chemistry along with the ablation parameters. This might relax the condition of non-equilibrium at the wall or, conversely, not change it. Measurements of N_2 concentrations in the boundary layer along the stagnation line could also refine the obtained calibration of nitrogen recombination efficiencies.

- The results achieved for nitridation could be used as an upper bound for a prior distribution in the calibration of air ablation in the VKI plasmatron. The knowledge extracted from the nitrogen flow experiments can be used to inform future air ablation experiments when it comes to nitridation. A full air ablation model could be calibrated by using different experimental datasets in air and nitrogen under the same plasma conditions. As nitridation would compete with oxidation for the surface carbon, the values obtained when atomic nitrogen is the only reactive species are probably higher than those obtained in air. The prior could be carefully chosen to reflect this knowledge.

- Given the limitations on what we can validate in wind tunnels, the methodologies developed in this thesis could help pave the way to achieve model calibrations and validations with flight data. Although prohibitively expensive, flight data provide an unprecedented window to the coupling of the various physical phenomena that cannot be captured on ground. Cubesat platforms, such as HyCUBE [246] and QARMAN [146], for which the object of study is the atmospheric entry itself, have been proposed and designed for this purpose.

Methodology oriented

- The Bayesian inference methodology developed for catalysis in Chapter 5 is particularly tailored to plasma wind tunnel data and physico-chemical models that consider thermal equilibrium. Moreover, the results are conditioned on the gas phase chemistry model parameters which are considered known. As seen in Chapter 6, there are some conditions for which the model proposed is not a good representation of the experimental data. New hypotheses were proposed and tested with a numerical experiment. It was shown that uncertainties stemming from the gas phase chemistry could explain the discrepancies observed. Anfuso et al. [245] are already looking into extending the optimal likelihood methodology developed in this thesis to cases where the gas phase chemistry is also considered unknown. This task is not free of caveats. For starters, the optimal likelihood problem could not have a global optimum, finding local optima for different nuisance parameters. Further, the experimental data as it is, with only heat fluxes and pressures, might not be enough to achieve successful calibrations. In sum, new methodological and experimental avenues may have to be studied and implemented.

- The methodologies developed in this work are heavily conditioned by the computational complexity of the fluid dynamic solvers. Calibrations of 2D, 3D and unsteady flow models could be accomplished in the future. Further, hypothesis testing studies could be run to assess the evidence for additional spatial and temporal structures that are not currently captured. This would allow us to have a more complete picture.

- Dealing with more complex computational problems (2D, 3D or unsteady) surely implies adopting different approaches to solving the inverse problem due to the exponentially more expensive model evaluations. Surrogate models of such flow models would either need active training techniques or adaptive multi-fidelity approaches (or both) to further reduce the number of model evaluations for the same accuracy. Capriati et al. [247] are developing methods to cope with the computationally demanding task of propagating uncertainties in complex unsteady 3D flows following an error control strategy and adaptive multi-fidelity surrogate models.

- The Bayesian inferences here presented do not account for model errors. We assume that the discrepancies between observations and model predictions are due only to observational errors. This makes the obtained posteriors be the result of experimental uncertainties and model discrepancies, moreover we do not have the capability to distinguish between them. New refined estimations and insights could be acomplished by including the model error as a different error source in the inverse problems. Leoni et al. [248] are developing an inverse approach that accounts for the model error with particular application to multiphase flows.

All in all, if we want to reliably use our state-of-the-art models to design atmopsheric entry vehicles, we need to devise an overarching strategy for model calibration and validation. Different methodologies can be tailored to the various ground-testing facilities, based on the methods presented in this thesis. The ensemble knowledge of the generated databases with their uncertainty estimations can be used to formulate suitable priors that inform the full models including possible coupling mechanisms. If flight data is not available from similar previous flights, the priors represent the best we can do, if not, they can be used to calibrate the full models with flight data and generate the posteriors we are after. Final calibrated models can be used to project accurate and relistic uncertainty estimates on the design parameters, enabling future missions.

To successfully tackle these objectives with the methods presented in this thesis, we need improvements in several fronts. Computational methods need to increase their efficiency at producing high quality solutions for low computational cost. Experimental techniques need to investigate new avenues for the direct and accurate probing of microscopic phenomena for relevant flight conditions. Further, we need to estimate reliable uncertainty levels on model data built upon well-established theories, such as quantum and statistical mechanics, as well as experimental data such as kinetics. The improvement and successful implementation of statistical methods for model calibration and validation hinders on all these different disciplines.

Appendices

Appendix A

Transport systems

This appendix describes the evaluation of the linear transport systems necessary for computing the transport properties shown in Chapter 2. For the most part, these equations can be found in the results of [76], and are reproduced here for clarity and completeness.

Binary diffusion coefficients for heavy-heavy and heavy-electron are expressed as

$$n\mathscr{D}_{ij} = \frac{3}{16}\sqrt{\frac{2\pi k_{\mathrm{B}} T_h \left(m_i + m_j\right)}{m_i m_j}}\frac{1}{\bar{Q}_{ij}^{(1,1)}}, \quad i, j \in \mathcal{H}, \tag{A.1}$$

$$n\mathscr{D}_{i\mathrm{e}} = \frac{3}{16}\sqrt{\frac{2\pi k_{\mathrm{B}} T_e}{m_e}}\frac{1}{\bar{Q}_{ie}^{(1,1)}}, \quad i \in \mathcal{H}, \tag{A.2}$$

$$n\mathscr{D}_{\mathrm{ee}} = \frac{3}{8}\sqrt{\frac{\pi k_{\mathrm{B}} T_{\mathrm{e}}}{m_{\mathrm{e}}}}\frac{1}{\bar{Q}_{\mathrm{ee}}^{(1,1)}}. \tag{A.3}$$

As discussed in Chapter 2, the transport systems result from Laguerre-Sonine polynomial approximations of the Chapman-Enskog approximation to the non-dimensionalized Boltzmann equation. The resulting systems are summarized in Tables A.1-A.2 for heavy-heavy interactions and all electron interactions, respectively.

The terms ϕ_{ij} and $\phi_{i\mathrm{e}}$ are the correction functions to consider a higher order Sonine polynomial for heavy-heavy interactions and heacy-electron interactions, respectively. First order and second order approximations read

$$\phi_{ij}(1) = 0, \tag{A.4}$$

$$\phi_{ij}(2) = -\frac{25}{8} k_{\mathrm{B}} \frac{n\mathscr{D}_{ij}}{x_i x_j} \sum_{k\in\mathcal{H}} \Lambda_{ik}^{01}\beta_{kj}, \tag{A.5}$$

$$\sum_{k\in\mathcal{H}} G_{ik}^{\lambda_h}\beta_{kj} = -2\Lambda_{ji}^{01}, \quad i, j \in \mathcal{H}, \tag{A.6}$$

$$\phi_{i\mathrm{e}}(1) = 0, \tag{A.7}$$

$$\phi_{i\mathrm{e}}(2) = -\frac{25}{8} k_{\mathrm{B}} \frac{n\mathscr{D}_{i\mathrm{e}}}{x_i x_{\mathrm{e}}} \frac{\Lambda_{\mathrm{ee}}^{01}\Lambda_{ie}^{01}}{\Lambda_{\mathrm{ee}}^{11}}, \tag{A.8}$$

for which the following relationship is used to fulfill Eq. (A.8) with the data from Table A.2

$$\Lambda_{ie}^{kl} = \frac{64 x_{\mathrm{e}}}{75 k_{\mathrm{B}}}\sqrt{\frac{m_{\mathrm{e}}}{2\pi k_{\mathrm{B}} T_{\mathrm{e}}}}\tilde{\Lambda}_{ie}^{kl}, \quad i \in \mathcal{S},\ k, l \in \{0, 1\}. \tag{A.9}$$

The terms A_{ij}^{*}, B_{ij}^{*} and C_{ij}^{*} in Table A.1 are the usual expressions for collision integral ratios and they read

Table A.1: *Summary of heavy particle transport subsystems used in this work,* $i, j \in \mathcal{H}$*.*

System	Formula
G_{ij}^{μ}	$\frac{x_i x_j}{n\mathscr{D}_{ij}} \frac{1}{m_i+m_j} \left(\frac{6}{5} A_{ij}^* - 2\right), \quad i \neq j$
G_{ii}^{μ}	$\sum_{\substack{j\in\mathcal{H} \\ j\neq i}} \frac{x_i x_j}{n\mathscr{D}_{ij}} \frac{1}{m_i+m_j} \left(\frac{6}{5} \frac{m_j}{m_i} A_{ij}^* + 2\right) + \frac{x_i^2}{\mu_i}$
$G_{ij}^{\lambda_\mathrm{h}}$	$\frac{1}{25 k_\mathrm{B}} \frac{x_i x_j}{n\mathscr{D}_{ij}} \frac{m_i m_j}{(m_i+m_j)^2} \left(16 A_{ij}^* + 12 B_{ij}^* - 55\right), \quad i \neq j$
$G_{ii}^{\lambda_\mathrm{h}}$	$\frac{1}{25 k_\mathrm{B}} \sum_{\substack{j\in\mathcal{H} \\ j\neq i}} \frac{x_i x_j}{n\mathscr{D}_{ij}} \frac{m_i m_j}{(m_i+m_j)^2} \left(16 A_{ij}^* - 12 \frac{m_j}{m_i} B_{ij}^* + 25 \frac{m_j}{m_i} + 30 \frac{m_i}{m_j}\right) + \frac{4 m_i}{15 k_\mathrm{B}} \frac{x_i^2}{\mu_i}$
G_{ij}^{V}	$-\frac{x_i x_j}{\mathscr{D}_{ij}} \left(1 + \phi_{ij}\right), \quad i \neq j$
G_{ii}^{V}	$\sum_{\substack{j\in\mathcal{H} \\ j\neq i}} \frac{x_i x_j}{\mathscr{D}_{ij}} \left(1 + \phi_{ij}\right) + \left(\frac{T_\mathrm{e}}{T_h}\right)^2 \frac{x_i x_\mathrm{e}}{\mathscr{D}_{i\mathrm{e}}} \left(1 + \phi_{i\mathrm{e}}\right)$
Λ_{ij}^{01}	$\frac{1}{25 k_\mathrm{B}} \frac{x_i x_j}{n\mathscr{D}_{ij}} \frac{m_i}{m_i+m_j} \left(12 C_{ij}^* - 10\right), \quad i \neq j$
Λ_{ii}^{01}	$-\frac{1}{25 k_\mathrm{B}} \sum_{\substack{j\in\mathcal{H} \\ j\neq i}} \frac{x_i x_j}{n\mathscr{D}_{ij}} \frac{m_j}{m_i+m_j} \left(12 C_{ij}^* - 10\right)$

$$A_{ij}^* = \frac{\bar{Q}_{ij}^{(2,2)}}{\bar{Q}_{ij}^{(1,1)}}, \tag{A.10}$$

$$B_{ij}^* = \frac{5\bar{Q}_{ij}^{(1,2)} - 4\bar{Q}_{ij}^{(1,3)}}{\bar{Q}_{ij}^{(1,1)}}, \tag{A.11}$$

$$C_{ij}^* = \frac{\bar{Q}_{ij}^{(1,2)}}{\bar{Q}_{ij}^{(1,1)}}. \tag{A.12}$$

The term μ_i refers to the viscosity coefficient for heavy particles and reads

$$\mu_i = \frac{5}{16} \frac{\sqrt{\pi k_\mathrm{B} T_\mathrm{h} m_i}}{\bar{Q}_{ii}^{(2,2)}}, \quad i \in \mathcal{H}. \tag{A.13}$$

Table A.2: *Summary of heavy particle-electron and electron-electron transport subsystems used in this work, $i \in \mathcal{H}$.*

System	Formula
$G^V_{i\mathrm{e}}$	$-\frac{T_\mathrm{e}}{T_\mathrm{h}}\frac{x_i x_\mathrm{e}}{\mathscr{D}_{i\mathrm{e}}}\left(1+\phi_{i\mathrm{e}}\right)$
G^V_{ee}	$\sum_{i\in\mathcal{H}}\frac{x_i x_\mathrm{e}}{\mathscr{D}_{i\mathrm{e}}}\left(1+\phi_{i\mathrm{e}}\right)$
$\tilde{\Lambda}^{01}_{i\mathrm{e}}$	$x_i\frac{T_\mathrm{e}}{T_\mathrm{h}}\left(\frac{5}{2}\bar{Q}^{(1,1)}_{\mathrm{e}j}-3\bar{Q}^{(1,2)}_{\mathrm{e}j}\right)$
$\tilde{\Lambda}^{01}_{\mathrm{ee}}$	$\sum_{j\in\mathcal{H}} x_j\left(\frac{5}{2}\bar{Q}^{(1,1)}_{\mathrm{e}j}-3\bar{Q}^{(1,2)}_{\mathrm{e}j}\right)$
$\tilde{\Lambda}^{11}_{\mathrm{ee}}$	$\sum_{j\in\mathcal{H}} x_j\left(\frac{25}{4}\bar{Q}^{(1,1)}_{\mathrm{e}j}-15\bar{Q}^{(1,2)}_{\mathrm{e}j}+12\bar{Q}^{(1,3)}_{\mathrm{e}j}\right)+x_\mathrm{e}\sqrt{2}\bar{Q}^{(2,2)}_{\mathrm{ee}}$
$\tilde{\Lambda}^{12}_{\mathrm{ee}}$	$\sum_{j\in\mathcal{H}} x_j\left(\frac{175}{16}\bar{Q}^{(1,1)}_{\mathrm{e}j}-\frac{315}{8}\bar{Q}^{(1,2)}_{\mathrm{e}j}+57\bar{Q}^{(1,3)}_{\mathrm{e}j}-30\bar{Q}^{(1,4)}_{\mathrm{e}j}\right)+x_\mathrm{e}\sqrt{2}\left(\frac{7}{4}\bar{Q}^{(2,2)}_{\mathrm{ee}}-2\bar{Q}^{(2,3)}_{\mathrm{ee}}\right)$
$\tilde{\Lambda}^{22}_{\mathrm{ee}}$	$\sum_{j\in\mathcal{H}} x_j\left(\frac{1225}{64}\bar{Q}^{(1,1)}_{\mathrm{e}j}-\frac{735}{8}\bar{Q}^{(1,2)}_{\mathrm{e}j}+\frac{399}{2}\bar{Q}^{(1,3)}_{\mathrm{e}j}-210\bar{Q}^{(1,4)}_{\mathrm{e}j}+90\bar{Q}^{(1,5)}_{\mathrm{e}j}\right)+x_\mathrm{e}\sqrt{2}\left(\frac{77}{16}\bar{Q}^{(2,2)}_{\mathrm{ee}}-7\bar{Q}^{(2,3)}_{\mathrm{ee}}+5\bar{Q}^{(2,4)}_{\mathrm{ee}}\right)$

Appendix B

Physico-chemical model data

This appendix details the various mixtures and physico-chemical data used for the simulations described in this thesis. The data here depicted include species involved, specific reactions considered, as well as the collision integral data necessary to compute the transport coefficients.

B.1 Mixtures

This section is devoted to the exposition of the chemistry model data used in the problems involving catalysis in CMC materials and nitridation calibrations.

The mixtures described in Sections 3.1.1-3.1.2 are summarized in Table B.1. The table provides lists of species included in the respective mixtures, and the numbers of species, reactions, and collision pairs. Species thermodynamic properties were computed using the RRHO model as described in Sections 3.1.1-3.1.2. The reaction mechanisms and rate constants employed for the mixtures are detailed in the proceeding section followed by the collision integral data required to compute transport coefficients.

Table B.1: *Summary of the mixtures used in Chapters 5-7.*

Mixture name	Species	# Species / Reactions	# Collision Pairs
air7	$O_2, N_2, NO, O, N,$ NO^+, e^-	7/21	28
nitrogen-carbon	e^-, C^+, C_2, C_3, CN C, N, N^+, N_2	9/37	45

B.2 Reaction mechanisms

This section presents the reaction mechanisms used for each of the mixtures summarized in the previous section. For each mechanism, the corresponding reactions, rate constants, and temperature dependencies are provided in Tables B.2-B.3.

B.3 Collision integrals

This section present summaries of the collision integral data used for each mixture presented in Section B.1. In Figs. B.1-B.2, all collision integrals are either explicitly taken from the given reference, or are computed using the Langevin (ion-neutral) and Coulomb (charged-charged) potentials.

Table B.2: *Gas phase chemical reactions used in this work for the catalysis studies (air7 mixture). Forward reaction rate coefficients are computed using the modified Arrhenius formula,* $k_f(T_f) = AT_f^{\beta}\exp(-T_\mathrm{a}/T_f)$. *Backward reaction rate coefficients are computed in order to satisfy equilibrium at the temperature associated with the reverse reaction,* $k_b = k_f(T_b)/k_{eq}(T_b)$. *The sources for the listed rate constants are provided in the last column.*

No.	Reaction	A m, s, mol	β	T_a K	Ref.
	Dissociation reactions				
1.	$\mathrm{O_2 + M \rightleftharpoons 2O + M}$ $\mathrm{M = N, NO}$	3.6×10^{18}	-1.00	59 500	[118]
2.	$\mathrm{O_2 + O \rightleftharpoons 2O + O}$	9.0×10^{19}	-1.00	59 500	[118]
3.	$\mathrm{O_2 + O_2 \rightleftharpoons 2O + O_2}$	3.24×10^{9}	-1.00	59 500	[118]
4.	$\mathrm{O_2 + N_2 \rightleftharpoons 2O + N_2}$	7.2×10^{18}	-1.00	59 500	[118]
5.	$\mathrm{N_2 + M \rightleftharpoons 2N + M}$ $\mathrm{M = O, NO, O_2}$	1.9×10^{17}	-0.50	113 000	[118]
6.	$\mathrm{N_2 + N \rightleftharpoons 2N + N}$	4.085×10^{22}	-1.50	113 000	[118]
7.	$\mathrm{N_2 + N_2 \rightleftharpoons 2N + N_2}$	4.7×10^{17}	-0.50	113000	[118]
8.	$\mathrm{NO + M \rightleftharpoons N + O + M}$ $\mathrm{M = N_2, O_2}$	3.9×10^{20}	-1.50	75 500	[118]
9.	$\mathrm{NO + M \rightleftharpoons N + O + M}$ $\mathrm{M = O, N, NO}$	7.8×10^{20}	-1.50	75 500	[118]
	Exchange reactions				
10.	$\mathrm{NO + O \rightleftharpoons O_2 + N}$	3.2×10^{9}	1.00	19 700	[118]
11.	$\mathrm{N_2 + O \rightleftharpoons NO + N}$	7.0×10^{13}	0.00	38 000	[118]
	Associative ionization reaction				
12.	$\mathrm{N + O \rightleftharpoons NO^+ + e^-}$	1.4×10^{6}	1.50	31 900	[118]
	Exchange ionization reaction				
13.	$\mathrm{O_2 + N_2 \rightleftharpoons NO + NO^+ + e^-}$	1.38×10^{20}	-1.84	141 000	[118]
	Heavy-impact ionization reactions				
14.	$\mathrm{N_2 + NO \rightleftharpoons N_2 + NO^+ + e^-}$	2.2×10^{15}	-0.35	108 000	[118]
15.	$\mathrm{O_2 + NO \rightleftharpoons NO^+ + O_2 + e^-}$	8.8×10^{15}	-0.35	108 000	[118]

Table B.3: *Gas phase chemical reactions used in this work for the nitridation studies (nitrogen-carbon mixture). Forward reaction rate coefficients are computed using the modified Arrhenius formula,* $k_f(T_f) = AT_f^{\beta}\exp(-T_\mathrm{a}/T_f)$*. Backward reaction rate coefficients are computed in order to satisfy equilibrium at the temperature associated with the reverse reaction,* $k_b = k_f(T_b)/k_{eq}(T_b)$*. The sources for the listed rate constants are provided in the last column.*

No.	Reaction	T_f K	A m, s, mol	β	T_a K	Ref.
	Dissociation reactions					
1.	$\mathrm{N_2 + M \rightleftharpoons 2N + M}$ $\mathrm{M = C, N, C^+, N^+}$	$\sqrt{TT^V}$	3.0×10^{22}	-1.60	113 200	[249]
2.	$\mathrm{N_2 + M \rightleftharpoons 2N + M}$ $\mathrm{M = N_2, C_2, C_3, CN}$	$\sqrt{TT^V}$	7.0×10^{21}	-1.60	113 200	[249]
3.	$\mathrm{N_2 + e^- \rightleftharpoons 2N + e^-}$	$\sqrt{TT^V}$	1.20×10^{25}	-1.60	113 200	[249]
4.	$\mathrm{C_2 + M \rightleftharpoons C + C + M}$	$\sqrt{TT^V}$	3.7×10^{14}	0.00	69 000	[249]
5.	$\mathrm{CN + M \rightleftharpoons C + N + M}$	$\sqrt{TT^V}$	2.5×10^{14}	0.00	71 000	[249]
6.	$\mathrm{C_3 + M \rightleftharpoons C_2 + C + M}$	$\sqrt{TT^V}$	6.3×10^{16}	-0.50	101 200	[250]
	Exchange reactions					
7.	$\mathrm{N_2 + C \rightleftharpoons CN + N}$	T	1.1×10^{14}	-0.11	23 200	[249]
8.	$\mathrm{CN + C \rightleftharpoons C_2 + N}$	T	5.0×10^{13}	0.00	13 000	[249]
	Electron-impact ionization reactions					
9.	$\mathrm{N + e^- \rightleftharpoons N^+ + e^- + e^-}$	T	5.08×10^{16}	0.00	121 000	[251]
10.	$\mathrm{C + e^- \rightleftharpoons C^+ + e^- + e^-}$	T	6.35×10^{15}	0.00	130 700	[251]

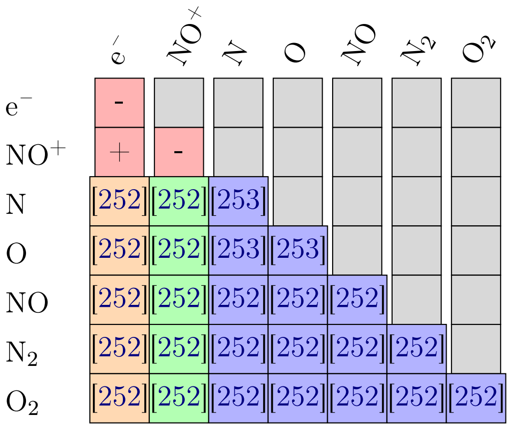

	e^-	NO^+	N	O	NO	N_2	O_2
$\mathrm{e^-}$	-						
$\mathrm{NO^+}$	+	-					
N	[252]	[252]	[253]				
O	[252]	[252]	[253]	[253]			
NO	[252]	[252]	[252]	[252]	[252]		
$\mathrm{N_2}$	[252]	[252]	[252]	[252]	[252]	[252]	
$\mathrm{O_2}$	[252]	[252]	[252]	[252]	[252]	[252]	[252]

Figure B.1: *Summary of collision integral data for the air7 mixture used in this work. Cell colors represent type of collision (red : charged, orange : electron-neutral, green : ion-neutral, blue : neutral-neutral). Numbers indicate reference source for each collision pair. + : attractive, - : repulsive.*

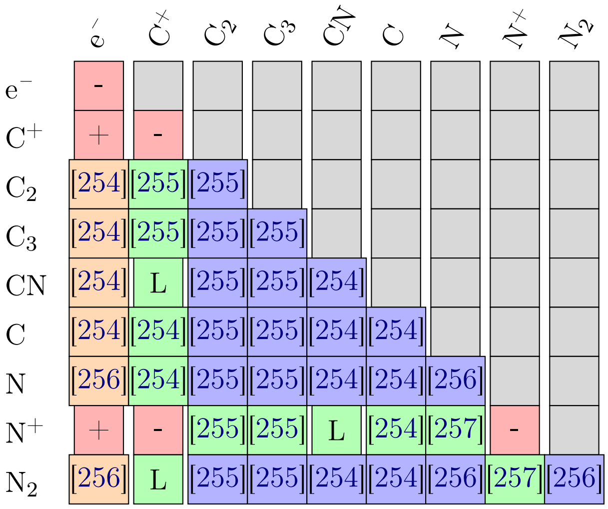

	e^-	C^+	C_2	C_3	CN	C	N	N^+	N_2
e^-	-								
C^+	+	-							
C_2	[254]	[255]	[255]						
C_3	[254]	[255]	[255]	[255]					
CN	[254]	L	[255]	[255]	[254]				
C	[254]	[254]	[255]	[255]	[254]	[254]			
N	[256]	[254]	[255]	[255]	[254]	[254]	[256]		
N^+	+	-	[255]	[255]	L	[254]	[257]	-	
N_2	[256]	L	[255]	[255]	[254]	[254]	[256]	[257]	[256]

Figure B.2: *Summary of collision integral data for the nitrogen-carbon mixture used in this work. Cell colors represent type of collision (red : charged, orange : electron-neutral, green : ion-neutral, blue : neutral-neutral). Numbers indicate reference source for each collision pair. + : attractive, - : repulsive, L : Langevin potential.*

Appendix C

VKI Plasmatron testing conditions

This appendix contains additional data and post-processing procedures related to the experiments depicted in Chapter 6.

C.1 Experimental conditions

Table C.1: *Experimental testing conditions and corresponding non-dimensional parameters.*

Test case	P_s [mbar]	P_w [kW]	Π_1 [-]	Π_2 [-]	Π_3 [-]	Π_4 [-]	Π_5 [-]
MTAt1	15	157	0.4053	0.3513	0.6454	0.3779	0.4487
MTAt2	15	202	0.3903	0.3158	0.5906	0.3309	0.4371
MTAt3	15	281	0.3856	0.3119	0.5850	0.3247	0.4344
MTAt4	50	185	0.3849	0.2952	0.5663	0.3089	0.4439
MTAt5	100	177	0.3765	0.2568	0.5344	0.2802	0.4481
MTAt6	100	191	0.3700	0.2524	0.5300	0.2709	0.4443
MTAt7	100	205	0.3644	0.2514	0.5310	0.2660	0.4414

C.2 Adaptation model

The test case MTAs1 is based on Panerai and Chazot [19] and Viladegut and Chazot [20] experimental campaigns. The targeted reference heat flux for this analysis is 700 kW/m^2. However, as Panerai and Chazot did not target this heat flux, a scaling factor is applied. The actual testing conditions of Panerai and Chazot's work are summarized below in Table C.2.

Table C.2: *Actual testing conditions extracted from Panerai and Chazot [19].*

Test case	P_s [mbar]	q_w^Cu [kW/m^2]	P_d [Pa]	$q_\mathrm{w}^\mathrm{TPS}$ [kW/m^2]	$T_\mathrm{w}^\mathrm{TPS}$ [K]
k1a	15	410	127	174	1400
k1b	15	760	162	331	1600
k2a	15	1150	232	476	1800
k2b	15	1465	290	626	2000

Relations between the reference heat fluxes and each of the other parameters tested are found. The linear regressions, with respective R^2, obtained for each of the parameters are illustrated in Figs. C.1, C.2 and C.3 for the dynamic pressure, TPS heat flux and TPS wall temperature, respectively. The relations are summarized in Eqs. (C.1)-(C.3).

$$P_\mathrm{d} = 0.1571 \times q_\mathrm{w}^\mathrm{Cu} + 54.08, \tag{C.1}$$

$$q_\mathrm{w}^\mathrm{TPS} = 0.4215 \times q_\mathrm{w}^\mathrm{Cu} + 2.89, \tag{C.2}$$

$$T_\mathrm{w}^\mathrm{TPS} = 0.5617 \times q_\mathrm{w}^\mathrm{Cu} + 1168.47. \tag{C.3}$$

The remaining testing conditions are extracted from Viladegut and Chazot's work as they tested quartz and copper together. The testing parameters are summarized in Table C.3

Table C.3: *Actual testing conditions extracted from Viladegut and Chazot [20].*

Test case	P_s [mbar]	q_w^Cu [kW/m^2]	q_w^Qz [kW/m^2]	Π_1 [-]	Π_2 [-]	Π_3 [-]	Π_4 [-]	Π_5 [-]
3a	15	700	233.8	0.4347	0.3137	0.5142	0.3407	0.4212

The scaling for any reference heat flux is done by replacing q_w^Cu in the previous equations by the targetted heat flux, in this case the 700 kW/m^2 from Viladegut and Chazot's experiment.

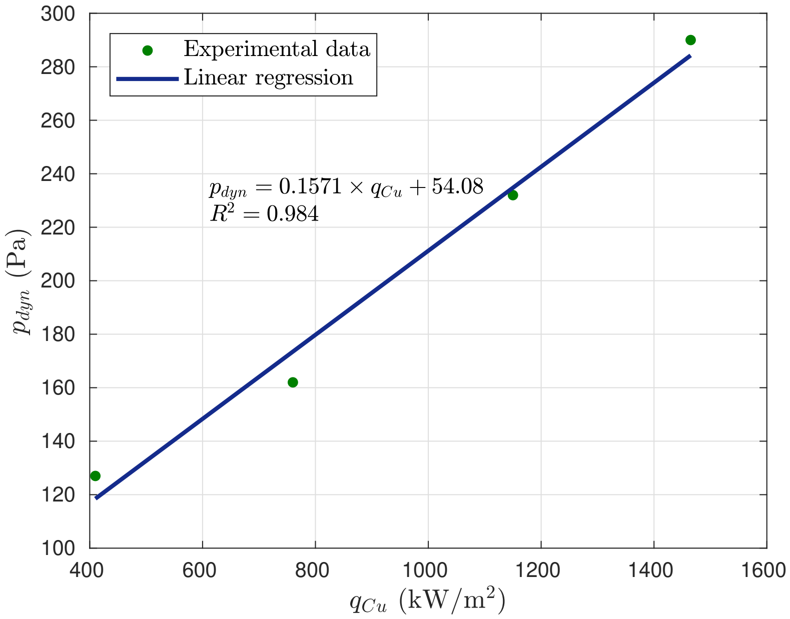

Figure C.1: *Linear regression between dynamic pressure and copper heat flux.*

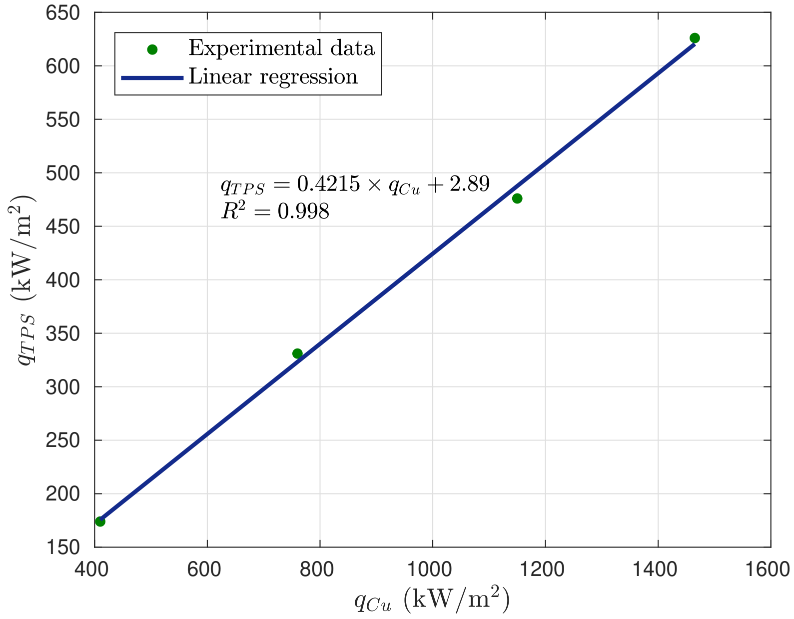

Figure C.2: *Linear regression between TPS and copper heat fluxes.*

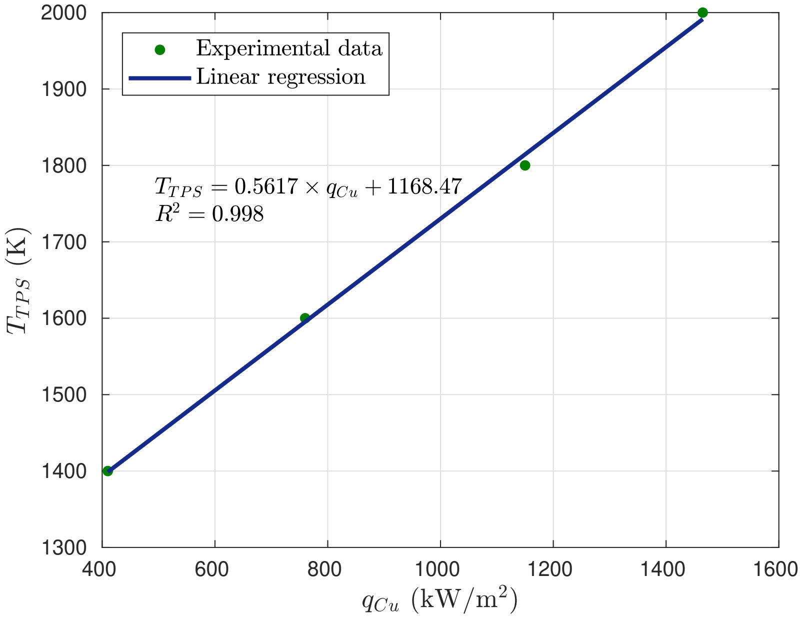

Figure C.3: *Linear regression between TPS wall temperature and copper heat flux.*

Appendix D

Complementary results for nitrogen ablation

This appendix contains the results concerning the cases not included in Section 7.7.1.

D.1 Prediction residuals

Figs. D.1-D.3 show the residuals for cases G4, G6 and G7 for recession rate $\dot{s}$, CN density ρ_{CN} and surface temperature T_{w} under the different modeling scenarios. We recall that we only take into account the recession rate measurements for case G6 for which the CN density residual is not shown.

D.2 Calibrated flowfield solutions

Figs. D.4-D.9 show the propagated posterior solutions of the stagnation line model for both the 1T SEB and 2T SEB models with their corresponding confidence intervals for cases G4, G6 and G7.

D.3 Posterior distributions of the surface parameters for the 2T model

Fig. D.10 shows samples of the 2D joint posterior distributions of the parameters α and β in the 2T surface balance model, as well as their marginal posteriors for cases G4, G6, and G7.

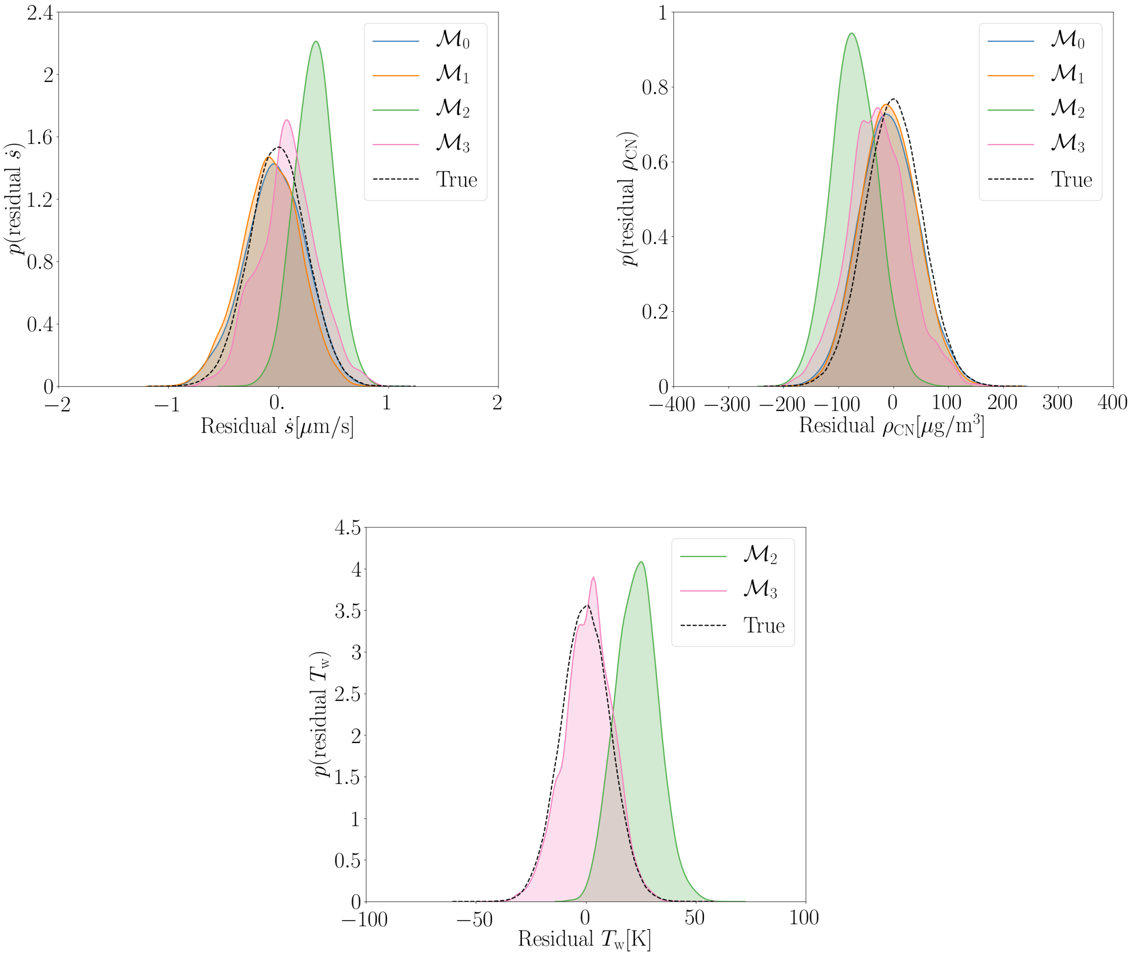

Figure D.1: *Residuals of recession rate $\dot{s}$, CN density ρ_{CN} and surface temperature T_{w} for the different models under conditions G4.*

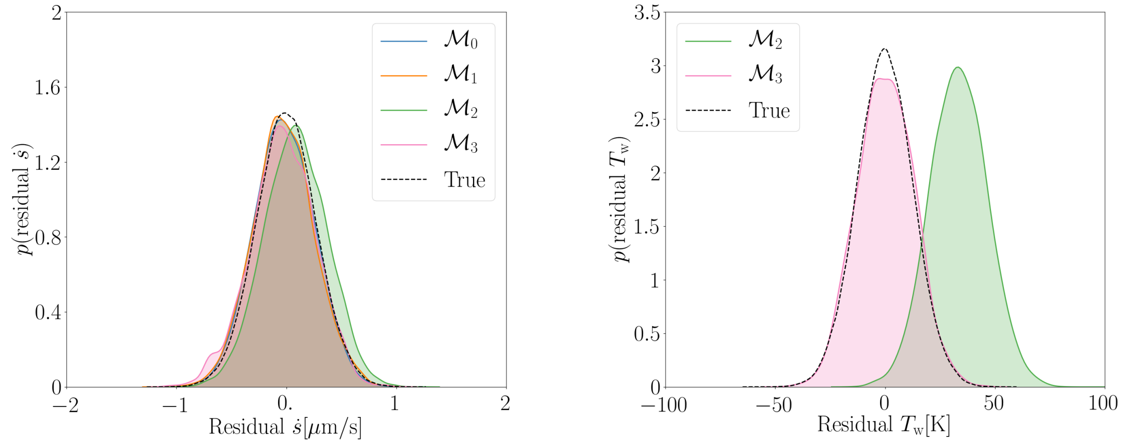

Figure D.2: *Residuals of recession rate $\dot{s}$ and surface temperature T_w for the different models under conditions G6.*

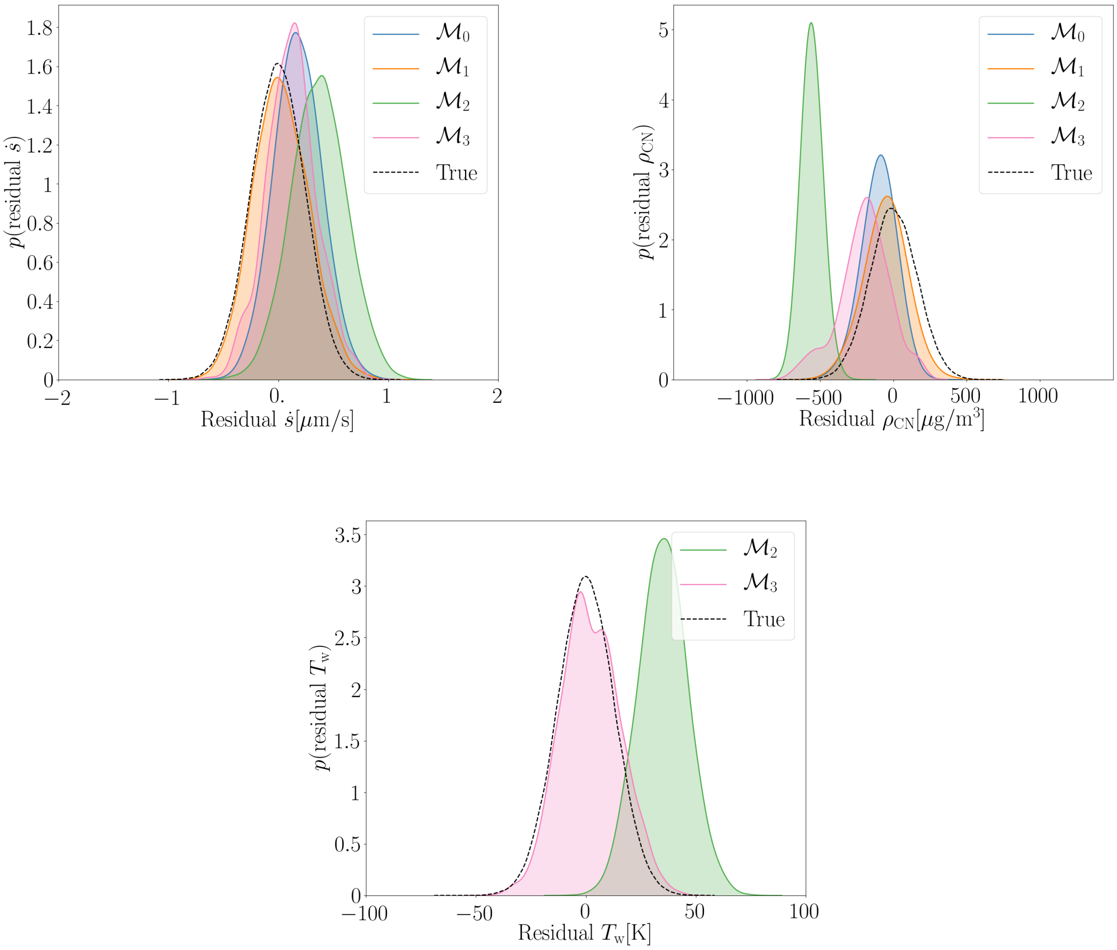

Figure D.3: *Residuals of recession rate $\dot{s}$, CN density ρ_{CN} and surface temperature T_{w} for the different models under conditions G7.*

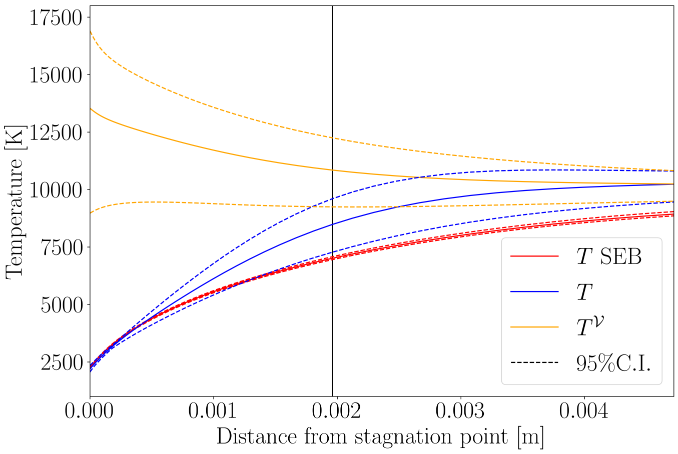

Figure D.4: *Propagated temperature profiles for the 1T SEB ($\mathcal{M}_2$) and 2T SEB ($\mathcal{M}_3$) models with their respective confidence intervals for case G4. The vertical black line represents the position of the spectrometer measurement.*

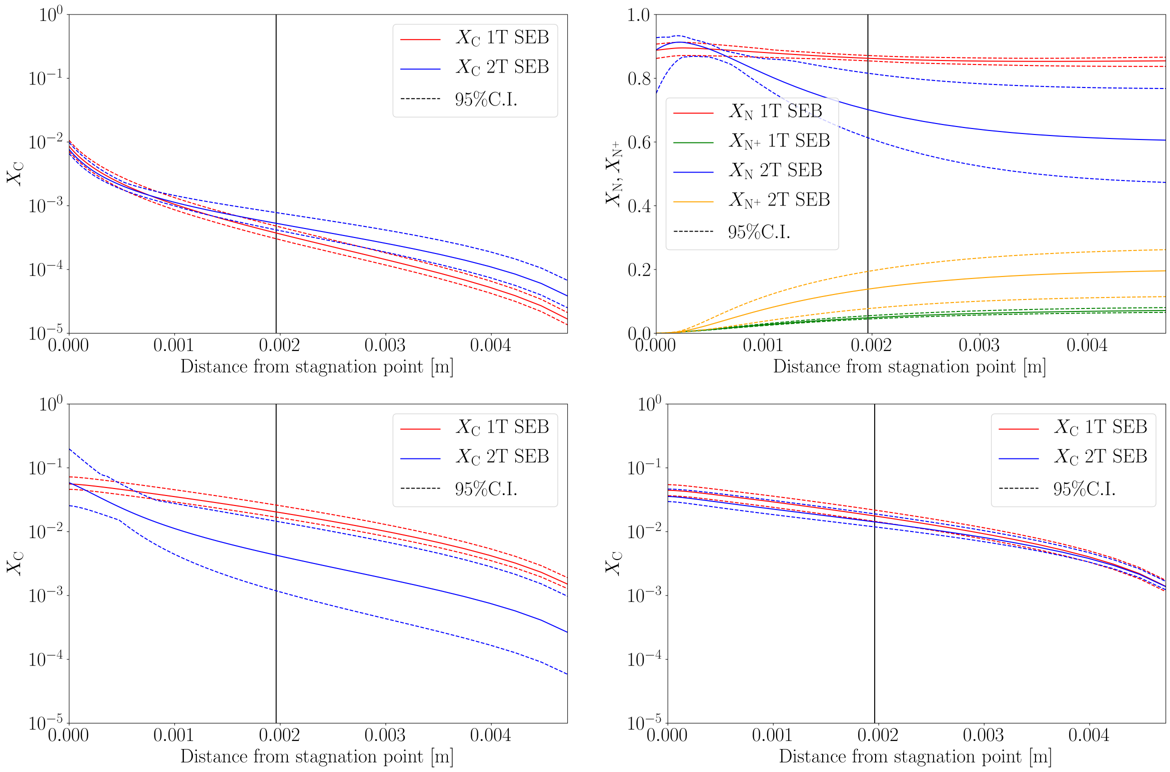

Figure D.5: *Propagated mole fraction profiles for the 1T SEB ($\mathcal{M}_2$) and 2T SEB ($\mathcal{M}_3$) models with their respective confidence intervals for case G4. The vertical black lines represent the position of the spectrometer measurement.*

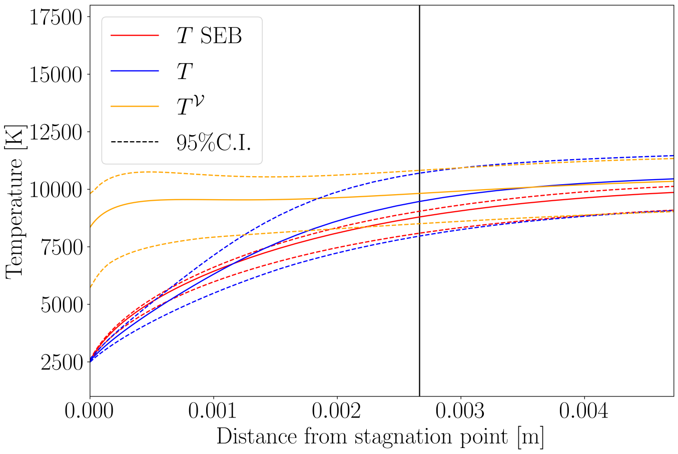

Figure D.6: *Propagated temperature profiles for the 1T SEB ($\mathcal{M}_2$) and 2T SEB ($\mathcal{M}_3$) models with their respective confidence intervals for case G6. The vertical black line represents the position of the spectrometer measurement.*

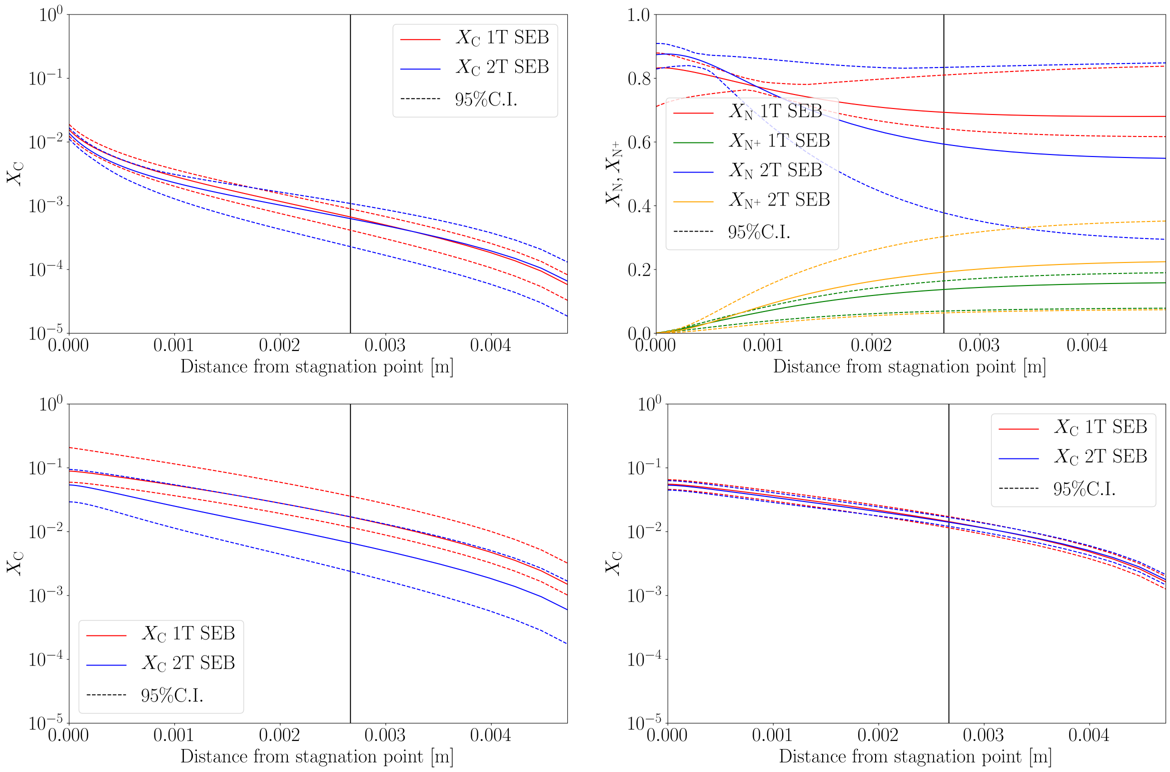

Figure D.7: *Propagated mole fraction profiles for the 1T SEB ($\mathcal{M}_2$) and 2T SEB ($\mathcal{M}_3$) models with their respective confidence intervals for case G6. The vertical black lines represent the position of the spectrometer measurement.*

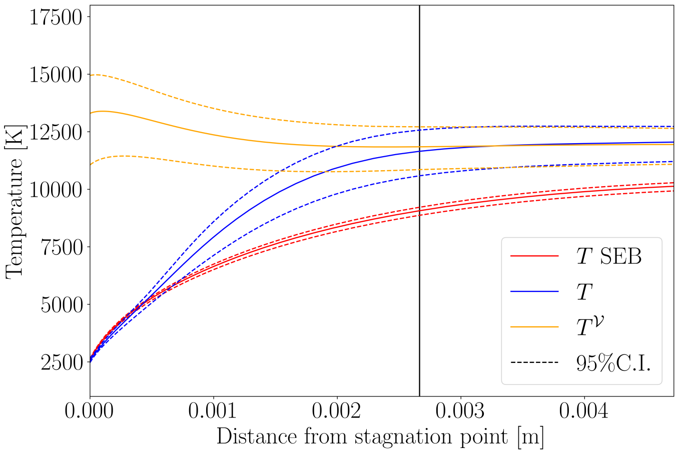

Figure D.8: *Propagated temperature profiles for the 1T SEB ($\mathcal{M}_2$) and 2T SEB ($\mathcal{M}_3$) models with their respective confidence intervals for case G7. The vertical black line represents the position of the spectrometer measurement.*

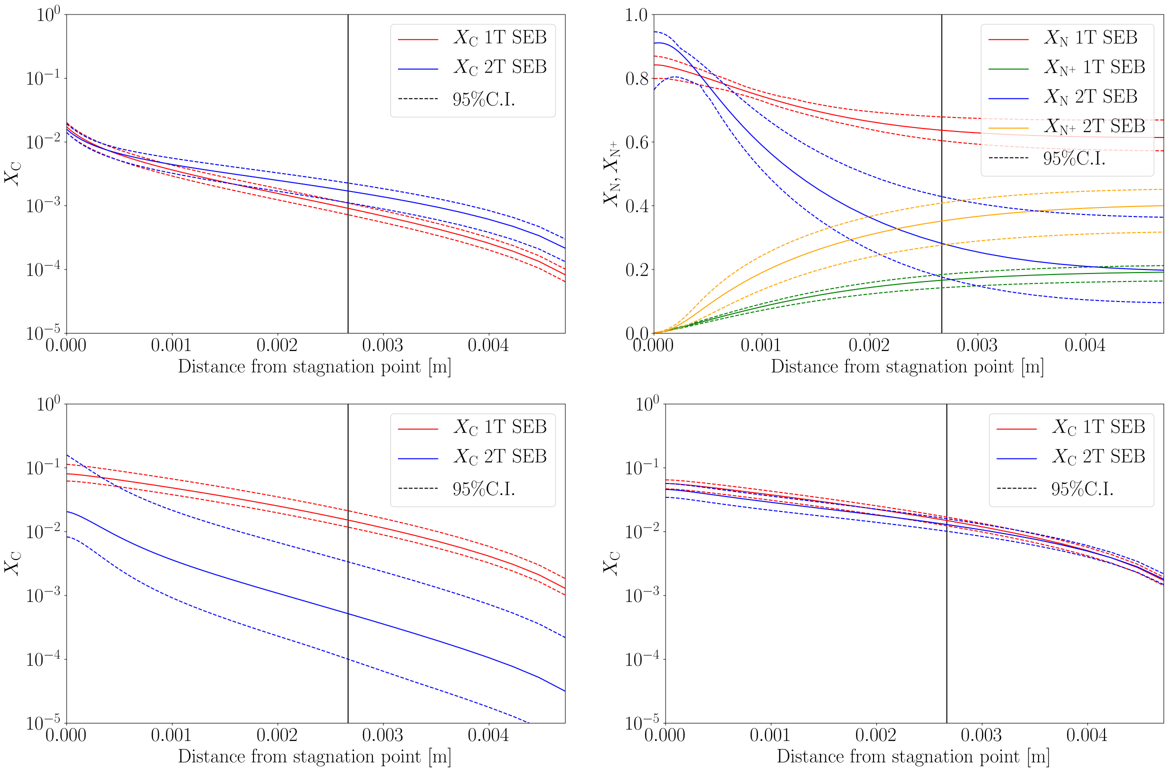

Figure D.9: *Propagated mole fraction profiles for the 1T SEB ($\mathcal{M}_2$) and 2T SEB ($\mathcal{M}_3$) models with their respective confidence intervals for case G7. The vertical black lines represent the position of the spectrometer measurement.*

Figure D.10: *Left: 100,000 samples from the joint posterior distributions of α and β. Right: posterior marginal distributions of α and β under conditions (from top to bottom) G4, G6 and G7.*

Bibliography

[1] J. B. Scoggins. *Development of numerical methods and study of coupled flow, radiation, and ablation phenomena for atmospheric entry.* PhD thesis, VKI/CentraleSupélec, 2017. xvii, 2, 22, 31, 35, 36, 59, 62, 63

[2] M. Wright. Presentation at Thermal and Fluid Analysis Workshop (TFAWS), Pasadena, CA, US. Available at `https://tfaws.nasa.gov`. xvii, 3

[3] B. Helber. *Material Response Characterization of Low-density Ablators in Atmospheric Entry Plasmas.* PhD thesis, VUB/VKI, 2016. xvii, xviii, 3, 4, 19, 53, 54, 70, 71, 72, 73, 76, 77, 136, 138, 161

[4] F. Panerai. *Aerothermochemistry Characterization of Thermal Protection Systems.* PhD thesis, Università degli Studi di Perugia,von Karman Institute for Fluid Dynamics, 2012. xvii, xviii, 19, 58, 65, 66, 67, 68, 69, 70, 74, 77, 112, 133, 135, 136, 138, 161

[5] F. Sanson, F. Panerai, T. E. Magin, and P. M. Congedo. Robust reconstruction of the catalytic properties of thermal protection materials from sparse high-enthalpy facility experimental data. *Experimental Thermal and Fluid Science*, 96:482–492, 2018. xxiii, 10, 53, 67, 110, 114, 118, 122

[6] B. Laub and E. Venkatapathy. Thermal protection system technology and facility needs for demanding future planetary missions. In *Proceedings of international workshop on planetary probe atmospheric entry and descent trajectory analysis and science*, pages 239 – 247, 2004. 1

[7] J. D. Anderson. *Hypersonic and high-temperature gas dynamics, second ed.* AIAA Education Series, 2006. 1, 55, 58

[8] G. Duffa. *Ablative Thermal Protection Systems Modeling.* AIAA Education Series, 2013. 1

[9] P. A. Gnoffo. Planetary-entry gas dynamics. *Annual Review of Fluid Mechanics*, 31:459–494, 1999. 2, 15, 18

[10] O. Chazot and F. Panerai. *High enthalpy facilities and plasma wind tunnels for aerothermodynamics ground testing in: Hypersonic Nonequilibrium Flows: Fundamentals and Recent Advances.* Ed. Eswar Josyula ARLF, 2015. 3

[11] H. G. Hornung. 28th Lanchester Memorial Lecture - Experimental real-gas hypersonics. *Aeronautical Journal*, 92:379–389, Dec 1988. 3

[12] F. K. Lu and D. E. Marren. *Principles of Hypersonic Test Facility Development*, pages 17–27.

[13] A. F. Kolesnikov. Conditions of simulation of stagnation point heat transfer from a high-enthalpy flow. *Fluid Dynamics*, 28(1):131–137, 1993. 3, 66

[14] A. F. Kolesnikov, A. N. Gordeev, and S. A. Vasil'evsky. Simulation of Stagnation Point Heating and Predicting Surface Catalysity for the EXPERT Re-Entry Conditions. In H. Lacoste and L. Ouwehand, editors, *6th European Symposium on Aerothermodynamics for Space Vehicles*, volume 659 of *ESA Special Publication*, page 34, January 2009. 3, 10, 108

[15] S. Pidan, M. Auweter-Kurtz, G. Herdrich, and M. Fertig. Recombination coefficients and spectral emissivity of silicon carbide-based thermal protection materials. *Journal of Thermophysics and Heat Transfer*, 19(4):566–571, 2005. 108

[16] M. Schüßler, M. Auweter-Kurtz, G. Herdrich, and S. Lein. Surface characterization of metallic and ceramic tps-materials for reusable space vehicles. *Acta Astronautica*, 65(5):676–686, 2009. 108

[17] D. Conte N. Sauvage, P. Tran, P. Vervisch, and A. Bourdonand A. Desportes. EADS-LV and CORIA Common Approach on Catalycity Measurement. In A. Wilson, editor, *Hot Structures and Thermal Protection Systems for Space Vehicles*, volume 521 of *ESA Special Publication*, page 313, apr 2003. 108

[18] D. Stewart, T. Gokcen, S. Sepka, D. Leiser, and M. Rezin. *Development of a Catalytic Coating for a Shuttle Flight Experiment.* 109

[19] F. Panerai and O. Chazot. Characterization of gas/surface interactions for ceramic matrix composites in high enthalpy, low pressure air flow. *Materials Chemistry and Physics*, 134 (2-3):597–607, 2012. 6, 53, 108, 109, 115, 117, 133, 136, 205

[20] A. Viladegut and O. Chazot. Empirical modeling of copper catalysis for enthalpy determination in plasma facilities. *Journal of Thermophysics and Heat Transfer*, 34(1):26–36, 2020. 3, 10, 109, 128, 129, 130, 133, 137, 138, 205, 206

[21] T. Suzuki, K. Fujita, and T. Sakai. Graphite nitridation in lower surface temperature regime. *Journal of Thermophysics and Heat Transfer*, 24(1), 2010. 4, 44, 150, 152, 174

[22] B. Helber, A. Turchi, and T. E. Magin. Determination of active nitridation reaction efficiency of graphite in inductively coupled plasma flows. *Carbon*, 125:582–594, 2017. 3, 4, 6, 44, 70, 150, 152, 154, 155, 157, 162, 170, 172, 174

[23] F. S. Milos and D. J. Rasky. Review of numerical procedures for computational surface thermochemistry. *Journal of Thermophysics and Heat Transfer*, 8, 1994. 4, 39

[24] D. Bianchi, F. Nasuti, and E. Martelli. Coupled analysis of flow and surface ablation in carbon-carbon rocket nozzles. *Journal of Spacecraft and Rockets*, 46(3), 2009. 41

[25] D. Bianchi, F. Nasuti, M. Onofri, and E. Martelli. Thermochemical erosion analysis for graphite/carbon-carbon rocket nozzles. *Journal of Propulsion and Power*, 27(1), 2011. 4, 41

[26] Joseph C. Ferguson, Francesco Panerai, Jean Lachaud, Alexandre Martin, Sean C.C. Bailey, and Nagi N. Mansour. Modeling the oxidation of low-density carbon fiber material based on micro-tomography. *Carbon*, 96:57–65, 2016. 5

[27] Francesco Panerai, Joseph C. Ferguson, Jean Lachaud, Alexandre Martin, Matthew J. Gasch, and Nagi N. Mansour. Micro-tomography based analysis of thermal conductivity, diffusivity and oxidation behavior of rigid and flexible fibrous insulators. *International Journal of Heat and Mass Transfer*, 108:801–811, 2017.

[28] Francesco Panerai, Thom Cochell, Alexandre Martin, and Jason D. White. Experimental measurements of the high-temperature oxidation of carbon fibers. *International Journal of Heat and Mass Transfer*, 136:972–986, 2019. 5

[29] V. J. Murray and T. K. Minton. Gas-surface interactions of atomic nitrogen with vitreous carbon. *Carbon*, 150:85–92, 2019. 5, 152

[30] V. J. Murray, P. Recio, A. Caracciolo, C. Miossec, N. Balucani, P. Casavecchia, and T. K. Minton. Oxidation and nitridation of vitreous carbon at high temperatures. *Carbon*, 167:388–402, 2020. 5, 152

[31] Savio Poovathingal, Thomas E. Schwartzentruber, Sriram Goverapet Srinivasan, and Adri C. T. van Duin. Large scale computational chemistry modeling of the oxidation of highly oriented pyrolytic graphite. *The Journal of Physical Chemistry A*, 117(13):2692–2703, 2013. 5

[32] A. Lagan, A. Lombardi, F. Pirani, P. Gamallo, R. Say s, I. Armenise, M. Cacciatore, F. Esposito, and M. Rutigliano. Molecular Physics of Elementary Processes Relevant to Hypersonics: Atom-Molecule, Molecule-Molecule and Atoms-Surface Processes. *The Open Plasma Physics Journal*, 7(1):48–59, jun 2014. 5

[33] S. Poovathingal, T. E. Schwartzentruber, V. J. Murray, and T. K. Minton. Molecular simulation of carbon ablation using beam experiments and resolved microstructure. *AIAA Journal*, 54(3):999–1010, 2016. 6

[34] S. Poovathingal, T. E. Schwartzentruber, V. J. Murray, T. K. Minton, and G. V. Candler. Finite-rate oxidation model for carbon surfaces from molecular beam experiments. *AIAA Journal*, 55(5):1644–1658, 2017. 6

[35] M. L. Taper and J. M. Ponciano. Evidential statistics as a statistical modern synthesis to support 21st century science. *Population Ecology*, 58(1):9–29, 2016. 6

[36] W. L. Oberkampf and C. J. Roy. *Verification and Validation in Scientific Computing*. Cambridge University Press, 2013. 6, 75, 77

[37] M. Hobson and A. Jaffe and A. Liddle and P. Mukherjee and D. Parkinson. *Bayesian Methods in Cosmology*. Cambridge University Press, 2009. 8

[38] P. C. Bhat. Multivariate analysis methods in particle physics. *Annual Review of Nuclear and Particle Science*, 61(1):281–309, 2011.

[39] K. Cranmer and J. Brehmer and G. Louppe. The frontier of simulation-based inference. *Proceedings of the National Academy of Sciences*, 117(48):30055–30062, 2020. 8

[40] K. Miki, M. Panesi, E. Prudencio, A. Maurente, S. H. Cheung, J. Jagodzinski, D. Goldstein, S. Prudhomme, K. Schulz, C. Simmons, J. Strand, and P. Varghese. *On the (In)Validation of a Thermochemical Model with EAST Shock Tube Radiation Measurements.* 9, 107

[41] M. Panesi, K. Miki, Serge Prudhomme, and A. Brandis. On the assessment of a bayesian validation methodology for data reduction models relevant to shock tube experiments. *Computer Methods in Applied Mechanics and Engineering*, 213-216:383–398, March 2012. 9, 10, 11

[42] K. Miki, M. Panesi, E. E. Prudencio, and S. Prudhomme. Estimation of the nitrogen ionization reaction rate using electric arc shock tube data and bayesian model analysis. *Physics of Plasmas*, 19(2):023507, 2012. 9

[43] Uncertainty quantification of a graphite nitridation experiment using a bayesian approach. *Experimental Thermal and Fluid Science*, 35(8):1588–1599, 2011. 9, 10, 153

[44] Luning Zhang, Dušan A. Pejaković, Jochen Marschall, Max Dougherty, and Douglas G. Fletcher. Laboratory investigation of the active nitridation of graphite by atomic nitrogen. *Journal of Thermophysics and Heat Transfer*, 26(1):10–21, 2012. 9, 150, 151, 153

[45] G. Terejanu, R. R. Upadhyay, and K. Miki. Bayesian experimental design for the active nitridation of graphite by atomic nitrogen. *Experimental Thermal and Fluid Science*, 36:178–193, 2012. 9, 11

[46] J. Tryoen, P. M. Congedo, R. Abgrall, N. Villedieu, and T. E. Magin. Bayesian-based method with metamodels for rebuilding freestream conditions in atmospheric entry flows. *AIAA Journal*, 52(10):2190–2197, 2014. 9, 110

[47] A. Cortesi. *Predictive numerical simulations for rebuilding freestream conditions in atmospheric entry flows.* PhD thesis, Université de Bordeaux/VKI, 2018. 9

[48] J. Ray, S. Kieweg, D. Dinzl, B. Carnes, V. G. Weirs, B. Freno, M. Howard, T. Smith, I. Nompelis, and G. V. Candler. Estimation of inflow uncertainties in laminar hypersonic double-cone experiments. *AIAA Journal*, 58(10):4461–4474, 2020. 10

[49] J. Salvatier, T. Wiecki, and C. Fonnesbeck. Probabilistic programming in python using pymc3. *PeerJ Comput. Sci.*, 2:e55, 2016. 10

[50] F. Pedregosa, G. Varoquaux, A. Gramfort, V. Michel, B. Thirion, O. Grisel, M. Blondel, P. Prettenhofer, R. Weiss, V. Dubourg, J. Vanderplas, A. Passos, D. Cournapeau, M. Brucher, M. Perrot, and E. Duchesnay. Scikit-learn: Machine learning in Python. *Journal of Machine Learning Research*, 12:2825–2830, 2011.

[51] R Core Team. *R: A Language and Environment for Statistical Computing.* R Foundation for Statistical Computing, Vienna, Austria, 2020. 10

[52] R. P. Feynman, R. Leighton, and M. Sands. *The Feynman Lectures on Physics, Vol. 2.* Addison-Wesley Publishing Company, Reading MA, 1989. 15

[53] P. A. Gnoffo and R. N. Gupta. Conservation Equations and Physical Models for Hypersonic Air Flows in Thermal and Chemical Nonequilibrium. *NASA Technical Paper*, February, 1989. 15

[54] M. G. Kapper and J. L. Cambier. Ionizing shocks in argon. Part II: Transient and multi-dimensional effects. *Journal of Applied Physics*, 109, 2011. 16

[55] M. G. Kapper and J. L. Cambier. Part I: Collisional-radiative model and steady-state structure. *Journal of Applied Physics*, 109, 2011.

[56] M. Panesi, R. L. Jaffe, D. W. Schwenke, and T. E. Magin. Rovibrational internal energy transfer and dissociation of $\mathrm{N}_2\left({}^1\Sigma_\mathrm{g}^+\right) - \mathrm{N}\left({}^4\mathrm{S}_\mathrm{u}\right)$ system in hypersonic flows. *The Journal of Chemical Physics*, 138, 2013. 16

[57] A. Cipullo, B. Helber, F. Panerai, L. Zeni, and O. Chazot. Investigation of Freestream Plasma Flow Produced by Inductively Coupled Plasma Wind Tunnel. *Journal of Thermophysics and Heat Transfer*, 28, 2014. 16, 19, 125

[58] C. O. Johnston, P. A. Gnoffo, and K. Sutton. Influence of ablation on radiative heating for earth entry. *Journal of Spacecraft and Rockets*, 46, 2009. 16

[59] L. Soucasse, J. B. Scoggins, P. Rivière, T. E. Magin, and A. Soufiani. Flow-radiationcoupling for atmospheric entries using a hybrid statistical narrow band model. *Journal of Quantitative Spectroscopy and Radiative Transfer*, 180:55–69, 2016. 16

[60] C.Park. *Nonequilibrium Hypersonic Aerothermodynamics.* Wiley, 1991. 16

[61] A. Munafò. *Multi-Scale Models and Computational Methods for Aerothermodynamics.* PhD thesis, VKI/ECP, 2014. 16, 53, 60, 61, 63, 154

[62] E. Torres. *Ab initio quantum-chemistry database for* $N_2(v, J) + N$ *in a state-to-state implementation of the DSMC method.* PhD thesis, University of Stuttgart/VKI, 2017. 16

[63] J. Lee. Basic governing equations for the flight regimes of aeroassisted orbital transfer vehicles. In *American Institute of Aeronautics and Astronautics*, Snowmass, Colorado, June 1984. 18, 38

[64] J. Lee. *Basic Governing Equations for the Flight Regimes of Aeroassisted Orbital Transfer Vehicles*, pages 3–53. H. F. Nelson, editor, Thermal Design of Aeroassisted Orbital Transfer Vehicles, AIAA, New York, January 1985. 18

[65] C. Park. Assessment of two-temperature kinetic model for dissociating and weakly-ionizing nitrogen. In *4th Thermophysics and Heat Transfer Conference, Boston, MA*, June 1986. 18, 36

[66] C. Park. Assessment of two-temperature kinetic model for ionizing air. In *AIAA*, Honolulu, Hawaii, June 1987. 18, 36

[67] Q. Wargnier, S. Faure, B. Graille, T. Magin, and M. Massot. Numerical treatment of the nonconservative product in a multiscale fluid model for plasmas in thermal nonequilibrium: Application to solar physics. *SIAM Journal on Scientific Computing*, 42(2):B492–B519, 2020. 18

[68] A. Bellemans, A. Munafò, T. E. Magin, G. Degrez, and A. Parente. Reduction of a collisional-radiative mechanism for argon plasma based on principal component analysis. *Physics of Plasmas*, 22(6):062108, 2015. 18

[69] D. Vanden Abeele. *An Efficient Computational Model for Inductively Coupled Air Plasma Flows under Thermal and Chemical Non-Equilibrium - with Application to Atmospheric Re-Entry Flow Studies.* PhD thesis, VKI/Katholieke Universiteit Leuven, 2000. 19

[70] P. Rini. *Analysis of differential diffusion phenomena in high enthalpy flows, with application to thermal protection material testing in ICP facilities.* PhD thesis, VKI/Université Libre de Bruxelles, 2006. 19

[71] W. G. Vicenti and C. H. Kruger. *Introduction to Physical Gas Dynamics.* Krieger Pub Co., 1975. 20, 21, 23, 58, 64, 170

[72] D. Fletcher. Fundamentals of Hypersonic Flow - Aerothermodynamics. *NATO STO-AVT*, 116, 2005. 21

[73] M. Panesi. *Physical Models for Nonequilibrium Plasma Flow Simulations at High Speed Re-Entry Conditions.* PhD thesis, VKI/Universita degli Studi di Pisa, 2009. 23, 37

[74] M. Mitchner and C. H. Kruger. *Partially Ionized Gases.* John Wiley and Sons, Inc, 1973. 29

[75] J. H. Ferziger and H. G. Kaper. *Mathematical Theory of Transport Processes in Gases.* North-Holland Publishing Company, 1972. 29, 32

[76] T. E. Magin and G. Degrez. Transport algorithms for partially ionized and unmagnetized plasmas. *Journal of Computational Physics*, 198:424–449, 2004. 29, 30, 197

[77] T. E. Magin and G. Degrez. Transport properties of partially ionized and unmagnetized plasmas. *Physical Review E*, 70, 2004. 29

[78] E. Nagnibeda and E. Kustova. *Non-Equilibrium Reacting Gas Flows: Kinetic Theory of Transport and Relaxation Processes.* Springer-Verlag Berlin Heidelberg, 2009. 29

[79] V. Giovangigli, B. Graille, T. E. Magin, and M. Massot. Multicomponent transport in weakly ionized mixtures. *Plasma Sources Science and Technology*, 19, 2010. 31

[80] D. Bruno and V. Giovangigli. Relaxation of internal temperature and volume viscosity. *Physics of Fluids*, 23, 2011. 31

[81] E. A. Mason, R. J. Munn, and F. J. Smith. Transport coefficients of ionized gases. *The Physics of Fluids*, 10(8):1827–1832, 1967. 33

[82] K. K. Kuo. *Principles of Combustion.* John Wiley and Sons, Inc., 2005. 34

[83] R. L. Jaffe, D. W. Schwenke, and M. Panesi. *First principles calculations of heavy particle rate coefficients*, volume 247. Timothy C. Lieuwen, editor, Hypersonic Nonequilibrium Flows: Fundamentals and Recent Advances, AIAA, 2015. 35

[84] L. Landau and E. Teller. *Theory of sound dispersion.* Physikalische Zeitschrift der Sowjetunion, 1936. 36

[85] E. E. Nikitin and J. Troe. 70 years of landau–teller theory for collisional energy transfer. semiclassical three-dimensional generalizations of the classical collinear model. *Phys. Chem. Chem. Phys.*, 10:1483–1501, 2008. 36

[86] M. Panesi, A. Munafò, T. E. Magin, and R. L. Jaffe. Nonequilibrium shock-heated nitrogen flows using a rovibrational state-to-state method. *Phys. Rev. E*, 90:013009, Jul 2014. 36

[87] R. C. Millikan and D. R. White. Systematics of vibrational relaxation. *Journal of Chemical Physics*, 39:3209–3213, 1963. 36, 64

[88] C. Park. *Nonequilibrium Hypersonic Aerothermodynamics.* Wiley, New York, 1990. 37, 145

[89] C. Park. *Modeling of hypersonic reacting flows.* Advances in Hypersonics, 1992. 37

[90] L. C. Hartung, R. A. Mitcheltree, and P. A. Gnoffo. Stagnation point nonequilibrium radiative heating and the influence of energy exchange models. *Journal of Thermophysics and Heat Transfer*, 6:412–418, 1992. 38

[91] R. B. Greendyke and L. C. Hartung. Convective and Radiative Heat Transfer Analysis for the Fire II Forebody. *Journal of Spacecraft and Rockets*, 31:986–992, 1994. 38

[92] A. Martin, H. Zhang, and K. A. Tagavi. An introduction to the derivation of surface balance equations without the excruciating pain. *International Journal of Heat and Mass Transfer*, 115:992 – 999, 2017. 39, 41

[93] A. Turchi. *A gas-surface interaction model for the numerical study of rocket nozzle flow sover pyrolyzing ablative materials.* PhD thesis, Sapienza Università di Roma, 2013. 41

[94] A. Turchi, D. Bianchi, F. Nasuti, and R. Marocco. Ablative material behavior in oxygen/methane thruster environment. In *43rd AIAA Thermophysics Conference*, 2012. 41

[95] M. Capriati, G. Bellas-Chatzigeorgis, A. Turchi, B. Helber, and T. E. Magin. Thermal non-equilibrium modeling for ablative gas-surface interaction. In *HiSST: 2nd International Conference on High-Speed Vehicle Science and Technology*, 2020. 41, 42

[96] B. Halpern and D. Rosner. Chemical energy accommodation at catalyst surfaces. flow reactor studies of the association of nitrogen atoms on metals at high temperatures. *Journal of the Chemical Society, Faraday Transactions*, 74:1883–1912, 1978. 42

[97] P. Rini, A. Garcia, T. E. Magin, and G. Degrez. Numerical Simulation of Nonequilibrium Stagnation-Line CO2 Flows with Catalyzed Surface Reactions. *Journal of Thermophysics and Heat Transfer*, 18, 2004. 42

[98] M. Barbato, S. Reggiani, C. Bruno, and J. Muylaert. Model for Heterogeneous Catalysis on Metal Surfaces with Applications to Hypersonic Flows. *Journal of Thermophysics and Heat Transfer*, 14, 2000. 43

[99] A. Viladegut, U. Duzel, and O. Chazot. Diffusion effects on the determination of surface catalysis in Inductively Coupled Plasma facility. *Chemical Physics*, 485–486:88–97, 2017. 42, 141, 146

[100] F. Nasuti, M. Barbato, and C. Bruno. Material-dependent catalytic recombination modeling for hypersonic flows. *Journal of Thermophysics and Heat Transfer*, 10(1):131–136, 1996. 42

[101] C. Sorensen, P. Valentini, and T. E. Schwartzentruber. Uncertainty analysis of reaction rates in a finite-rate surface-catalysis model. *Journal of Thermophysics and Heat Transfer*, 26(3):407–416, 2012.

[102] Georgios Bellas-Chatzigeorgis, Paolo F. Barbante, and Thierry E. Magin. Energy accommodation coefficient calculation methodology using state-to-state catalysis applied to hypersonic flows. *AIAA Journal*, 58(1):278–290, 2020. 42

[103] R. Goulard. On catalytic recombination rates in hypersonic stagnation heat transfer. In *Jet Propulsion*, volume 28 (11), pages 737–745, 1958. 42, 66

[104] R. S. C. Davuluri, H. Zhang, and A. Martin. Numerical study of spallation phenomenon in an arc-jet environment. *Journal of Thermophysics and Heat Transfer*, 30, 2016. 43

[105] S. V. Zhluktov and T. Abe. Viscous shock-layer simulation of airflow past ablating blunt body with carbon surface. *Journal of Thermophysics and Heat Transfer*, 13(1):50–59, 1999. 44

[106] P. F. Barbante. *Accurate and Efficient Modelling of High Temperature Nonequilibrium Air Flows*. PhD thesis, ULB/VKI, 2001. 53, 54, 55, 58, 111

[107] P. F. Barbante, G. Degrez, and G. S. R. Sarma. Computation of Nonequilibrium High-Temperature Axisymmetric Boundary-Layer Flows. *Journal of Thermophysics and Heat Transfer*, 16(4):490–497, 2002.

[108] P. F. Barbante and O. Chazot. Flight Extrapolation of Plasma Wind Tunnel Stagnation Region Flowfield. *Journal of Thermophysics and Heat Transfer*, 20(3):493–499, 2006. 53

[109] A. Turchi, B. Helber, A. Munafò, and T. E. Magin. *Development and Testing of an Ablation Model Based on Plasma Wind Tunnel Experiments*. 53

[110] G. Bellas. *Development of Advanced Gas-surface Interaction Models for Chemically Reacting Flows for Re-entry Conditions*. PhD thesis, VKI/Politecnico di Milano, 2018. 53, 64, 161

[111] F. White. *Viscous Fluid Flows, 2nd Ed.* McGraw-Hill, 1991. 54, 55

[112] S. Wüthrich. *Numerical Simulation of Non-Equilibrium Chemically Reacting Hypersonic Flows by Means of a Coupled Euler/Boundary Layer Method.* PhD thesis, EPFL, 1992. 55

[113] R. T. Davis. Numerical solution of the hypersonic viscous shock-layer equations. *AIAA Journal*, 8(5):193–206, 1970. 55

[114] A. A. Dorodnitsyn. Laminar boundary layer in compressible fluid. *Doklady Akademii Nauk, SSSR*, 34:213–219, 1942. 55

[115] I. Lees. Laminar heat transfer over blunt-nosed bodies at hypersonic flight speeds. *Jet Propulsion*, 26:259–269, 1956. 55

[116] C. Hirsch. *Numerical Computation of Internal and External Flows.* John Wiley and Sons, Inc., New York, NY, 1990. 58, 64

[117] B. Bottin, D. Vanden Abeele, M. Carbonaro, G. Degrez, and G. S. R. P. Sarma. Thermodynamic and transport properties for inductive plasma modeling. *Journal of Thermophysics and Heat Transfer*, 13:343–350, 1999. 58

[118] M. G. Dunn and S. W. Kang. Theoretical and Experimental Studies of Reentry Plasmas. Technical report, NASA CR-2232, 1973. 58, 145, 202

[119] A. Viladegut. *Assessment of Gas-Surface Interaction Modelling for Lifting Body Re-Entry Flight Design.* PhD thesis, VKI/UPC, 2017. 58, 67, 136, 138, 161

[120] A. Klomfass and S. Müller. A quasi-onedimensional approach for hypersonic stagnation-point flows. *Technical report, Internal Report*, 1996. 59

[121] A. Turchi, J. J. Matesanz-Saiz, T. E. Magin, and O. Chazot. On the flight extrapolation of stagnation-point ablative material plasma wind tunnel tests. In *Proceedings of 8th European Symposium on Aerothermodynamics for Space Vehicles*, 2015. 59

[122] K. Kitamura and E. Shima. Towards shock-stable and accurate hypersonic heating computations: A new pressure flux for ausm-family schemes. *Journal of Computational Physics*, 245:62–83, 2013. 61

[123] B. Dias. *Thermal ablation and radiation modeling of meteor phenomena.* PhD thesis, Université Catolique de Louvain/VKI, 2020. 61, 154

[124] G. V. Candler and R. W. MacCormack. Computation of weakly ionized hypersonic flows in thermochemical nonequilibrium. *Journal of Thermophysics and Heat Transfer*, 5(3):266–273, 1991. 61, 64

[125] B. van Leer. Towards the ultimate conservative difference scheme. v. a second-order sequel to godunov's method. *Journal of Computational Physics*, 32(1):101 – 136, 1979. 61

[126] G. D. van Albada, B. van Leer, and W. W. Roberts, Jr. A comparative study of computational methods in cosmic gas dynamics. *Astronomy and Astrophysics*, 108(1):76–84, April 1982. 61

[127] J. Blazek. *Computational Fluid Dynamics: Principles and Applications.* Elsevier, Amsterdam, 2. ed., 6, 2008. 62

[128] M. S. Liou and B. van Leer. Choice of implicit and explicit operators for the upwind differencing method. In *26th AIAA Aerospace Sciences Meeting, Reno, Nevada*, volume AIAA Paper 1988-624, 1988. 62

[129] J. D. Ramshaw and C. H. Chang. Friction-weighted self-consistent effective binary diffusion approximation. *Journal of Non-Equilibrium Thermodynamics*, 21(3):223–232, 1996. 63

[130] J. B. Scoggins, V. Leroy, G. Bellas-Chatzigeorgis, B. Dias, and T E. Magin. Mutation++: Multicomponent thermodynamic and transport properties for ionized gases in c++. *SoftwareX*, 12:100575, 2020. 64, 74

[131] D. Olynick, Y. K. Chen, and M. E. Tauber. Aerothermodynamics of the stardust sample return capsule. *Journal of Spacecrafts and Rockets*, 36:442–462, 1999. 64

[132] B. Bottin, O. Chazot, M. Carbonaro, V. Van der Haegen, and S. Paris. The VKI Plasmatron Characteristics and Performance. In *Measurement Techniques for High Temperature and Plasma Flows, RTO-EN-8*, pages 6–1, 6–24, 1999. 64

[133] B. Bottin. *Aerothermodynamic Model of an Inductively-coupled Plasma Wind Tunnel.* PhD thesis, VKI/Université de Liège, 1999. 65

[134] J. A. Fay and F. R. Riddell. Theory of Stagnation Point Heat Transfer in Dissociated Air. *Journal of the Aerospace Sciences*, 25(2):73–85, 1958. 66

[135] H. W. Krassilchikoff. Procedures for the determination of the cold copper catalycity. Technical report, VKI Project Report 2006-18, von Karman Institute for Fluid Dynamics, 06 2006. 67, 112

[136] M. Barker. On the use of very small pitot-tubes for measuring wind velocity. *Proceedings of the Royal Society A: Mathematical, Physical and Engineering Sciences*, 101, 1922. 69, 74, 112, 145, 154

[137] F. Homann. The Effect of High Viscosity on the Flow Around a Cylinder and Around a Sphere. Technical report, NACA Technical Memorandum 1334, 1952. 69

[138] W. K. Widger Jr. and M. P. Woodall. Integration of the Planck Blackbody Radiation Function. *Bulletin of the American Meteorological Society*, 57(10):1217–1219, October 1976. 69

[139] C. Park and D. Bogdanoff. Shock-tube measurements of nitridation coefficients of solid carbon. *Journal of Thermophysics and Heat Transfer*, 20(3), 2006. 71, 150

[140] P. Boubert and P. Vervisch. Cn spectroscopy and physico–chemistry in the boundary layer of a c/sic tile in a low pressure nitrogen/carbon dioxide plasma flow. *The Journal of Chemical Physics*, 112(23):10482–10490, 2000. 71

[141] T. E. Magin. *A Model for Inductive Plasma Wind Tunnels.* PhD thesis, ULB/VKI, 2004. 73

[142] G. Degrez, D. Vanden Abeele, P. Barbante, and B. Bottin. Numerical simulation of inductively coupled plasma flows under chemical non-equilibrium. *International Journal of Numerical Methods for Heat & Fluid Flow*, 14(4):538–558, 2004.

[143] D. Vanden Abeele and G. Degrez. Efficient Computational Model for Inductive Plasma Flows. *AIAA Journal*, 38(2):234–242, 2000. 73

[144] A. Lani, N. Villedieu, K. Bensassi, L. Koloszar, M. Vymazal, S. M. Yalim, and M. Panesi. COOLFluiD: an open computational platform for multi-physics simulation and research. In *21st AIAA Computational Fluid Dynamics Conference*, 2013-2589. 74

[145] G. Degrez, P. Barbante, M. de la Llave, T. E. Magin, and O. Chazot. Determination of the catalytic properties of TPS materials in the VKI ICP facilities. In *European Congress on Computational Methods in Applied Sciences and Engineering ECCOMAS Computational Fluid Dynamics Conference 2001 Swansea, Wales, UK, 4-7 September 2001*, 2001. 74, 112, 154

[146] I. Sakraker. *Aerothermodynamics of Pre-Flight and In-Flight Testing Methodologies for Atmospheric Entry Probes.* PhD thesis, ULg/VKI, 2016. 74, 112, 154, 192

[147] J. K. Ghosh, M. Delampady, and T. Samanta. *An Introduction to Bayesian Analysis: Theory and Methods.* Springer, 2006. 75

[148] C. J. Roy and W. L. Oberkampf. A comprehensive framework for verification, validation, and uncertainty quantification in scientific computing. *Computer Methods in Applied Mechanics and Engineering*, 200:2131–2144, 2011. 75

[149] S. Ferson, W. L. Oberkampf, and L. Ginzburg. Model validation and predictive capability for the thermal challenge problem. *Computer Methods in Applied Mechanics and Engineering*, 197:2408–2430, 2008. 75

[150] G. Iaccarino. Uncertainty quantification in computational science. *STO-AVT-235 VKI Lecture Series on Uncertainty quantification in computational fluid dynamics*, 2013. 75

[151] A. Gelman, J. B. Carlin, H. S. Stern, D. B. Dunson, A. Vehtari, and D. B. Rubin. *Bayesian Data Analysis.* Chapman and Hall/CRC Texts in Statistical Science, 2003. 75, 85

[152] G. Shafer. *A mathematical theory of evidence.* Princeton University Press, 1976. 75

[153] H. J. Zimmermann. *Fuzzy set theory and its applications.* Kluwer Academic Publishers, 1996. 75

[154] M. Panesi, K. Miki, S. Prudhomme, and A. Brandis. On the assessment of a Bayesian validation methodology for data reduction models relevant to shock tube experiments. *Computer Methods in Applied Mechanics and Engineering*, page 383–398, 2012. 76, 77

[155] Charles W. Groetsch. *Inverse Problems in the Mathematical Sciences.* Vieweg+Teubner Verlag, 1993. 80

[156] A. N. Tikhonov, A. Goncharsky, V. V. Stepanov, and A. G. Yagola. *Numerical Methods for the Solution of Ill-Posed Problems.* Springer Netherlands, 1995.

[157] Curtis R. Vogel. *Computational Methods for Inverse Problems.* Society for Industrial and Applied Mathematics, 2002. 80

[158] David J. C. MacKay. *Information Theory, Inference & Learning Algorithms.* Cambridge University Press, USA, 2002. 81, 83

[159] Shiliang Sun. A review of deterministic approximate inference techniques for bayesian machine learning. *Neural Computing and Applications*, 23(7):2039–2050, 2013. 81

[160] J. Kaipio and E. Somersalo. *Statistical and Computational Inverse Problems.* Springer-Verlag, New York, 2005. 83, 84, 85, 112, 159

[161] D. S. Sivia and J. Skilling. *Data Analysis - A Bayesian Tutorial.* Oxford Science Publications. Oxford University Press, 2nd edition, 2006. 83, 85, 86, 116, 161

[162] C. P. Robert, N. Chopin, and J. Rousseau. Rejoinder: Harold jeffreys's theory of probability revisited. *Statistical Science*, 24(2):191–194, 2009. 85, 166

[163] E. T. Jaynes. Information theory and statistical mechanics. *Phys. Rev.*, 106:620–630, May 1957. 85

[164] John Skilling. Nested sampling for general Bayesian computation. *Bayesian Analysis*, 1(4):833 – 859, 2006. 86

[165] J. S. Liu. *Monte Carlo Strategies in Scientific Computing.* Springer Series in Statistics. Springer, 2001. 87

[166] N. Metropolis, A. W. Rosenbluth, M. N. Rosenbluth, A. H. Teller, and E. Teller. Equation of state calculations by fast computing machines. *The Journal of Chemical Physics*, 21(6):1087–1092, 1953. 88

[167] W. K. Hastings. Monte carlo sampling methods using markov chains and their applications. *Biometrika*, 57(1):97–109, 1970. 88

[168] G. O. Roberts, A. Gelman, and W. R. Gilks. Weak convergence and optimal scaling of random walk metropolis algorithms. *Annals of Applied Probability*, 1997. 89

[169] G. O. Roberts and J. S. Rosenthal. Optimal scaling for various metropolis-hastings algorithms. *Statistical Science*, 2001. 89

[170] Steve Brooks, Andrew Gelman, Galin Jones, and Xiao-Li Meng. *Handbook of Markov Chain Monte Carlo.* CRC press, 2011. 89, 90

[171] H. Haario, E. Saksman, and J. Tamminen. An adaptive metropolis algorithm. *Bernoulli*, 7:223–242, 1998. 89

[172] A. E. Raftery and S. M. Lewis. The number of iterations, convergence diagnostics and generic metropolis algorithms. In *In Practical Markov Chain Monte Carlo (W.R. Gilks, D.J. Spiegelhalter and*, pages 115–130. Chapman and Hall, 1995. 90

[173] M. K. Cowles and B. P. Carlin. Markov chain monte carlo convergence diagnostics: A comparative review. *Journal of the American Statistical Association*, 91(434):883–904, 1996. 90

[174] J. A. Hoeting, D. Madigan, A. E. Raftery, and C. T. Volinsky. Bayesian model averaging: A tutorial. *Statistical Science*, 14(4):382–401, 1999. 94, 95

[175] H. Jeffreys. *Theory of Probability*. Oxford, Oxford, England, third edition, 1961. 95

[176] Robert E. Kass and Adrian E. Raftery. Bayes factors. *Journal of the American Statistical Association*, 90(430):773–795, 1995. 95

[177] G. Schwarz. Estimating the dimension of a model. *The Annals of Statistics*, 6:461–464, 1978. 95

[178] H. Akaike. A new look at the statistical model identification. *IEEE Transactions on Automatic Control*, 19(6):716–723, 1974. 95

[179] Jie Ding, Vahid Tarokh, and Yuhong Yang. Model selection techniques: An overview. *IEEE Signal Processing Magazine*, 35(6):16–34, 2018. 95

[180] T. C. Chamberlin. The method of multiple working hypotheses. *Science*, 148(3671):754–759, 1965. 95

[181] H. V. Roberts. Probabilistic prediction. *Journal of the American Statistical Association*, 60(309):50–62, 1965. 95

[182] A. Tarantola. *Inverse Problem Theory and Methods for Model Parameter Estimation*. Society for Industrial and Applied Mathematics, USA, 2004. 96

[183] Y. M. Marzouk, H. N. Najm, and L. A. Rahn. Stochastic spectral methods for efficient bayesian solution of inverse problems. *Journal of Computational Physics*, 224(2), 6 2007. 96

[184] Chapter 12 response surface methods. In Rolf Carlson, editor, *Design and Optimization in Organic Synthesis*, volume 8 of *Data Handling in Science and Technology*, pages 249–324. Elsevier, 1992. 96

[185] D.S. Broomhead and D. Lowe. Multivariable functional interpolation and adaptive networks. *Complex Systems*, 2:321–355, 1988. 96

[186] J. Friedman, T. Hastie, and R. Tibshirani. The elements of statistical learning, 2001. 96

[187] Christopher M. Bishop. *Pattern Recognition and Machine Learning (Information Science and Statistics)*. Springer, 1 edition, 2007. 96

[188] C. E. Rasmussen and C. K. I. Williams. *Gaussian processes for machine learning*. Adaptive computation and machine learning. MIT Press, 2006. 96, 97, 98

[189] P. Chen, N. Zabaras, and I. Bilionis. Uncertainty propagation using infinite mixture of gaussian processes and variational bayesian inference. *Journal of Computational Physics*, 284:291–333, 2015. 97

[190] C. K. I. Williams. Prediction with gaussian processes: From linear regression to linear prediction and beyond. In *Learning and Inference in Graphical Models*, pages 599–621. Kluwer, 1997. 99

[191] L. Pronzato and W. G. Müller. Design of computer experiments: space filling and beyond. *Statistics and Computing*, 22(3):681–701, 2012. 99

[192] D. Bursztyn and D. M. Steinberg. Comparison of designs for computer experiments. *Journal of Statistical Planning and Inference*, 136(3):1103 – 1119, 2006. 99

[193] M. D. McKay, R. J. Beckman, and W. J. Conover. Comparison the three methods for selecting values of input variable in the analysis of output from a computer code. *Technometrics; (United States)*, 21(2), 5 1979. 99

[194] B. Iooss and P. Lemaître. *A Review on Global Sensitivity Analysis Methods.* Dellino G., Meloni C. (eds) Uncertainty Management in Simulation-Optimization of Complex Systems. Operations Research/Computer Science Interfaces Series, Springer, Boston, MA, 2015. 101

[195] E. Borgonovo and E. Plischke. Sensitivity analysis: A review of recent advances. *European Journal of Operational Research*, 248(3):869 – 887, 2016. 101

[196] M. D. Morris. Factorial sampling plans for preliminary computational experiments. *Technometrics*, 33(2):161–174, 1991. 101

[197] C. K. Park and K. Ahn. A new approach for measuring uncertainty importance and distributional sensitivity in probabilistic safety assessment. *Reliability Engineering and System Safety*, 46(3):253 – 261, 1994. 101

[198] E. Borgonovo. A new uncertainty importance measure. *Reliability Engineering and System Safety*, 92(6):771 – 784, 2007. 101

[199] I. M. Sobol'. Sensitivity estimates for nonlinear mathematical models. *Mathematical modelling and Computational Experiments*, pages 407–414, 1993. 101, 102

[200] I. M. Sobol'. Global sensitivity indices for nonlinear mathematical models and their monte carlo estimates. *Mathematics and Computers in Simulation*, 55(1):271 – 280, 2001. The Second IMACS Seminar on Monte Carlo Methods. 101, 102

[201] Gianluca Geraci, Pietro Marco Congedo, Remi Abgrall, and Gianluca Iaccarino. High-order statistics in global sensitivity analysis: decomposition and model reduction. *Computer Methods in Applied Mechanics and Engineering*, Jan 2016. 101

[202] B. Iooss, F. Van Dorpe, and N. Devictor. Response surfaces and sensitivity analyses for an environmental model of dose calculations. *Reliability Engineering and System Safety*, 91(10):1241 – 1251, 2006. The Fourth International Conference on Sensitivity Analysis of Model Output (SAMO 2004). 104

[203] M. Marseguerra, R. Masini, E. Zio, and G. Cojazzi. Variance decomposition-based sensitivity analysis via neural networks. *Reliability Engineering and System Safety*, 79(2):229 – 238, 2003. SAMO 2001: Methodological advances and innovative applications of sensitivity analysis. 104

[204] A. Marrel, B. Iooss, F. Van Dorpe, and E. Volkova. An efficient methodology for modeling complex computer codes with gaussian processes. *Computational Statistics and Data Analysis*, 52(10):4731 – 4744, 2008. 104

[205] I. Chorkendorff and J. W. Niemantsverdriet. *Concepts of Modern Catalysis and Kinetics, 3rd Edition.* Wiley, 2017. 107

[206] L. Weiping, L. Xiaoyan, H. Faming, and F. Mingfu. Prediction of soil water retention curve using bayesian updating from limited measurement data. *Applied Mathematical Modelling*, 76:380–395, 2019. 108

[207] J. M. Emery, M. D. Grigoriu, and R. V. Field Jr. Bayesian methods for characterizing unknown parameters of material models. *Applied Mathematical Modelling*, 40:6395–6411, 2016.

[208] Y. Li, X. Wang, C. Wang, M. Xu, and L. Wang. Non-probabilistic bayesian update method for model validation. *Applied Mathematical Modelling*, 58:388–403, 2018. 108

[209] A. Wirgin. Influence of nuisance parameter uncertainty on the retrieval of the thermal conductivity of the macroscopically-homogeneous material within a cylinder from exterior temperature measurements. *Applied Mathematical Modelling*, 39:5278–5298, 2015. 108

[210] M. Balat, M. Czerniak, and J. M. Badie. Thermal and chemical approaches for oxygen catalytic recombination evaluation on ceramic materials at high temperature. *Applied Surface Science*, 120(3):225–238, 1997. 109

[211] M. Balat-Pichelin, J. M. Badie, R. Berjoan, and P. Boubert. Recombination coefficient of atomic oxygen on ceramic materials under earth re-entry conditions by optical emission spectroscopy. *Chemical Physics*, 291(2):181–194, 2003. 109

[212] L. Bedra and M. Balat-Pichelin. Comparative modeling study and experimental results of atomic oxygen recombination on silica-based surfaces at high temperature. *Aerospace Science and Technology*, 9(4):318–328, 2005. 109

[213] M. Balat-Pichelin, L. Bedra, O. Gerasimova, and P. Boubert. Recombination of atomic oxygen on alpha-al2o3 at high temperature under air microwave-induced plasma. *Chemical Physics*, 340(1):217–226, 2007. 109

[214] J. B. Pallix and R. A. Copeland. Measurement of catalytic recombination coefficients on quartz using laser-induced fluorescence. *Journal of Thermophysics and Heat Transfer*, 10(2):224–233, 1996. 109

[215] D. Stewart. *Determination of surface catalytic efficiency for thermal protection materials - Room temperature to their upper use limit.* 109

[216] S. Sepka, Y. Chen, J. Marschall, and R. A. Copeland. Experimental investigation of surface reactions in carbon monoxide and oxygen mixtures. *Journal of Thermophysics and Heat Transfer*, 14(1):45–52, 2000. 109

[217] Jochen Marschall, Richard Copeland, Helen Hwang, and Michael Wright. *Surface Catalysis Experiments on Metal Surfaces in Oxygen and Carbon Monoxide Mixtures.* 109

[218] Jochen Marschall. *Laboratory determination of thermal protection system materials surface catalytic properties*, chapter 11, page 11 1–32. 2007. 109

[219] Andrea F. Cortesi, Paul G. Constantine, Thierry E. Magin, and Pietro M. Congedo. Forward and backward uncertainty quantification with active subspaces: Application to hypersonic flows around a cylinder. *Journal of Computational Physics*, 407:109079, 2020. 110

[220] F. Sanson, N. Villedieu, F. Panerai, O. Chazot, P. M. Congedo, and T. E. Magin. Quantification of uncertainty on the catalytic property of reusable thermal protection materials from high enthalpy experiments. *Experimental Thermal and Fluid Science*, 82:414–423, 2016. 110, 112

[221] G. O. Roberts and J. S. Rosenthal. Optimal Scaling for Various Metropolis-Hastings Algorithms. *Statistical Science*, 16:351–367, 2001. 112, 159

[222] J. A. Nelder and R. Mead. A simplex method for function minimization. In *Comput. J.*, volume 7 (4), page 308–313, 1965. 115, 159

[223] J. C. Greaves and J. W. Linnett. The recombination of oxygen atoms at surfaces. In *Trans. Faraday Soc.*, volume 54, pages 1323–1330, 1958. 115

[224] J. C. Greaves and J. W. Linnett. Recombination of atoms at surfaces - part 5: Oxygen atoms at oxide surfaces. In *Trans. Faraday Soc.*, volume 55, pages 1346–1354, 1959.

[225] R. A. Young. Measurements of the diffusion coefficient of atomic nitrogen in molecular nitrogen and the catalytic efficiency of silver and copper oxide surfaces. *The Journal of Chemical Physics*, 34:1295, 1961.

[226] P. G. Dickens. Recombination of oxygen atoms on oxide surfaces. part 1.-activation energies of recombination. In *Trans. Faraday Soc.*, volume 60, pages 1272–1285, 1964.

[227] R. A. Hartunian, W. P. Thompson, and S. Safron. Measurements of catalytic efficiency of silver for oxygen atoms and the O-O2 diffusion coefficient. *The Journal of Chemical Physics*, 43:4003, 1965.

[228] A. L. Myerson. Exposure-dependent surface recombination efficiencies of atomic oxygen. *The Journal of Chemical Physics*, 50:1228, 1969.

[229] G. A. Melin and R. J. Madix. Energy accommodation during oxygen atom recombination on metal surfaces. In *Trans. Faraday Soc.*, volume 67, pages 198–211, 1971.

[230] P. Cauquot, S. Cavadias, and J. Amouroux. Thermal energy accomodation from oxygen atoms recombination on metallic surfaces. *Journal of Thermophysics and Heat Transfer*, 12 (2):206–213, 1998.

[231] J. M. Meyers, W. P. Owens, and D. G. Fletcher. Surface catalyzed reaction efficiencies in nitrogen and oxygen plasmas from laser induced fluorescence measurements. In *44th AIAA Thermophysics Conference, AIAA*, volume 31 (2), pages 410–420, 2013.

[232] D. M. Driver and S. Sepka. Side arm reactor study of copper catalysis. In *45th AIAA Thermophysics Conference, AIAA*, 2015-2666. 115

[233] P. J. Diggle and P. J. Ribeiro. *Model-Based Geostatistics*, volume 228(6), pages 1862–1902. Springer-Verlag, New York, 2007. 117

[234] W. Zang, A. Lani, and M. Panesi. Analysis of non-equilibrium phenomena in inductively coupled plasma generators. *Physics of Plasmas*, 23, 2016. 125

[235] R.N. Gupta, J.M. Yos, R.A. Thompson, and K.P. Lee. A Review of Reaction Rates and Thermodynamic and Transport Properties for an 11-Species Air Model for Chemical and Thermal Nonequilibrium Calculations to 30000 K. Technical report, NASA RP-1232, 1990. 145

[236] D. Luís, A. del Val, and O. Chazot. Characterization under Uncertainty of Catalytic Phenomena in Ceramic Matrix Composites Materials for Spacecraft Thermal Protection Systems. In *8th European Conference for Aeronautics and Aerospace Sciences (EUCASS)*, 2019. 147

[237] F. Panerai, J.C. Ferguson, J. Lachaud, A. Martin, M.J. Gasch, and N.N. Mansour. Micro-tomography based analysis of thermal conductivity, diffusivity and oxidation behavior of rigid and flexible fibrous insulators. *International Journal of Heat and Mass Transfer*, 108:801–811, 2017. 149

[238] Harold W. Goldstein. The reaction of active nitrogen with graphite. *The Journal of Physical Chemistry*, 68(1):39–42, 1964. 151

[239] Chul Park and David W. Bogdanoff. Shock-tube measurement of nitridation coefficient of solid carbon. *Journal of Thermophysics and Heat Transfer*, 20(3):487–492, 2006. 151

[240] Toshiyuki Suzuki, Kazuhisa Fujita, and Takeharu Sakai. Graphite nitridation in lower surface temperature regime. *Journal of Thermophysics and Heat Transfer*, 24(1):212–215, 2010. 152, 170, 172, 174

[241] Krishna Sandeep Prata, Timothy K. Minton, and Thomas E. Schwartzentruber. *Air-Carbon Ablation Model for Hypersonic Flight from Molecular Beam Data*. 153

[242] Y. M. Marzouk and H. N. Najm. Dimensionality reduction and polynomial chaos acceleration of bayesian inference in inverse problems. *Journal of Computational Physics*, 2009. 159

[243] D. Le Quang. *Spectroscopic Measurements of Sub- and Supersonic Plasma Flows for theInvestigation of Atmospheric Re-Entry Shock Layer Radiation*. PhD thesis, Université Blaise Pascal,von Karman Institute for Fluid Dynamics, 2014. 162

[244] Eckhard Limpert, Werner A. Stahel, and Markus Abbt. Log-normal Distributions across the Sciences: Keys and Clues. *BioScience*, 51(5):341–352, 2001. 169

[245] E. Anfuso, A. Bellemans, and O. Chazot. Investigation of aerothermodynamic phenomena of aerospace flight in ground testing facilities. 12th VKI Symposium of Scientific Research, March 2021. 191, 192

[246] A. Hayes. HyCUBE: A reconfigurable cubesat-like platform for hypersonic flight testing. 11th Ablation Workshop, September 2019. 192

[247] M. Capriati, T. E. Magin, and P. M. Congedo. Simulation of a 3D unsteady hypersonic flow under uncertainty. 11th VKI Symposium of Scientific Research, May 2020. 192

[248] N. Leoni, P. M. Congedo, O. P. Le Maître, and M. Rodio. Bayesian Inference of Model Error in Imprecise Models. In *WCCM-ECCOMAS*, Paris, France, Jan 2021. 193

[249] Chul Park, John T. Howe, Richard L. Jaffe, and Graham V. Candler. Review of chemical-kinetic problems of future nasa missions. ii - mars entries. *Journal of Thermophysics and Heat Transfer*, 8(1):9–23, 1994. 203

[250] *A new technique for low-to-high altitude predictions of ablative hypersonic flowfields*, June 1991. 203

[251] J. Wilson. Ionization rate of air behind high-speed shock waves. *The Physics of Fluids*, 9(10):1913–1921, 1966. 203

[252] M. Capitelli, C. Gorse, S. Longo, and D. Giordano. *Transport properties of high temperature air species*. 203

[253] James R. Stallcop, Harry Partridge, and Eugene Levin. Analytical fits for the determination of the transport properties of air. *Journal of Thermophysics and Heat Transfer*, 10(4):697–699, 1996. 203

[254] Michael J. Wright, Helen H. Hwang, and David W. Schwenke. Recommended collision integrals for transport property computations part ii: Mars and venus entries. *AIAA Journal*, 45(1):281–288, 2007. 204

[255] A. Bellemans and T. E. Magin. Calculation of collision integrals for ablation species. In *8th European Conference on Aerodynamics for Space Vehicles, Lisbon, Portugal, March, 2-6*, 2015. 204

[256] Michael J. Wright, Deepak Bose, Grant E. Palmer, and Eugene Levin. Recommended collision integrals for transport property computations part 1: Air species. *AIAA Journal*, 43(12):2558–2564, 2005. 204

[257] Eugene Levin and Michael J. Wright. Collision integrals for ion-neutral interactions of nitrogen and oxygen. *Journal of Thermophysics and Heat Transfer*, 18(1):143–147, 2004. 204

Titre : Calibration Bayésienne et évaluation de modèles et expériences d’interaction gaz-surface pour les plasmas d’entrée atmosphérique

Mots clés : Entrée Atmosphérique; Inférence Bayésienne; Interaction Gaz-Surface; Ablation; Catalyse; Quantification d’Incertitude

Résumé : L’étude des phénomènes d’interaction gaz-surface pour les véhicules d’entrée atmosphérique est basée sur le développement de modèles théoriques prédictifs et sur les capacités des installations expérimentales actuelles. Toutefois, en raison de la complexité de la physique et des divers phénomènes qui doivent être étudiés dans ces installations, les simulations tant numériques qu’expérimentales génèrent des données qui présentent des incertitudes. Cependant, il est courant dans le domaine de l’aérothermodynamique de recourir à des méthodes de calibration et de validation non adaptées à un traitement rigoureux de ces incertitudes.

Cette thèse étudie le processus d’inférence scientifique et ses ramifications dans certaines expériences d’interaction gaz-surface. Ses principales contributions sont l’amélioration et la reformulation de la calibration de modèles en tant que problème statistique inverse et l’extension résultante des bases de données actuelles pour la catalyse et l’ablation. La calibration des modèles utilise le formalisme Bayésien où la caractérisation complète des distributions de probabilités postérieures des paramètres sélectionnés est calculée.

La première partie de la thèse présente une revue des modèles théoriques, des expériences et des codes de simulation numérique utilisés pour étudier la catalyse et l’ablation dans le Plasmatron, la soufflerie à plasma de l’Institut von Karman. Cette partie se termine par un résumé des sources possibles d’incertitude présentes dans les données théoriques-numériques et expérimentales. Ensuite, les méthodes utilisées pour traiter mathématiquement ces sources d’incertitude sont présentées en détail.

La deuxième partie présente les différentes contributions originales de cette thèse. Pour les matériaux catalytiques, une méthodologie de vraisemblance optimale pour l’inférence Bayésienne est développée. Cette méthodologie offre une caractérisation complète de l’incertitude des paramètres catalytiques avec une diminution de 20% de l’écart type par rapport aux travaux antérieurs. En utilisant cette méthodologie, une stratégie de test produisant les données expérimentales de catalyse les plus informatives à ce jour est proposée. Ensuite, des expériences et des analyses stochastiques sont effectuées, enrichissant les bases de données expérimentales de catalyse existantes pour les composés à matrice céramique à l’aide d’estimations précises de l’incertitude.

La dernière contribution est la reformulation du problème d’inférence des efficacités de réaction de l’azote à la surface d’un matériau ablatif en graphite à partir des données de soufflerie à plasma. Il s’agit de la première étude dans la littérature où différentes observations de la même expérience sont utilisées ensemble pour évaluer leur cohérence et les paramètres d’ablation qui en résultent. Une loi d’Arrhenius stochastique est déduite en utilisant toutes les données disponibles, étendant la gamme de conditions à des températures de surface plus basses, là où il n’y a pas de données expérimentales fiables. L’incertitude épistémique qui affecte la définition du modèle et les conditions aux limites d’ablation sont étudiées par des méthodes de test d’hypothèses. L’incertitude finale sur l’efficacité de la réaction azotée est obtenue en moyennant les résultats obtenus avec les différents modèles.

Cette thèse met en évidence que le processus d’inférence scientifique peut également imposer des hypothèses sur la nature du problème et avoir un impact sur la manière dont les chercheurs parviennent à des conclusions sur leur travail. En fin de compte, cette thèse contribue aux premiers efforts d’introduction de techniques précises et rigoureuses de quantification de l’incertitude dans le domaine de recherche de l’entrée atmosphérique. Les méthodologies présentées ici permettront in fine le développement de modèles prédictifs avec estimation de niveaux de confiance.

Title : Bayesian calibration and assessment of gas-surface interaction models and experiments in atmospheric entry plasmas

Keywords : Atmospheric Entry; Bayesian Inference; Gas-surface Interaction; Ablation; Catalysis; Uncertanity Quantification

Abstract : The investigation of gas-surface interaction phenomena for atmospheric entry vehicles relies on the development of predictive theoretical models and the capabilities of current experimental facilities. However, due to the complexity of the physics and the various phenomena that need to be investigated in ground-testing facilities, both numerical and experimental processes generate data subjected to uncertainties. Nevertheless, it remains a common practice in the field of aerothermodynamics to resort to calibration and validation methods that are not apt for rigorous uncertainty treatment.

This thesis investigates the process of scientific inference and its ramifications for selected gas-surface interaction experiments. Its main contributions are the improvement and re-formulation of model calibrations as statistical inverse problems with the consequent extension of current databases for catalysis and ablation. The model calibrations are posed using the Bayesian formalism where a complete characterization of the posterior probability distributions of selected parameters are computed.

The first part of the thesis presents a review of the theoretical models, experiments and numerical codes used to study catalysis and ablation in the context of the von Karman Institute's Plasmatron wind tunnel. This part ends with a summary on the potential uncertainty sources present in both theoretical-numerical and experimental data. Subsequently, the methods used to deal with these uncertainty sources are introduced in detail.

The second part of the thesis presents the various original contributions of this thesis. For catalytic materials, an optimal likelihood framework for Bayesian calibration is proposed. This methodology offers a complete uncertainty characterization of catalytic parameters with a decrease of 20% in the standard deviation with respect to previous works. Building on this framework, a testing strategy which produces the most informative catalysis experiments to date is proposed. Experiments and consequent stochastic analyses are performed, enriching existing catalysis experimental databases for ceramic matrix composites with accurate uncertainty estimations.

The last contribution deals with the re-formulation of the inference problem for nitridation reaction efficiencies of a graphite ablative material from plasma wind tunnel data. This is the first contribution in the literature where different measurements of the same flowfield are used jointly to assess their consistency and the resulting ablation parameters. An Arrhenius law is calibrated using all available data, extending the range of conditions to lower surface temperatures where no account of reliable experimental data is found. Epistemic uncertainties affecting the model definition and ablative wall conditions are gauged through various hypothesis testing studies. The final account on the nitridation reaction efficiency uncertainties is given by averaging the results obtained under the different models.

This thesis highlights the fact that the process of scientific inference can also carry deep assumptions about the nature of the problem and it can impact how researchers reach conclusions about their work. Ultimately, this thesis contributes to the early efforts of introducing accurate and rigorous uncertainty quantification techniques in atmospheric entry research. The methodologies here presented go in line with developing predictive models with estimated confidence levels.

Institut Polytechnique de Paris
91120 Palaiseau, France